

DISS. ETH NO. 23149

Toward using atmospheric carbon dioxide observations to estimate the biospheric carbon flux of the Swiss Plateau

A dissertation submitted to
ETH ZURICH

for the degree of
Doctor of Sciences

presented by
BRIAN JOHANNES ONEY
MSc. Global Change Ecology., Uni. Bayreuth
born November 9, 1984
citizen of USA

accepted on the recommendation of
Prof. Dr. Nicolas Gruber, examiner
Dr. Dominik Brunner, co-examiner
Dr. Christoph Gerbig, co-examiner

2016

Contents

Abstract	v
Zusammenfassung	vii
1 Background	1
1.1 “Bottom-up” carbon flux estimation	5
1.2 “Top-Down”, inverse carbon flux estimation	7
1.3 Regional-scale inverse carbon flux modeling	11
1.4 This work	17
2 Atmospheric carbon measurements in the CarboCount CH Project	19
2.1 Introduction	19
2.2 Reference gases	20
2.3 Measurement system at Lägern-Hochwacht	21
2.4 Measurement calibration and uncertainty	22
2.5 Ambient and reference gas measurements	31
2.6 Practical monitoring considerations	33
2.7 Conclusions	36
3 The CarboCount CH sites: characterization of a dense greenhouse gas observation network	39
3.1 Abstract	40
3.2 Introduction	40
3.3 Data and methods	42
3.4 Results and discussion	47
4 A CO₂-based method to determine the regional biospheric signal in atmospheric CO₂	61
4.1 Abstract	62
4.2 Introduction	62
4.3 CO ₂ data analysis framework	64
4.4 Data and methods	65
4.5 Results & discussion	71
4.6 Conclusions	85
5 Synthesis and outlook	87
5.1 Summary	87
5.2 Lessons learned	89
5.3 Outlook	90
A Measurement data processing code	95
A.1 Introduction	95
A.2 Data Processing and Management	96

Curriculum vitae	131
Thanks	133

Abstract

The lack of knowledge of the terrestrial carbon cycle translates into uncertain climate change projections due to the strong, yet uncertain relationship between terrestrial carbon fluxes and climate. Atmospheric carbon observations (defined here as the sum of CO₂, CH₄, and CO) integrate information on carbon fluxes on Earth's surface, which can be used to assess the understanding of these processes through inverse carbon flux modeling. Due to the high spatial and temporal variability of terrestrial carbon fluxes, atmospheric observations representative of the regional scale ($\sim 10\text{--}1000\text{ km}$) are necessary to better understand these fluxes. My contributions have aided the goal of development of a comprehensive carbon observation and modeling system. This system aims to better quantify and understand natural fluxes and anthropogenic emissions over the Swiss Plateau, as part of the CarboCount project, using observations from its newly established network of four sites: Beromünster, Frübüel, Gimmiz, and Lägern-Hochwacht.

The accurate measurement of atmospheric carbon is a prerequisite of inverse carbon flux modeling. Therefore, reference gas cylinders were prepared, their mixing ratios referenced to the respective international scales, and distributed to the observation sites, in order to complete site construction. The simple measurement system at Lägern-Hochwacht has, except for a single pump failure and an extended failure to store data, successfully operated since August 2012 and delivered data sets with a temporal coverage of more than 97 %. Therefore, a detailed description of its instrumentation is presented. The measurements of all four sites were repeatedly evaluated for quality with the reference gases. The uncertainty assessment of these measurements and their temporal aggregation are presented and discussed. Finally, gathered experience is offered for the future long-term, cost-effective monitoring efforts of atmospheric carbon.

The value of an atmospheric carbon monitoring site to regional-scale studies depends on the information contained in its observations. The seasonal and diurnal meteorological variability of the lower troposphere play an important role in determining this information. Therefore, the characteristics relevant to forthcoming regional scale modeling studies of the established observation sites were investigated, and strengths and weaknesses of the site's data sets as well as the employed atmospheric transport models are discussed. Due to local topography, tower characteristics, and site elevation, among others, observations differ between sites, especially during nighttime. However, these observations differ much less during daytime, owing to intense daytime vertical mixing. From the analysis of simulated surface sensitivity, it is likely that atmospheric carbon observations consistently representative of the Swiss Plateau are provided by Beromünster and Lägern-Hochwacht. On the other hand, temporal filtering of the observations from Gimmiz and Frübüel is likely necessary to remove local influence, due likely to the model's inability to accurately represent transport in the lower troposphere. Furthermore, due to the complex terrain directly surrounding Lägern-Hochwacht, similar filtering of its observations may be also necessary. These observations contain much information reflecting the complexity of the Swiss Plateau landscape, and will assuredly provide a challenge for future inverse modeling studies.

To constrain biospheric carbon fluxes with carbon dioxide CO₂ observations, it is necessary to first isolate the biospheric component of these observations. The standard procedure to accomplish this entails using an

atmospheric transport model to simulate the anthropogenic CO₂ component and the initial or background CO₂ mixing ratios. However, this introduces considerable uncertainty into the biospheric component and thereby the inverted biospheric carbon fluxes. With this in mind, a method to isolate the biospheric portion of CO₂ observations using carbon monoxide (CO) observations is developed, presented, and evaluated using observations from the Beromünster and Lägern-Hochwacht sites. Basically, this method scales CO observations above background CO mixing ratios to anthropogenic CO₂ using the observed wintertime CO₂/CO regional signal relationship. The evaluation suggests that the proposed method substantially improves our ability to determine the biospheric CO₂ signal. Performance of the method decreased when anomalously CO-enriched air masses were brought by northeasterly winds. Qualitative interpretation of the resulting biospheric signals confirms the expectation that the Swiss Plateau acted as a carbon sink during the major growing season of 2013 (May to August). Furthermore, the biospheric signals and related carbon fluxes are sensitive to solar radiation, precipitation, and ambient air temperature. Here, higher air temperatures (> 20°C) likely correlate with a diminished strength of the Swiss Plateau carbon sink.

This work not only contributed to the successful installation and operation of a new observation network, but also lays the foundations for future inverse carbon flux modeling studies. Accomplishments include: gaining invaluable observation site operation experience, demonstration of the rich information observed at the observation sites, indication which sites are suited to regional-scale carbon studies, and the development of a method to isolate the biospheric signal from CO₂ observations while circumventing problems of the standard approach. All of this sets the stage both for future observation endeavors and provides detailed insight for future carbon flux inversion work.

Zusammenfassung

Mangelndes Wissen über den terrestrischen Kohlenstoffkreislauf führt zu unsicheren Projektionen des Klimawandels aufgrund der starken, aber unsicheren Beziehung zwischen terrestrischen Kohlenstoffflüssen und dem Klima. Atmosphärische Kohlenstoffmessungen (hier die Summe von CO_2 , CH_4 , und CO) integrieren Informationen über Kohlenstoffflüsse auf der Erdoberfläche, die verwendet werden können, um das Verständnis dieser Prozesse zu beurteilen anhand inverser Modellierung der Kohlenstoffflüsse. Aufgrund der hohen räumlichen und zeitlichen Variabilität terrestrischer Kohlenstoffflüsse, sind CO_2 -Beobachtungen notwendig, die für regionalen Skalen (~ 10 – 1000 km) repräsentativ sind, um diese Flüsse besser zu verstehen. Diese im Rahmen des CarboCount Projekts durchgeführte Arbeit zielt darauf ab, das Verständnis der Kohlenstoffflüssen im Schweizer Mittelland mit Beobachtungen von vier neu etablierten Standorte zu erweitern: Beromünster, Frübüel, Gimmiz und Lägern-Hochwacht.

Die inverse Kohlenstoffflussmodellierung setzt die genaue Messung von atmosphärischem Kohlenstoff voraus. Deshalb wurden Referenzgasflaschen vorbereitet, ihre Mischungsverhältnisse auf internationalen Messskalen bestimmt und auf die Messstationen verteilt, um den Standortaufbau zu vervollständigen. Das Messsystem bei Lägern-Hochwacht hat ausser eines Pumpenausfalls seit August 2012 erfolgreich gemessen und lieferte Datensätze mit einer zeitlichen Abdeckung von mehr als 97 %. Darum wird eine ausführliche Beschreibung der Instrumentierung von diesem Messstandort vorgestellt. Mit den Referenzgasen wurden die Messungen aller vier Standorte laufend auf Qualität geprüft. Die Unsicherheitsabschätzung dieser Messungen und ihre zeitliche Aggregation werden vorgestellt und besprochen. Schlussendlich werden Empfehlungen für die langfristige und kosteneffektive Überwachung von atmosphärischen Kohlenstoff gegeben.

Der Wert eines atmosphärischen Kohlenstoffmessstandorts für Studien der regionalen Skala ist abhängig von der in den Beobachtungen enthaltenen Information. Die saisonale und tägliche meteorologische Variabilität der unteren Troposphäre bestimmt zu einem grossen Teil diese Informationen. Darum wurden die für bevorstehende Modellstudien relevante Eigenschaften der etablierten Messstandorte untersucht, und die Stärken und Schwächen der dazugehörigen Datensätze sowie die verwendeten atmosphärischen Transportmodelle diskutiert. Durch lokale Topographie und Messstandorteigenschaften wie zum Beispiel die Höhe des Einlasses, waren Beobachtungen zwischen den Standorten unterschiedlich, insbesondere während der Nacht. Aufgrund der intensiven vertikalen Durchmischung unterschieden sie sich tagsüber hingegen nur wenig. Anhand einer Analyse der Sensitivität gegenüber der Landesoberfläche, ist es wahrscheinlich dass die atmosphärische Kohlenstoffmessungen von Beromünster und Lägern-Hochwacht generell repräsentativ für das Schweizer Mittelland sind. Für die Standorte Gimmiz und Frübüel ist andererseits eine zeitliche Filterung notwendig um lokale Einflüsse zu entfernen, da das aktuelle Transportmodell die in der unteren Troposphäre vorhandene meteorologische Variabilität nicht ausreichend akkurat darstellen kann. Weiterhin könnte wegen des unmittelbar an Lägern-Hochwacht angrenzenden räumlich komplexen Geländes eine ähnliche Filterung der Beobachtungen erforderlich sein. Die Datensätze spiegeln die Komplexität des Schweizer Mittellands wieder, die sicher eine Herausforderung für künftige inverse Modellierungsstudien wieder.

Um biosphärische Kohlenstoffflüsse mit Kohlendioxidmessungen (CO_2) zu bestimmen, ist es notwendig die

biosphärische Komponente von diesen Beobachtungen zu trennen. Das Standardverfahren dazu verwendet ein atmosphärisches Transportmodell für die Simulation der anthropogenen CO₂ Komponente sowie die CO₂ Randbedingungen oder Hintergrundmischungsverhältnissen. Aber dies verursacht in der Regel erhebliche Unsicherheiten in der biosphärische Komponente, und damit in die invertierten biosphärischen Kohlenstoffflüsse. Ein in diesem Projekt entwickeltes Verfahren zur Trennung der biosphärischen Komponente von CO₂-Beobachtungen unter Verwendung von Kohlenmonoxidmessungen (CO) soll vorgestellt und anhand der Beobachtungen von den Beromünster und Lägern-Hochwacht Messstandorten evaluiert werden. Grundsätzlich skaliert diese Methode CO-Beobachtungen über den Hintergrundmischungsverhältnisse zu der anthropogenen Komponente von CO₂ mit Hilfe der während des Winters beobachteten Verhältnisse zwischen den regionalen CO und CO₂ Signalen. Die Bewertung deutet darauf hin, dass die vorgeschlagene Methode unsere Fähigkeit, das biosphärische CO₂ Signal zu bestimmen, deutlich verbessert. Die Verbesserung fällt aber geringer aus, wenn Luftmassen, die ungewöhnlich hoch mit CO angereichert sind, aus dem Nordosten zur Schweiz fließen. Qualitative Interpretation der resultierenden biosphärische Signale bestätigen die Erwartung, dass das Schweizer Mittelland als Kohlenstoffs Senke während der Hauptvegetationszeit des Jahres 2013 (Mai bis August) fungierte. Weiterhin reagieren die Biosphärensignale und die damit verbundenen Kohlenstoffflüssen wie von der Literatur zu erwarteten auf Sonneneinstrahlung, Niederschlag und Lufttemperatur. Dazu beobachten wir eine positive Korrelation zwischen höheren Lufttemperaturen ($> 20^{\circ}\text{C}$) und einer weniger starken Kohlenstoffs Senke des Schweizer Mittellands.

Zu den wichtigen Leistungen der Arbeit gehört die Sammlung von Betriebserfahrungen auf den Messstandorten, die von unschätzbarem Wert sind, das Erstellen erster Datenanalysen, das Finden von Hinweisen darauf welche Beobachtungen geeignet sind um auf regionalen Skalen Kohlenstoffflussstudien durchzuführen, und die Entwicklung einer Methode zur Trennung des biosphärischen CO₂ Signals ohne Modell- und Inventarunsicherheiten zu übertragen. Alles in allem schafft dies eine fundierte Grundlage für künftige Messkampagnen und stellt einen guten Anknüpfungspunkt für nachfolgende Studien zu Kohlenstoffflussinversionen dar.

Chapter 1

Background

Atmospheric carbon consists mainly of carbon dioxide (CO_2) and methane (CH_4). Before the Industrial Revolution, their atmospheric mole fractions, in molar parts per million (ppm) of CO_2 and CH_4 varied from 180 to 280 ppm, and from 0.35 to 0.8 ppm during the last 800,000 years, respectively, along with glacial cycles and thereby global temperature [Petit *et al.*, 1999; Siegenthaler *et al.*, 2005; Loulergue *et al.*, 2008; Lüthi *et al.*, 2008]. With increasing technological progress, the Industrial Revolution began around 1750 AD, and the ability to harvest and consume natural resources increased vehemently. Coal and, later on, oil began to be harvested and burned at unprecedented rates, which caused the atmospheric mole fractions of CO_2 to increase. Growing scientific concern about the influence of increasing CO_2 mole fractions, a persistent greenhouse gas, on global temperature [Arrhenius, 1896; Callendar, 1949], eventually lead to the beginning of long-term monitoring in 1958 at Mauna Loa, Hawai'i and at the South Pole, Antarctica [Keeling, 1960]. Since then, monitoring of CH_4 , a more potent but less persistent greenhouse gas, was initiated in the early 1980s [Dlugokencky *et al.*, 1998]. Towards the end of 2015, atmospheric mole fractions of CO_2 and CH_4 were approximately 400 ppm and 1.9 ppm, respectively.

During the period 2000-2010, observations indicate that 200 Pg (Pg: 10^{15} grams) of carbon flowed annually between the atmosphere and the Earth's surface (Figure 1.1), mainly in the form of CO_2 . During the seasonal cycle, land ecosystems breath in ~ 123 Pg of carbon during the solar summer [Beer *et al.*, 2010], which is used and respired shortly thereafter or stored as plant tissue, most of which dies and decomposes as solar winter begins. This behavior is highly dependent on weather and climate. The marine biosphere exhibits similar behavior, but has less amplitude (± 80 PgC) and is highly dependent on ocean circulation and carbonate chemistry. Before the Industrial Revolution, these large, seasonal fluxes were smaller (Figure 1.1, black arrows) and roughly balanced each other in the course of a year. However, since then the carbon cycle has intensified with the increasing atmospheric carbon mole fractions, and accumulations or sinks of carbon in the ocean and land biosphere have also increased (Figure 1.1, red arrows).

Paleoclimatic studies indicate that the carbon cycle was tightly coupled with climate [Siegenthaler *et al.*, 2005]. The scientific consensus about the current temperature anomaly is that CO_2 mole fractions are very likely driving climate [Stocker *et al.*, 2013]. Therefore, to understand future climate change, we must understand the global carbon cycle. To this end, we must first understand and reproduce the unnatural or anthropogenic fluxes of CO_2 into the global carbon cycle from 1750 to now (until 2011; Figure 1.2). From historical statistics of fossil fuel use and cement production [Andres *et al.*, 2012], and land-use change [Houghton *et al.*, 2012], we can reconstruct past anthropogenic CO_2 emissions. From atmospheric mole fractions, we precisely know that 240 ± 10 PgC has remained in the atmosphere. From profile observations of oceanic pCO_2 and inverse modeling, stable isotope ratios of CO_2 [Ciais *et al.*, 1995], as well as from observations of atmospheric oxygen [Keeling *et al.*, 1993; Battle *et al.*, 2000], we have a confident estimate of -155 ± 30 PgC that has been

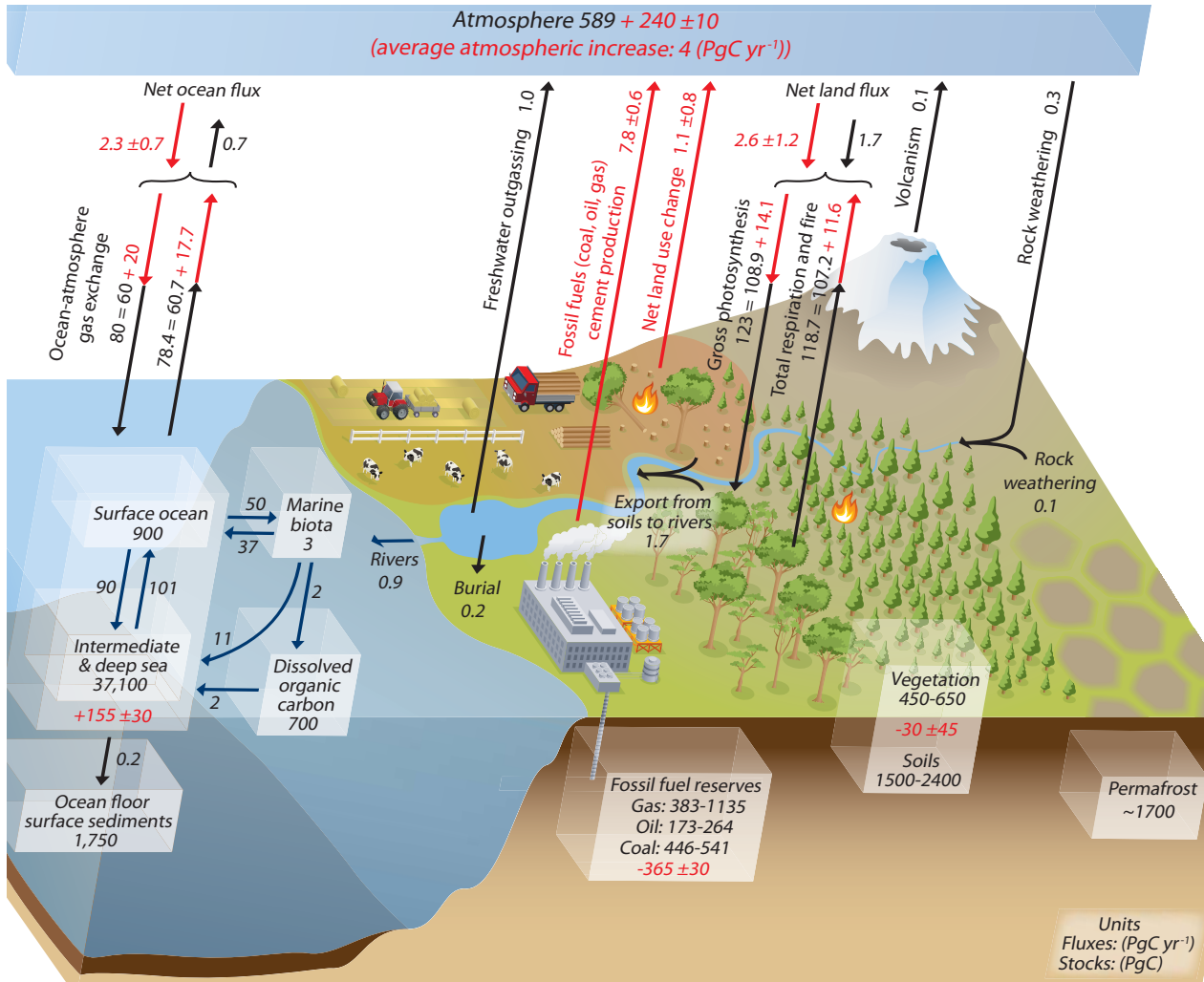


Figure 1.1: The global carbon cycle depicted as pools and fluxes. Arrows and their annotations denote annual carbon fluxes (PgC yr^{-1}). Boxes represent the carbon pools (PgC). Preindustrial flux and pool magnitudes are black and additional anthropogenic fluxes and pools are red. Figure is slightly modified from *Ciais et al.* [2013].

absorbed by the ocean [*Sabine et al.*, 2004; *Khaliwala et al.*, 2013]. Because there is little scientific consensus about the directly determined flux of atmospheric, anthropogenic CO_2 into the natural land biosphere, after accounting for land use change ($+180 \pm 80 \text{ PgC}$), the magnitude of the land biospheric flux of $-160 \pm 90 \text{ PgC}$ (1750–2011, from Table 6.1 in *Ciais et al.* 2013) is determined by subtracting atmospheric accumulation and oceanic anthropogenic carbon uptake from known anthropogenic emissions (Figure 1.2). The anthropogenic carbon flux into natural land ecosystems, or the terrestrial biosphere, exhibits two interesting features. First, interannual variability of this sink is large and appears to co-vary with climate, especially drought events [*Ciais et al.*, 2005; *Peters et al.*, 2007; *Reichstein et al.*, 2007; *Phillips et al.*, 2009]. Second, this sink appears to be increasing in magnitude [*Ballantyne et al.*, 2012]. A major goal of understanding the carbon cycle is to answer the question whether this sink will continue to increase, or will climate change cause this sink to become a source.

Terrestrial carbon cycle dynamics are difficult to predict due to the complex relationships between weather and climate, and the numerous and diverse terrestrial ecosystems of the land biosphere [*Heimann and Reichstein*, 2008]. That is, general scientific consensus does not exist about the reaction of the land biosphere to rising

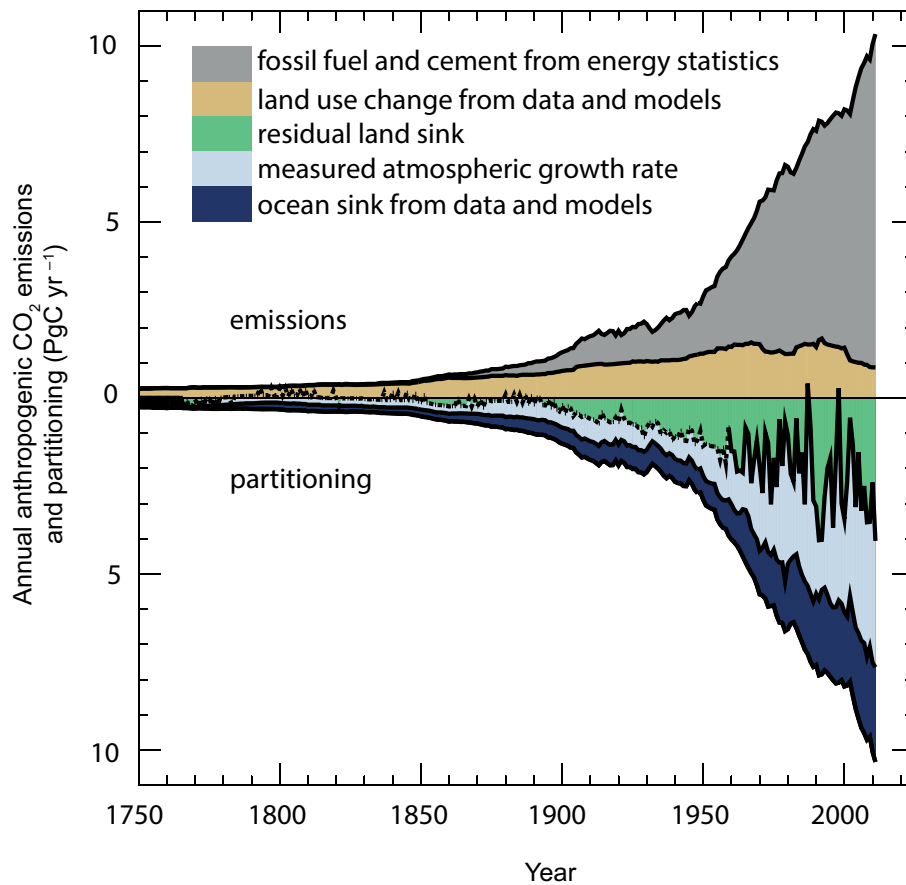


Figure 1.2: Partitioning of annual anthropogenic CO₂ emissions from 1750 to 2011 (positive) between the three major sinks: atmosphere, ocean, and land. Figure is slightly modified from *Ciais et al.* [2013].

temperatures, rising CO₂ mole fractions i.e. the atmospheric fertilization affect [*Prentice and Harrison*, 2009], and a changing, and possibly intensifying hydrological cycle [*Ciais et al.*, 2013]. The uncertainties in future climate projections are numerous, but the lack of consensus about the relationship between climate and the terrestrial carbon cycle is mainly responsible for the spread of future climate projections (Figure 1.3). This contrasts with consensus about the reaction of the ocean carbon cycle to these drivers. Therefore, terrestrial carbon cycle scientists are tasked with explaining this contemporary anthropogenic carbon flux into the land biosphere.

The carbon cycle is an immense and wondrous phenomenon of planet Earth, and the rest of this thesis chapter briefly introduces the range of accepted methods to determine the carbon flux from the land biosphere to the atmosphere. After partial review of the methods to determine the terrestrial carbon flux, the focus shifts to the study of regional-scale carbon fluxes and sets the stage for the scientific contributions of this thesis. This lack of review will hopefully be excused given the breadth and depth of scientific inquiry into the global carbon cycle up to this point in time, and given the scope of this thesis. For a comprehensive review of carbon cycle literature, please see the Intergovernmental Panel on Climate Change's fifth synthesis report [*Stocker et al.*, 2013], specifically Chapter 6 [*Ciais et al.*, 2013]. For ongoing updates of the magnitudes of these fluxes please see *Le Quéré et al.* [2015].

Natural carbon fluxes at the land surface include vegetation photosynthesis and respiration where plants take in CO₂ through their stomata and, together with the sun's rays and water, synthesize sugar, also

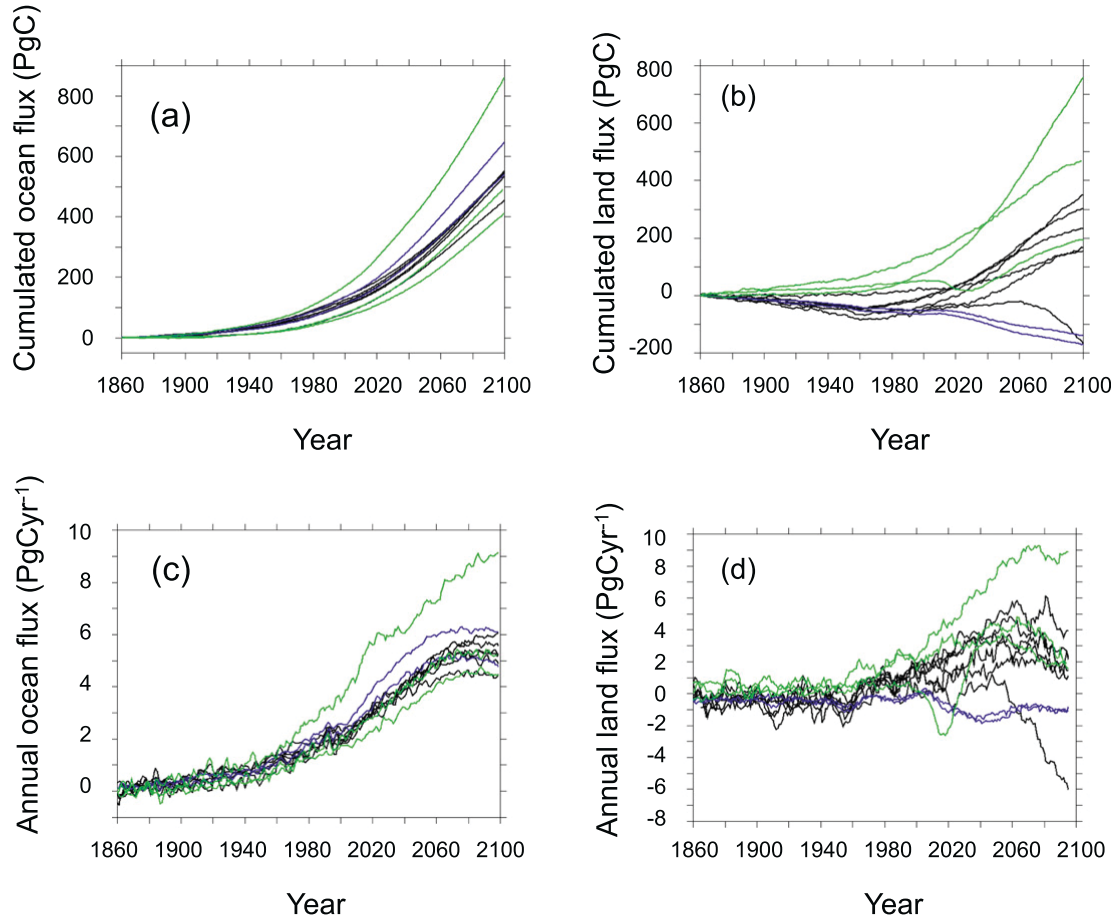


Figure 1.3: Range of accumulated (PgC) and annual carbon flux (PgCyr^{-1}) from the atmosphere into the ocean or land surface as estimated by land surface models, which are driven by CO_2 emissions, and simulate the feedbacks between the carbon cycle and climate differently. The figure and simulations are from the fifth phase of the Coupled Model Intercomparison Project [CMIP5; *Friedlingstein et al.*, 2014].

known as gross primary production (GPP), which is stored for later use or used shortly thereafter, and respired back to the atmosphere as CO_2 , also known as autotrophic respiration (RA). Not all of this carbon is released back to the atmosphere within the lifetime of the plant. Plants concentrate carbon in the form of plant tissue, which can fall prey to herbivores or burn, also resulting in the release back to the atmosphere. Heterotrophic respiration (RH) describes the consumption or decomposition of organic matter by animals and microorganisms, mainly soil biota, and subsequent release to the atmosphere as CO_2 . On longer timescales, the soil carbon, which is not metabolized and respired by the soil biota, is either retained and buried, or is washed into the oceans by rivers [*Regnier et al.*, 2013; *Le Quéré et al.*, 2015]. This natural cycle can also be disturbed by fire, insects, among other natural calamities.

Unnatural fluxes caused by human activity, henceforth anthropogenic, mainly include fossil fuel and cement production emissions, and emissions from land-use change. Fossil fuel emissions are determined using historical fuel consumption [*Andres et al.*, 2012]. Land-use change carbon fluxes result from the initial land-use change and release of carbon, as well as from the following uptake of carbon of mainly crops or grasslands that replaced the original land cover [*Houghton*, 2003].

There are many approaches to determine the carbon fluxes over land. These tend to favor either extrapolation of small-scale (1–1000 m) observations to large-scale areas (Section 1.1), or partition global-scale observations

into small-scale components (Section 1.2). The latter can be adapted and supplemented with approaches to also best represent the small-scale observations (Section 1.3).

1.1 “Bottom-up” carbon flux estimation

A challenge of contemporary land carbon flux studies is to construct spatially and temporally accurate anthropogenic and biospheric flux inventories. Because it is unfeasible to exhaustively measure carbon fluxes at all land surfaces, one is forced to scale local observations up to larger areas. Therefore, assumptions need to be made about how fluxes behave elsewhere, which introduces an uncertainty of extrapolation.

1.1.1 Spatially explicit anthropogenic carbon fluxes

Total estimates of anthropogenic emissions are well-known from statistics of fuel consumption and cement production, although their uncertainty increases with their magnitude, as it has in recent decades [Ballantyne *et al.*, 2015]. In an atmospheric transport modeling context, these emissions need to be spatially and temporally disaggregated, which is a formidable task. For example, annual national greenhouse gas emissions are reported to the United Nations Framework Convention on Climate Change (UNFCCC), and these can be disaggregated based on spatial population density or consumption, or a combination thereof, among others. Furthermore, seasonal variation of fuel consumption rates also needs to be taken into account, but vary between and within countries. Much work has gone into constructing consistent temporally and spatially resolved emission inventories, e.g. for the US [Gurney *et al.*, 2009], Europe [Ciais *et al.*, 2010a; Thiruchittampalam, 2014], and the world [Olivier *et al.*, 2005, 2011]. Nonetheless, these inventories have considerable uncertainties.

The land-use change flux since 1750 (180 ± 80 PgC) is the least certain of the anthropogenic fluxes. The bookkeeping approach [Houghton, 1999] compiles historical estimates of land-use change and applies a model of the net carbon flux caused by the initial land-use change (e.g. deforestation) and recovery or land-use. Land surface models and remote-sensing data (see below) have also been employed to improve estimates of the land-use change flux. The bookkeeping approach remains the preferred method, but all of three approaches are roughly consistent [Ciais *et al.*, 2013].

1.1.2 Observations of the land biosphere

Relative to the anthropogenic fluxes, land biosphere fluxes are much less certain. This immense task has been approached from many perspectives, and include observations and simulations from:

1. Direct flux observations using eddy covariance methods,
2. Forest growth inventories, and
3. Satellite observations of vegetation distribution and activity.

Direct surface carbon flux observations are derived from the correlation of simultaneous high-frequency measurements of CO₂ and the vertical wind speed [Baldocchi *et al.*, 1988; Foken, 2008]. These observations have been carried out in the global long-term observation network called FluxNet [Baldocchi *et al.*, 2001]. They have proven invaluable to investigate the response of the observed land cover type to climate, such as precipitation, temperature, and incoming solar radiation [e.g. Law *et al.*, 2002], and have contributed much to understanding the terrestrial carbon cycle. These observations are however representative only of a local scale (< 1 km).

Inventories of timber and forest growth maintained by forest agencies around the world also record CO₂ uptake on longer time scales (> 10 years) as forest biomass. According to *Pan et al.* [2011] forests may account for the entire annual terrestrial carbon sink of approximately -2 PgC. Taking the vegetation pool from Figure 1.1 as 550 PgC, and the global forest carbon pool from *Pan et al.* [2011] approximately 80 % of the vegetation carbon pool takes the form of a tree. Indeed, most of land-use change emissions can be attributed to deforestation [*Houghton*, 2003], which, since the beginning of the twentieth century, has occurred mainly in the tropics, as tropical countries have developed [*Houghton*, 2003].

Satellite imagery has enabled the long-term remote sensing of land surfaces since the launch of the first Landsat satellite in 1972. The extensive Landsat imagery has enabled the study of large-scale land cover change, most importantly for forest cover change [*Hansen et al.*, 2013]. Long-term observations of seasonal variation in vegetation greenness have also been especially fruitful for recording large-scale vegetation dynamics [*Stöckli and Vidale*, 2004], especially in under-sampled regions [*Anyamba and Tucker*, 2005; *Beck et al.*, 2006]. Recently, the ability to directly observe plant photosynthesis and thereby GPP with measurements of fluorescence has boosted understanding of short-term carbon cycle dynamics [*Frankenberg et al.*, 2011, 2014]. Also, the LIDAR (light detection and ranging) retrievals of forest canopy structure allows assessment of the vertical structure and serve as a proxy for carbon stocks. This has recently been particularly useful for under-sampled tropical regions [*Saatchi et al.*, 2011; *Baccini et al.*, 2012]. Furthermore, synthetic aperture radar (SAR) can also directly map biomass and thus carbon stocks [*Le Toan et al.*, 2011].

1.1.3 Integration and upscaling of land biosphere observations

Integration of the mentioned direct or indirect observations of natural carbon fluxes can take many forms. For example, remotely sensed data can provide detailed land cover maps, phenology, and indirect photosynthesis information to a land surface model [e.g. *Stöckli et al.*, 2008]. Land surface models are important components of weather and climate models and have originally been developed to simulate the exchange of heat, momentum and water between the land and the atmosphere. As vegetation plays an important role in these exchange fluxes, the coverage and properties of vegetation need to be properly represented.

Simple land surface models used in numerical weather prediction attempt to capture the short-term variability of heat and water surface fluxes and are driven by short-term (< 30 days) weather, where vegetation distribution remains constant and disturbances are ignored [*Noilhan and Planton*, 1989]. They have also been used to calculate GPP and RA [*Sellers et al.*, 1996; *Mahadevan et al.*, 2008; *Groenendijk et al.*, 2011]. Simplifying the land surface is a formidable task, and the range of complexity of these models is large, and largely reflects their application. More complex land surface models have been used to simulate past and future climates and therefore must account for vegetation change and variable climate forcings such as CO₂ as well as solar variability, depending on the time scale [*Bonan et al.*, 2002b; *Bonan and Levis*, 2006]. To meet these primary goals on longer timescales, realistic representation of variables determining spatial vegetation distribution such as climate change, disturbances, the major biogeochemical cycles, especially those of nitrogen and carbon, must be taken into account [*Ciais et al.*, 2013].

Eddy covariance measurement sites, although of local scale, sample the majority of the world's biomes [*Baldocchi et al.*, 2001], and offer valuable data sets to evaluate and constrain land surface models [*Stöckli et al.*, 2008; *Mahadevan et al.*, 2008]. Due to the global network, FluxNet observations can be directly scaled up based on observed relationships between climate and carbon fluxes. *Jung et al.* [2011] recently scaled eddy covariance measurements up to the global scale. Their estimate of CO₂ uptake is consistent with previous upscaled estimates [*Beer et al.*, 2010], but total ecosystem respiration (heterotrophic and autotrophic combined) is biased low by approximately 5–10 PgC.

What about the respiration flux from larger animals? It seems that large (> 1 kg) animals likely would not

contribute to heterotrophic respiration estimates based on eddy covariance measurements. Furthermore, the directly respired CO₂ from domesticated animals also does not appear to be included in emission inventories [Powers *et al.*, 2014]. Given the large animal biomass of approximately 0.15 PgC [Smil, 2003], which eats approximately 3 % of its body weight per day, assimilates approximately 20 % thereof and expels the rest as CO₂ or soon-to-be-decomposed organic matter, we arrive at a very rough flux estimate of approximately 1.5 PgC yr⁻¹ ($0.15 \times 0.03 \times 365 \times 0.8$), which appears to not be accounted for. Within the context of the annual terrestrial carbon cycle variability (approximately ± 120 PgC yr⁻¹ from Figure 1.1), this estimate appears to be negligible but would push typically underestimated annual total ecosystem respiration rates in the correct direction.

1.2 “Top-Down”, inverse carbon flux estimation

The basic tenet of inverse “top-down” surface carbon flux estimation is to determine carbon surface fluxes using observed atmospheric CO₂ mole fractions and an atmospheric transport model. The difficulty of modeling the observed variability of atmospheric carbon mole fractions lies in accounting for and adequately representing the various processes driving this variability. Observed mole fractions can be mainly attributed to four processes: upwind biospheric and anthropogenic surface fluxes, advected “background” mole fractions (beyond the short-term influence of surface fluxes), and atmospheric mixing. Of these processes, the biospheric surface fluxes and atmospheric mixing are the least well understood and therefore most difficult to predict. To better understand biospheric fluxes, observed atmospheric CO₂ mole fractions, spatially and temporally resolved surface flux inventories, and atmospheric models are necessary.

1.2.1 Atmospheric carbon dioxide observations

Charles Keeling and colleagues initiated long-term observations of CO₂ at Mount Mauna Loa, Hawai‘i and South Pole Antarctica in 1958 (Figure 1.4). After demonstration of large annual increases of atmospheric CO₂ mole fractions [Keeling, 1960], the US National Oceanic and Atmospheric Administration (NOAA) began to collect samples of CO₂ across the globe in the late 1960s [Komhyr *et al.*, 1985]. These observations were taken at locations and times which were useful to determine the global mole fractions, in order to avoid the large variability resulting from local influence. As scientific interest shifted towards better understanding of the sources of smaller-scale variability, more observations were necessary.

Parallel to these observation efforts, technological advances also improved measurement capabilities. Initial long-term monitoring relied on flask samples for measurement in the laboratory of CO₂ mole fractions. Increasing electronic miniaturization and spectrometric advances allowed the construction of smaller, less expensive, field-deployable measurement devices. Generally, gas spectrometry relies on the Lambert-Beer law to determine light transmission through a gas sample. Techniques usually employ a light source emitting within a spectral region which is absorbed by the targeted gas species. Major advances include near infrared (<http://www.licor.com/>), fluorescence-based [Gerbig *et al.*, 1996], and cavity ring-down spectrometers [Crosson, 2008], as well as integrated measurement systems [Stephens *et al.*, 2011] which are, above all, field deployable. These autonomous, precise measurement devices have greatly eased atmospheric observation efforts.

In order to minimize the local influence, the first tall tower collecting atmospheric CO₂ observations was instrumented in North Carolina in June 1992 [Bakwin *et al.*, 1995]. These observations were paramount to demonstrate the information content provided by observed, semi-continuous vertical CO₂ mole fraction profiles, leading to the instrumentation of a second tower in Wisconsin in October 1994 [Bakwin *et al.*, 1998]. Later in 1992, the Energy Research Centre of the Netherlands supplemented the meteorological observation

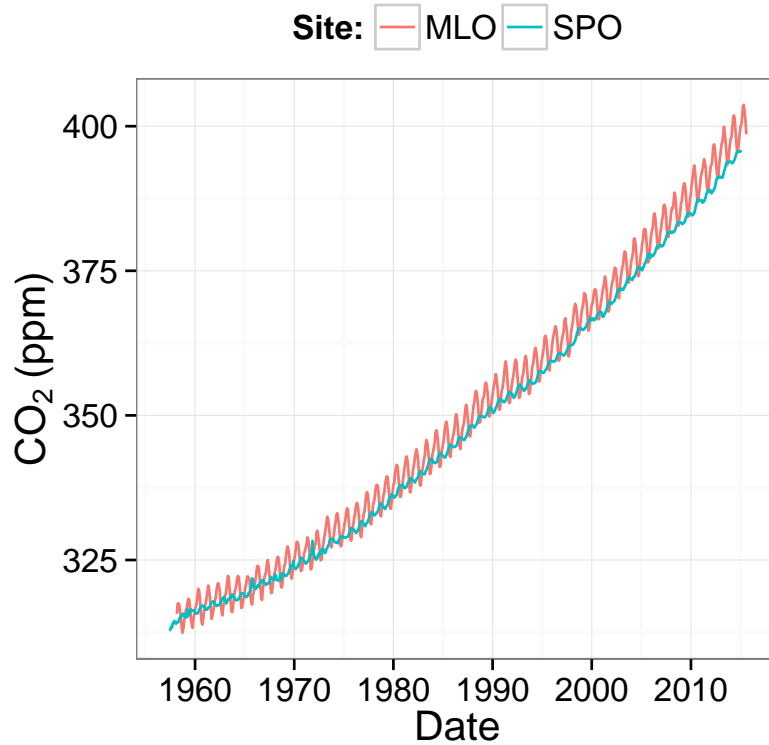


Figure 1.4: CO₂ time series measured at Mauna Loa, Hawai'i (MLO) and the South Pole Antarctica (SPO) by the Scripps Institute of Oceanography [Keeling *et al.*, 2001].

tower near Cabauw, southwest of Utrecht, Netherlands, with CO₂ and CH₄ measurement devices [Vermeulen *et al.*, 2011]. In 1994, a tall tower was instrumented with a CO₂ analyzer at Hegyhatsal, Hungary [Haszpra, 1995]. The expanding North American [Worthy *et al.*, 2003; Andrews *et al.*, 2014] and European [Vermeulen *et al.*, 2004] tall tower observation networks have since greatly improved our ability to observe the land surface.

Ongoing efforts to constrain the terrestrial carbon flux, especially its interannual variability, have led to fruitful short-term research projects being maintained, extended, and upgraded to monitor more atmospheric species over longer periods of time. In Europe, the Integrated Carbon Observation System (ICOS) provides a framework for observation of carbon fluxes as well as atmospheric carbon mole fractions. It integrates existing carbon monitoring infrastructure and facilitates expansion of its network. On a similar note, the Integrated non-CO₂ Greenhouse gas Observing System (InGOS) focuses on CH₄, N₂O, SF₆ and halocarbons, and H₂. Together, these two infrastructure projects constitute an important effort to monitor the European greenhouse gas balance over climate-relevant time scales.

The Eurasian continent comprises Earth's largest land surface, but the ecosystems within Russia and China are not as well sampled as those of Europe. In 2002, a Japanese-Russian collaboration instrumented the Berezochka tower in central Siberian Russia [Sasakawa *et al.*, 2010; Saeki *et al.*, 2013], and slowly expanded the Japan-Russia Siberian Tall Tower Inland Observation Network (JR-STATION). Outside the JR-STATION project, a German-Russian collaboration constructed and instrumented the Zottino Tall Tower Observatory (ZOTTO) by September 2006 [Kozlova and Manning, 2009], which was re-equipped in 2009 [Winderlich *et al.*, 2010]. Additionally, the construction and instrumentation of a tower at Ambarchik in North Siberian Russia, bordering on the Arctic Ocean, was completed in 2014, further extending the continuous long-term

Asian greenhouse gas monitoring infrastructure (Reum, Goeckede, Heimann, pers. comm.).

Unfortunately, few continuous greenhouse gas observations of equatorial regions exist. The Large Scale Biosphere-Atmosphere Experiment in Amazonia (LBA) intensively collected CO₂ and other trace gas observations at several Amazonian sites during 1999 [Andreae *et al.*, 2002]. Although time-limited, this pilot study provided data suggesting a weak carbon sink of Amazonian land surfaces, which contradicted previous global inverse modeling studies. Numerous short-term airborne sampling campaigns have been carried out in the Amazonas [Gatti *et al.*, 2014], but no continuous long-term greenhouse gas observations were made until the Amazon Tall Tower Observatory (ATTO) site began observations in 2012. The scientific community anxiously awaits the story the ATTO observations will tell [Wade, 2015].

The Global Atmosphere Watch (GAW) coordinates a global network of observation stations calibration and data quality centers, and world data centers. This important effort facilitates standardization of calibration procedures, and eases data exchange between experimentalists and modelers. To this end, The World Data Centre for Greenhouse Gases (WDCGG, <http://gaw.kishou.go.jp/wdcgg/>) under the GAW program collects and disseminates greenhouse gas observations. It is difficult to come by usage statistics, but GLOBALVIEW from NOAA appears to be the most cited data source for CO₂.

1.2.2 Atmospheric transport modeling of CO₂

Atmospheric CO₂ is usually treated as a passive tracer, and its mole fraction is thus simulated to be only influenced by surface fluxes [Keeling *et al.*, 1989], thereby ignoring minute atmospheric sources. Atmospheric transport is commonly simulated in a Eulerian framework which discretizes space into a three-dimensional grid and transports CO₂ masses in space and time [Heimann and Keeling, 1989; Heimann, 1996; Heimann and Körner, 2003; Krol *et al.*, 2005]. To simulate the CO₂ mole fraction time series at an observation site, one samples the CO₂ fields at the observation site position in the model.

Atmospheric transport can also be simulated in a Lagrangian framework. Lagrangian models can be run in backward mode (receptor-oriented i.e. simulating upwind surface influence of sites) tracking the movement and provenance of air parcels that would be observed at the observation site [Seibert and Frank, 2004]. The use of Lagrangian transport modeling for carbon flux studies is relatively new [Lin *et al.*, 2003], especially the use of FLEXPART [Stohl *et al.*, 2005]. Therefore, its description is warranted. The Lagrangian particle dispersion model (LPDM) FLEXPART, which simulates the transport and dispersion of air parcels (particles) via turbulent, advective, and convective processes, is driven offline by meteorological fields [Stohl *et al.*, 2005]. In each simulation, N particles are released from the site’s position at site-dependent heights above ground corresponding to the targeted observation inlet’s position and tracked backwards in space and time over Δt_t or until they have left the simulation domain. The residence times τ of air parcels near the surface describe sensitivity to surface fluxes.

These spatially gridded residence times within the simulation domain are computed as follows:

$$\tau_{ik}(t, \Delta t_t) = \frac{\Delta t_t}{NK} \sum_{n=1}^N f_{ikn}, \quad (1.2.1)$$

where f is the binary switch of a single particle’s n position in grid cell i at time k , recorded K times during the simulation [Seibert and Frank, 2004; Stohl *et al.*, 2005].

To simulate the dry air mole fraction χ of the targeted chemical species, the residence times τ (Eq. (1.2.1)) are scaled by the dry air density ρ (m³ kg⁻¹), multiplied with the mass surface flux (kg s⁻¹ m⁻²; elements of \mathbf{x} in Eq. (1.2.3)), and then converted into a volume flux by the sampling height h of particles, i.e. below 100 m air is assumed to be well-mixed and therefore influenced by surface fluxes. Molar mass factors M_{air}

and M_{gas} then convert this into the desired mole fraction [Eq. (1.2.2) *Seibert and Frank, 2004; Stohl et al., 2005*].

$$\chi = \frac{M_{air}}{M_{gas}h} \sum_i \sum_k \frac{\tau_{ik}(h)\dot{q}_{ik}}{\rho_{ik}} \quad (1.2.2)$$

1.2.3 Bayesian flux inversion

In principle, atmospheric transport from land surfaces to an observation site can be simulated in a Eulerian or Lagrangian framework. To notate according to past inversion work, the transport equation (1.2.3) can be written as:

$$\mathbf{y} = \mathbf{H}\mathbf{x} \quad (1.2.3)$$

where \mathbf{y} is a vector of observations, \mathbf{H} is the transport model ("observation operator" in parlance) connecting the observation with the surface fluxes \mathbf{x} [*Seibert and Frank, 2004*]. In Equation (1.2.2), τ_{ik} operates linearly on the sources \dot{q}_{ik} , and would correspond to \mathbf{H} and \mathbf{x} in Equation (1.2.3), respectively.

Most carbon surface flux inversion studies often employ a Bayesian cost function (Eq. 1.2.4), which assumes Gaussian statistics and therefore employs a derivation of the equation of the normal distribution. The derivation typically aims to reconcile the differences between the simulated $\mathbf{H}\mathbf{x}$ and the observed mole fraction \mathbf{y} , while deviations of the state vector \mathbf{x} (the unknown parameters or quantities) from what is already "known" about the surface fluxes are penalized i.e. the differences between the unknowns \mathbf{x} are not allowed to substantially diverge from \mathbf{x}_{prior} . Combined uncertainties of the observations and transport model (\mathbf{C}_{obs}^{-1}), and prior fluxes (\mathbf{C}_{prior}^{-1}) also influence the solution, but may have a subjective nature [*Enting, 2002; Michalak et al., 2005*]. That is, these covariance matrices can be used to further influence the solution.

$$J = \frac{1}{2}(\mathbf{y} - \mathbf{H}\mathbf{x})^T \mathbf{C}_{obs}^{-1}(\mathbf{y} - \mathbf{H}\mathbf{x}) + \frac{1}{2}(\mathbf{x} - \mathbf{x}_{prior})^T \mathbf{C}_{prior}^{-1}(\mathbf{x} - \mathbf{x}_{prior}), \quad (1.2.4)$$

There are many approaches to modifying and applying this equation, and the reader is referred to some relevant literature: *Enting [2002]; Peters et al. [2005]; Bocquet [2008]*.

1.2.4 Previous modeling and flux inversion studies

Coarse, global, three-dimensional atmospheric transport models were initially used to infer surface fluxes of CO₂ from atmospheric CO₂ mole fraction observations [*Keeling et al., 1989*]. These carbon flux inversions coarsely discretized the land surface into continental regions [*Bousquet et al., 1999*]. The TransCom 3 model intercomparison experiments provided an important platform to compare both inversion methods and transport models [*Gurney et al., 2002; Bakwin et al., 2004; Gurney et al., 2004*], but the resulting inverted fluxes from these inversions were sometimes contradictory. Regardless of the same observations, same regions, and the same prior carbon flux, they found a large spread between inverted fluxes, which results mainly from the different transport schemes. *Stephens et al. [2007]* selected the results of those models which could best reproduce observed vertical CO₂ gradients, and hence transport, and the inverted carbon fluxes from this subset of models were roughly consistent. They indicated a weaker Northern hemispheric sink than previously thought. Further along, higher resolution models and the expanding CO₂ observation network were employed [*Rödenbeck et al., 2003; Peters et al., 2007; Chevallier et al., 2010; Peters et al., 2010; Broquet et al., 2011*].

The availability of a consistent, computationally affordable inversion method [*Peters et al., 2005*] as well as observations from the long-term tall tower network across the USA and Canada were the necessary ingredients for CarbonTracker [*Peters et al., 2007*]. This continental-scale (1,000–10,000 km) inversion is zoomed in on

North America at $1^\circ \times 1^\circ$, and it estimates sets of weekly scaling factors of biosphere carbon fluxes, using an ensemble Kalman filter [Peters *et al.*, 2005]. This method was then extended to focus on Europe [Peters *et al.*, 2010], using the CHIOTTO network’s observations. Broquet *et al.* [2011] estimated summertime European fluxes at $0.5^\circ \times 0.5^\circ$, and followed up with improved uncertainty estimates and evaluation metrics [Broquet *et al.*, 2013]. They reported good simulation of seasonal CO₂ variability and thus fluxes, but the net annual flux remains uncertain. Therefore, long-term trends of the European biospheric fluxes cannot yet be determined reliably, and thereby their long-term reaction to climate also remains uncertain.

1.2.5 Challenges

Atmospheric transport model uncertainties are difficult to address. Sources of uncertainty specific to carbon flux inversion studies can be aggregation, representation, and rectification errors. The most common way to deal with these errors is to exclude or temporally smooth observations when the corresponding simulated CO₂ mole fractions are highly uncertain.

The representation error relates to the inherent mismatch between observed CO₂ variability and the true variability within the area of the overlying model grid cell [Gerbig *et al.*, 2003a]. For example, local surface influence on observations from an area smaller than the grid cell’s area may dilute the information representative of a larger area i.e. the overlying model grid cell. This error tends to increase with the size of the overlying grid cell [Gerbig *et al.*, 2003a; Tolk *et al.*, 2008]. In global inversions, this problem was avoided by using temporally smoothed, extended data from background observation sites as in the GLOBALVIEW-CO₂ product [Masarie and Tans, 1995], which filters out this information. Another approach to this problem is to exclude locally influenced observations [Brooks *et al.*, 2012].

The rectification error results from the temporal mismatch of vertical mixing and carbon flux dynamics [Denning *et al.*, 1996; Lin and Gerbig, 2005]. For example, negative or CO₂ uptake fluxes correspond to a time of the year and the day when vertical mixing is greatest. On the other hand, positive or respiration fluxes at nighttime or during winter correspond to weak vertical mixing. If not captured in the atmospheric transport model, this temporal mismatch causes erroneous vertical distributions of CO₂ mole fractions. This is best diagnosed with comparison of the observed and simulated vertical profiles of CO₂ mole fractions, or observation of independent tracers such as radon [Schmidt *et al.*, 1996].

The aggregation error results from the aggregation of spatial and temporal information of the carbon fluxes used in the inversion, by disregarding the spatial uncertainty of the aggregated fluxes in the inversion [Kaminski *et al.*, 2001]. That is, it may result from the designation of a single biospheric land cover type for a region where more than one different land cover types exist. For example, a region of $100 \times 100 \text{ km}^2$ has a total land cover that is 51 % forest and 49 % grassland, and the overlying grid cell would be assigned the predominant forest land cover type. Thereby, the observations would be driven by both forest and grassland fluxes, but the flux inversion would wholly lump it together with forest land cover types. Land surface models face a similar simplification error and Bonan *et al.* [2002a] offer a solution to represent a grid cell covering a collection of land cover types as fractional land cover types.

1.3 Regional-scale inverse carbon flux modeling

As introduced, bottom-up approaches suffer from the lack of representativity, and global top-down approaches suffer from aggregation errors. The regional scale allows resolution of these shortcomings by realistically representing the processes of bottom-up approaches while maintaining compliance with the global picture. Additional to the study of natural carbon flux variability, the regional scale can measure most administrative units, i.e. most administrative units have a horizontal dimension within 100–1,000 km. Therefore, regional-

scale carbon studies have the potential to appropriately verify national carbon emissions as reported to the UNFCCC.

Regional-scale carbon flux studies shift the focus from slow, smooth global variations of CO₂ mole fractions to the rich information contained in relatively high frequency observations within the atmospheric boundary layer (ABL) above land surfaces. This large observed variability of atmospheric CO₂ mole fractions is mainly driven by upwind anthropogenic emissions and biospheric CO₂ fluxes. Ideally, upwind land surfaces within 1,000-10,000 km measurably affect mole fractions at the sampling location, whereas the local surface influence (< 10 km) is relatively weak.

This intermediate field of view resolves the heterogeneous spatial distribution of natural, agricultural, industrial, and residential land cover. Each of these land cover types has its own unique surface flux signature. Furthermore, natural land cover contains diverse ecosystems, which have different flux signatures, but also agriculture cultivates many different crops. Topography further adds to the spatial and temporal heterogeneity of carbon surface fluxes, due to its affect on meteorology. In order to understand this high spatial variability and resulting highly variable observations, high-resolution representation is necessary.

For inland regional-scale carbon flux modeling studies, a minimal atmospheric CO₂ budget should consist of the regional anthropogenic (CO_{2,A}) and biospheric (CO_{2,B}) signals, as well as initial and boundary conditions (CO_{2,BG}). It follows then that:

$$\text{CO}_2 = \text{CO}_{2,\text{BG}} + \text{CO}_{2,\text{B}} + \text{CO}_{2,\text{A}}, \quad (1.3.1)$$

where the high variability and information content in the last two terms is represented in an atmospheric transport model, and spatially and temporally explicit surface flux inventories.

1.3.1 Regional-scale carbon flux inversion

Higher resolution lessens the discussed problems that plague coarse-scale carbon flux studies [Lin *et al.*, 2003]. On the other hand, regional-scale modeling systems need to account for transport of CO₂ from outside the domain and eventually for recirculation of CO₂ tracers back into the region of interest [Roedenbeck *et al.*, 2009; Rigby *et al.*, 2011]. Especially, small uncertainties here can strongly influence the determination of carbon fluxes within the region of interest [Goeckede *et al.*, 2010a].

Higher spatial resolution has the potential to reduce the representation error by accounting for the spatial heterogeneity and complex topography that may surround an observation site [Gerbig *et al.*, 2003a; Tolk *et al.*, 2008]. The validity of the assumption that a site's observations are representative of an overlying grid cell depends on the observation site characteristics [surroundings, sampling height, etc. Tolk *et al.*, 2008]. Here, a grid cell should be no bigger than 30×30 km² [Gerbig *et al.*, 2003a], and ideally less than 10 km. To some degree, representation error will remain because of the balance struck between the need to mimic reality and computational capabilities. Nonetheless, a receptor-oriented Lagrangian transport framework such as STILT and FLEXPART allows flexible determination of the output grid and can therefore significantly reduce this uncertainty.

Arguably the most important contributor to the rectification error [Denning *et al.*, 1996; Ahmadov *et al.*, 2007; van der Molen and Dolman, 2007] and thus transport uncertainty in general is mesoscale topography-induced air flow. Because the “world is not flat”, i.e., because most of the world can be considered complex terrain [Rotach *et al.*, 2014], the influence of topography generally alters airflow and also affects regional climate. This can be remedied in regional-scale modeling by moving to a spatial resolution which is sufficiently fine for the study region.

Higher spatial resolution also enables the underlying biophysical processes or the fluxes to be explicitly estimated in an inverse modeling framework without making a gross aggregation error (Figure 1.6). In a

parameter inversion, the inversion solves for the optimal set of biosphere parameters that yield the most probable flux [Rayner *et al.*, 2005; Scholze *et al.*, 2007; Tolk *et al.*, 2011; Meesters *et al.*, 2012]. Here, the inversion directly constrains the response of the biosphere to weather and climate. However, the observed variability contains only information about upwind land surfaces. A form of aggregation error is therefore made, in that it is assumed that the spatial variation within a certain land cover type is negligible, which has been shown to be questionable [Groenendijk *et al.*, 2011]. Therefore, this pre-constraint must have good reasoning. As outlined by Tolk *et al.* [2011], nonlinear relationships within the biosphere model require advanced inversion techniques, such as an ensemble Kalman filter. Also, to avoid so-called aliasing effects, where the wrong parameter is corrected, one must be confident that the parameters in question are properly constrained [Tolk *et al.*, 2011]. Additionally, the direct comparison of high-resolution biospheric flux simulations with directly measured surface fluxes is a possible evaluation tool [Ahmadov *et al.*, 2007; Broquet *et al.*, 2011; Tolk *et al.*, 2011; Meesters *et al.*, 2012].

A pixel inversion solves for the most probable flux or associated scaling factor of the flux within a land cover type [Figure 1.6 Tolk *et al.*, 2011; Meesters *et al.*, 2012]. It is thereby less rigid than the parameter inversion method, because it typically makes fewer presumptions about the relationship between biospheric flux variability and climate. To reduce the issue of too many under-constrained pixels (and correspondingly too many degrees of freedom), a spatial correlation between fluxes of the same land cover type within a certain spatial distance of each other is introduced to the prior covariance matrix (\mathbf{C}_{prior}^{-1}). Here, the correlation length scale needs to be well justified, and the land cover data needs to be accurate [Tolk *et al.*, 2011].

1.3.2 Previous regional-scale work

The CO₂ budget and rectification airborne study (COBRA) during August 2000 intensively sampled the continental biospheric CO₂ signals from the North American continent, by collecting vertical, continuous profiles of CO₂ and CO [Gerbig *et al.*, 2003a]. Concurring with the conclusions of Bakwin *et al.* [1995], they found most of the information of the continental surface fluxes to be within the ABL, whereas free tropospheric CO₂ variability was low (Figure 1.5). Furthermore, they found that the maximum spatial increment allowable to resolve the information contained in the observations within the lower ABL is approximately ~30 km. Further COBRA studies have also contributed much to regional-scale carbon flux modeling [Lin *et al.*, 2006; Matross *et al.*, 2006].

With higher intensity, the CarboEurope Regional Experiment Strategy project supplemented a dense surface flux observation network in southwestern France with tall tower mole fraction observations and a short aircraft measurement campaign [Dolman *et al.*, 2006]. These observations have been instrumental in guiding further European measurement campaigns. This campaign has proven especially fruitful to evaluate and develop transport and surface flux modeling strategies, including model development [Ahmadov *et al.*, 2007], model intercomparison [Ahmadov *et al.*, 2009], investigation of the rectification error [Ahmadov *et al.*, 2007], and representation errors [Tolk *et al.*, 2008], as well as the development of inverse regional modeling frameworks [Lauvaux *et al.*, 2008, 2009a, b]. However, for annual studies, long-term atmospheric monitoring is necessary.

The US-American tall tower network was augmented with several tall towers in the upper Midwest in order to over-sample the potentially large carbon fluxes from maize [Miles *et al.*, 2012]. Previous research had indicated a large carbon sink in the Northern hemisphere’s land [Gurney *et al.*, 2004] and in particular the potential carbon sink of maize [Suyker *et al.*, 2005; Verma *et al.*, 2005], which is cultivated in the upper Midwest USA—so much that it is known as the “corn belt”. Therefore, as part of the Mid-continental intense measurement campaign with the objective to sample an agricultural area 500×800 km², the construction of an unprecedentedly dense network of greenhouse gas observation tall towers was initiated in 2006, and was augmented with an airborne measurement campaign during the summer of 2007. These observations have

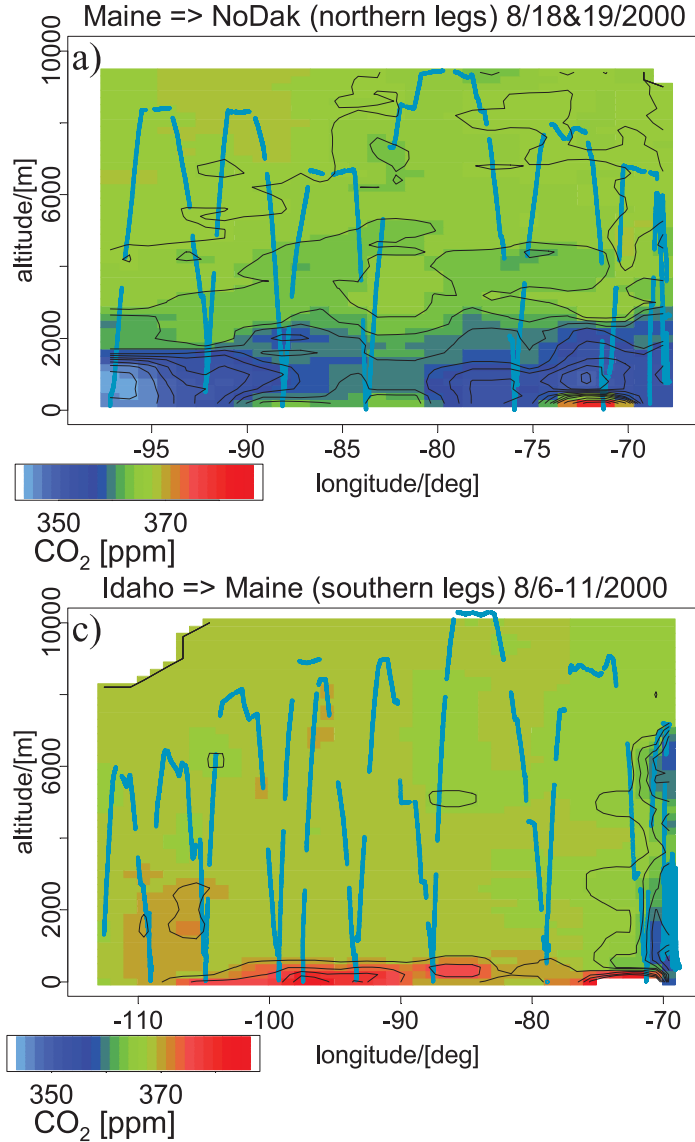


Figure 1.5: Vertical, zonal profiles of CO₂ observations from **a** Maine to North Dakota and **c** from Idaho to Maine, USA, taken during the COBRA-2000 intense measurement campaign. From *Gerbige et al.* [2003a]

also served as an intense testing bed for modeling studies. *Corbin et al.* [2010] demonstrated the necessity to explicitly include crop fluxes, especially those of maize, in surface flux modeling studies. *Schuh et al.* [2013] further demonstrated the necessity of high-resolution modeling in order to reproduce the spatial flux patterns in an inverse modeling framework. *Ogle et al.* [2015] demonstrated the limits and possibilities of using inverse flux modeling to verify national biospheric carbon budgets. Results from observed between-site CO₂ gradients [*Miles et al.*, 2012] and site-exclusion inverse modeling tests [*Lauvaux et al.*, 2012b] suggest that footprint modeling and surface flux characteristics of the target region should guide regional-scale observation network design.

The Dutch CHIOTTO tower Cabauw and the long-established, coastal tall tower Lütjehad were supplemented with two rural tall towers, Loobos and Hengelman, for the year of 2008. Twice-weekly aircraft flux observations were also made during this period in order to evaluate inverted fluxes. The theoretical inversion

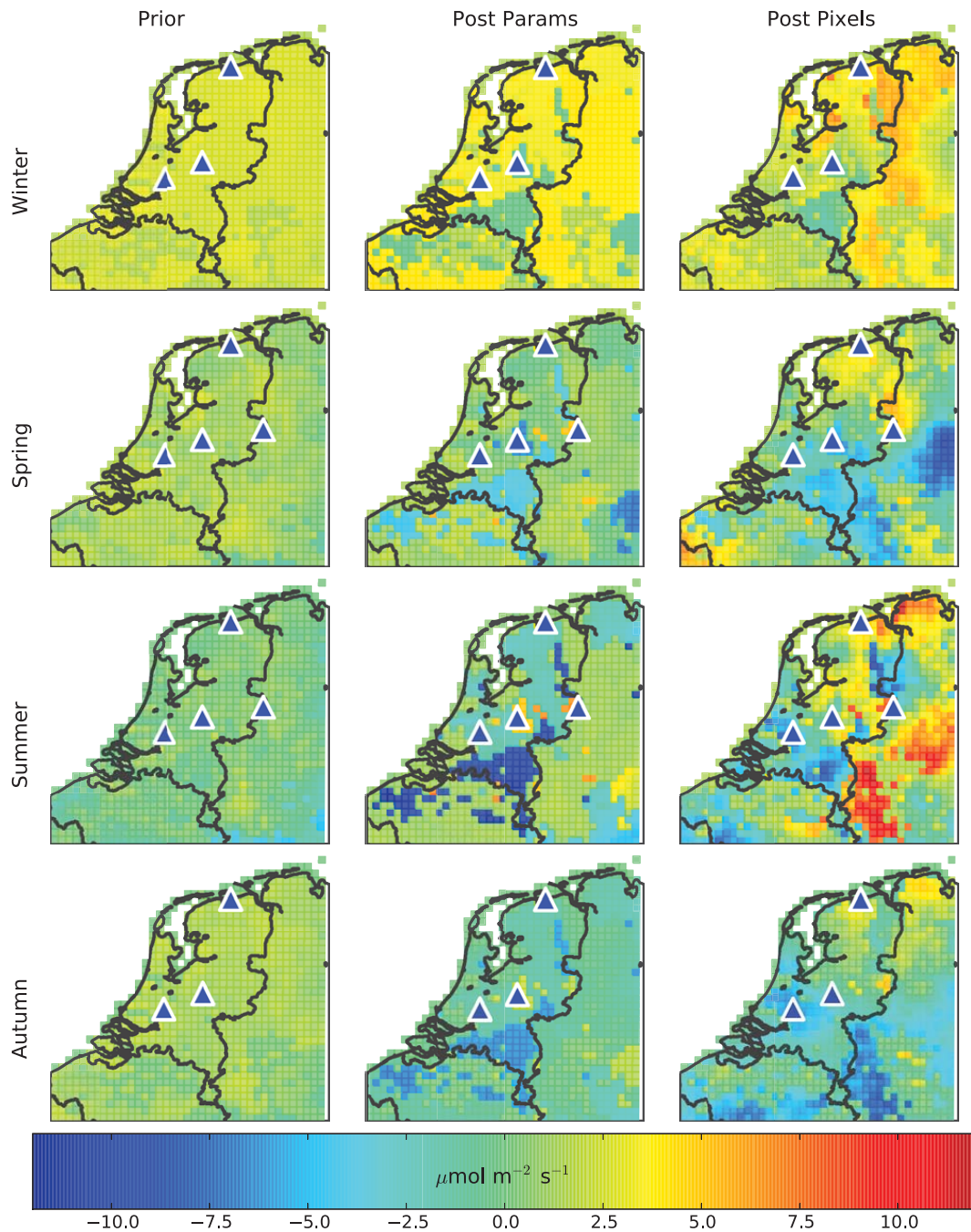


Figure 1.6: Retrievals of biospheric surface carbon fluxes constraining seasonal sets of biosphere model parameters (Post Params) and seasonal flux inventories (Post Pixels) compared with “known” biospheric fluxes (Prior). Taken from *Meesters et al.* [2012].

work of *Tolk et al.* [2011] laid the necessary foundation for the following work of *Meesters et al.* [2012], who applied and compared a pixel-based and parameter-based inversion method to constrain surface fluxes over the Netherlands (Figure 1.6). Their work identified some of the important pitfalls of inverse flux modeling. First, poor representation of nocturnal mixing may be related to an aliasing effect within the parameter inversion, which results in the prediction of negative respiration fluxes. Second, seasonal sets of parameters may be necessary to reduce the rigidity of a parameter inversion. Third, a separate land cover type dedicated

solely to maize is likely necessary.

Several studies have augmented existing tower observations with aircraft campaigns [Matross *et al.*, 2006; Pillai *et al.*, 2011], or equipping FluxNet sites with calibrated CO₂ measurement devices [Goeckede *et al.*, 2010b], the latter being more useful for budgeting studies, due to the high temporal coverage. Goeckede *et al.* [2010b] and Pillai *et al.* [2011] were some of the first studies to demonstrate the value of high-resolution transport simulations above complex terrain.

1.3.3 Challenges for regional-scale carbon flux studies

The most important aspect of trace gas mole fraction modeling is the ability to simulate the movement of air parcels, and thereby the transport of their constituents. Driven by both advances in meteorological simulation and computational capabilities, the increase in spatial resolution of transport models to less than 30 kilometers allowed the more realistic representation of advection and convection as well as turbulence.

Lin *et al.* [2006] laid out the problems presented by the information-rich data sets representative of regional-scale areas. A summary of these and additional issues in regional-scale carbon flux modeling mainly includes transport model aspects, namely:

1. Accurate modeling of horizontal and vertical mixing is necessary to reproduce steep observed mole fraction vertical gradients (Figure 1.5).
2. Accounting for mesoscale topography induced airflow is necessary.
3. Mass conservation of transported tracers is absolutely necessary. Here, off-line transport models are especially sensitive to this issue.
4. The variable response of diverse ecosystems to weather is resolved at this scale and therefore requires realistic representation.
5. Sources of uncertainty require detailed analysis and inclusion in a flux inversion.
6. Limited-area modeling requires both accurate determination of “background” mole fractions and accounting for possible reentry of CO₂ masses originating within the area of interest.

Much work has been done to solve these problems as the field of regional carbon flux modeling has advanced. Improving spatial resolution appears to be the most endeavor. Although the field is inherently interdisciplinary, a great deal of progress can be seen.

Radon is a radioactive noble gas with a half-life of 3.82 days which is emitted mainly from soil, and spatially explicit radon emission inventories for modeling exist [Szegvary *et al.*, 2007; Karstens *et al.*, 2015]. Its use to correct for model transport uncertainties is established [Zahorowski *et al.*, 2004; Hirsch, 2007], and new applications and refinements are continually being added [van der Laan *et al.*, 2014]. Gamnitzer *et al.* [2006] provide an example of correcting the modeled regional fossil fuel signal by folding the simultaneous ratios of observed and modeled radon.

With the potential uncertainty contribution of about 30 % to modeled CO₂ mole fractions [Gerbig *et al.*, 2008], capturing vertical exchange of CO₂ within the ABL is a prerequisite for accurate quantification of surface carbon fluxes. The field of numerical weather prediction aims primarily at accurate prediction of temperature, wind, and precipitation. This may explain why vertical mixing tends to be poorly represented across models [Brunner *et al.*, 2015], as indicated by the ability to predict the height of the ABL. Brunner *et al.* [2015] found that vertical mixing was overestimated in an ensemble of regional-scale models, especially in winter, which they evaluated at an airport in Canada and in Europe. Kretschmer *et al.* [2014] present an approach to

improve vertical mixing representation by geostatistical interpolation of observed ABL heights (radiosonde) to the model grid. This assignment of ABL heights had a positive effect on the simulation performance of CO₂ mole fractions and is a pragmatic step forward in reducing transport uncertainty. Nonetheless, improved simulation of vertical mixing would be the optimal solution.

1.4 This work

1.4.1 The CarboCount CH Project

The combination of top-down and bottom-up methods at a resolution that can resolve apparent variability of biospheric carbon fluxes is arguably the best way towards understanding terrestrial carbon fluxes. With this in mind, the CarboCount CH project aims to develop and implement a prototype atmospheric monitoring network and carbon flux modeling framework for CO₂ and CH₄ for Switzerland. At its core is a dense network of tower observation sites, and the fusion of the resulting observations with atmospheric transport models and highly detailed anthropogenic and biospheric flux inventories. The CarboCount CH observation sites possess diverse orographic characteristics that provide for challenging meteorological transport modeling, which warrants high-resolution atmospheric transport modeling. Furthermore, the strengths and weaknesses of each particular site need investigation to guide future observation networks. Eddy-covariance measurements from Swiss FluxNet can be used to evaluate the inverted regional-scale carbon fluxes. Furthermore, the inverted fluxes can be used to compare with a comprehensive land surface model of the carbon and nitrogen cycle, also developed within the project. Finally, results from this study could be integral in the development of a national greenhouse gas verification system.

1.4.2 My role

My work encompasses the two major components of top-down surface carbon flux determination: atmospheric CO₂ mole fraction observations and their simulation. My goal is to lay the foundations for subsequent work to constrain a biospheric CO₂ flux inventory using an atmospheric transport model and CO₂ observations.

My goals as an integral part of the CarboCount CH Project include:

1. Successful construction and maintenance of an atmospheric carbon monitoring site,
2. Understand what is driving the variability observed at this and the other CarboCount network observation sites,
3. Simulation of this observed variability using high-resolution atmospheric transport modeling of anthropogenic and biospheric carbon fluxes across the Swiss Plateau using FLEXPART-COSMO,
4. Investigation of the strong relationship between CO and CO₂ observed at the network's sites.

However, the prerequisites for meaningful inversion of carbon surface fluxes over the Swiss Plateau are numerous. This preliminary work includes:

1. filling and calibration of reference gas bottles, and observation network deployment,
2. collection and processing of high-quality atmospheric carbon observations,
3. determination of which observations are representative of the regional scale,
4. assessment of possible atmospheric model transport uncertainties,

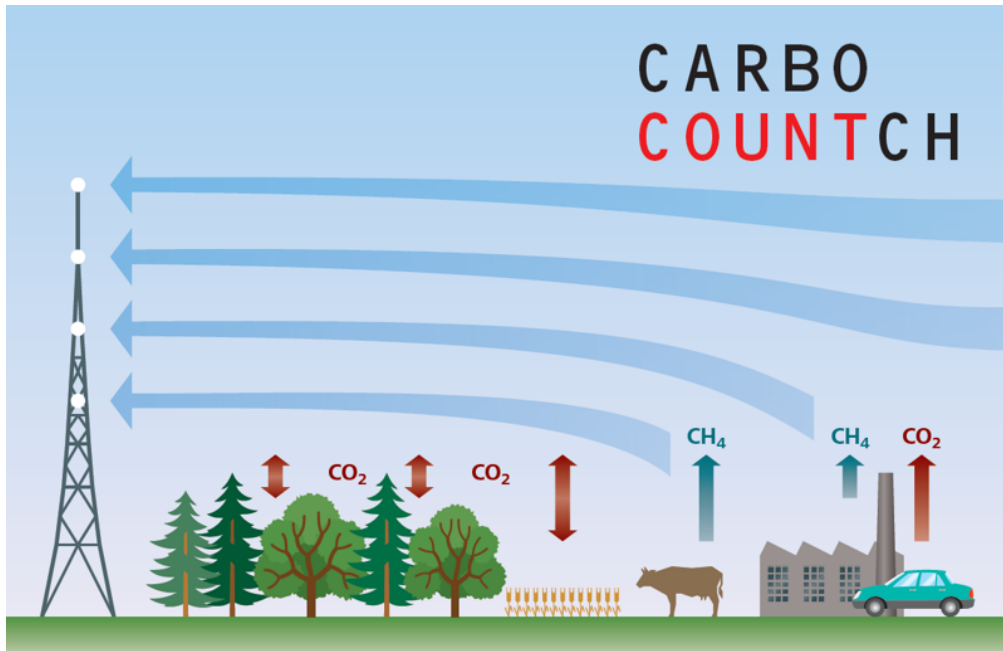


Figure 1.7: Schematic representation of the fundamental CarboCount CH project elements: tower observations, carbon fluxes (bidirectional arrows), and transport models (unidirectional arrows). Figure kindly provided by the Graphics Department, Empa.

5. investigation of the target region's characteristics,
6. preparation of anthropogenic and biospheric flux inventories, as well as collection of background CO_2 fields,
7. tracer transport modeling and mole fraction simulation at all observation sites.

To reach these goals, with much help from colleagues, I have designed, constructed, and installed a measurement system at Lägern-Hochwacht, which was mostly duplicated at Frübüel. Detailed description of this instrumentation is presented in Chapter 2. Furthermore, I detail the processing, calibration, temporal aggregation, and uncertainty estimation of the atmospheric carbon observations from these and the two remaining CarboCount sites, Beromünster and Gimmiz. Finally, the experience gained through the operation of the Frübüel and Lägern-Hochwacht observation sites is discussed and offered to future monitoring efforts.

In Chapter 3, the observation site characteristics relevant to forthcoming regional-scale modeling studies are investigated. This is accomplished by comparing the observed meteorology and the meteorological model which drives FLEXPART-COSMO in this study, COSMO-2. Assessing the upwind surface influence on each observation site using FLEXPART-COSMO in light of the observed regional signals uncovers what is driving the observed variability. Finally, the strengths and weaknesses of the site's observations as well as the employed atmospheric transport models are discussed. These results will hopefully guide and aid subsequent network deployments aimed at inverse carbon flux modeling studies of the Swiss Plateau.

In Chapter 4, a method to isolate the biospheric portion of CO_2 observations using CO observations is applied to Beromünster and Lägern-Hochwacht observations. The isolation of the biospheric signal from observed CO_2 mole fractions requires the subtraction of both background and anthropogenic signals, which, in the standard approach, requires estimation of these components with an atmospheric transport model, and background fields and anthropogenic emission inventories. This standard approach inevitably introduces uncertainty into the “observed” biospheric signal, which translate into the inverted biospheric flux inventories. Here, we propose a CO -based method to provide better estimates of the observed biospheric signal.

Chapter 2

Atmospheric carbon measurements in the CarboCount CH Project

2.1 Introduction

Regulating greenhouse gas emissions is necessary to curb rising atmospheric greenhouse gas mole fractions in order to avoid dangerous climate change [Stocker *et al.*, 2013]. To this end, atmospheric carbon measurements representative of administrative regions are of particular importance to regulating anthropogenic carbon emissions [Ciais *et al.*, 2014]. The monitoring and resulting regulation of carbon emissions should be supplemented with inverse carbon flux modeling using high-quality atmospheric carbon measurements containing information about the administrative region of interest [Ciais *et al.*, 2014].

With the aim to quantify carbon fluxes and thereby the Swiss carbon budget, the measurement sites of the CarboCount CH network strategically spread across the Swiss Plateau (Table 2.1). The Beromünster site has a 217 m tall tower and is on a gentle hill 30 km southeast of Bern. The Frübüel site is an eddy covariance measurement site [Zeeman *et al.*, 2010] located on Zugerberg ~10 km south of the city of Zug. The Gimmiz site has a small water tower in a relatively flat area ~2 km northwest of Aarberg in the Seeland region. The Lägern-Hochwacht site has a small tower atop the steeply sloped mountain ridge ~20 km north-northwest of Zurich. The strengths and weaknesses of each site's characteristics and observations relevant to regional-scale carbon flux modeling are assessed in Chapter 3.

We have equipped the sites with PICARRO cavity ring-down spectrometers [Crosson, 2008] due to their relatively low cost, and reputation of being low maintenance and providing highly precise measurements [Richardson *et al.*, 2012]. Although PICARRO measurement devices have been shown to measure greenhouse gases precisely and stably in the field [Richardson *et al.*, 2012; Andrews *et al.*, 2014], their absolute measurements drift slightly on time-scales of hours, days, weeks, and months depending on the trace gas species. Therefore, similar to other measurement techniques, these devices require repeated calibration during field deployment relative to an accepted international scale, in order to be able to compare with other measurements made elsewhere.

This chapter partly documents the methodologies and experience gained from atmospheric carbon measurements at the CarboCount sites. It describes the measurement system in place at Lägern-Hochwacht, and thereby to a large degree that in place at Frübüel. The intricacies of the complex, multiple-height measurement system at Beromünster are described by Berhanu *et al.* [2016], and thereby to a lesser degree that in place at Gimmiz. Furthermore, this chapter documents the aggregation, calibration, and uncertainty estimates of the network's measurements. It also offers practical experience and suggestions regarding the

Table 2.1: Location and instrumentation of the measurement sites of the SNF Sinergia CarboCount CH Project.

Site	Height(s) (m.a.g.l.)	Alt.	Lat., Lon.	Device	Serial	Gases
Beromünster	212, 132, 72, 45, 12	797	47.1896, 8.1755	PICARRO G2401	CFKADS2038	CO ₂ , CH ₄ , CO, H ₂ O
				PICARRO G2311-f	CFHADS2018	CO ₂ , CH ₄ , H ₂ O
Früebüel	4	982	47.1158, 8.5378	PICARRO G2301	CFADS2256	CO ₂ , CH ₄ , H ₂ O
Gimmiz	32	443	47.0536, 7.2480	PICARRO G2301	CFADS2255	CO ₂ , CH ₄ , H ₂ O
				HORIBA APMA 360	207006 & 306002	CO (& H ₂ O)
Lägern- Hochwacht	32, 23	840	47.4822, 8.3973	PICARRO G2401	CFKADS2043	CO ₂ , CH ₄ , CO, H ₂ O

elements of this chain of measurement activities, which link up to provide high-quality observations for inverse carbon flux modeling.

2.2 Reference gases

Ambient atmospheric carbon mole fractions can exhibit high variability depending on the measurement site's location. Large variability is expected in the Northern Hemisphere (Figure 1.4), especially above land surfaces such as the Swiss Plateau. The accuracy of employed measurement devices within this range needs to be investigated. The range of mixing ratios of the reference gas bottles were therefore prepared in order to cover the expected range of ambient atmospheric carbon mole fractions. Specifically, this allows assessment of the accuracy of the measurement devices along the continuum of observed mole fractions.

Table 2.2: Approximate reference gas mole fractions of aluminum bottles. Mole fractions have units of $\mu\text{mol mol}^{-1}$ mole fraction or molar parts per million (ppm).

Gas Bottle	CO ₂	CH ₄	CO	No. of Bottles
High	470 or 530	2.4	0.24 or 1.4	7
Low	380	1.9	0.15	6
Working	400	2.1	0.20	5
Target	400	2.1	0.20	3

To this end, 30 L aluminum bottles were filled to their capacity of 2015 psi for the CarboCount CH project, with “high”, “low”, and “target” mole fractions (Table 2.2). They were filled with ambient air using a modified scuba diving pump at Empa Dübendorf, Switzerland, and dried in between the pump and the bottles with magnesium perchlorate to minimize water vapor and its effects in the aluminum cylinders. Therefore, the bottles shown in Table 2.2 have mole fractions below approximately 100 molar parts per million (ppm) H₂O. Additionally, the very high CO mole fractions among the high bottles were prepared for the HORIBA CO measurement device in place at Gimmiz. The bottle's atmospheric carbon mole fractions were determined relative to the gas-specific international reference scales (CO₂: WMO X2007, *Zhao and Tans* 2006; CH₄: WMO X2004, *Dlugokencky et al.* 2005; CO: WMO CO X2014, *Novelli et al.* 1991). This was repeated several times for months after having filled the cylinders, to check for mole fractions to stabilize as well as to ensure accuracy of the mole fraction measurements. We report uncertainties of these child reference gases σ_{st} to approximately be (ppm) CO₂: 0.12, CH₄: 0.0003, and CO: 0.001. Afterwards, the reference gas bottles

have been distributed to the measurement sites.

2.3 Measurement system at Lägern-Hochwacht

2.3.1 General setting

Ambient air samples at Lägern-Hochwacht are collected at the top of a tower managed by SkyGuide LLC at a height of 872 meters asl, or 32 meters above ground level (agl), which corresponds to about 10 meters above the surrounding tree canopy. It is possible to sample a second inlet at approximately tree height (23.5 agl). The site has been equipped with a Picarro G2401 cavity ring-down spectrometer [Crosson, 2008] measurement device, measuring dry air mole fractions of CO₂, CH₄, CO, and H₂O trace gases. The measurement system is housed in the building at the base of the tower on a standard rack (48.3 × 59.7 × 198.1 cm), which is electrically grounded. The measurement room's temperature is not regulated and varies from approximately 10 to 25°C in winter and summer, respectively. Therefore, during the colder months, the bottom half of the rack is encased in 6-cm-thick Styrofoam padding, which raises the local temperature near the electrical instruments to approximately 20 degrees Celsius, which is the recommended operating temperature. Component details are listed in Table 2.3, and the corresponding schematic is shown in Figure 2.1.

2.3.2 Gas flow

Ambient air is suctioned through a fine paper filter inside the inlet housing down through a 40-meter-long, single piece of 12mm (OD) Synflex tubing at 10 l min⁻¹ for approximately 13 s (Figure 2.1 and Table 2.3). It then flows through a one meter snippet of 1/2" Teflon tubing into the valve box, where it then flows through 1/4" Synflex tubing. The airstream then splits at the first tee-junction, to pass through the flow meter (FM1 or FM2), and on through the remaining 1/4" Synflex tubing to the purge pump (P1). For measurement, air can flow from this junction at approximately 0.205 l min⁻¹ for about 4 s through < 1 m of 1/4" Synflex, two 3-way solenoid valves (V1 & V2), a 7 μm filter to the measurement device's measurement cavity, and through reinforced plastic tubing to the device pump (P2). Total residence time of ambient air samples in the tubing is approximately 18 s.

Sampling of the reference gases is carried out by simultaneously switching the second valve (V2) and one of the valves V3-V6. Brass three-stage pressure regulators maintain a constant, low overpressure (~10-15 psi above ambient) on valves (V3-V6), which suffices to supply enough air to the measurement device. Reference gas then flows serially through the valves and through a mass flow controller at 0.21 l min⁻¹. This serial airflow flushes any remnant reference gas or ambient air which has diffused in through the overflow. For example, upon switching on valve V2 and V3, air flows from the reference gas bottle through 1/16" stainless steel tubing, valve V3, and the mass flow controller (MFC). After this, reference gas can either flow through valve V2, through 1/4" Synflex tubing and into the measurement device, or through the overflow into the measurement room.

Valves are powered by the PICARRO and are only switched to sample reference gases or to sample the lower height. Should the valve box fail, standard measurement setting is to sample the top inlet. This setting assures that little strain is placed on the instruments and that energy use is minimal. It also assures that little or no risk exists of reference gas being lost due to a power outage. The mass flow controller is constantly open and could be used to detect internal valve leaks.

After a valve transition, the air sampled is a mixture of the previous and current gases, which invalidates the measurement. The amount of time necessary for equilibration was determined with reference gas measure-

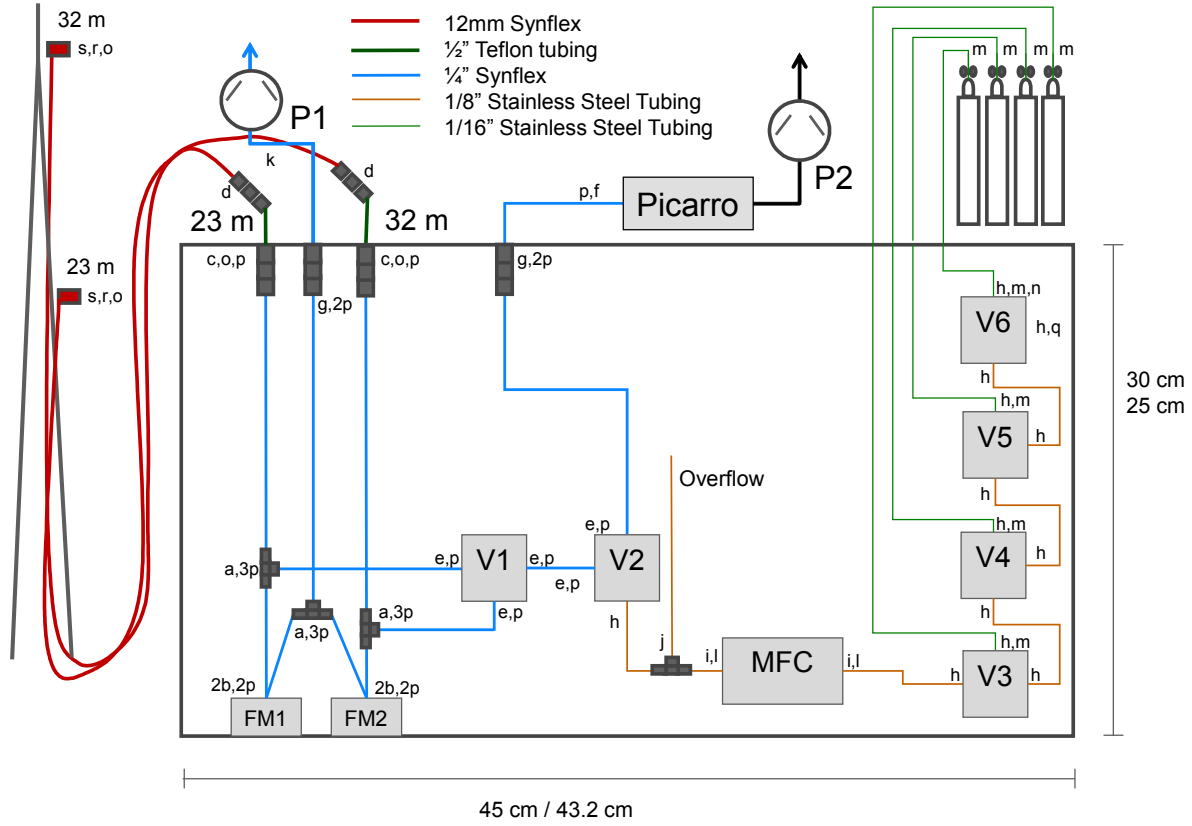


Figure 2.1: Airflow schematic at Lägern-Hochwacht.

ments to be 9 min for Lägern-Hochwacht and Frübüel. Due to these relatively long equilibration times of approximately 9 minutes and the relatively small vertical distance between the two inlets at Lägern-Hochwacht, the lower inlet was never sampled.

2.4 Measurement calibration and uncertainty

In general, measurements of a fundamental quantity such as light, electrical current, time, and/or mass are taken and these measured signals s_{meas} are related to the desired quantity. The PICARRO instruments used in the network report measured signals as mole fractions by applying internal calibration factors, but these still need to be translated into mole fractions relative to the respective international scales. For the PICARRO devices, concurring with *Rella et al.* [2013], we have observed a linear relationship between known mixing ratios and measured signals and therefore employ Equation (2.4.1). Here, reference gas cylinders supply gas of known mole fraction at regular intervals to the measurement devices and the relationship between these known mole fractions and the measured signals is described by the calibration coefficients a and b . This is done at regular intervals, because the relationship between known mole fractions and measured signals can change with time. Finally, this relationship is then carried over and applied to temporally proximal measured signals of ambient air.

$$c_{cal} = a + b \times s_{meas}. \quad (2.4.1)$$

Measurements are affected by different sources of uncertainty. Uncertainty analysis needs to assess both random and systematic components. According to *Andrews et al.* [2014], three types of trace gas measurement

Table 2.3: Parts of Lägern-Hochwacht measurement system which was mostly replicated at Früebüel. The legend indicates unapparent parts in Figure 2.1. The lower half contains specific Swagelok® parts.

Leg.	Name	No.	Description	Part Number
	PICARRO G2401	1	4-channel spectrometer	
V1-6	GEMS sensors 3-way solenoid valves	6	#10 - 32 UNF connections	GH3315-12VDC
	Synflex 1300 100 m tubing	1	OD: 12mm ID: 8.2 mm	440.1012.210
FM1-2	Fisher Scientific Flowmeter	2	2-25 l/min 2 - 1/8" NPT(F) connections	EW-32460-48
	Scott-Marrin 301 Aluminum cylinders	5	CGA590, Size 150	03S-150A-590B
	Scott-Marrin Brass 2-Stage press. reg.	5	0-75 PSI, 1/8" outlet,	05-2SB30-590-D2T
P2	KNF Gas pump	1	> 21 l/min, oil-free, w/ potentiometer	Type N 920 AP.29.18
P1	Thomas pump	1	26 l/min	52061704
MFC	Voegtlin Mass flow controller	1	20-1000 l/min, G1/4" inner thread	GSC-B4SA-BB23
s	Solberg MFG Inlet housing + 2 filters	2	2 1/2" H x 6" OD	F-15-050
	APC Uninterruptible Power Supply	1	Back-UPS Pro 1200	BR1200GI
	Hitachi 500GB harrdisk	1		7K1000.D
	Teflon tubing 2 m	1	lightning protection	FT-01 5096 5500
	1m 1/8" tubing	1		SS-T2-S-028-6ME
	10m 1/16" tubing	1		SS-T1-S-014-6ME
f	Dust filter	1	7 micron filter	SS-4FW-7
a	Tee	3	1/4" all	SS-400-3
j	Tee	1	1/8" all	SS-200-3
b	1/4" Male Fitting NPT	4	1/4" OD to 1/8" NPT	B-400-1-2
h	1/8" Male Fitting UNF 10-32	14	10-32 to 1/8"	SS-200-1-0157
m	Reducer	8	1/8" to 1/16"	SS-100-R-2
e	1/4" Male Fitting UNF 10-32	6	10-32 UNF to 1/4"	SS-400-1-0256
g	Bulkhead Union - 1/4"	2	1/4" to 1/4"	SS-400-61
c	Bulkhead Union - 1/4" to 1/2"	2	1/4" to 1/2"	SS-810-61-4
d	Reducer Union	2	12mm to 1/2"	SS-12M0-6-8
i	Male Connector - MFC in/out	2	1/8" Tube OD x 1/4" Male ISO Par. Thread	SS-200-1-4RS
l	Carbon Steel Gasket	2	1/4" ISO Parallel Thread (RS)	S-4-RS-2V
o	Inserts for synflex tubing	10	12mm OD and 8mm ID	SS-12M5-8M
p	Inserts for synflex tubing	50	1/4" OD and 0.17mm ID	SS-405-170
k	Male NPT-Fitting	1	1/4" NPT Connection with Pump	B-400-1-4
r	Female NPT-Bulkhead Union	2	Mount for inlets and reducer to 12mm	SS-12M0-71-8
q	Plug	1	1/8" Plug (removed for 4th bottle)	SS-200-P
n	Cap	1	1/16" cap for valve V6	SS-100-C

uncertainty can be separately reported:

1. uncertainty related to the calibration scale σ_{sc} ,
2. analytical uncertainty σ_a consisting of non-random and random uncertainty,
3. standard error of the reported one-minute mean values composed of both instrument noise and atmospheric variability σ_v .

These uncertainties are used to specify the relative weight of each standard gas measurement, when calculating the calibration coefficients a and b . The uncertainty of the calibration scale is constant in time and can be given separately, whereas the two other uncertainties vary with time and can be reported individually for every one-minute average. Random uncertainties can be reduced by temporal averaging, but systematic uncertainties can not be reduced in this way. The final, combined analytical uncertainty calculation considers both random uncertainties due to instrument noise and systematic uncertainties due to the uncertainty of the calibration, and other potential systematic uncertainties.

The uncertainty of the reference gas value determined in the laboratory σ_{st} is a constant value, which includes the uncertainty of the mother standards used to transfer the scale, but may also contain the uncertainty of the scale (σ_{sc}). Here, however, these uncertainties of the parent standards were not included in the uncertainty treatment of the child standards (Table 2.2). That is, it is assumed that the mole fractions of the parent standards are known exactly. Uncertainties in the mother standards could easily be added at the end, if needed, as they apply to all observations in the same way. Uncertainties of the mole fractions of children standard gases are taken from the regression analysis performed to calibrate the employed measurement device.

We consider the contribution to the random part of the analytical uncertainty to come from the instrument's precision or noise, defined here as the standard error of the one-minute mean of a reference gas measurement. Here, the precision σ_p of a one-minute value is reported from a target gas measurement, which lasted m minutes and contained n different data points with the standard deviation σ . It is computed as:

$$\sigma_p = b \frac{\sigma}{\sqrt{n/m}}, \quad (2.4.2)$$

where b is the time-interpolated slope of the calibration curve.

Systematic uncertainty in the calibration coefficients comes from uncertainties in the reference gas measurements which are composed of the uncertainties σ_{st} of the known reference gas and the uncertainty of the mean $\sigma_{s,meas}$ of the measured reference gas measurements. The uncertainty of the mean is calculated from the standard deviation σ and number of measurements N during the calibration as:

$$\sigma_{s,meas} = \frac{\sigma}{\sqrt{N}}. \quad (2.4.3)$$

The systematic uncertainty here is introduced by the calculation of calibration coefficients also known as the calibration curve fitting uncertainty σ_f . It is computed as:

$$\sigma_f = \sqrt{\sigma_a^2 + s_{meas}^2 \sigma_b^2 + 2s_{meas} \sigma_{ab}}, \quad (2.4.4)$$

where uncertainties of slope σ_b and intercept σ_a , the measured signal s_{meas} , as well as their covariance σ_{ab} are considered. This formulation computes the 67% confidence interval of the calibration curve (Figure 2.2).

The instrument's precision and the uncertainty of the calibration curve's fit are assumed to be independent. The total analytical uncertainty is the combination of the uncertainty due to instrument noise and the uncertainty of the fit and is computed as:

$$\sigma_t = \sqrt{\sigma_p^2 + \sigma_f^2}. \quad (2.4.5)$$

Other sources of uncertainty can be considered, such as water dilution, sampling biases, among others. We address these in Section 2.4.2. Finally, for ambient measurements in between two calibrations, the calibration coefficients of a and b are linearly interpolated to the given time, and the calibration curve fitting uncertainty σ_f is temporally propagated.

2.4.1 Calibration coefficients and uncertainty

Depending on the measurement device's stability, different types of calibration can be considered:

1. “span”: to determine instrument response function (Figure 2.2),
2. “offset”: to account for short-term instrument baseline drifts in between span calibrations,
3. zero level: when baseline drift is problematic near zero.

What is referred to as a “span calibration”, hereafter, is the sequential measurement of at least two reference gases with low and high trace gas mole fractions which cover the range of ambient observed mole fractions. The goal here is to derive the measurement instrument's response function in the range of observed variation. Ambient measurements outside the mole fraction range of the reference gases are flagged (see Section 2.4.6).

As mentioned, we assume a fully linear instrument response and thus describe a span calibration as a line which may or may not be forced through zero as illustrated in Figure 2.2. Uncertainties of the measured signals (Figure 2.2, horizontal arrows) and the reference gas mole fractions (Figure 2.2, vertical arrows) need to be accounted for as they determine both the slope of the line and the confidence interval. The red lines in Figure 2.2 represent the 67% confidence range of the linear regression. This case of a non-zero offset depicts that the uncertainty of the calibration is smallest for mole fractions in between the low and high references and grows rapidly outside this range. This uncertainty of the calibration curve is computed for each measurement as an important element of the overall measurement uncertainty.

Given reference gas measurements of high and low reference gases, a two-point calibration with a free intercept can be performed. Here, the slope and intercept and their uncertainties and their covariance can be derived analytically and computed as:

$$b = \frac{c_{st,2} - c_{st,1}}{s_{meas,2} - s_{meas,1}} \quad (2.4.6)$$

$$a = \frac{c_{st,1}s_{meas,1} - c_{st,2}s_{meas,2}}{s_{meas,2} - s_{meas,1}} \quad (2.4.7)$$

$$\sigma_b = b \sqrt{\frac{\sigma_{c,st,1}^2 + \sigma_{c,st,2}^2}{(c_{st,2} - c_{st,1})^2} + \frac{\sigma_{s,meas,1}^2 + \sigma_{s,meas,2}^2}{(s_{meas,2} - s_{meas,1})^2}} \quad (2.4.8)$$

$$\sigma_a = \sqrt{\frac{(c_{st,2} - c_{st,1})^2 (s_{meas,2}^2 \sigma_{s,meas,1}^2 + s_{meas,1}^2 \sigma_{s,meas,2}^2)}{(s_{meas,2} - s_{meas,1})^4} + \frac{s_{meas,2}^2 \sigma_{c,st,1}^2 + s_{meas,1}^2 \sigma_{c,st,2}^2}{(s_{meas,2} - s_{meas,1})^2}} \quad (2.4.9)$$

$$\sigma_{ab} = -\frac{(c_{st,2} - c_{st,1})^2 (s_{meas,2} \sigma_{s,meas,1}^2 + s_{meas,1} \sigma_{s,meas,2}^2)}{(s_{meas,2} - s_{meas,1})^4} - \frac{s_{meas,2} \sigma_{c,st,1}^2 + s_{meas,1} \sigma_{c,st,2}^2}{(s_{meas,2} - s_{meas,1})^2}, \quad (2.4.10)$$

where i is the index of the reference gas, $c_{st,i}$ is the known reference mole fraction, and $s_{meas,2}$ is the measured signal.

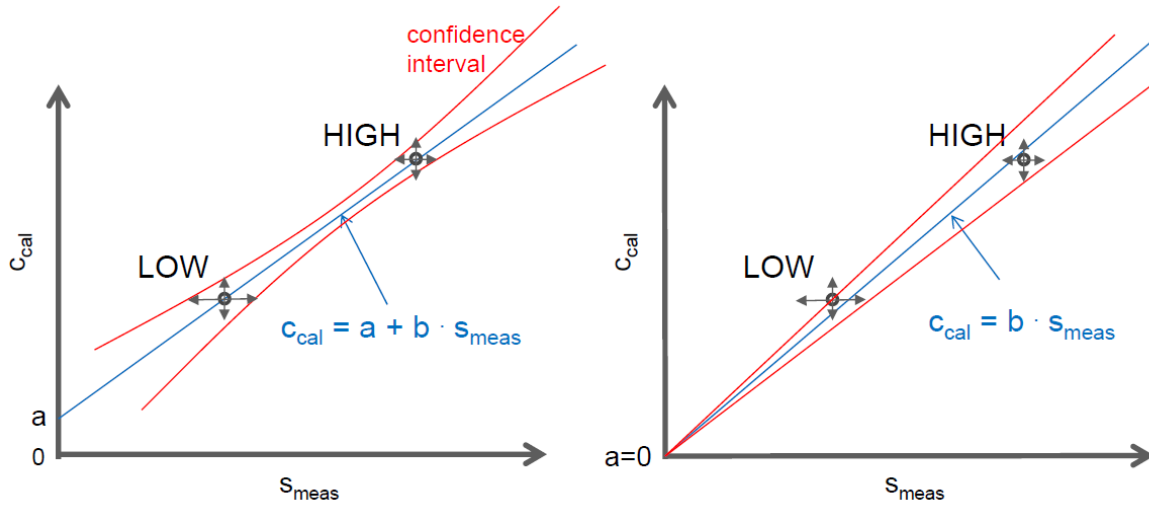


Figure 2.2: Left: Calibration with offset a and slope b . Standard errors of the calibration measurements are indicated by the horizontal arrows. Right: Similar to the left panel but the regression is forced through zero. Additional reference gas measurements may be included in both cases.

In a multiple-point calibration with free intercept or forced through origin, the values of $s_{meas,i}$, $c_{st,i}$, $\sigma_{s,meas,i}$, and $\sigma_{c,st,i}$ are used in weighted total least squares (WTLS) regression [Krystek and Anton, 2008], which takes into account the uncertainties of individual points in both coordinate directions. The WTLS algorithm directly yields σ_a , σ_b , and σ_{ab} .

In the case of a single point calibration forced through origin, the slope b can be calculated from the ratio of c_{st} to s_{meas} . The offset and its uncertainty are assumed to be zero, while the uncertainty of the slope is derived as:

$$\sigma_b = b \sqrt{\left(\frac{\sigma_{c,st}}{c_{st}}\right)^2 + \left(\frac{\sigma_{s,meas}}{s_{meas}}\right)^2}. \quad (2.4.11)$$

In case of significant instrument drifts, it makes sense to perform additional, frequent "offset calibrations" in between span calibrations. For this, a "working" gas is sampled immediately before or after span calibrations and in regular intervals in between two span calibrations. The mole fractions of this working gas do not need to be known accurately and can be done with gases housed in less expensive, high-volume cylinders. Specifically, this temporal adjustment to the set of span calibration coefficients is calculated as:

$$a_{adj}(t) = a(t) + c_{cal,w,mid}(t) - c_{cal,int,w}(t), \quad (2.4.12)$$

where for a reference gas measurement at time t in between two span calibrations at times t_1 and t_2 , the slopes $b(t_1)$ and $b(t_2)$ are linearly interpolated to time t . At the time of a working gas measurement, the temporally interpolated, intermediate span offset a_t is adjusted according to the difference between the interpolated, calibrated working gas mole fraction $c_{cal,int,w}(t)$ and the observed $c_{cal,w,mid}(t)$. These are also interpolated from times t_1 and t_2 to time t (Figure 2.4).

2.4.2 Further uncertainty considerations

Other sources of uncertainty, identified and unidentified, can contribute to measurement uncertainty. Andrews *et al.* [2014] investigated analyzer baseline drift of PICARRO devices and found it to be small, and we therefore neglect this possible source of uncertainty.

Water vapor effects are a potential source of uncertainty in CRDS measurements. However, *Rella et al.* [2013] have shown that sufficient accuracy is maintained when measuring dry air CH_4 and CO_2 mole fractions in humid air. That is, the water correction performed by the PICARRO software works well. However, CO is only partially water corrected, but the algorithm for that is unknown. *Chen et al.* [2013] provide a solution to correct PICARRO CO measurements for water dilution and pressure broadening effects. In the CarboCount CH network, this uncertainty has been ignored.

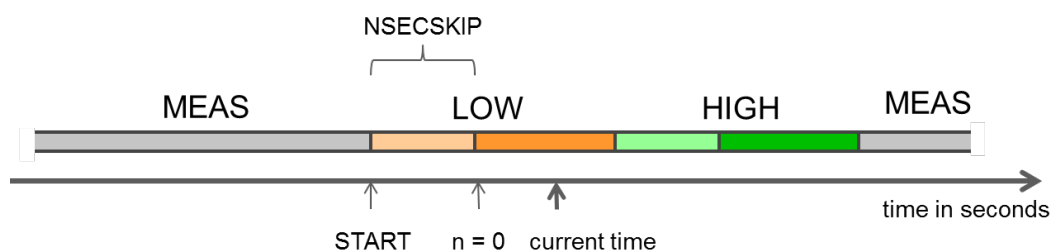


Figure 2.3: Example sequence with one LOW and HIGH reference gas measurements between ambient measurements MEAS.

For a certain and variable amount of time after a valve switch, the air flowing to the measurement device is a mixture of previously and currently sampled gases (Figure 2.3). In the measurement system at Lägern-Hochwacht, the length of this equilibration time varies with the amount of residual water in the sampling line between the second valve (V2) and the measurement device, which varies with the difference between the ambient and measurement room's temperature. At both Frübüel and Lägern-Hochwacht, the amount of time necessary for equilibration was found to be 9 minutes, as determined visually by switching from ambient measurements to reference gas sampling. Therefore, all measurement data less than 9 minutes after valve transition are discarded. This time of the equilibration is transferred to ambient air measurements i.e. when switching from standard gas to ambient measurements or when switching sampling heights. Therefore, the uncertainty of equilibration due to proximity to a preceding valve transition is assumed to be zero. Due to a different setup at Beromünster, the equilibration time is much shorter with ~ 2 minutes sufficing to flush the tubing [*Berhanu et al.*, 2016].

Sampling bias describes the uncertainty introduced by the measurement system. For example, a leak in the tubing between the inlet and the measurement device would greatly affect gas samples. Initial and recurring, periodical leak tests during ambient measurements were carried out i.e. when the pressure inside the measurement system was less than ambient pressure. Directly after installation, highly concentrated CO (450 ppm) was applied to the outside of all fittings, while mole fractions were monitored. Later in the campaign, breathing onto the fittings was also unable to uncover any leaks. As a simple test later on in the campaign, the measurement inlet was plugged and a vacuum was successfully created between the inlet and measurement device. After these initial and recurring tests, it can be said that a significant sampling bias is likely absent.

2.4.3 Target gas measurements

"Target" reference gas measurements are not used for determining calibration coefficients and serve as an independent evaluation of the validity of the calibration procedure and of the representativeness of the estimated analytical uncertainty. The mole fractions of target gas references have to be stable over time. Target calibrations are treated in the same way as ambient measurements with regard to calibration. The difference between the known mole fraction and calibrated measured signals of the target gas provides a direct measure of the overall accuracy and overall validity of the calibration procedure.

In our case, target calibrations are additionally used to determine instrument precision or random analytical uncertainty of ambient air measurements. Furthermore, we report an independent measure of uncertainty based on target gas measurements. The difference between calibrated target gas measurements and known reference gas mole fractions is computed. These differences are reported directly as well as a temporally smoothed root mean squared error.

2.4.4 Calibration of ambient measurements

Ambient air samples are ideally collected in between two reference gas measurement cycles. Here, the calibration curve may have changed. It is assumed that such changes occur slowly with time. Therefore, temporally binning calibration curve coefficients are interpolated to the time of the measurements. Depending on the quality of the calibrations, it may be necessary to average coefficients from multiple calibrations.

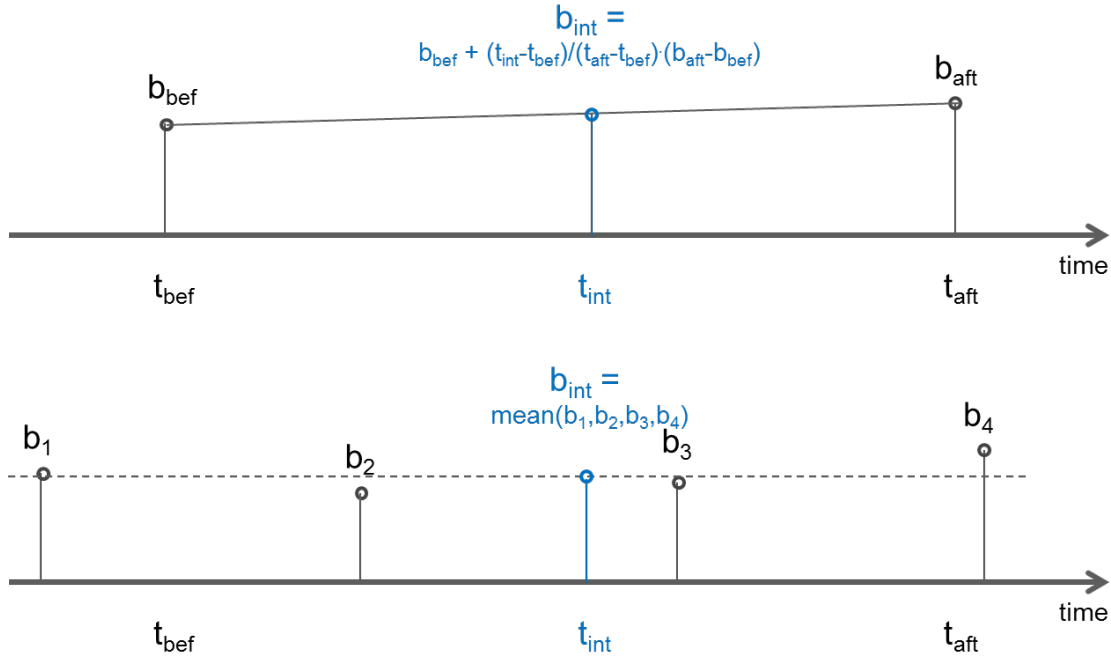


Figure 2.4: Schematic of temporal interpolation (top) or temporal averaging (bottom) of calibration coefficients from “span” calibrations binning the targeted processing time t_{int} .

The two options are illustrated in Figure 2.4 for the span coefficient b . The upper panel of Figure 2.4 describes a simple linear interpolation of the slope b between calibrations before and after the current time t_{int} . The lower panel describes the situation where a mean coefficient is computed from all calibrations within a given time range (e.g. ± 3 days) of t_{int} . In the first case, calibration coefficients change continuously with time. In the second case, calibration coefficients are constant for a certain period but change stepwise whenever a new calibration appears in the moving time-window. Due to the high quality and the temporal stability of the measurement systems in CarboCount CH, the first approach has been implemented. If this approach appears to be suboptimal, a further option using local regression instead of a moving mean would possibly be better suited.

As in Equation (2.4.1), a measured signal $s_{meas,t}$ at time t_{int} is calibrated as

$$c_{cal,t_{int}} = a_{t_{int}} + b_{t_{int}} s_{meas,t_{int}}. \quad (2.4.13)$$

The linear interpolation of calibration coefficients to the time t_{int} of a certain measurement is

$$w_2 = \frac{t_{int} - t_1}{t_2 - t_1} \quad (2.4.14)$$

$$w_1 = 1 - w_2 \quad (2.4.15)$$

$$b_{t_{int}} = w_1 b_1 + w_2 b_2 \quad (2.4.16)$$

$$a_{t_{int}} = w_1 a_1 + w_2 a_2, \quad (2.4.17)$$

where t_{int} is in between times t_1 and t_2 , and the weights w depend on the temporal distance from times t_1 and t_2 . The interpolation of the related uncertainties is computed as:

$$\sigma_{a,t_{int}} = \sqrt{w_1^2 \sigma_{a,1}^2 + w_2^2 \sigma_{a,2}^2} \quad (2.4.18)$$

$$\sigma_{b,t_{int}} = \sqrt{w_1^2 \sigma_{b,1}^2 + w_2^2 \sigma_{b,2}^2} \quad (2.4.19)$$

$$\sigma_{ab,t_{int}} = w_1^2 \sigma_{ab,1} + w_2^2 \sigma_{ab,2}. \quad (2.4.20)$$

2.4.4.1 Observed variability

Observed mole fractions can vary much during one-minute intervals. This variability is the combination of uncertainty introduced by the measurement system and true atmospheric variability during the one-minute averaging period. The standard error of a one-minute mean value $\sigma_{s,v}$ is the standard deviation σ_v divided by the square root of the number N of all samples during a one-minute interval:

$$\sigma_{s,v} = \frac{\sigma_v}{\sqrt{N}}. \quad (2.4.21)$$

This uncertainty is typically larger than the precision σ_p . Because the random analytical uncertainty has been estimated for one-minute averages, true atmospheric variability can then be estimated. Therefore, as mentioned, target gas measurements are used to determine the random analytical uncertainty of ambient air measurements.

2.4.5 Higher time aggregates

Short-term temporal variability is of random nature and therefore not interesting in the context of regional-scale modeling. The variation due to random atmospheric variability can also be reduced with temporal averaging. For efficiency, higher time aggregates are computed from the averaged, calibrated one-minute data. The combined uncertainty of these time aggregates needs to consider random and non-random components of the one-minute values and the uncertainty due to incomplete temporal coverage. The temporal average is given by:

$$\bar{c} = \frac{1}{N} \sum_i^N c_{cal,i}, \quad (2.4.22)$$

and its uncertainty is composed of the analytical uncertainty $\sigma_{\bar{c},a}$ and, eventually, the uncertainty due to missing values σ_u (under-sampling):

$$\sigma_{\bar{c}} = \sqrt{\sigma_{\bar{c},a}^2 + \sigma_u^2}. \quad (2.4.23)$$

The analytical uncertainty of the mean can be calculated from the random σ_p and the non-random σ_f contributions of the analytical uncertainty of the individual one-minute measurements. When non-random uncertainty is not constant over time, the total analytical uncertainty of the mean is:

$$\sigma_{\bar{c},a}^2 = \frac{1}{N^2} \sum_i^N \sigma_{a,p,i}^2 + \frac{1}{N} \sum_i^N \sigma_{a,f,i}^2. \quad (2.4.24)$$

The uncertainty due to missing values σ_u is calculated as:

$$\sigma_u^2 = \left(1 - \frac{N}{N_{max}}\right) \frac{1}{N} S^2 \quad (2.4.25)$$

$$S^2 = \frac{1}{N-1} \sum_i^N (c_{cal,i} - \bar{c})^2, \quad (2.4.26)$$

where N_{max} is the number of samples that could have been taken by continuous, uninterrupted sampling, N is the number of measurements made, and S is the variance observed during the aggregation interval. To precisely specify the observed variability for higher time aggregates (ten-minute, hourly, and three-hourly) of period K , the period's standard error of the mean $\sigma_{s,K}$ should also be calculated from the raw sampling data, in the same manner as for the one-minute aggregates.

Ideally, the observed variability of higher time aggregates should be calculated from the high-frequency measured signals. For efficiency, this can also be approximated from the one-minute aggregates. This requires that the observed variability in each one-minute interval $\sigma_{s,1,i}$, the standard deviation of the one-minute averages, the number of measured signals for each one-minute interval $n_{1,i}$, and the one-minute mean values $c_{1,i}$ are available. Then $\sigma_{s,K}$ can be calculated as:

$$\sigma_{s,K} = \sqrt{\sigma_{s,v}^2 + \sigma_{s,p}^2} \quad (2.4.27)$$

$$\sigma_{s,v} = \frac{\frac{\sum_i^N (c_{cal,i} - \bar{c})^2}{N-1}}{\sqrt{\sum_i n_i}} \quad (2.4.28)$$

$$\sigma_{s,p} = \frac{\sum_i \sigma_{s,1,i}^2}{m}, \quad (2.4.29)$$

where m is the number of one-minute averages included in the higher time aggregate, $\sigma_{s,v}$ is the uncertainty of the one-minute averages, and $\sigma_{s,p}$ is the standard error of the one-minute averages. In a situation with a constant mean (little variability on time scales beyond one-minute) this approximation appears to overestimate the directly observed variability. When there is high variability, this formulation is a good approximation. The observed variability of higher time aggregates is expected to be larger than the analytical uncertainty of higher time aggregates.

2.4.6 Quality control

Even with a well-functioning measurement device, erroneous values still arise for reasons listed in Table 2.4. Automatic exclusion of erroneous values is partially applicable, but the need for manual inspection still exists. This requires careful consideration and justification to exclude anomalous but otherwise undisturbed

Table 2.4: Flag table for CarboCount CH measurement data.

Code	Description	Notes
0	No event compromising data quality or precision	Highest data quality such that a calibration is near, the precision is high, the measured mole fraction lies within the range of reference gas mole fractions.
1	Uncertainty of a value is greater than 1 per mil	The calculated uncertainty does not meet quality requirements.
2	Measured mole fraction is outside of the calibration mole fraction range	Measured mole fractions outside the range spanned by the low and high reference gas calibration mole fractions, or one-point calibration.
4	Reference gas measurements are far removed in time	The nearest calibration coefficients are temporally interpolated.
8	Critically low average number of measurements	Poor quality data, the device may measure more than one gas and may not measure each gas regularly.
16	Unassigned	
32	Unassigned	
64	Unassigned	
128	Data are not usable	Due to work done on the device, tower or other activities that may contaminate samples.
NaN	Device did not measure or data occurred in a valve transition	Due to power loss, valve change etc., the data are not present.

measurements. The flagging system described in Table 2.4 is a result of the uncertainties considered and encountered during the CarboCount site operations. It is based on a binary system which allows combining different flags from co-occurring events into a single number. This flagging system is applied to each measured gas separately. It is somewhat automated, but manual application of flagging system to ambient and calibration measurements is nonetheless necessary to assure good data quality.

2.5 Ambient and reference gas measurements

2.5.1 Uncertainty estimates

The ability to accurately estimate the known mole fraction of the target reference gas throughout the measurement campaign with the calibration routines lends credibility to its effectiveness. The target uncertainties as reported here demonstrate the validity of our calibration routine (Figure 2.5, summaries in Table 2.5). Calibrated target gas measurements of CO₂ and CH₄ typically deviate ~ 0.07 and ~ 0.0005 ppm from known target reference gas mole fractions, which implies compatibility with WMO guidelines of ± 0.1 ppm and ± 0.002 ppm, respectively. *Richardson et al.* [2012] attained similar results during the Mid-Continental Intensive measurement campaign with PICARRO analyzers.

Table 2.5: Root mean square error (in ppm) between known and calibrated target reference gas mole fractions during their period of measurement (see Figure 2.5).

Site	CO ₂	CH ₄	CO
Beromünster	0.061	0.0018	0.0037
Früebühl	0.079	0.0004	
Gimmiz	0.077	0.00029	
Lägern-Hochwacht	0.049	0.00027	0.0025

Differences between sites are due mainly to differences in reference gas sampling routines. At Beromünster,

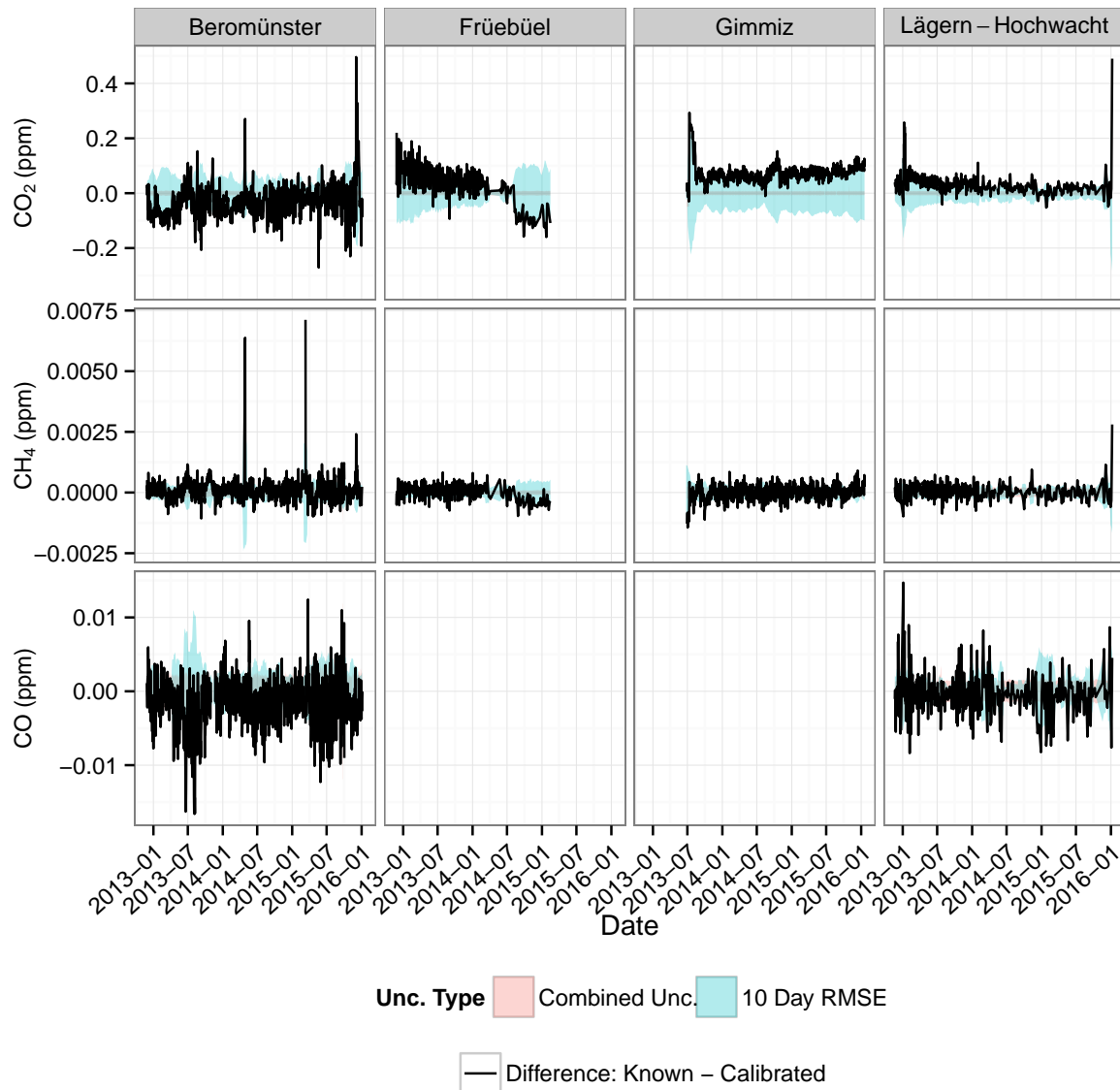


Figure 2.5: Target gas calibration results at the CarboCount CH sites. Individual differences between known and calibrated target gas molar ratios are plotted, with independent analytical and target uncertainty bands (\pm).

shorter sampling times of 6 minutes (4 minutes after valve change) likely result in more variable target gas measurements, which contrasts with that at Frübüel or Lägern-Hochwacht of 15 minutes (6 minutes after valve change). Furthermore, it appears that some target gas mole fractions could be known better, such as the CO₂ mole fraction at Gimmiz. Similarly, a target gas bottle change at Frübüel during the summer of 2014 also influenced the CH₄ target uncertainty, leading to a small bias between known and calibrated mole fractions. Here, it may be that the determination of the child cylinder is not as certain as thought. These small deviations are still well within WMO quality requirements, but illuminate the possible problems with relying on target gas measurements for uncertainty estimation.

CO measurements at Beromünster and Lägern-Hochwacht, on the other hand, include significant random systematic uncertainty due to the measurement device. Nonetheless, calibrated target measurements typically

deviate ~ 0.003 ppm from known target gas mole fractions. Here, the quality of these measurements fulfill WMO guidelines extended compatibility goals of ± 0.005 ppm, but fail to meet the stricter compatibility goals of ± 0.002 ppm.

Directly estimating the analytical uncertainty grossly underestimates the apparent uncertainty of all gases, suggesting an additional unconsidered source of uncertainty. The ignorance of the uncertainties of scale and of the determined mole fractions of the parent standards may contribute the necessary constant uncertainties necessary to remove a possible low bias of the estimated uncertainties. Also likely would be contributions of baseline drift and water correction uncertainties inherent to the PICARRO devices. Together, these uncertainty contributions would inflate the estimated uncertainties. Furthermore, we likely do not have realistic estimates for the CO measurements at Gimmiz, because the analytical uncertainties are not representative. Investigation is necessary to improve calibration and uncertainty estimation in general and especially the uncertainty of the CO measurements at Gimmiz, where target gas measurements were not carried out for CO.

Altogether, these observed time series are of good quality (Table 2.5), especially with regard to observed regional signal variability (please compare Figure 2.6 to the MLO time-series in Figure 1.4). As emphasized by *Tans and Zellweger* [2014], regional scale modeling studies need to maintain consistency of reference scales within the measurement network.

2.5.2 Measurement time series

The network's atmospheric carbon measurements exhibit large seasonal and daily variability. The seasonal CO₂ cycle is most pronounced, but is also considerable in both CO and CH₄. For example, the trend of increasing CO₂ mole fractions is visible from the lowest mole fractions (Figure 2.6), but is small relative to the annual range of observed mole fractions.

The diurnal variability is also very large, and is greatest in summer at Gimmiz (Figure 2.7). Here, the diurnal variability is present also during winter, and is therefore most likely due to ABL dynamics, as will be discussed in more detail in the following Chapter.

2.6 Practical monitoring considerations

With the goal of meeting the WMO's greenhouse gas measurement guidelines [*Tans and Zellweger*, 2014], while keeping maintenance costs minimal, measurement system failures need to be avoided and repetitive tasks need to be automated. To meet these goals within the CarboCount project, a considerable initial investment was required. This has been successful in keeping further costs low. The following contains what was learned from the measurements made at Lägern-Hochwacht, and to a large degree also at Fröebühl.

Filling and determination of reference gas bottles can be a cumbersome and costly task, especially if reference gases need to be calibrated by an external laboratory. Measurement of reference gases for span calibration was initially frequent at the CarboCount sites: every 20 hours a target gas measurement and every 40 hours a measurement of high and low mole fraction reference gases were sampled for 15 minutes each. On February 6, 2014, a less frequent reference gas measurement routine was implemented, measuring target, low, and high reference gases every 100 hours. Here, the target reference gas was sequentially sampled 5 hours later in the sampling cycle i.e. directly after the span reference measurement, then 5 hours afterwards, then 10 hours afterwards, and so on. The target gas reference measurement steps through the calibration cycle and time of day to possibly uncover the effect of changing room temperature. As can be seen in Figure 2.5, the larger temporal distance from span reference measurements and seasonally varying room temperature effects likely

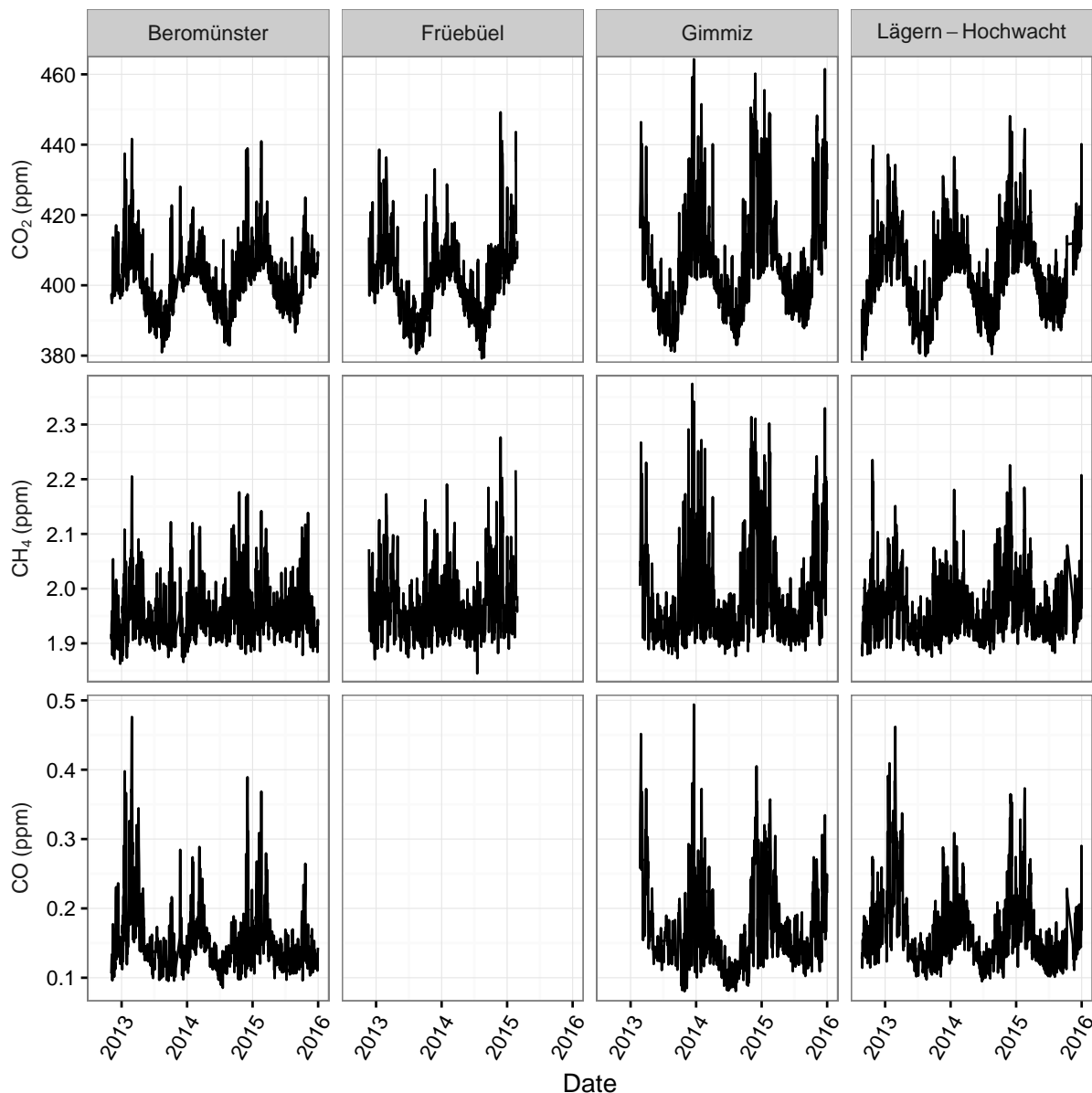


Figure 2.6: Atmospheric carbon measurements (CO_2 , CH_4 , & CO) during afternoon (1200-1500 UTC, 1300-1600 LT) at the CarboCount CH sites. The Beromünster data are from the highest sampling height (212 m).

did not affect target uncertainty. Therefore, the infrequent sampling and use of reference gas greatly reduces costs, but appeared to not have compromised data quality. Furthermore, Beromünster span calibration gas sampling is carried out weekly, which also does not seem to affect data quality. A longer calibration interval may be considered in the future, but would need testing, which could be performed with currently available standard gas measurements.

2.6.1 Equipment

Several problems of the measurement systems were avoided or solved after discovery, and current equipment recommendations are in Table 2.3. First and foremost, the quality of the standard PICARRO pumps was

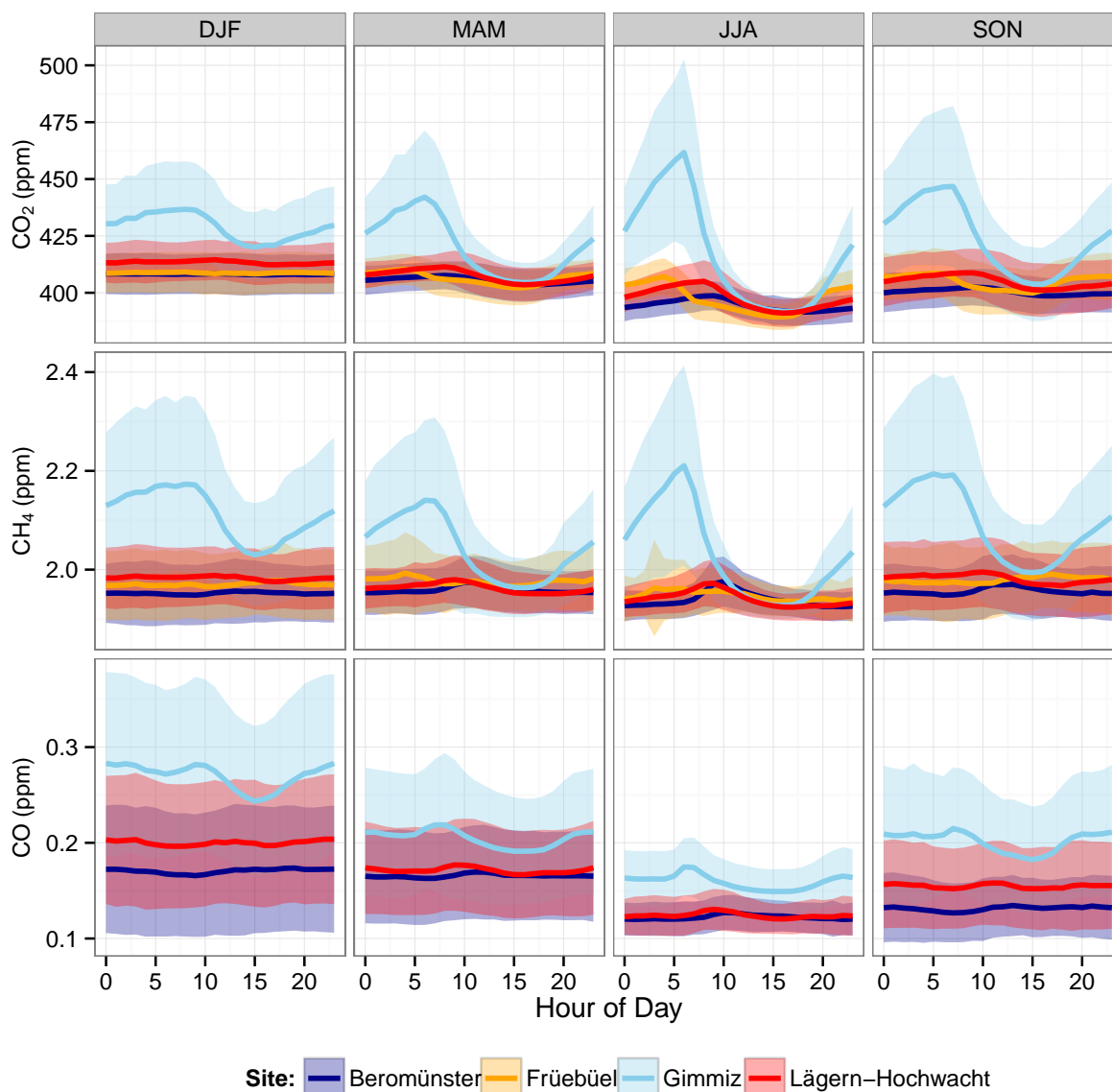


Figure 2.7: Seasonal average daily cycles of observed atmospheric carbon mole fractions from the CarboCount CH sites. Uncertainty bands correspond to $\pm 1\sigma$ at the respective time of day. Time zone is UTC.

not sufficient for sustained monitoring. Within four months of deployment, three of four pumps had failed. Most pumps were replaced with higher-quality, stronger pumps, which have operated reliably since.

After the initial pump failure at Lägern-Hochwacht, the measurement device began to measure some gases less frequently ($1\text{--}2\text{ min}^{-1}$ vs. $20\text{--}25\text{ min}^{-1}$). In order to solve this problem, one of the laser's voltage needed to be manually adjusted. Since then, this procedure was carried out three more times, but has not been necessary since April 2014. To uncover this problem, it is necessary to monitor the number of measurements being made or monitor the raw data file sizes. Both of these tests can only be done using the raw data files, and it is therefore not advisable to opt for the temporally averaged "DataLog_User_Sync" PICARRO data.

In order to avoid a potential failure of the computer's hard disk as well as to ensure sufficient storage capacity, the stock hard disk was replaced with a higher capacity hard disk. Initially, the valve control board could

power only five of six valves, which also needed replacement.

The three-stage brass regulators repeatedly stopped allowing airflow. This was fixed by removing the bonnet nut on the back of the main regulator's body and adjusting the underlying screw nut. Further measurement campaigns will likely not use these pressure regulators.

2.6.2 Operational data processing considerations

An automated data transfer and data control system was set up to retrieve measurements from the field-deployed instrument in near real-time. Data was sent hourly to an sFTP server via broadband Internet connection. A broadband USB Internet connection is regularly toggled on and off, in order to not overstrain the USB-broadband Internet stick. New data are sent with `rsync` (Cygwin). Data older than three months are moved to a non-standard file location, in order to reduce the computational strain of retrieving and comparing file attributes. Three-hourly automatic checks are carried out. First, notifications are sent if data has not been received in the last three hours. Second, file sizes are checked, for reasons previously discussed.

Upon initial aggregation to one-minute values, data after a valve change are discarded and remaining data are then split into ambient and reference gas measurements. For this, it was practical to define site- and time-dependent valve information, which specifies what is being sampled (valve configuration) and the time necessary for measured signals to equilibrate after valve change (Figure 2.3). This form of site- and time-dependent valve information greatly eases data processing when valve configuration changes take place, such as reference gas bottle changes. Finally, due to changes in the reference scale or drifts in reference gas mole fractions during the measurement campaign, this information greatly facilitates retroactive calibration.

Furthermore, time and site-dependent device information was defined, which specifies the serial number of the device, period of deployment, the measured gas species, and possible erroneous values. This also eases data processing, when the devices are replaced, or to account for certain anomalies in the data that are specific to a certain device and gas species. Most importantly, device changes indicate a change in the calibration coefficients, which implies no temporal interpolation of these temporally adjacent but different sets of calibration coefficients.

These forms of information organization constitute a minimum amount of measurement site documentation in order to make the processing calibration of CarboCount CH affordable and timely. Examples of this and an overview of the code to process the measurement data from the network can be found in Appendix A (specifically Tables A.1 & A.2).

2.7 Conclusions

Precise and accurate measurement of atmospheric carbon constitutes an important step toward understanding carbon fluxes between the atmosphere and Earth's surface in a top-down modeling framework. Here, we described and discussed the measurement system of Lägern-Hochwacht, a CarboCount CH Swiss Sinergia Project measurement site. Then, we described and discussed the measurement uncertainty estimation CarboCount CH sites: Beromünster, Frübüel, Gimmiz, and Lägern-Hochwacht.

At Lägern-Hochwacht from 2012-08-23 to 2015-10-01, the measurement system operated 99% of the time. The single major break in measurements was due to a pump failure. A similar measurement system at Frübüel also reported a good temporal coverage (96% temporal coverage). The few measurement gaps at Frübüel were due to the failure of measurement device's pump and power outages. The need for long equilibration times of 9 minutes after a valve switch to reference gas measurement are reconciled by the infrequent calibrations, as well as by the robustness and simplicity of the measurement system.

Across all sites, we report CO_2 and CH_4 measurements calibrated against the corresponding international reference scales. The calibration of independently measured target reference gases suggests an accuracy of the CO_2 and CH_4 measurements ~ 0.07 ppm and ~ 0.0004 ppm. Except for Frübüel, CO was also continuously measured, was similarly calibrated, and was determined to have a determined accuracy of ~ 0.004 ppm at Beromünster and Lägern-Hochwacht. This is mostly due to the poor instrument precision. This can be lessened with temporal averaging. Further investigation is necessary of the calibration and uncertainty estimation of the CO measurements at Gimmiz, where target gas measurements were not carried out.

Chapter 3

The CarboCount CH sites: characterization of a dense greenhouse gas observation network

Published in Atmospheric Chemistry and Physics, 15, 11147–11164, 2015

Authors: Brian Oney^{1,2}, Stephan Henne¹, Nicolas Gruber^{2,3}, Markus Leuenberger⁴, Ines Bamberger^{5,a}, Werner Eugster⁵, Dominik Brunner^{1,2}

¹ Lab. for Air Pollution/Environmental Technology, Dübendorf, Switzerland

² ETH Zurich, Center for Climate Systems Modeling, Zurich, Switzerland

³ ETH Zurich, Inst. of Biogeochemistry and Pollutant Dynamics, Zurich, Switzerland

⁴ Univ. of Bern, Physics Inst., Climate and Environmental Division, and Oeschger Centre for Climate Change Research, Bern, Switzerland

⁵ ETH Zurich, Inst. of Agricultural Sciences, Zurich, Switzerland

^a now at: Karlsruhe Institute of Technology, Institute of Meteorology and Climate Research – Atmospheric Environmental Research, Garmisch-Partenkirchen, Germany

3.1 Abstract

We describe a new rural network of four densely placed (< 100 km apart), continuous atmospheric carbon (CO_2 , CH_4 , and CO) measurement sites in north-central Switzerland and analyze its suitability for regional-scale (~ 100 – 500 km) carbon flux studies. We characterize each site for the period from March 2013 to February 2014 by analyzing surrounding land cover, observed local meteorology, and sensitivity to surface fluxes, as simulated with the Lagrangian particle dispersion model FLEXPART-COSMO (FLEXible PARTicle dispersion model-Consortium for Small-Scale Modeling).

The Beromünster measurements are made on a tall tower (212 m) located on a gentle hill. At Beromünster, regional CO_2 signals (measurement minus background) vary diurnally from -4 to $+4$ ppmv, on average, and are simulated to come from nearly the entire Swiss Plateau, where 50 % of surface influence is simulated to be within 130–260 km distance. The Frübüel site measurements are made 4 m above ground on the flank of a gently sloping mountain. Nearby (< 50 km) pasture and forest fluxes exert the most simulated surface influence, except during convective summertime days when the site is mainly influenced by the eastern Swiss Plateau, which results in summertime regional CO_2 signals varying diurnally from -5 to $+12$ ppmv and elevated summer daytime CH_4 signals ($+30$ ppbv above other sites). The Gimmiz site measurements are made on a small tower (32 m) in flat terrain. Here, strong summertime regional signals (-5 to $+60$ ppmv CO_2) stem from large, nearby (< 50 km) crop and anthropogenic fluxes of the Seeland region, except during warm or windy days when simulated surface influence is of regional scale (< 250 km). The Lägern-Hochwacht measurements are made on a small tower (32 m) on top of the steep Lägern crest, where simulated surface influence is typically of regional scale (130–300 km) causing summertime regional signals to vary from -5 to $+8$ ppmv CO_2 . Here, considerable anthropogenic influence from the nearby industrialized region near Zurich causes the average wintertime regional CO_2 signals to be 5 ppmv above the regional signals simultaneously measured at the Frübüel site.

We find that the suitability of the data sets from our current observation network for regional carbon budgeting studies largely depends on the ability of the high-resolution (2 km) atmospheric transport model to correctly capture the temporal dynamics of the stratification of the lower atmosphere at the different sites. The current version of the atmospheric transport model captures these dynamics well, but it clearly reaches its limits at the sites in steep topography and at the sites that generally remain in the surface layer. Trace gas transport and inverse modeling studies will be necessary to determine the impact of these limitations on our ability to derive reliable regional-scale carbon flux estimates in the complex Swiss landscape.

3.2 Introduction

The exchange of carbon dioxide (CO_2) with the terrestrial biosphere dominates the observed year-to-year variability in the global carbon sinks [Battle *et al.*, 2000; Sarmiento *et al.*, 2010; Le Quéré *et al.*, 2010] even though land surfaces cover only 30 % of Earth’s surface area. Yet, our ability to quantify this variability in the net terrestrial carbon flux directly from observations has remained limited [Ciais *et al.*, 2014]. As a result, in most attempts to determine the global carbon budget, the net terrestrial carbon flux is estimated as the difference between the observed atmospheric carbon growth rate, and the sum of oceanic and anthropogenic carbon fluxes [Sarmiento *et al.*, 2010; Le Quéré *et al.*, 2013]. Additionally, the lack of understanding of the feedbacks between climate change and the terrestrial biosphere translates into one of the greatest uncertainties of future climate change projections [Heimann and Reichstein, 2008]. An important step toward the reduction of this uncertainty is a better understanding of how the terrestrial biosphere responds to climatic fluctuations and trends. As the processes governing this response are inherently local to regional, this requires the determination of terrestrial carbon fluxes at high spatial resolution [Gerbig *et al.*, 2009].

The currently employed methods to determine terrestrial carbon fluxes from observations include global networks of background CO_2 measurements [Tans *et al.*, 1996] that permit the determination of fluxes at continental scales [Gerbige *et al.*, 2003b] and eddy covariance-based surface flux measurements that have a small-scale (~ 1 km) footprint [Baldocchi *et al.*, 2001]. This leaves an obvious gap at intermediate scales (10–10 000 km), which clearly needs to be filled in order to reliably determine the terrestrial carbon budget [Ciais *et al.*, 2014]. The establishment of the North American [Bakwin *et al.*, 1998] and European [http://www.chiotto.org/; Vermeulen *et al.*, 2004] tall tower networks represented a big step in this direction, but the high spatial heterogeneity of land cover and the correspondingly large variations in the CO_2 fluxes require even denser observation networks, especially in order to target regional-scale (< 1000 km) carbon fluxes [Dolman *et al.*, 2009; Lauvaux *et al.*, 2012a]. The spatial density of a measurement network required to resolve the spatial distribution of carbon fluxes is dependent on the region of interest and the corresponding carbon flux signatures, and largely remains an open question [Groenendijk *et al.*, 2011; Lauvaux *et al.*, 2012a].

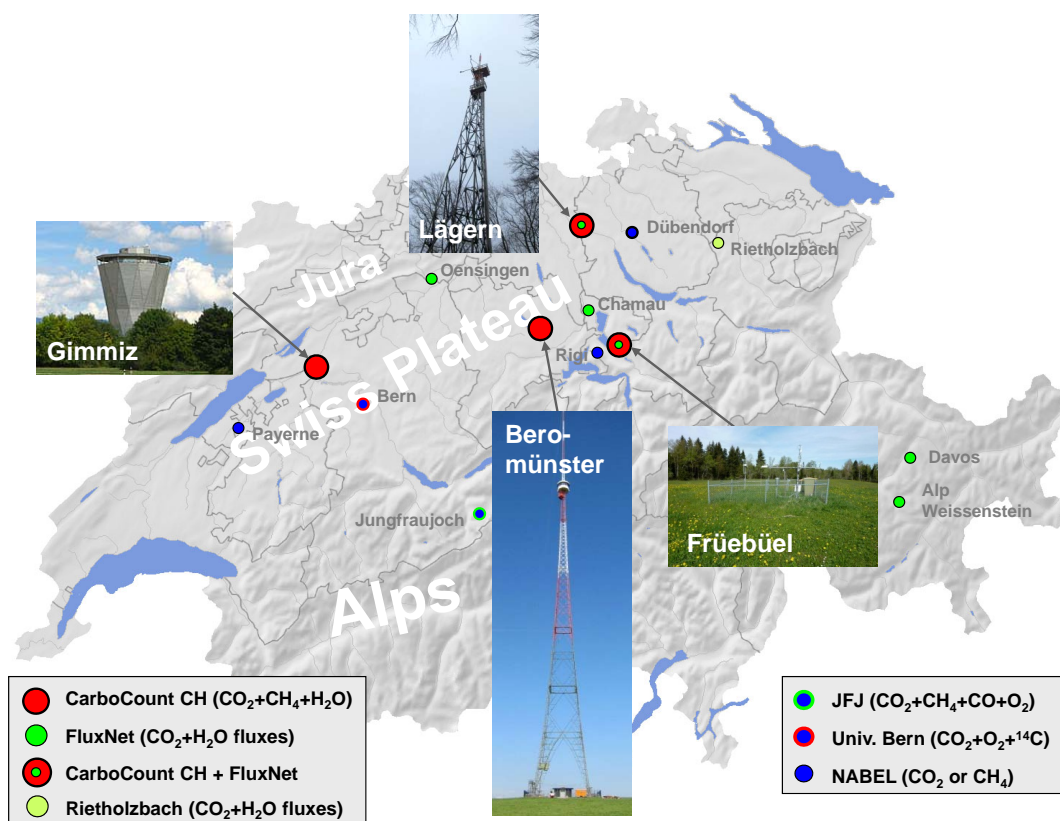


Figure 3.1: An overview of CarboCount CH measurement site locations within Switzerland: Beromünster (BEO), Fruebüel (FRU), Gimmiz (GIM), and Läger-Hochwacht (LAE). The sites are concentrated along the Swiss Plateau. The measurement heights and locations are listed in Table 3.1. Also shown are other sites with greenhouse gas concentration or flux measurements that complement the network. These include the sites of the Swiss FluxNet, the high Alpine research station Jungfrauoch, and sites of the Swiss air pollution monitoring network NABEL (National Air Pollution Monitoring Network).

Short-term measurement campaigns, such as the Large-Scale Biosphere-Atmosphere Experiment in Amazonia [Andreae *et al.*, 2002], the CO_2 Budget and Rectification Airborne study [Gerbige *et al.*, 2003a], and the CarboEurope Regional Experiment Strategy study [Dolman *et al.*, 2006], have demonstrated the value of regional scale (< 1000 km) data sets, but lacked the temporal coverage for the calculation of annual carbon budgets and the investigation of seasonal carbon flux variation. The Mid-Continent Intensive (MCI) measurement

campaign attempted to oversample the US upper midwest over a longer period of time [2007–2009; *Miles et al.*, 2012], but even with an average distance of approximately 188 km between eight towers, *Lauvaux et al.* [2012a] found that the spatial density of the measurement network was insufficient to consistently retrieve the spatial distribution of carbon fluxes.

The CarboCount CH project (<http://www.carbocount.ch>) was designed to overcome some of these limitations. It intends to quantify terrestrial carbon fluxes at high temporal and spatial resolutions for multiple years through a combination of greenhouse gas concentration measurements and high-resolution atmospheric transport modeling. Four greenhouse gas measurement sites have been established in the Swiss Plateau (Fig. 3.1), which is a densely settled, partly flat and hilly region between the Alps and Jura mountains approximately 50 km by 200 km in size with an average altitude of ~ 450 m a.s.l. (above sea level). The measurement sites are located in rural areas and the average distance between sites is 85 km. The main goal of the CarboCount CH project is to better understand surface fluxes of carbon, which for carbon dioxide (CO_2) mainly consist of anthropogenic emissions and biospheric activity, and for methane (CH_4) mainly ($\sim 80\%$) of agricultural emissions [*Hiller et al.*, 2014].

The CarboCount CH measurement network includes measurement sites in complex terrain, which warrants the use of high-resolution transport models [*Pillai et al.*, 2011]. A measurement site’s local environment, especially the topography and land cover within a 3 km distance, exerts influence on the local meteorology and thereby largely determines the local surface influence on observed trace gas concentrations [*Vesala et al.*, 2008]. Currently, most surface flux estimation studies use only afternoon measurements from sites in flat terrain when the ABL (atmospheric boundary layer) is thickest and well-mixed to reduce the sensitivity to errors in the representation of the ABL by the atmospheric transport models [*Gerbige et al.*, 2009; *Pillai et al.*, 2012; *Kretschmer et al.*, 2014]. At mountain sites, conversely, nighttime or early morning measurements above the stable ABL are preferentially used due to the difficulties in correctly representing the daytime convective ABL above steep terrain. In inverse modeling studies using coarse resolution models, measurements from mountain sites are usually discarded all together.

The purpose of this study is to characterize the CarboCount CH observation network. We describe the local environment of each of the four measurement sites and investigate how much the local environment influences meteorology and greenhouse gas measurements. Furthermore, we assess the sensitivity of each measurement site to regional surface fluxes with the Lagrangian particle dispersion model FLEXPART-COSMO (FLEXible PARTicle dispersion model-Consortium for Small-Scale Modeling). Due to the dependence on the employed atmospheric transport model to represent local and regional surface influences, we evaluate simulated meteorology in order to uncover possible transport simulation problems. Thus, we assess the information content of each site’s measurements and establish potential guidelines for future transport and inverse modeling studies.

3.3 Data and methods

3.3.1 Measurement data

The four measurement sites of the CarboCount CH network (Fig. 3.1, Table 3.1) were equipped with PICARRO (Santa Clara, California, USA) cavity ring-down spectrometers for greenhouse gases measurements [*Crosson*, 2008; *Rella et al.*, 2013]. Additionally, meteorological variables including horizontal wind, humidity, dewpoint, and temperature were measured at all four sites. At Beromünster (BEO), air was sampled from five different heights (212, 132, 72, 45, and 12 m a.g.l. – above ground level), and carbon dioxide (CO_2), methane (CH_4), water (H_2O) and carbon monoxide (CO) were measured with a PICARRO G2401 analyzer. Meteorology was measured at all heights with Gill MetPak II remote weather stations (Gill Instruments Ltd., Hampshire, UK). Data used in this study were taken from the highest height. At Gimmiz (GIM), CO_2 , CH_4 ,

Table 3.1: Details of the four measurement sites of the CarboCount CH network. From left to right: the site name, the site code, measurement commencement date, the measurement height(s), measured trace gases, the site’s altitude (m a.s.l.), and the geographic site locations.

Site	Code	Date	Gases	Device	Height(s)	Alt.	Lat., Lon.
Beromünster	BEO	3 Nov 2012	CO ₂ , CH ₄ , CO, H ₂ O	PICARRO G2401	212, 132, 72,	797	47.1896, 8.1755
			CO ₂ , CH ₄ , H ₂ O	PICARRO G2311-f	45, 12		
Früebüel	FRU	21 Nov 2012	CO ₂ , CH ₄ , H ₂ O	PICARRO G2301	4	982	47.1158, 8.5378
Gimmiz	GIM	22 Feb 2013	CO ₂ , CH ₄ , H ₂ O CO	PICARRO G2301 Horiba APMA 360	32	443	47.0536, 7.2480
Lägern-Hochwacht	LAE	23 Aug 2012	CO ₂ , CH ₄ , CO, H ₂ O	PICARRO G2401	32	840	47.4822, 8.3973

and H₂O concentrations were measured with a PICARRO G2301 and CO with a Horiba APMA360, all of which were taken at 32 m a.g.l. The same meteorology instrumentation at Beromünster was employed here. At Früebüel (FRU), which is also a Swiss FluxNet site [Zeeman *et al.*, 2010], CO₂, CH₄, and H₂O concentrations were measured with a PICARRO G2301 at 4 m a.g.l. and meteorology variables were measured at a height of 2 m a.g.l. [Bamberger *et al.*, 2016]. On the 32 m tower at Lägern-Hochwacht (LAE), CO₂, CH₄, CO, and H₂O concentrations were measured with a PICARRO G2401. Here, MeteoSwiss measured the following meteorological variables: wind (Vaisala WA25 Wind Set, Vaisala Inc., Helsinki, Finland), temperature and humidity (Vaisala HMP155), and pressure (Vaisala PTB-220).

CO₂ and CH₄ measurements were calibrated against the corresponding international reference scales: WMO X2007 for CO₂ [Zhao and Tans, 2006] and WMO X2004 for CH₄ [Dlugokencky *et al.*, 2005]. The calibration of target gas measurements – not used for the determination of calibration coefficients – suggests an accuracy of the CO₂ and CH₄ measurements of ~ 0.07 ppmv and ~ 0.5 ppbv, respectively, computed as the 10-day averaging window RMSE (root mean square error) of individual target measurements during the study period. Measurements were summarized to hourly averages for the 1-year period from 1 March 2013 to 28 February 2014 considered in this study.

In order to derive regional signals of the trace gas concentrations at each site, a background concentration was estimated and subtracted from the measurements. The background concentration was estimated using the “robust extraction of baseline signal” method [Ruckstuhl *et al.*, 2012] from measurements at the high Alpine research station Jungfraujoch, which mainly samples free tropospheric air [Zellweger *et al.*, 2003; Henne *et al.*, 2010]. Measurements at Jungfraujoch were made with a PICARRO G2401 analyzer and referenced to the same calibration scales [Schibig *et al.*, 2015]. We investigated the validity of the assumption that this background concentration estimate corresponds to background concentrations by comparing with NOAA’s Marine Boundary Layer reference (MBL¹) at the corresponding latitude. We found them to be very similar (not shown), but the annual peak-to-peak amplitude of the Jungfraujoch background concentration estimate (~ 8 ppmv) is less than that of the MBL estimate (~ 14 ppmv). However, the qualitative purpose of considering regional signals in this study remains unaffected by these differences.

For Switzerland, agricultural CH₄ emissions constitute more than 80 % of the total emissions and show high spatial variation, but their temporal variations are small and predominantly seasonal [Hiller *et al.*, 2014] due to seasonal relocation of cattle. Therefore, within a season, variations of methane concentrations serve as an atmospheric tracer and specifically as a proxy for the effect of the diurnally varying ABL.

¹<http://www.esrl.noaa.gov/gmd/ccgg/mb1/mb1.html>.

3.3.2 COSMO meteorology and FLEXPART-COSMO simulations

The sensitivity of the four measurement sites to upwind surface fluxes was assessed using a Lagrangian particle dispersion model (LPDM) driven by meteorological fields from a high-resolution numerical weather prediction (NWP) model. As input for the transport simulations we used hourly analysis fields from the operational weather forecast system of the Swiss national weather service, MeteoSwiss, which is based on the NWP model COSMO. COSMO is a state-of-the-art non-hydrostatic, limited-area NWP model [Baldauf *et al.*, 2011] developed by the Consortium for Small-Scale Modeling under the guidance of the German weather service (DWD; Offenbach, Germany). It is the operational weather forecast model of the national weather services in Germany, Greece, Italy, Poland, Romania, and Russia. In the version COSMO-CLM (Climate Limited area Modeling), optimized for climate simulations, it is used by a wide community of regional climate modelers (<http://www.clm-community.eu>).

The operational setup for COSMO simulations of MeteoSwiss includes two nested domains. The outer domain covers large parts of Europe at about $7\text{ km} \times 7\text{ km}$ resolution (COSMO-7). The inner domain covers the Alpine region including Switzerland, Austria and parts of Germany, France and Italy at about $2\text{ km} \times 2\text{ km}$ resolution (COSMO-2). COSMO-7 is driven by European Centre for Medium Range Weather Forecast (ECMWF) analysis fields of ECMWF’s global IFS (Integrated Forecasting System) model and provides the boundary conditions for the COSMO-2 simulation. Hourly analysis fields are produced for both model domains applying the observational nudging technique [Schraff, 1997] to surface observations of pressure, relative humidity and wind. Similarly, measurements of the same variables plus ambient temperature as taken with sondes and profilers are also assimilated. In addition, a latent heat nudging scheme [Stephan *et al.*, 2008] is used for the COSMO-2 domain to incorporate radar derived rain rates².

COSMO-2 provides the high resolution necessary to represent the complex topography in the Alpine area and the topography-induced mesoscale weather patterns. In order to evaluate the ability of COSMO-2 to represent the local meteorology at the four measurement sites, we interpolated COSMO-2 analysis fields horizontally to each site and vertically to 18 altitude levels between 10 and 3240 m above model ground. This allows us to compare COSMO-2 with meteorological measurements at different heights above ground. Furthermore, it allows assessing the effect of a mismatch between the true altitude of a site and its representation in the model where the topography is smoothed due to the limited model resolution. Although the gentle hill at Beromünster and the flat area around Gimmiz are well represented, the model’s elevation at the mountain sites Frübüel and Lägern-Hochwacht are 169 and 274 m, respectively, lower than the true elevation. Therefore, we compared COSMO-2 output at two different levels, i.e., at the altitude of the measurement a.s.l. (“true”), and at the measurement height a.m.g.l. (above model ground level; “model”). The true altitudes and the corresponding model altitudes are summarized in Table 3.2.

Hourly COSMO analysis fields were used to drive offline atmospheric transport simulations with a modified version of the LPDM FLEXPART [Stohl *et al.*, 2005]. FLEXPART simulates the transport and dispersion

²For more details see <http://cosmo-model.org/content/tasks/operational/default.htm>.

Table 3.2: Simulation characteristics for the four measurement sites of the CarboCount CH network. Listed from left to right are the FLEXPART-COSMO particle release heights (above model ground level), the “true” site altitudes (m a.s.l.), smoothed COSMO numerical weather prediction model’s ($\sim 4\text{ km}^2$) site altitude, and the geographic site locations.

Site	Meas. height	Rel. heights	Alt.	Alt. COSMO	Lat., Lon.
Beromünster	212	212	797	723	47.1896, 8.1755
Frübüel	5	50–100	982	813	47.1158, 8.5378
Gimmiz	32	32	443	452	47.0536, 7.2480
Lägern-Hochwacht	32	100–200	840	566	47.4822, 8.3973

of infinitesimally small air parcels (referred to as particles) by advective as well as turbulent and convective transport. It can be run either in forward mode (source-oriented, i.e., released from sources) or backward mode (receptor-oriented, i.e., released backward from receptors). The advective component is calculated from the 3-D wind fields provided by COSMO, and the turbulent transport is based on the scheme of *Hanna* [1982], which diagnoses ABL and turbulence profiles for stable, neutral and unstable boundary layers based on the Monin–Obukhov similarity theory. FLEXPART was modified to run directly on the native grid of COSMO, which is a rotated longitude–latitude grid on a hybrid geometric (i.e., fixed in space) vertical coordinate system. The fact that the original FLEXPART model already operates on a fixed-in-space co-ordinate system greatly facilitated the adaptation to COSMO. In order to be as compatible as possible with the driving NWP (Numerical Weather Prediction) model, the same version of the Tiedtke sub-grid convection scheme [Tiedtke, 1989] as used in COSMO-7 was implemented in FLEXPART-COSMO, replacing the standard Emanuel convection scheme [Forster *et al.*, 2007]. Convection is treated as a grid-scale process in COSMO-2 and, hence, no sub-grid convection parameterization is run in either COSMO or FLEXPART-COSMO for the $2\text{ km} \times 2\text{ km}$ domain. From all four sites, backward transport simulations with FLEXPART-COSMO were started every 3 h to trace the origin of the observed air parcels. In each simulation, 50 000 particles were released from the site’s position at site-dependent heights above ground and traced backward in time over 4 days or until they left the simulation domain. The simulations were performed in a nested configuration with COSMO-2 providing the meteorological inputs for the inner domain and COSMO-7 for the outer domain once the particles left the COSMO-2 region. Simulated residence times τ ($\text{s m}^3 \text{ kg}^{-1}$; described in Sect. 3.3.4) were generated for two separate output domains: a high-resolution grid over Switzerland at $0.02^\circ \times 0.015^\circ$ horizontal resolution extending from 4.97 to 11.05° E and 45.4875 to 48.5475° N , and a coarser European grid at $0.16^\circ \times 0.12^\circ$ resolution extending from -11.92 to 21.04° E and 36.06 to 57.42° N . Due to the relatively well-represented topography at Beromünster and Gimmiz, we chose to release particles at the measurement height above model ground level. The relatively poor representation of topography around Fräebühl and Lägern-Hochwacht, however, led us to release particles from a layer between “true” and “model” height rather than from a single height. The particle release heights were chosen based on meteorological evaluation of COSMO presented below and are listed in Table 3.2.

3.3.3 Land cover data set

In order to evaluate the sensitivity of the measurement sites to different land cover types (LCTs), a data set of fractional land cover was produced for the FLEXPART-COSMO output domains. The land cover data set consists of LCTs classified according to the land-unit/plant functional type approach used in the land surface model CLM4 [Bonan *et al.*, 2002b, a; Lawrence *et al.*, 2011]. Two same calibration scales

3.3.4 Regional surface influence metrics

We define surface sensitivity τ_{100} ($\text{s m}^3 \text{ kg}^{-1}$) as the residence time of the particles in a 100 m thick layer above model ground divided by the density of dry air in that layer. A layer thickness of 100 m was selected as a compromise between the requirement of selecting a height low enough to be always located in the well-mixed part of the ABL and high enough to allow for a statistically sufficient number of particles in the layer. The results were largely insensitive to this choice as confirmed by comparing with results for τ_{50} (50 m) and τ_{200} (200 m). Maps of the total residence time summed over the (4-day) simulation period are commonly referred to as footprints and describe the sensitivity of a measurement site to upwind surface fluxes [Seibert and Frank, 2004]. For this study only monthly or seasonally averaged residence times were used to characterize the surface influence of the four sites and are hereafter referred to as mean surface sensitivities, $\bar{\tau}$. Hereafter temporally averaged quantities also have an overline.

The spatial sum of monthly mean surface sensitivities, the total surface sensitivity \bar{T}_t , gives a direct approximation of how much the air parcels arriving at a site have been in contact with the simulation domain's surface during the simulation period and is defined as

$$\bar{T}_t = \sum_{i,j} \bar{\tau}_{i,j}, \quad (3.3.1)$$

where i and j are spatial indices.

Short-term variations in observed trace gas concentrations are mainly determined by upwind surface fluxes, which vary with the associated land cover type. In order to investigate the influence of different LCTs on each measurement site, monthly LCT contributions (C_{LCT}) were calculated as the weighted mean of LCT fractions $f_{\text{LCT},i,j}$ over the FLEXPART output grid, using monthly mean surface sensitivities $\bar{\tau}_{i,j}$ as weights (Eq. 3.3.2). With equal surface flux strengths, each LCT would contribute the respective fraction C_{LCT} of the observed signal.

$$C_{\text{LCT}} = \frac{1}{\bar{T}_t} \sum_{i,j} \bar{\tau}_{i,j} \cdot f_{\text{LCT},i,j} \quad (3.3.2)$$

In order to better gauge the decrease of surface sensitivity with increasing distance, we define the radial surface sensitivity \bar{T}_k for a site as

$$\bar{T}_k = \frac{1}{\Delta d} \sum_{i,j} \bar{\tau}_{i,j} \quad \forall i,j : \quad d_k < d_{i,j} < d_k + \Delta d, \quad (3.3.3)$$

where $d_{i,j}$ is the great-circle distance of the grid cell with indices i and j from the measurement's site position, and index k defines a discrete distance bin of width Δd .

In order to compare the area of surface influence of each site, we investigated cumulative surface sensitivities defined as

$$s(\tau) = \sum_{i,j} \bar{\tau}_{i,j} \quad \forall i,j : \quad \bar{\tau}_{i,j} > \tau. \quad (3.3.4)$$

The area of surface influence is then defined as the region surrounding the site bounded by the isoline τ_{s50} , at which the cumulated surface sensitivity includes 50 % of the total surface sensitivity:

$$\tau_{\text{s50}} : s(\tau_{\text{s50}}) = 0.5 \bar{T}_t. \quad (3.3.5)$$

Similar metrics were computed by *Gloor et al.* [2001] using trajectory simulations. They derived a concentration footprint from the decay of the correlation between population density, integrated along the trajectories, and C_2Cl_4 measurements with increasing distance from the measurement site. Although they showed the robustness of their methods, we argue that the independence of \bar{T}_k and τ_{s50} from trace gas measurements and associated surface fluxes constitutes an improvement of the definition of the concentration footprint. Furthermore, the application of an LPDM model that better describes atmospheric transport and dispersion constitutes a clear improvement over their approach but comes at much higher computational cost.

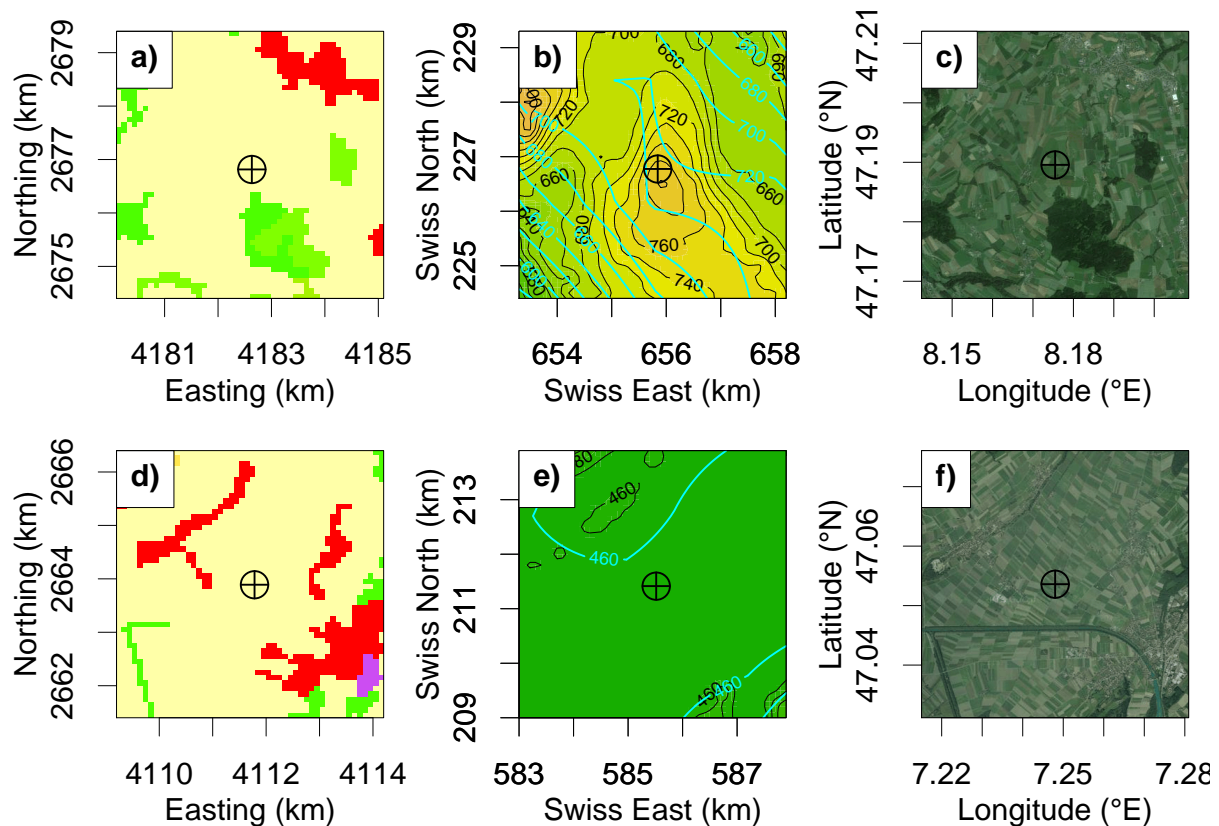


Figure 3.2: Site surroundings including land use (first column), topography (second column), and Google aerial photo (third column), with Beromünster (a–c) in the first row, and Gimmiz (d–f) in the second row. The land use (a and d) is based on CORINE 2006 land cover classes color coded as follows – urban: red; food croplands: beige; evergreen forest: green; deciduous forest: light green; pasture: light brown; agroforestry areas: tan. Cyan contour lines in the topography panels (b and e) denote the COSMO-2 model topography.

3.4 Results and discussion

3.4.1 Local site characteristics

The Beromünster site is a 212 m tall, decommissioned radio tower located on a gentle hill in an agricultural area in central Switzerland with an elevation of 797 m a.s.l. at the base (Fig. 3.2). Several small farms are located in the vicinity of the tower, and the town of Beromünster (< 7000 inhabitants) is approximately 2 km to the north. The adjacent valley bottoms are at an elevation of approximately 500 and 650 m a.s.l. Beromünster’s surroundings consist of a mosaic of agricultural uses: crops, managed grasslands, and a forested area towards the south.

The 32 m tall water tower near Gimmiz is the westernmost site of the network and is located in the flat Seeland region, a former wetland area which was converted to agricultural land in the nineteenth century (Fig. 3.2). The town of Aarberg (< 5000 inhabitants) is at a distance of approximately 2 km to the southwest and a farm is situated 200 m to the northeast. The flat area around Gimmiz mainly consists of agricultural plots of seasonal crops, known as the “vegetable garden” of Switzerland. Furthermore, the area directly surrounding Gimmiz is under groundwater protection and further surroundings are under water protection, which means that cattle grazing and use of fertilizer is tightly regulated or forbidden.

About 30 km to the southeast of Beromünster, Frübüel, a Swiss FluxNet site [Zeeman *et al.*, 2010], is located

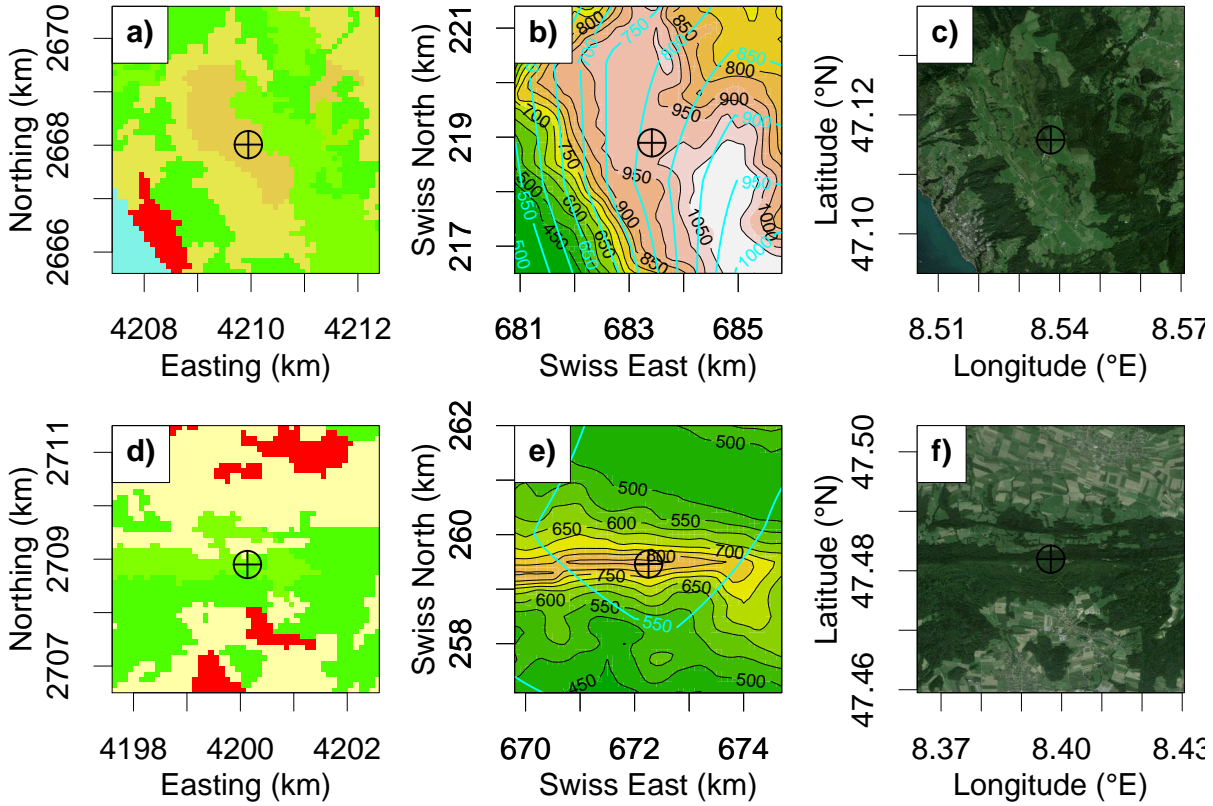


Figure 3.3: Similar to Fig. 3.2 with Frübüel (a–c) in the first row and Lägern-Hochwacht (d–f) in the second row.

at an altitude of 987 m a.s.l. on the flank of the gently sloping prealpine Zugerberg, some 500 m above the valley floor (Fig. 3.3). The region consists of glacial lakes, managed forests and seasonal pastures. The city of Zug 10 km to the north and the small town of Walchwil 2 km to the southwest are the major nearby anthropogenic sources. A small farm is located approximately 300 m to the south. Seasonal pasture surrounds the site, and approximately 50 m to the west there is a small patch of forest, the canopy of which is higher than the measurement inlet at 4 m a.g.l.

The site Lägern-Hochwacht, a 32 m tall tower, is located on the east–west oriented mountain ridge Lägern, at an altitude of 840 m a.s.l., and is north of the city of Zurich in the most industrialized and densely settled area of Switzerland (Fig. 3.3). The terrain falls off steeply to the north and south from the site, and the Lägern crest extends about 10 km westwards at a similar altitude. Lägern-Hochwacht is surrounded by deciduous and coniferous forest with a maximal canopy height of 20 m.

3.4.1.1 Model topography and land cover

Although the main topographic features of Switzerland are represented, the spatial resolution of 2 km creates large differences between true and model topography at the two mountain sites Frübüel and Lägern-Hochwacht (see Table 3.1 and Fig. 3.3, second column). In the model topography, the general shape of the Zugerberg remains, but the site’s altitude is much lower (169 m). The steep Lägern crest is not identifiable in the model topography; therefore, the site’s model altitude is much lower (274 m). On the other hand, Beromünster’s altitude is slightly lower in the model topography (74 m), but the local topographical features remain identifiable. Furthermore, the plain topography surrounding Gimmiz compares well with the model

topography and the site’s model altitude is slightly higher (9 m).

The land cover in Switzerland is highly fragmented at scales smaller than 2 km (Figs. 3.2, 3.3, third column). The actual variety of land cover, specifically plant functional types, is usually highly simplified in land surface models. *Groenendijk et al.* [2011] concluded that this simplification may have significant consequences for regional carbon flux modeling, especially in highly heterogeneous landscapes, such as Switzerland. Therefore, the influence of local fluxes on measured concentrations will still likely be difficult to simulate even at this relatively high resolution.

3.4.2 Local meteorology and diurnal cycle

The measured wind roses indicate frequent air flow channeling between the Jura mountain range and the Alps, resulting in either southwesterly or northeasterly wind directions (Fig. 3.4). Frübüel is an exception, where the local environment likely redirects prevailing winds. Due to its high measurement altitude (the highest), Beromünster observed the highest wind speeds. At Gimmiz, lower wind speeds due to lower measurement altitude and high frequency of northeasterly winds, colloquially known as “Bise”, are measured. Frübüel occasionally observes strong winds from southeasterly directions during foehn events [*Bamberger et al.*, 2016]. Similar to Beromünster, Lägern-Hochwacht observed high wind speeds, which were highly channeled from either the northeast or southwest.

At Beromünster, the diurnal cycles of measured wind speed show higher values during nighttime than daytime, indicating presence in the mixed layer during daytime and transition to the nocturnal residual layer during nighttime (Figs. 3.5, 3.6). In summer, specific humidity exhibits an increase between 07:00 and 10:00 UTC (08:00–11:00 LT) and a simultaneous decrease in wind speed, which likely occurs as the expanding mixed layer gradually ascends past the tower top. The peak of specific humidity corresponds temporally to that of summertime regional methane signals (ΔCH_4), further indicating mixed layer influence. Summertime regional CO_2 signals (ΔCO_2) show only a small diurnal (± 4 ppmv) variability, which corresponds to the expectation of a weak signal from diurnal surface flux variations at the top of a tall tower [*Andrews et al.*, 2014]. Wintertime diurnal variability is hardly discernible in both CO_2 and CH_4 concentrations, indicating a weak influence of ABL dynamics.

At Gimmiz, the increase in wind speed during the day and decrease during the night indicates the constant presence of the measurement inlet in the surface layer, contrary to Beromünster (Figs. 3.5, 3.6). In summer and winter, CO_2 and CH_4 are negatively correlated with wind speed, further emphasizing the influence of diurnal ABL dynamics. The nighttime increase of more than 60 ppmv suggests rapid accumulation of ΔCO_2 in the shallow nocturnal boundary layer, and although nocturnal regional advection of ΔCO_2 may also contribute to the nighttime enrichment [*Eugster and Siegrist*, 2000], low wind speeds at night suggest that the surface influence is limited to a few tens of kilometers from the site. Both the high wintertime CO_2 concentrations (30 ppmv above background) and the high correlation between wintertime ΔCH_4 and ΔCO_2 indicate that wintertime diurnal ABL dynamics are responsible for observed diurnal variability. Please note that the winter was atypically mild [2.3°C above the norm from 1961 to 1990; *MeteoSwiss*, 2014] for regions north of the Alpine divide, which would have caused increased wintertime respiration, and contributed to the high observed CO_2 concentrations.

At Frübüel, the large magnitude in the temperature’s daily cycle, the low measured wind speeds, and the high humidity indicate a strong surface influence (Figs. 3.7, 3.8) and is consistent with the near-surface measurement height. During summer, CO_2 concentrations decreased in the morning along with an increase in temperature and humidity, both before wind speed increased. This typifies the influence of photosynthetic activity and further indicates a strong local surface influence.

The second mountaintop site Lägern-Hochwacht shows a similar behavior to Beromünster with a delayed

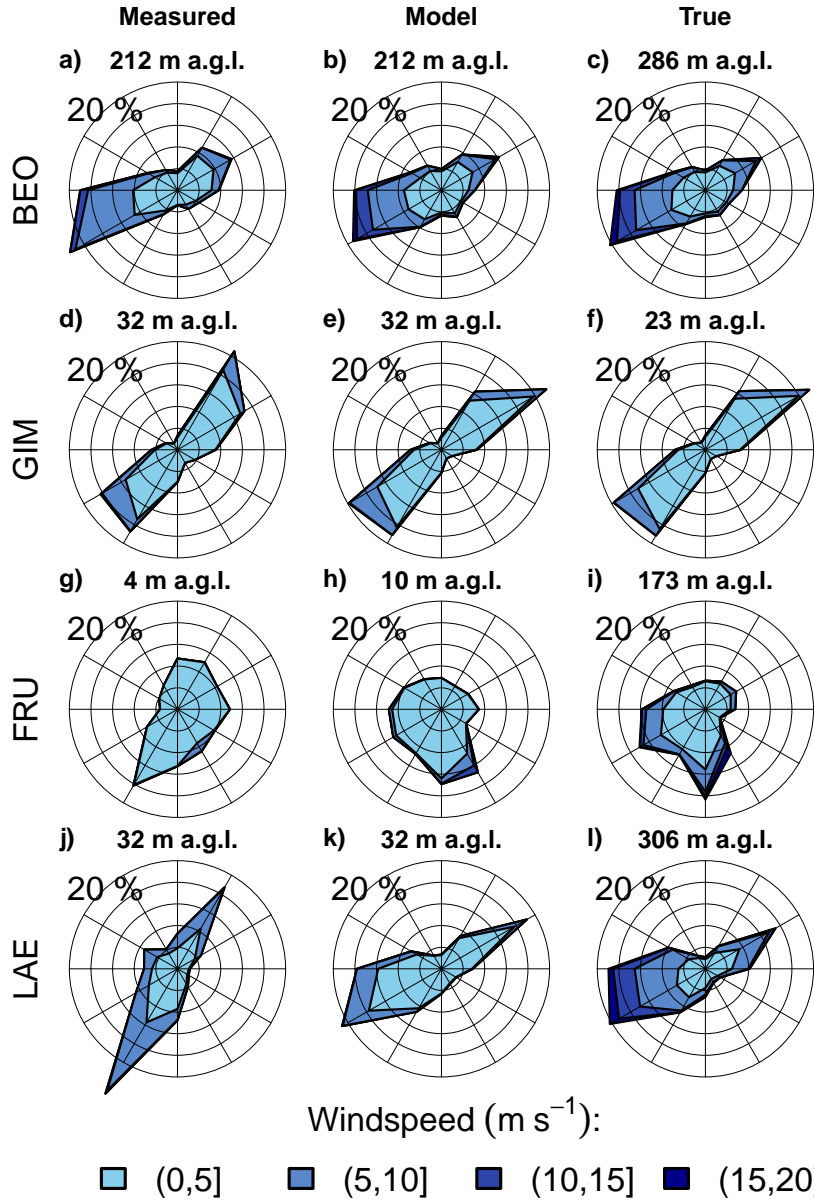


Figure 3.4: Wind roses at the four measurement sites during the study period (1 March 2013–28 February 2014) for observed (first column) and simulated horizontal wind at two different model heights: at the height of the measurement a.m.g.l. (Model, second column), and at the true height of the measurement a.s.l. (True, third column). The wind roses display the wind speed probability distribution split into incident 30° wind direction bins. Wind from the north is upward and circular lines demarcate graduating 5th percentiles. Labels above each panel show the height above ground for the measurements (first column) and height above the COSMO-2 model ground for the simulated data (second and third columns).

increase in daytime temperatures and higher wind speeds at night than during the day (Figs. 3.7, 3.8). Especially during summer, the diurnal cycles of measured wind speed show higher values during nighttime than daytime, which indicates a shift from the mixed layer during daytime to the residual layer during nighttime, and an increased influence of nocturnal jets. Specific humidity exhibits an increase between 06:00 and 09:00 UTC (07:00–10:00 LT) and a simultaneous decrease in wind speed, further indicating a shift to the mixed layer. The delay in the decrease of ΔCO_2 and peak of ΔCH_4 at 09:00 UTC indicate upward mixing of air containing nocturnally accumulated CO_2 and CH_4 , which we also observe at Beromünster.

On average, the mixed layer begins to influence Lägern-Hochwacht measurements an hour earlier than at Beromünster. During winter, the additional 5 ppmv offset above that of Frübüel in the flat diurnal cycle of ΔCO_2 and ΔCH_4 concentrations indicates nearby anthropogenic sources and weak influence from ABL dynamics, respectively.

3.4.2.1 COSMO-2 meteorology evaluation

Beromünster’s simulated wind roses compare well with the observed wind roses, but high wind speeds are simulated too frequently (Fig. 3.4). Simulated and measured diurnal cycles agree well in all seasons, and simulations at the measurement height above model ground level at 212 m agree slightly better (Figs. 3.5, 3.6). Small differences from the measurements include an overestimation of wind speeds in the afternoon in summer and a delayed and too small increase in temperature during winter.

At Frübüel, neither the dominating wind directions nor the wind speeds are well reproduced by the COSMO-2 model, suggesting strong localized influences on wind patterns. The lowest model output level (10 m a.g.l.) compares best with the near-surface meteorological characteristics of Frübüel. Because the model is evaluated at the center of the lowest model layer at about 10 m a.g.l. and the meteorological measurements are closer to the surface at 2 m a.g.l., a general overestimation of wind speeds is expected. The timing of simulated and measured diurnal variations of humidity and wind speed correspond, but humidity is biased low and wind speed is biased high throughout the day. Furthermore, the amplitude of the daily temperature cycle is underestimated, most notably in winter. On the other hand, simulated wintertime temperatures show a warm bias even at the true station height, well above the surface.

At Gimmiz, the simulated wind roses compare well, but a small bias in the northeastern wind direction exists. The diurnal cycle simulations agree well with the measurements in summer and winter. However, simulated nighttime temperature and wind speed are overestimated, suggesting an unrealistically well-mixed nighttime ABL, which in an inverse modeling framework would likely lead to an overestimation of nighttime respiration, due to an overly diluted trace gas signal.

In the highly smoothed model topography, Lägern-Hochwacht is more similar to Beromünster (compare cyan lines in Figs. 3.2b and 3.3b). Therefore, the rotation to a more north-southerly axis of observed winds is most likely a local topographic effect exerted by the east-west oriented ridge on the prevailing southwesterly and northeasterly winds. The simulated wintertime temperature is too high on average at all heights shown, similar to Frübüel. The measured meteorology is usually bracketed by the simulations evaluated at 32 m a.m.g.l. and at the true height (306 m a.m.g.l.), indicating that the site would be represented best by an intermediate simulation height.

Where the “model” and “true” topography are similar, simulated and measured meteorology show good agreement for Beromünster and Gimmiz. Contrastingly, local meteorology is not reproduced accurately at the mountaintop sites due likely to the smoothed model topography. The relatively poor meteorology simulations could cause problems with simulating trace gas observations if either the influence of local sources and sinks near the site were important and not well represented or if the local topography or meteorology induces vertical transport that the transport model misrepresents.

At Beromünster and Gimmiz, where “true” and “model” topography differs little, measurements and simulations agree best at the measurement height above model ground level. For Frübüel and Lägern-Hochwacht, the optimal simulation height above model ground, according to the meteorology evaluation, appears to be between the “model” measurement height and the “true” measurement height.

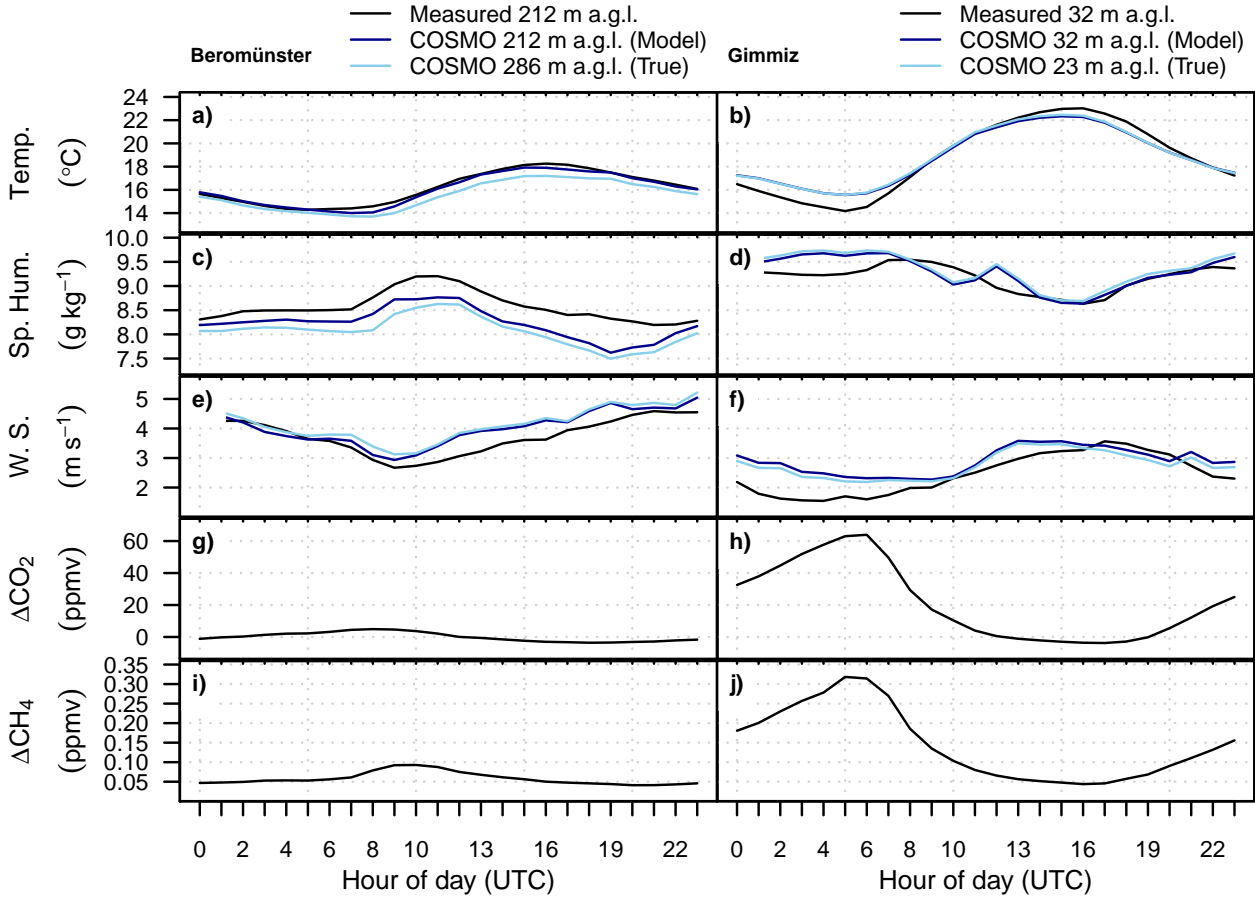


Figure 3.5: Mean summer (June–August 2013) diurnal cycle of measured and simulated local meteorology at the sites Beromünster and Gimmiz: **(a and b)** temperature, **(c and d)** specific humidity (Sp. Hum.), and **(e and f)** wind speed (W. S.). Also shown are mean diurnal cycles of measured **(g and h)** regional CO_2 signals (ΔCO_2), and **(i and j)** regional CH_4 signals (ΔCH_4). The measurement and simulation heights above ground are listed in the figure legends. Simulated meteorology is shown for two different heights, the height of the measurement a.m.g.l. (Model, dark blue), and the simulation height a.m.g.l., which corresponds to the “true” measurement altitude a.s.l. (True, light blue). The time zone in Switzerland is central European time (CET or UTC + 1).

3.4.3 Regional surface influence

3.4.3.1 Measured regional signals

Over the Swiss Plateau, daytime monthly averaged regional CO_2 signals (ΔCO_2) vary from -5 ppmv during warm summer days to $+15$ ppmv during cold winter days (Fig. 3.9a, b). During the warmer months, at daytime, intense vertical mixing caused regional CO_2 signals to be similar across sites. During the months of May and November, stormy weather reduced diurnal variation and the differences in regional signals between sites.

With a similar temporal pattern to CO_2 regional signals, daytime monthly averaged regional CH_4 signals (ΔCH_4) vary from $+0.05$ ppmv ($+50$ ppbv) during warm summer days to $+0.1$ ppmv ($+100$ ppbv) during cold winter days (Fig. 3.9c, d). Due to the same meteorological conditions conducive to vertical mixing during summer days and the months of May and November, regional CH_4 signals are similar across the measurement network.

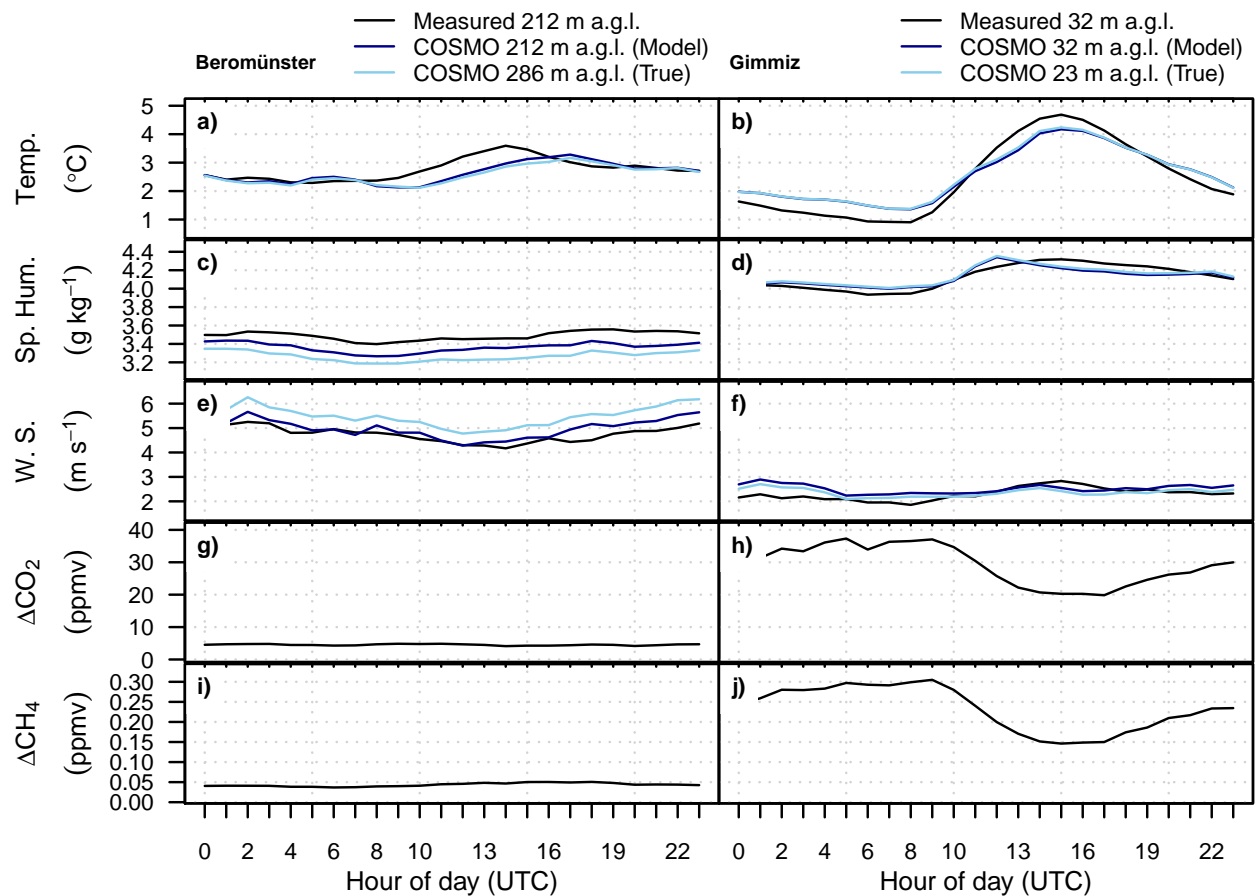


Figure 3.6: Similar to Fig. 3.5, the mean diurnal cycles during winter (December 2013–February 2014) at the sites Beromünster and Gimmiz.

On the other hand, the atmospheric stratification that accompanies reduced solar heating caused regional signals to differ more between measurement sites during nighttime and winter. For example, the cold and fair weather during December and associated high atmospheric stratification reduced diurnal variation and increased the differences between sites. Furthermore, due to a combination of site characteristics and atmospheric stratification, regional signals differed most between Beromünster and Gimmiz.

The small diurnal variation of observed regional CO_2 and CH_4 signals at Beromünster is expected, being vertically distant enough from the surrounding land surface to rarely observe nocturnal respiration fluxes. This damped signal contrasts that of the other sites and is often similar to the daytime measurement values of other sites. Interestingly, summer nighttime measurements are similar to the background estimate. Also, the higher daytime regional CH_4 signals during summertime coincide with the location in an area of very high cattle density [Hiller *et al.*, 2014]. During winter, relatively low CO_2 measurements indicate minimal anthropogenic influence.

The large diurnal variation in both of the observed regional signals at Gimmiz is difficult to understand. The strong CO_2 signals are likely related to the combination of fluxes from nearby settlements and crops and a stable nocturnal boundary layer. The summertime peak in nighttime regional signals points toward a biogenic cause. Both the high water table and the practice of till farming may also contribute to the biogenic CO_2 fluxes, and the high water table would aid in understanding the strong CH_4 signals. Again, the strong nighttime regional signals may also be due to nocturnal regional advection of CO_2 [Eugster and Siegrist, 2000], although low wind speeds do not support this hypothesis.

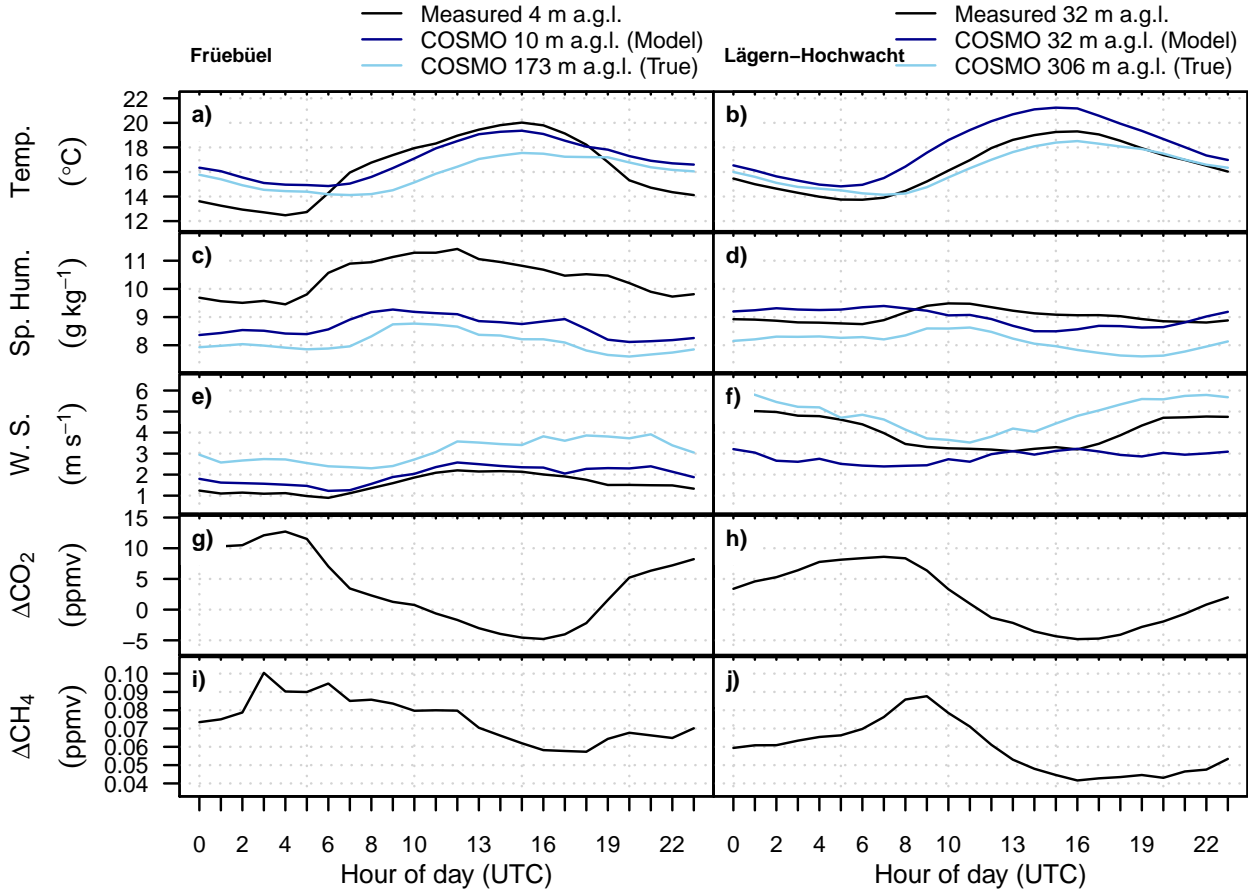


Figure 3.7: Similar to Fig. 3.5, the mean diurnal cycles during summer (June–August 2013) at the sites Früebüel and Lägern-Hochwacht. The Früebüel meteorological measurements were made at 2 m a.g.l.

At Früebüel, local topography is not conducive to a stable nocturnal surface layer and therefore the nighttime regional CO₂ signals are likely not as high as would be expected in flat terrain. The summertime peak in nighttime regional CO₂ signals is not as intense as that of Gimmiz but shows similar annual variation, pointing towards respiration fluxes. As at Beromünster, relatively low wintertime CO₂ measurements indicate minimal anthropogenic influence. The higher daytime regional CH₄ signals during summertime coincide with the location in an area of high cattle density, also similar to Beromünster.

At Lägern-Hochwacht, the observed diurnal variation of regional CO₂ signals is small, similar to Beromünster (Fig. 3.9). During winter, the elevated day- and nighttime regional signals indicate a strong anthropogenic influence, which corresponds with the surrounding industrialized area.

3.4.3.2 Simulated surface influence

The monthly total surface sensitivities (\bar{T}_t) differ most between sites during periods of higher atmospheric stratification (Fig. 3.9e, f), which is mainly due to the difference between particle release altitude at the site and average altitude of the surrounding (< 500 km) land surfaces. Therefore, the difference between Beromünster and Gimmiz is greatest and results from their locations on a tall tower on top of a hill or on a flat plain on a small tower with associated particle release altitudes at 1014 and 485 m a.s.l., respectively. In short, air parcels arriving at Gimmiz had the most contact with the land surface, whereas air parcels arriving at Beromünster had the least contact with the land surface.

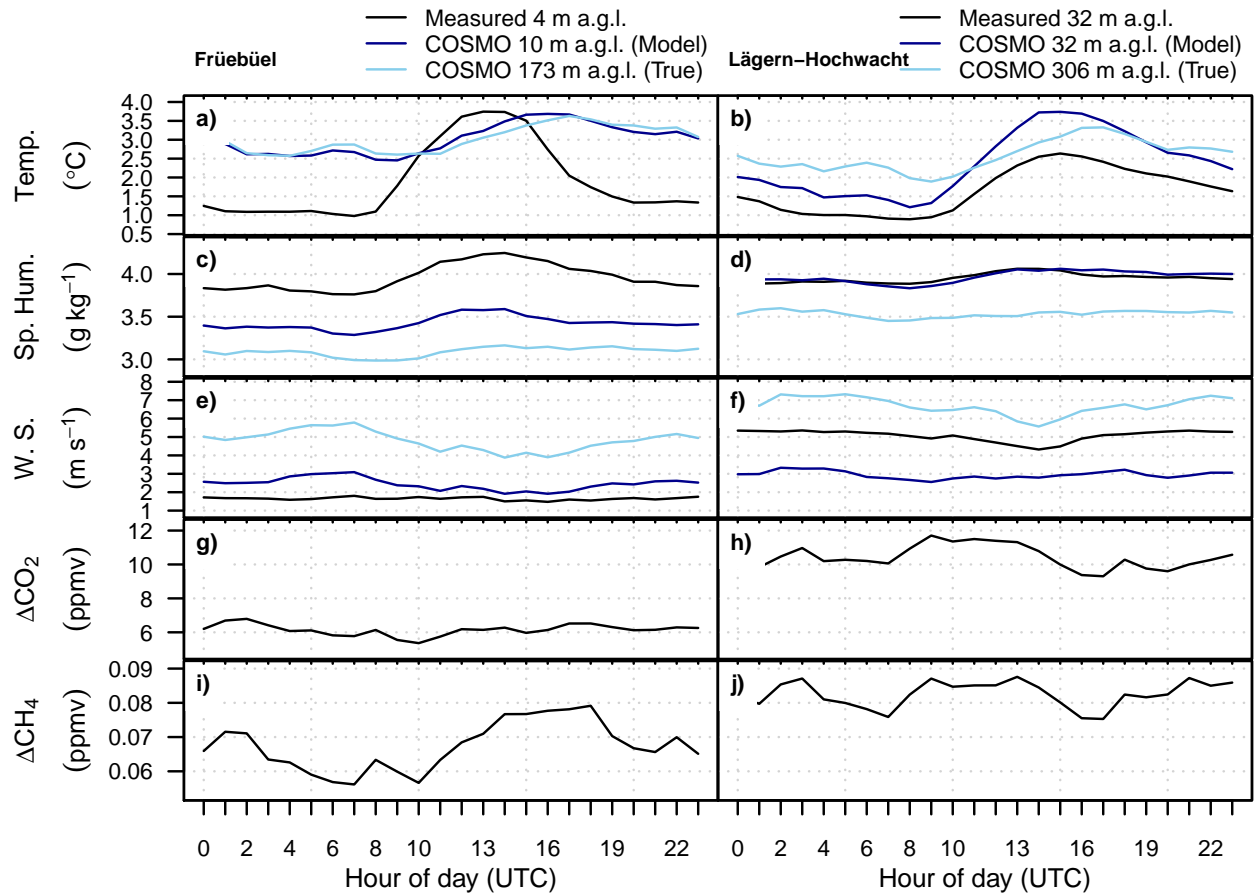


Figure 3.8: Similar to Fig. 3.5, mean diurnal cycles during winter (December 2013–February 2014) at the sites Frübüel and Lägern-Hochwacht. The Frübüel meteorological measurements were made at 2 m a.g.l.

The annual variation of the total surface sensitivities is very similar to the observed regional greenhouse gas signals, which indicates qualitative success in simulating surface sensitivity (Fig. 3.9). For example, during the warmer months, at daytime, increased vertical mixing causes total surface sensitivities to be similar across sites. During the months of May and November, stormy weather also reduced differences between sites. Total surface sensitivity differences between measurement sites increased during nighttime and winter, similar to the regional signals. Again, the cold and clear weather during December and associated high air mass stratification reduced diurnal variation and increased the differences between sites. That is, for the same reasons we qualitatively understand annual and diurnal variation in regional signals, we can understand variation in total surface sensitivity.

Potential monthly LCT contributions, C_{LCT} , vary little throughout the year and on average reflect the typical land cover for Switzerland and central Europe (Fig. 3.10). At all sites, the arriving air parcels spent about $\sim 30\%$ directly above forest LCTs and about $\sim 50\text{--}60\%$ of the time above crop and grassland LCTs combined. For example, in Fig. 3.10a, air parcels, which were observed during the month of March 2013 at Beromünster and were in contact with the surface (< 100 m a.m.g.l.), spent approximately 20 % of the time over the evergreen forest LCT, 10 % of the time over the deciduous forest LCT, 20 % over the grassland LCT, and 30 % over the crop LCT.

Given the contrasting meteorological conditions of night and day, and winter and summer, mean surface sensitivity generally decreased with increasing distance from the sites (Fig. 3.11), as expected. The average distance at which 50 % of the total sensitivity had accumulated is between 50 km (summer nighttime and

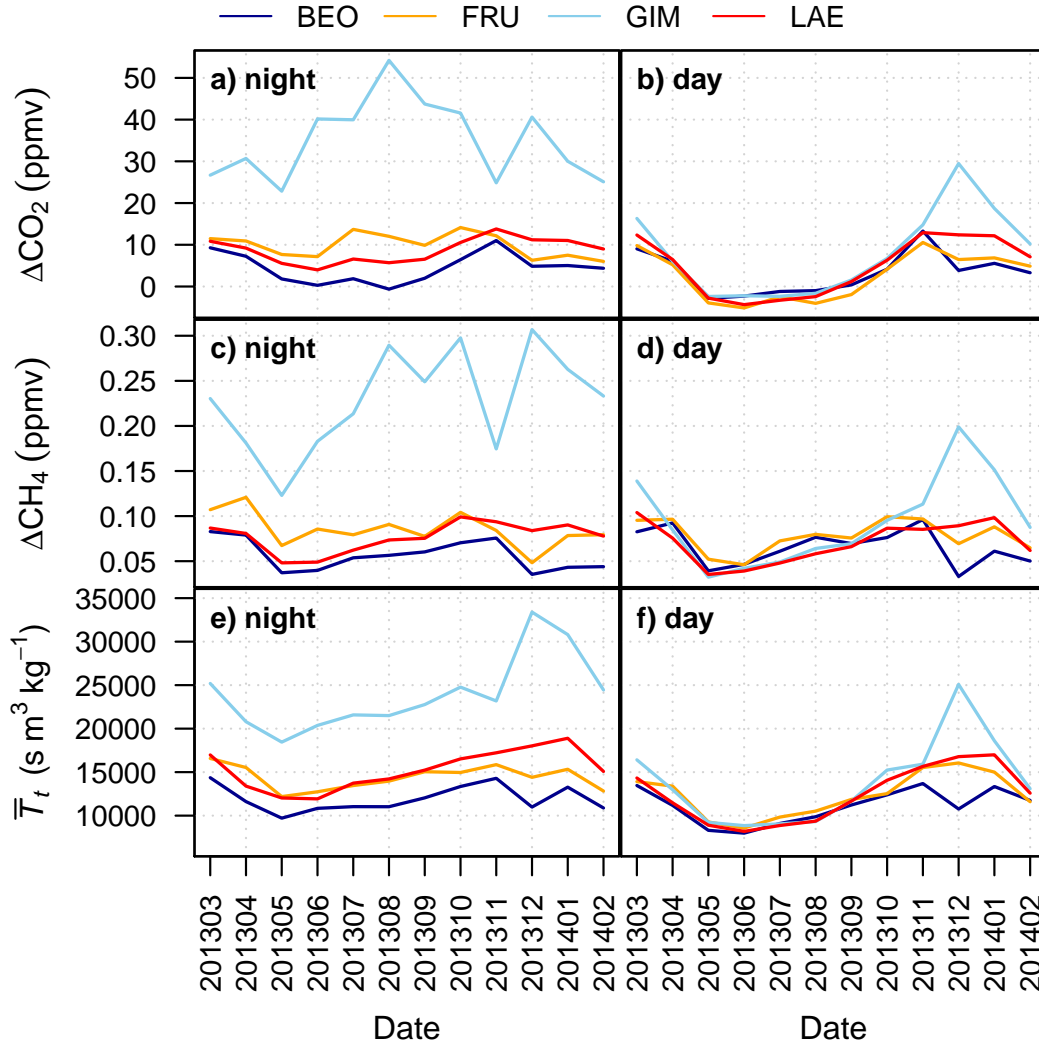


Figure 3.9: Monthly (YYYYMM) mean nighttime (00:00–03:00 UTC; **a**, **c**, and **e**) and daytime (12:00–15:00 UTC; **b**, **d**, and **f**) measured regional carbon dioxide signals, ΔCO_2 , measured regional methane signals, ΔCH_4 , and simulated monthly total surface sensitivities, \bar{T}_t (Eq. 3.3.1), during the study’s time period (1 March 2013–28 February 2014). Regional signals are computed as the measured concentration minus a background concentration estimate from Jungfraujoch, and total surface sensitivities provide a linear estimate of how much arriving air parcels at a measurement site have been in contact with the model domain’s surface.

winter) and 300 km (summer daytime) and is larger for Beromünster and Lägern-Hochwacht than for Frübüel and Gimmiz (Fig. 3.11, vertical dotted lines).

The areas of surface influence exhibit much geographic overlap during periods of increased vertical mixing, during summer days, and are smaller and overlap less during periods of decreased vertical mixing, at night and during winter (Fig. 3.12). In the summer afternoon, all sites exhibit a similar area of surface influence due to the rapid vertical mixing in the mixed layer. The northeast–southwest orientation of the areas of surface influence is consistent with observed air flow channeling between the Jura mountain range and the Alps (Fig. 3.4). Abnormally frequent southerly winds during January and February 2014 caused areas of surface influence to be pronounced towards the south during the winter.

When considering the area of surface influence or the distance-dependent decay of surface sensitivity during

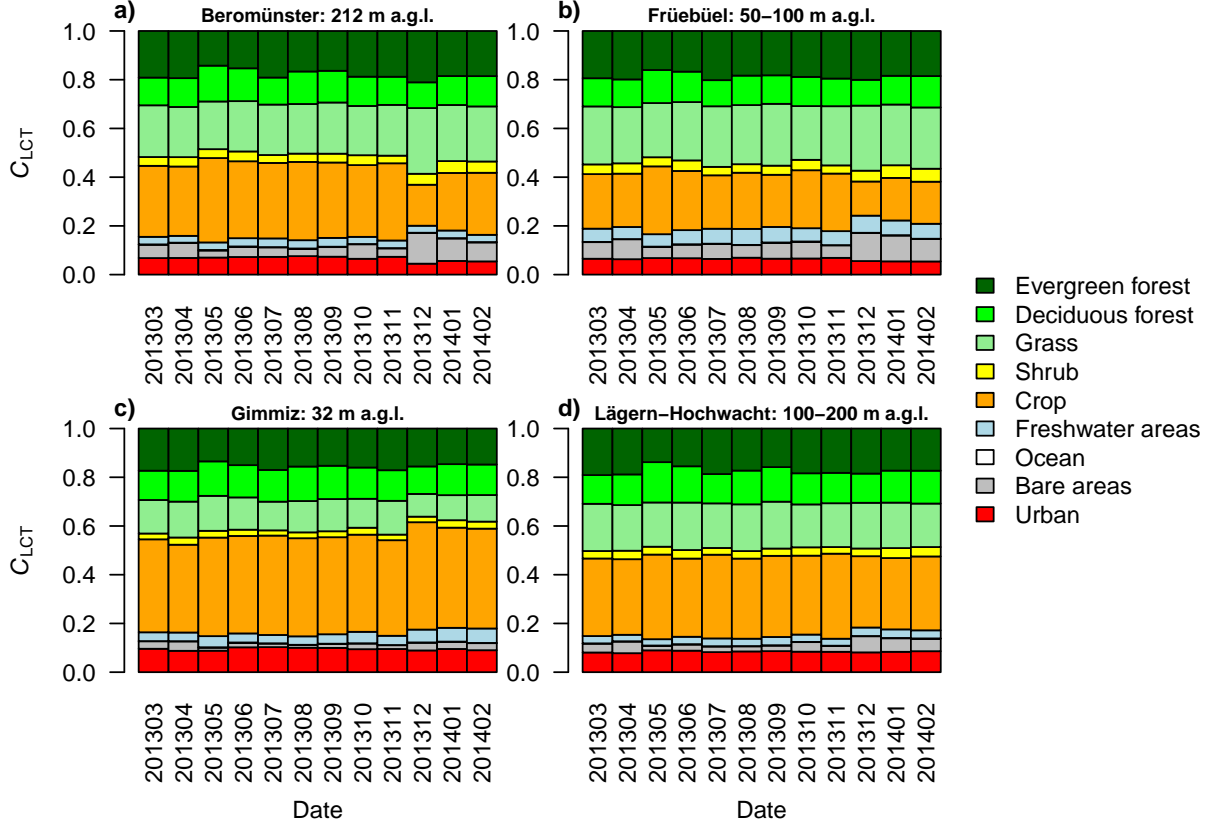


Figure 3.10: Monthly (YYYYMM) land cover type (LCT) contributions C_{LCT} (Eq. 3.3.2) for Beromünster (a), Fräebüel (b), Gimmiz (c), and Lägern-Hochwacht (d), calculated as the pixel-wise multiplication of the monthly mean surface sensitivities with the respective LCT fraction and divided by the monthly averaged total surface sensitivities.

periods of higher atmospheric stratification, Gimmiz and Fräebüel are similar and Beromünster and Lägern-Hochwacht are also similar. This shows the effect of presence within the surface layer on surface sensitivity. That is, presence within the surface layer usually results in a sharp decrease of surface sensitivity with distance and a correspondingly small area of surface influence as seen at Gimmiz and Fräebüel. Contrastingly, the location above the surface layer during periods of higher atmospheric stratification results in an initial increase of surface sensitivity with distance before decreasing, and results in a relatively large area of surface influence as seen at Beromünster and Lägern-Hochwacht at nighttime and during winter.

Beromünster exhibits the lowest total surface sensitivity of the sites (Fig. 3.9), and surface sensitivity initially increases before decreasing (except summer afternoon) as distance from the measurement site position increases (Fig. 3.11). Here, we find the conceptual understanding of the exponential decay of surface sensitivity with increasing distance from a tall tower site, as presented by *Gloor et al.* [2001], to be valid only during well mixed conditions (Fig. 3.11c). The area of surface influence is the largest of all sites on average (Fig. 3.12), as expected. Beromünster exhibits high sensitivity to grasslands, which, along with being located in an intense dairy farming area [*Hiller et al.*, 2014], would potentially increase influence of agricultural methane emissions. The LCTs observed at Beromünster represent typical land cover for Switzerland.

Gimmiz exhibits a high total surface influence (Fig. 3.9) that decreases sharply with increasing distance from the site (Fig. 3.11). The area of surface influence for Gimmiz covers the Seeland on average (Fig. 3.12). Opposite to Beromünster, the cold and clear weather during December caused increased coupling to the nearby

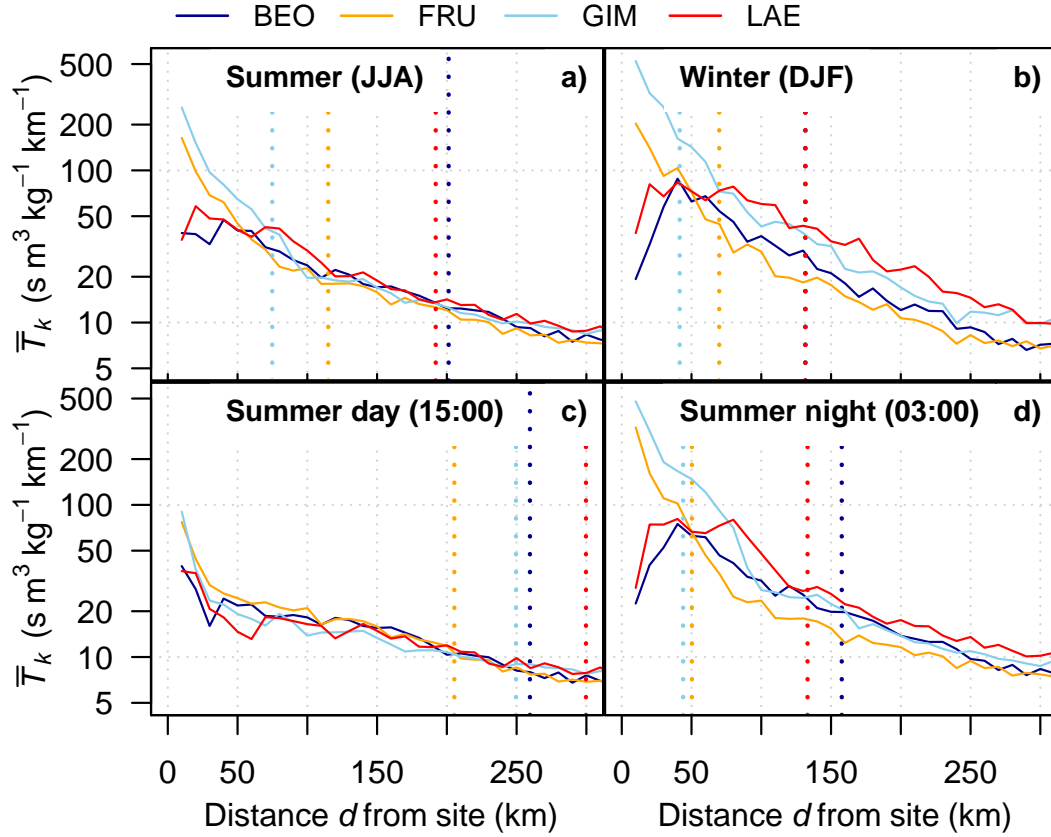


Figure 3.11: Surface sensitivities as a function of distance from the measurement site position \bar{T}_k (Eq. 3.3.3). Lines are color coded according to measurement site (Beromünster: dark blue, Frübüel: orange, Gimmiz: light blue, Lägern-Hochwacht: red). The vertical dotted line is the radius at which the cumulative surface sensitivity starting from the measurement site’s position reaches 50 % of the simulation domain total, τ_{50} . (a) Summer (June–August 2013), (b) winter (December 2013–February 2014), and (c) and (d) summer afternoon (15:00 UTC) and at nighttime (03:00 UTC), respectively. Please note the logarithmic y axis and that, during winter, for Beromünster and Lägern-Hochwacht the 50 % vertical dotted lines overlap. The site-specific particle release heights are listed in Table 3.2. Local time is central European time (CET or UTC + 1).

surface (< 50 km, Fig. 3.11) and higher total surface sensitivity (Fig. 3.9), which corresponds to the small wintertime area of surface influence (Fig. 3.12). Gimmiz exhibits a high sensitivity to crop LCTs (Fig. 3.10), which is due to pronounced near-field surface sensitivity (especially in December) and the intense agricultural activity typical of the Seeland region. Qualitative understanding of the observed higher wintertime CO_2 at Gimmiz (Fig. 3.9) is aided by the higher surface sensitivity to urban areas (Fig. 3.10).

Frübüel exhibits an area of surface influence pronounced to the south, covering the immediate prealpine area well (Fig. 3.12). Due to the frequent presence in the surface layer, the surface sensitivity decreases quickly with increasing distance (Fig. 3.11). Total surface sensitivity at Frübüel during wintertime is relatively small (Fig. 3.9). This is likely due to the higher particle release altitude (853–913 m a.s.l.) and the corresponding vertical distance from the average altitude of the Swiss Plateau (~ 450 m a.s.l.). Similar to Beromünster, Frübüel exhibits high sensitivity to grasslands (Fig. 3.10) and therefore the influence of methane emissions may be increased [Hiller *et al.*, 2014]. Frübüel shows the highest sensitivity to “bare”, Alpine areas and “freshwater areas” due to the proximity to the Alps, and the many nearby prealpine lakes.

The surface sensitivity as a function of distance (Fig. 3.11) and area of surface influence (Fig. 3.12) of

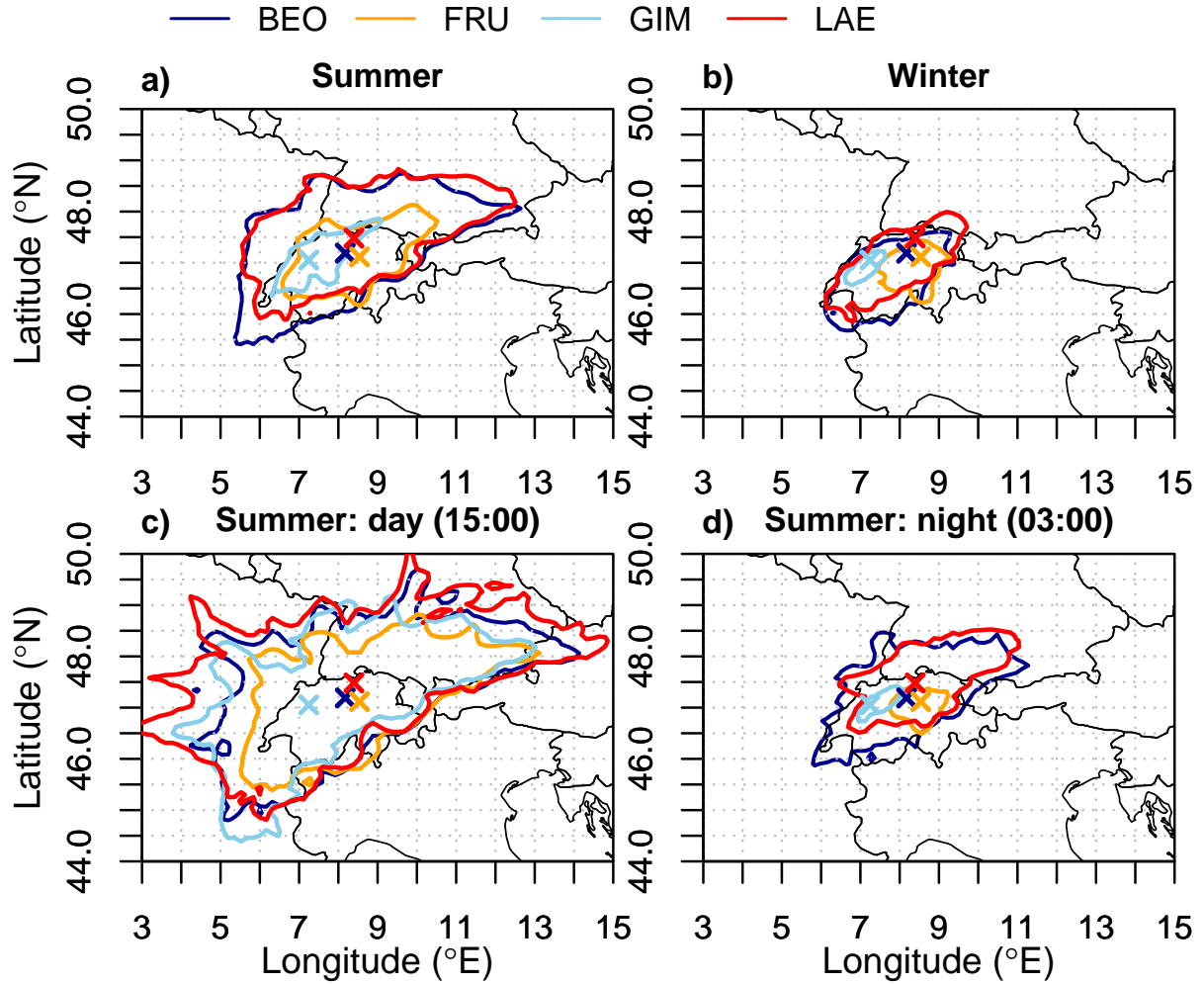


Figure 3.12: Area of surface influence (Eq. 3.3.5) defined as the isoline at the site-dependent value τ_{s50} encompassing 50 % of the total mean surface sensitivities. Lines are color coded according to measurement site – Beromünster: dark blue, Fröebüel: orange, Gimmiz: light blue, Lägern-Hochwacht: red. (a) Summer (June–August, 2013), (b) winter (December 2013–February 2014), and (c) and (d) summer (June–August 2013) in the afternoon (15:00 UTC) and at nighttime (03:00 UTC), respectively. Local time is central European time (CET or UTC + 1).

Lägern-Hochwacht show similarity to those of Beromünster. Total surface sensitivities are greater than those of Beromünster but less than those of the other sites (Fig. 3.9), which the relatively large areas of surface influence also indicate. The comparably high sensitivity to distant surfaces is due to the elevated release height and small vertical distance from surrounding land surfaces. The particle release altitudes are lower (666–766 m a.s.l.) than Beromünster or Fröebüel and thereby vertically closer to the average Swiss Plateau altitude (~ 450 m a.s.l.). This results in relatively higher total surface sensitivity during periods of increased atmospheric stratification (Fig. 3.9), which, with the increased sensitivity to urban areas (Fig. 3.10), help to qualitatively explain comparably high observed wintertime CO_2 concentrations.

The four measurement sites of the CarboCount CH network provide complementary data sets to constrain emissions from the Swiss Plateau but would not be useful for constraining emissions south of the Alpine divide, for example. At Gimmiz and Fröebüel, the local environment exerts much influence, causing strong local signals to dominate the time series. Therefore, a measurement data filter to remove the strong local signal will be necessary for the Fröebüel measurements and likely for the Gimmiz measurements. On the other

hand, the local environment (< 10 km) exerts little influence on the measurements made at Beromünster and Lägern-Hochwacht, where mainly regional-scale signals are observed.

Measurement sites in complex terrain still present formidable challenges for numerical weather prediction and thereby atmospheric transport modeling. The differences we found between simulated and measured local meteorology are likely due to differences between true and model topography. The ability to simulate local meteorology likely translates into the ability to accurately simulate local surface influence, which is an important aspect to simulate due to the potentially large contribution of local surface fluxes to observed greenhouse gas concentration variation, such as at the sites Frübüel and Gimmiz. Furthermore, the requirements for the spatial density and infrastructure of the measurement network are driven by periods of high atmospheric stratification and by local wind patterns. For example, due to the likely constant presence in the surface layer and resulting highly variable area of surface influence, the time series from Gimmiz is mainly useful for constraining Swiss Plateau emissions during warm days, although the tower is the same height as the tower at Lägern-Hochwacht. We recommend similar meteorological model evaluation and regional influence studies when making preliminary considerations about measurement network design and deployment.

Land cover and vegetation types influencing arriving air parcel concentrations vary little throughout the year and differences between sites are due to proximal (< 50 km) land cover. Nonetheless, the observed greenhouse gas concentrations differ substantially between sites. Thus, the collected information-rich data sets present a formidable challenge for terrestrial carbon flux modelers.

Acknowledgements

This study was funded by the Swiss National Funds (SNF) as part of the “CarboCount CH” Sinergia Project (grant CRSII2_136273). We acknowledge the use of the Jungfraujoch trace gas measurements carried out by Martin Steinbacher, Empa, in the framework of the Integrated Carbon Observation System in Switzerland (ICOS-CH), SNF grant 20FI21_1489921. We also acknowledge MeteoSwiss for the provision of their operational COSMO analysis products and of the meteorological measurements at Lägern-Hochwacht. Swiss Fluxnet is acknowledged for the meteorological measurements at Frübüel. We thank Tesfaye Berhanu and Lukas Emmenegger for reading draft versions and giving helpful comments. We also acknowledge the *R Core Team* [2014] for their hard work maintaining and developing the R software (version 3.1.0).

Edited by: C. Gerbig

Chapter 4

A CO-based method to determine the regional biospheric signal in atmospheric CO₂

Manuscript submitted to Tellus B

Authors: Brian Oney^{1,2}, Nicolas Gruber^{2,3}, Stephan Henne¹, Markus Leuenberger⁴, Dominik Brunner^{1,2}

¹ Lab. for Air Pollution/Environmental Technology, Dübendorf, Switzerland

² ETH Zurich, Center for Climate Systems Modeling, Zurich, Switzerland

³ ETH Zurich, Inst. of Biogeochemistry and Pollutant Dynamics, Zurich, Switzerland

⁴ Univ. of Bern, Physics Inst., Climate and Environmental Division, and Oeschger Centre for Climate Change Research, Bern, Switzerland

NOTE: The Beromünster site abbreviation BEO has been changed to BRM and the Lägern-Hochwacht site abbreviation LAE has been changed to LHW, and are thus different from the previous Chapter.

4.1 Abstract

Regional-scale inverse modeling of atmospheric carbon dioxide (CO₂) holds promise to determine the net CO₂ fluxes between the land biosphere and the atmosphere. This approach requires not only high fidelity of atmospheric transport and mixing, but also an accurate estimation of the contribution of the anthropogenic and background CO₂ signals to isolate the biospheric CO₂ signal from the atmospheric CO₂ variations. Thus, uncertainties in any of these three components directly impact the quality of the biospheric flux inversion. Here, we present and evaluate a carbon monoxide (CO)-based method to reduce these uncertainties solely on the basis of co-located observations. To this end, we use simultaneous observations of CO₂ and CO from a background observation site to determine the background mole fractions for both gases, and the regional anthropogenic component of CO together with an estimate of the anthropogenic CO/CO₂ concentration ratio to determine the anthropogenic CO₂ component. We apply this method to two sites of the CarboCount CH observation network in the Swiss Plateau, Beromünster and Lägern-Hochwacht, and use the high-altitude site Jungfraujoch as background for the year 2013. Since such a background site is not always available, we also explore the possibility to use observations from the sites themselves to derive the background. We contrast the method with the standard approach of isolating the biospheric CO₂ component by subtracting the anthropogenic and background components simulated by an atmospheric transport model. These tests reveal superior results from the observation-based method with retrieved wintertime biospheric signals being small and having little variance. Both observation- and model-based methods have difficulty to explain observations from late-winter and springtime pollution events in 2013, when anomalously cold temperatures and northeasterly winds tended to bring highly CO-enriched air masses to Switzerland. The uncertainty of anthropogenic CO/CO₂ emission ratios is currently the most important factor limiting the method. Further, our results highlight that care needs to be taken when the background component is determined from the site's observations. Nonetheless found, future atmospheric carbon monitoring efforts would profit greatly from at least measuring CO alongside CO₂.

4.2 Introduction

The accurate determination of the net fluxes of carbon dioxide (CO₂) between the atmosphere and the land biosphere is a key objective for global carbon research, as it represents currently the least well-known component of the global carbon budget [Le Quéré *et al.*, 2015]. The reasons for this limited quantitative understanding of the land biosphere fluxes are manifold, but include their high spatiotemporal variability and the complexity of the underlying processes governing these fluxes. Due to the time- and space-integrative nature of atmospheric transport and mixing, the inversion of atmospheric CO₂ observations has played a very important role in overcoming some of these challenges [Ciais *et al.*, 2010a]. However, this approach hinges very sensitively on the ability of atmospheric transport models to accurately connect surface fluxes with the variability of atmospheric CO₂ at the observing sites [Baker *et al.*, 2006; Gurney *et al.*, 2003; Lin and Gerbig, 2005; Gerbig *et al.*, 2008]. The method also requires the accurate determination of other contributions to the observed CO₂ variability, namely anthropogenic emissions, air-sea CO₂ fluxes, and CO₂ fluxes from other systems, such as lakes and rivers [Regnier *et al.*, 2013]. In the most commonly chosen atmospheric CO₂ inversion approach, the contribution of these processes to the CO₂ variability at the observing sites is quantified by estimating these surface fluxes based on independent constraints, and then by using these as boundary conditions in the atmospheric transport model [Gurney *et al.*, 2004, 2008; Peylin *et al.*, 2013]. The biospheric signal to be inverted is then estimated after subtraction of these other components from the observed atmospheric CO₂, which may introduce significant uncertainties [Ballantyne *et al.*, 2015]. Thus any bias in the estimates of the surface fluxes in these components and any error in atmospheric transport acting on these surface fluxes will cause a bias in the estimated biospheric signal, and hence a bias in the inversely

estimated net biospheric flux [Goeckede *et al.*, 2010b].

This problem tends to become worse in regional inversions, i.e., in inversions where the optimization of the fluxes is conducted over a limited domain only [e.g. Gerbig *et al.*, 2003b; Peylin *et al.*, 2005]. Here, one needs to consider an additional contribution to the observed atmospheric CO₂ variations, namely the “background” CO₂ concentration that originates from outside the regional domain of interest and is then transported to the observing sites within the domain [Goeckede *et al.*, 2010b]. In most regional inversions that focus on terrestrial systems, the air-sea CO₂ fluxes are negligible, so that in the context of these inversions, the observed atmospheric CO₂ is assumed to be driven only by anthropogenic and biospheric CO₂ fluxes originating from sources and sinks within the domain, and the background CO₂ stemming from outside the domain. In the case of regional-scale inversions, the anthropogenic and background components are usually estimated from simulations with an atmospheric transport model, and the regional biospheric component is then isolated by subtracting these components from the observations [e.g. Goeckede *et al.*, 2010a; Broquet *et al.*, 2011; Meesters *et al.*, 2012]. This biospheric component can then be used to estimate the biospheric CO₂ fluxes by means of inverse modeling [Gerbig *et al.*, 2003b].

The main concerns with using regional-scale atmospheric transport models to estimate the anthropogenic and background components are the combined uncertainties from the transport model, the anthropogenic emission inventory used to compute the regional anthropogenic contribution, and the background concentration field typically taken from a global or continental-scale CO₂ assimilation model. The relative contribution to the overall uncertainty likely varies from study to study depending on the size of the domain, the magnitude of fossil fuel emissions and the complexity of the atmospheric transport. Also, the CO₂ concentration fields used as boundary conditions for the nested model [e.g. Goeckede *et al.*, 2010a; Broquet *et al.*, 2011; Pillai *et al.*, 2011, 2012; Meesters *et al.*, 2012] may contain biases, which can have a large effect on the resulting inverted biospheric CO₂ fluxes [Peylin *et al.*, 2005; Goeckede *et al.*, 2010b]. A further complication in the context of regional inverse modeling is the risk to assimilate the same observations that have already been assimilated in the global model [Roedenbeck *et al.*, 2009; Rigby *et al.*, 2011].

Deriving background concentrations directly from the observations at a given site or a nearby background site is a common method in inverse modeling studies of halocarbons [Manning *et al.*, 2003; Brunner *et al.*, 2012; Hu *et al.*, 2015], but to our knowledge, this has not yet been used in the formal inverse modeling of atmospheric CO₂. In order to avoid some of the pitfalls associated with the model-based estimation of the background and anthropogenic components of the measured CO₂ concentrations, observation-based estimates of these two components can be used.

The applicability of CO as a tracer for anthropogenic CO₂ emanates from both being tightly linked with combustion processes [Zondervan and Meijer, 1996; Potosnak *et al.*, 1999; Gerbig *et al.*, 2003b]. Anthropogenic CO is a product of incomplete combustion of carbon-based fuels and therefore the molar ratio of CO : CO₂ is a direct measure of the efficiency of the combustion. But CO has also other important sources such as wildfires and the atmospheric oxidation of methane and non-methane hydrocarbons (NMHC). Oxidation of methane is thought to provide a mostly uniform global background of CO of about 25 ppb [Holloway *et al.*, 2000] and can therefore be neglected in regional-scale inversions. Duncan *et al.* [2007] estimate that oxidation of anthropogenic and biospheric NMHC contributes about 7% and 15% of the global CO source, respectively, the former taking place mostly in northern mid-latitudes and the latter in the tropics. This is a non-negligible contribution and thus needs to be considered together with the emissions from wildfires. CO is removed by hydroxyl oxidation to CO₂, and has a highly variable atmospheric lifetime (22 days in July [Miller *et al.*, 2012] versus 254 days in January in the northern hemisphere at mid-latitudes [Sander *et al.*, 2006]). Recognizing these challenges, CO observations provide the basis for a potentially accurate and cost-efficient method to estimate the anthropogenic contribution to the observed CO₂ concentrations. CO is measured not only at many air quality monitoring sites, but also increasingly at greenhouse gas observation

sites [Zellweger *et al.*, 2012].

An alternative tracer for the anthropogenic component of atmospheric CO₂ is its isotopic composition, namely its ¹⁴C content. This is a well-suited and well-studied proxy of CO₂ produced from the burning of fossil fuel and the production of clinker (CO_{2,FF}) [Levin *et al.*, 2003] due to the absence of ¹⁴C from fossil fuel and limestone [CaCO₃ Suess, 1955]. Relative to the comparatively inexpensive and simple nature of continuous CO observations, ¹⁴C observations are expensive and labor-intensive, currently preventing routine, continuous observations. The ¹⁴C observations can be further combined with the continuous CO observations in order to account for the varying ratios of fossil fuel CO₂ to CO [Levin and Karstens, 2007; Vogel *et al.*, 2010; Van Der Laan *et al.*, 2010; Vogel *et al.*, 2013]. Furthermore, the use of ¹⁴C as an anthropogenic CO₂ tracer is further limited by ¹⁴C emissions from nuclear power plants [Graven and Gruber, 2011] and its inability to distinguish between CO₂ from biofuel burning and biospheric respiration. The relative importance of these non-fossil sources is likely to increase in the future given the general need to replace fossil fuels by renewable fuels, such as wood, biogas, and ethanol.

Despite these uncertainties, CO and ¹⁴C observation-based estimates of the fossil fuel component provide a powerful alternative to the model-based estimates. But there is one downside that applies to both CO and ¹⁴C, and that is the need to subtract the background signal, which may be obtained from simultaneously measured CO or ¹⁴C at a remote background site [Levin *et al.*, 2003].

The determination of the background signal in atmospheric CO₂ from background stations has issues as well. Background observations need to be representative of the boundary of the region of interest. Even for less locally influenced sites or background sites, one needs to filter the observations for pollution and depletion events [Thoning *et al.*, 1989]. As an alternative, some studies used GLOBALVIEW¹ as a source of background information [e.g. Gerbig *et al.*, 2003b]. GLOBALVIEW is a gap-filled, meridionally averaged, and temporally smoothed data product generated from the observations of the global network of background observation sites filtered for local effects [Masarie and Tans, 1995]. GLOBALVIEW provides a useful global reference but is not necessarily a well suited estimate for a continental background needed in regional-scale modeling.

This study aims to develop and evaluate several CO-based approaches to estimate the anthropogenic and background components in atmospheric CO₂, from which the biospheric signal and its uncertainty can be derived. Our goal is to quantify these signals without introducing model transport and/or anthropogenic emission uncertainties. To this end we will be using co-located and nearly continuous CO and CO₂ observations from two sites within the CarboCount CH observation network in Switzerland [Oney *et al.*, 2015] for the year 2013. Oney *et al.* [2015] showed that these site's observations are representative of the Swiss Plateau, the most densely populated and agriculturally used region in Switzerland between the Alps in the south and the Jura mountains in the north. The plateau extends about 300 km in southwest-northeast direction and has an area of about $\sim 13,000$ km². To demonstrate the benefits of the observation-based method, it is compared with model simulations of the individual CO₂ components employing state-of-the-art CO₂ inventories of anthropogenic emissions and biosphere fluxes combined with a high-resolution Lagrangian transport model.

4.3 CO₂ data analysis framework

Following the conceptual framework for regional inversions presented by Gerbig *et al.* [2003b], we consider atmospheric CO₂ as being composed of three components, i.e., background (CO_{2,BG}), and regional anthropogenic (CO_{2,A}) and biospheric (CO_{2,B}) signals (Eq. (4.3.1)). Given observations of CO₂ and estimates of

¹<http://www.esrl.noaa.gov/gmd/ccgg/globalview>

$\text{CO}_{2,\text{BG}}$ and $\text{CO}_{2,\text{A}}$, $\text{CO}_{2,\text{B}}$ can be determined as the residual

$$\text{CO}_{2,\text{B}} = \text{CO}_2 - \text{CO}_{2,\text{BG}} - \text{CO}_{2,\text{A}}. \quad (4.3.1)$$

Similarly, we consider atmospheric CO to be composed of background and regional signals, but in contrast to CO_2 , the regional signal is assumed to be solely anthropogenic, i.e. stemming from the burning of fuels. This simplification seems justified given that oxidation of natural NMHC's is a source of only about 5 Tg yr^{-1} of CO over Europe as compared to direct emissions of 42 Tg yr^{-1} and oxidation of anthropogenic NMHC of 15 Tg yr^{-1} as estimated for the year 2000 by *Mészáros et al.* [2005]. Oxidation of methane is expected to contribute to the CO background but not to regional enhancements. Furthermore, emissions from biomass burning can be neglected, since wildfires are rare in Switzerland and Central Europe and no major events were reported for the year 2013. Accepting this simplification, the regional anthropogenic signal CO_A is given by

$$\text{CO}_\text{A} = \text{CO} - \text{CO}_{\text{BG}}. \quad (4.3.2)$$

The anthropogenic CO_2 signal, i.e., $\text{CO}_{2,\text{A}}$ can then be estimated from the anthropogenic CO signal using a CO_2/CO apparent ratio β (Eq. (4.3.3)), i.e. that observed at an observation site, derived from the slope of a regression between anthropogenic CO_2 and CO regional signals:

$$\text{CO}_{2,\text{A}} = \beta \times \text{CO}_\text{A}. \quad (4.3.3)$$

Combining equations 4.3.1 to 4.3.2 we obtain the regional biospheric signal

$$\text{CO}_{2,\text{B}} = \text{CO}_2 - \text{CO}_{2,\text{BG}} - \beta(\text{CO} - \text{CO}_{\text{BG}}). \quad (4.3.4)$$

Given co-located observations of CO and CO_2 , a site-specific β . Eq. (4.3.4) yields biospheric CO_2 signals derived solely from observations. Note that the two backgrounds CO_{BG} and $\text{CO}_{2,\text{BG}}$ need to be derived in a consistent way using the same method and the same observation site for both signals. However, CO_{BG} , $\text{CO}_{2,\text{BG}}$, and β are dependent on choices made during derivation. Therefore, their effect on the resulting biospheric signals will be evaluated in a set of sensitivity experiments. An overview of derivation of all background and anthropogenic component variants of the observation-based approach as well as two standard model-based approaches is presented in Table 4.2. Details will be given in the following section.

4.4 Data and methods

4.4.1 Observations

Table 4.1: Simulation characteristics for two observation sites of the CarboCount CH network. Listed from left to right are observation heights (m above ground level), FLEXPART-COSMO particle release heights (m above model ground level), the “true” site altitudes (m above sea level), smoothed COSMO numerical weather prediction model’s ($\sim 4 \text{ km}^2$) site altitude, and the geographic site locations.

Site	Meas. Height	Rel. Heights	Alt.	Alt. COSMO	Lat., Lon.
Beromünster	212	212	797	723	47.1896, 8.1755
Lägern-Hochwacht	32	100–200	840	566	47.4822, 8.3973

CO_2 and CO observations for the year 2013 were taken from two sites of the CarboCount CH network

[Oney *et al.*, 2015], i.e., Beromünster (BRM) and Lägern-Hochwacht (LHW), and from the high Alpine site Jungfraujoch (JFJ) [Schibig *et al.*, 2015]. Of the four sites of the CarboCount CH network, the two sites BRM and LHW were identified to be sensitive to surface fluxes from large parts of the Swiss Plateau [Oney *et al.*, 2015]. BRM is a 217 m tall decommissioned radio transmission tower situated on a moderate hill at 797 m a.s.l. (above sea level) at the southern border of the central Swiss Plateau. A detailed description of the observation system at BRM is presented in Berhanu *et al.* [2016]. LHW is a mountain top site at 840 m a.s.l. on a steeply sloping east-west oriented crest in the northeastern part of the Swiss Plateau. JFJ is located at 3650 m a.s.l. and is mostly sampling free tropospheric air [Zellweger *et al.*, 2003; Henne *et al.*, 2010]. It is therefore often used to characterize background conditions over continental Europe [e.g. Levin *et al.*, 2003; Gamnitzer *et al.*, 2006]. All sites were equipped with PICARRO (Santa Clara, California, USA) G2401 cavity ring-down spectrometers [Crosson, 2008; Rella *et al.*, 2013] that measure CO₂, methane (CH₄), water vapor (H₂O) and CO at approximately 0.5 Hz. Beromünster observations used in this study were taken from the highest of five sampling heights at 212 m, sampled four times per hour for three minutes. Lägern-Hochwacht observations were made from the tower at a height of 32 m.

CO₂ and CO measurements were calibrated against the corresponding international reference scales, WMO X2007 for CO₂ [Zhao and Tans, 2006], and WMO X2014a for CO. The calibration of target gas measurements, which are not used for the calculation of calibration coefficients, indicates an accuracy of the CO₂ and CO measurements of ~ 0.07 ppm and ~ 4 ppb, respectively, computed as the 10-day averaging window root mean square error (RMSE) of individual target measurements. We take this quantity as the respective uncertainty σ of both gases. For this study, all observations were aggregated to 3-hourly averages during the one-year period of 2013-01-01 to 2013-12-31.

4.4.2 Observation-based CO₂ components

4.4.2.1 Background signals

In order to generate the background signals for CO and CO₂, i.e., CO_{2,BG} and CO_{2,BG}, respectively, at the two observation sites Beromünster and Lägern-Hochwacht, we took the CO₂ and CO data from Jungfraujoch and applied the “robust estimation of baseline signal” method [REBS, Ruckstuhl *et al.*, 2012] with a 45-day local regression window (bandwidth). The REBS method aims to preserve seasonal variability while removing short-term plume events and synoptic scale variability. Deviations from a smooth background concentration are iteratively given less weight until a robust baseline is achieved. The application of the method must account for the sources of atmospheric variability. For example, applying the REBS method to CO₂ must account for the possibility of both negative and positive deviations from the background concentration. For the case of CO, on the other hand, we can safely assume that regional signals will be positive.

The baseline signal for CO was obtained from the three-hourly CO observations by employing a tuning factor (b) of 3.5, a local regression window width (local neighborhood or bandwidth) of 45 days, and a maximum of 10 iterations to derive asymmetric robustness weights. The scale parameters within the respective local regression window were calculated from the below-baseline fit residuals [Ruckstuhl *et al.*, 2012]. For CO₂, we used exactly the same parameters, but applied symmetric instead of asymmetric robustness weights to account for the fact that short-term deviations from the background can be either positive or negative. Also, the scale parameters within the local regression window were calculated from all fit residuals.

In order to test whether the background concentrations could also be estimated in the absence of a nearby background site such as Jungfraujoch, we also derived background concentrations directly from the observations at the target sites (BRM, LHW). The same REBS settings were applied as described above for Jungfraujoch. The smoothness of the REBS background depends on the width of the regression window and since this choice is somewhat arbitrary, we tested the sensitivity of the results to shorter (30-day) and longer

(60-day) windows in addition to the preferred 45-day window.

Table 4.2: An overview of the model and observation based CO₂ component estimates. All observation-based estimates (obs*) calculate the CO₂ background with a 45-day REBS, and translate CO above a similar CO background estimate with the designated β . All modeled estimates were calculated with FLEXPART-COSMO and the data product listed.

Case	Background	Biospheric	Anthropogenic
obs1	JFJ	Residual	β_{obs}
obs2	JFJ	Residual	β_{mod}
obs3	JFJ	Residual	$\beta_{mod,week}$
obs4	JFJ	Residual	$\beta_{mod,3hr}$
obs5	SITE	Residual	β_{obs}
obs6	SITE	Residual	β_{mod}
obs7	SITE	Residual	$\beta_{mod,week}$
obs8	SITE	Residual	$\beta_{mod,3hr}$
mod1	MACC	VPRM	CarboCount
mob1	MACC	Residual	CarboCount

4.4.2.2 Anthropogenic CO₂ signal

The anthropogenic CO₂ signal, CO_{2,A}, was estimated by scaling the anthropogenic CO signal, CO_A, with the scaling factor β (ppm CO₂/ppb CO; see Eq. (4.3.3)), which we derived using two different methods.

A first method was based on the observed relationship between the regional signals of CO₂ and CO at our CarboCount CH sites (obs1, Table 4.2). We assumed that the biospheric influence on the regional signal was negligible during wintertime (January, February, and December) and that therefore any variations in the regional signal stemmed from anthropogenic sources only, i.e., CO_{2,A} \gg CO_{2,B}. We then estimated β_{obs} from observed wintertime regional signals (CO₂-CO_{2,BG} and CO_A) as the slope of a total weighted least squares regression [Krystek and Anton, 2008] forced through the origin. The regression takes into account uncertainties of both regional CO₂ and CO signals, and yields a single scaling factor β_{obs} (Eq. (4.4.1)).

$$\text{CO}_2 - \text{CO}_{2,BG} = \beta_{obs} \times \text{CO}_A + \epsilon \quad (4.4.1)$$

where ϵ is the error term assumed to be normally distributed around zero. This assumption holds during winter when variations in both gases mainly result from similar combustion processes. Satar *et al.* [2016] show that this ratio varies seasonally, and approaches a value representative of the CO₂ : CO ratio of combustion processes only during winter. Since we can only derive a meaningful β from wintertime data, we assumed that β_{obs} is valid for the whole study period and used it to scale all CO_A to CO_{2,A}.

A second method relies on model simulated CO₂ and CO signals at the two observation sites (see Sect. 4.4.4). In this case, the total weighted least squares regression is applied to modeled regional anthropogenic CO_{2,A} and CO_A signals. The corresponding annual mean apparent ratio is denoted β_{mod} and can be interpreted as an average molar ratio between CO₂ and CO emissions weighted by each site’s field of view or “footprint” (see Sect. 4.4.4). However, these CO₂/CO emission ratios vary in time and space substantially. Therefore, we also determined weekly ($\beta_{mod,week}$) and three-hourly ($\beta_{mod,3hr}$) ratios to account for variability of the ratio expected from the combined effect of the variability represented in emission inventories and the influence of variations in air mass provenance and mixing.

4.4.3 Uncertainty of the biospheric signal

Since the biospheric signal is determined by difference, its uncertainty ($\sigma_{\text{CO}_2,\text{B}}$) accumulates the uncertainty of the individual observation-based components. Assuming independence of the individual components, we can determine $\sigma_{\text{CO}_2,\text{B}}$ by quadratically summing the uncertainty of each component of Eq. (4.3.1), i.e., the uncertainty of the background signal ($\sigma_{\text{CO}_2,\text{BG}}$), of the anthropogenic signal ($\sigma_{\text{CO}_2,\text{A}}$), and of the CO₂ observations (σ_{CO_2}) :

$$\sigma_{\text{CO}_2,\text{B}} = \sqrt{\sigma_{\text{CO}_2}^2 + \sigma_{\text{CO}_2,\text{BG}}^2 + \sigma_{\text{CO}_2,\text{A}}^2}, \quad (4.4.2)$$

where the uncertainty of the anthropogenic CO₂ signal is

$$\sigma_{\text{CO}_2,\text{A}}^2 = \beta^2(\sigma_{\text{CO}}^2 + \sigma_{\text{CO}_{\text{BG}}}^2) + \sigma_{\beta}^2(\text{CO} - \text{CO}_{\text{BG}})^2. \quad (4.4.3)$$

A constant (for the year of 2013) estimate of $\sigma_{\text{CO}_2,\text{BG}}$ was provided by the REBS algorithm. The uncertainty of the scaling factor, i.e., σ_{β} was obtained directly as the uncertainty of the slope of the weighted total least squares regression. Finally, σ_{CO} was taken directly from the CO observations.

4.4.4 Model simulated CO₂ components

In order to evaluate our observation-based method, the state-of-the-art Lagrangian transport model FLEXPART [Stohl *et al.*, 2005] was employed to directly estimate each of the components of Eq. (4.3.1), with regional-scale anthropogenic and biospheric surface flux inventories, and a global model providing background CO₂ concentrations. Furthermore, in order to investigate β , we also simulated CO_A.

4.4.4.1 Atmospheric tracer transport model

The Lagrangian particle dispersion model FLEXPART [Stohl *et al.*, 2005] that simulates the transport and dispersion of air parcels (particles) via turbulent, advective, and convective processes, was driven offline by hourly COSMO analysis fields from the operational analysis archive of MeteoSwiss. The model was run over a European domain ranging from 18.60°E to 23.21°W and 35.05°N to 57.53°N with a horizontal resolution of 0.06° × 0.06° (Figure 4.1).

FLEXPART-COSMO was run in backward mode (receptor-oriented, i.e., simulating upwind surface influence of sites) every 3 hours to simulate the movement and provenance of observed air parcels. In each simulation, 50,000 particles were released from the site's position at site-dependent heights above ground and traced backward in time 4 days or until they left the simulation domain.

After being scaled with the dry air density ρ , residence times τ (s m³ kg⁻¹) were recorded for a high-resolution output domain over Switzerland (4.97°E to 11.05°E and 45.49°N to 48.55°N) at 0.02° × 0.015° resolution, and a European output domain (11.92°E to 21.04°E and 36.06°N to 57.42°N) at 0.16° × 0.12° resolution. Residence times were then folded with regional surface flux inventories to arrive at dry air mole fractions [Seibert and Frank, 2004], which are estimates of respective regional signals. FLEXPART particle trajectory end points are defined by their time and position at the end of the simulation or when leaving the simulation domain. These endpoints are used to calculate initial and boundary conditions (Sect. 4.4.4.2). Further description of FLEXPART-COSMO can be found in Oney *et al.* [2015]. The particle release heights at the observation sites were chosen based on a meteorological evaluation of COSMO in Oney *et al.* [2015] and are listed in Table 4.1.

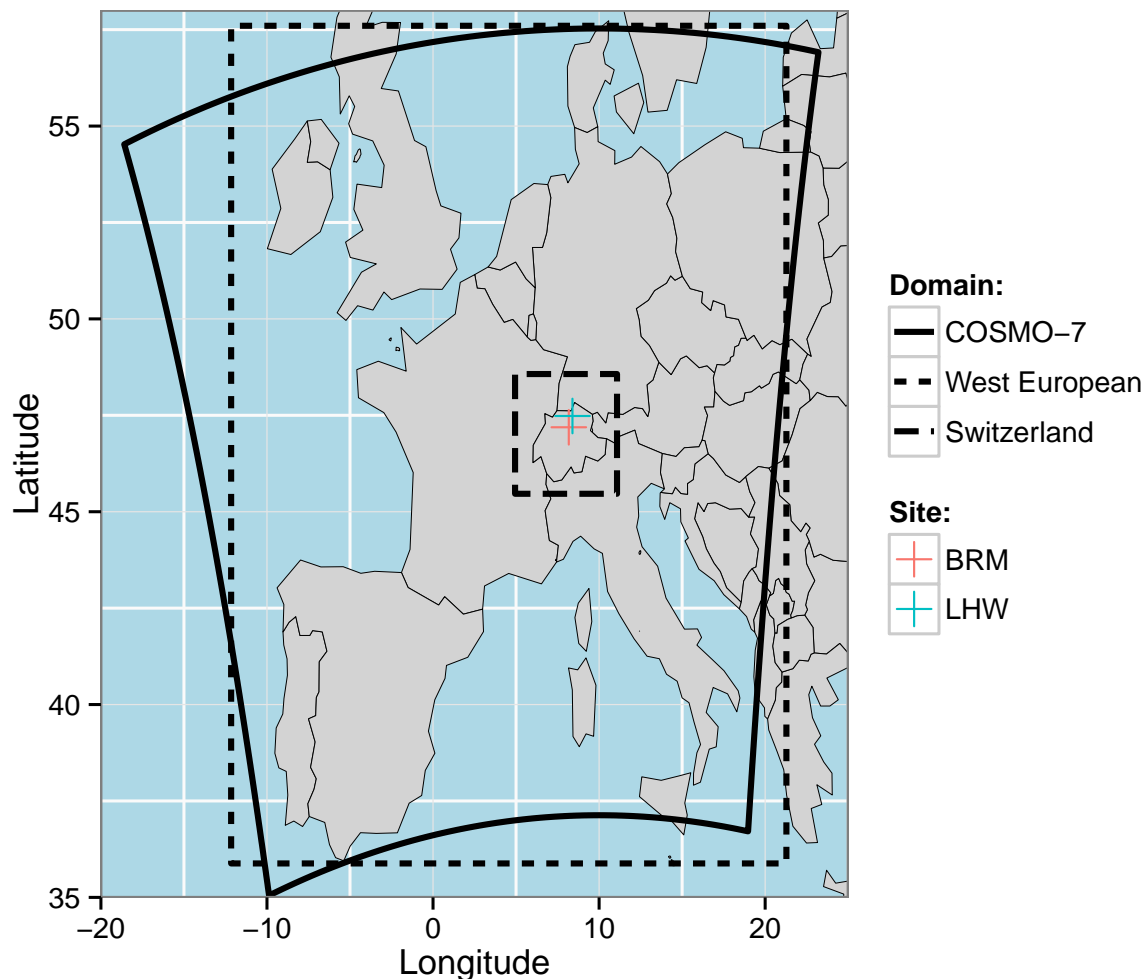
4.4.4.2 Lateral boundary conditions for CO₂

Figure 4.1: Simulation domains of this study. The COSMO-7 represents the driving meteorology. The west European and Switzerland domains comprise the areas where surface sensitivity and flux influence is calculated for the past 4 days to simulate regional signals. Outside these temporal and spatial domains the initial concentration is taken as the background signal.

The lateral boundary conditions for atmospheric CO₂ for the European domain were deduced from a global CO₂ atmospheric transport model by interpolating the 3-D CO₂ mole fraction fields to the 50,000 particle trajectory end points of each FLEXPART simulation and computing the average of the interpolated values. For each end point, the temporally closest 3-D model field was used for interpolation. Global CO₂ fields were provided by the data assimilation system of the Monitoring Atmospheric Composition and Climate (MACC) project of the European Centre for Medium Range Weather Forecast (ECMWF) [Chevallier *et al.*, 2010; Chevallier, 2013]. We used the simulation version MACC-II/v13r1 [Chevallier, 2015] in which global surface observations including those at Jungfraujoch were assimilated, but those the CarboCount CH sites were not assimilated.

4.4.4.3 Anthropogenic CO₂ & CO signals

The anthropogenic emission inventories of CO₂ and CO were generated by merging relatively coarse global and European inventories with high-resolution inventories available for Switzerland. For CO₂, the global EDGAR v4.2 FT2010 “Fast Track” inventory [Olivier *et al.*, 2011] available at $0.1^\circ \times 0.1^\circ$ resolution was merged with a new high-resolution ($500\text{ m} \times 500\text{ m}$) inventory for Switzerland developed by the company Meteotest, Switzerland, on behalf of the project CarboCount CH, hereafter referred to as the “CarboCount” inventory. The latest year available in both inventories was 2010, but the Swiss inventory was scaled to match the total for 2012 as officially reported to the United Nations Framework Convention on Climate Change [FOEN, 2014]. Both emission inventories include the emissions from the burning of fossil fuels, the burning of biomass (wood), and the production of cement.

For CO, the European TNO-MACC II emission inventory [Kuenen *et al.*, 2014] available at approximately $7\text{ km} \times 7\text{ km}$ resolution for the year 2009 was merged with a high-resolution ($200\text{ m} \times 200\text{ m}$) CO inventory of Switzerland from 2005. Due to the large, mostly negative trends in European CO emissions, both inventories were scaled by nation to match officially reported values of the year 2012 (latest year available), while preserving the emission’s spatial distribution. Country totals reported to the Convention on Long-range Transboundary Air Pollution (LRTAP) were obtained from the EMEP/CEIP web database (<http://www.ceip.at/>). As is the case for CO₂, the emission inventory for CO includes the burning of both fossil and modern fuels, while cement manufacturing does not lead to an emission of CO.

For both CO₂ and CO emissions, temporal profiles describing diurnal, day-of-week and monthly variations were prescribed based on sector-specific profiles developed in the project EURODELTA-II [Thunis *et al.*, 2008], similar to Peylin *et al.* [2011]. These profiles have been developed for a source classification according to SNAP (Standardized Nomenclature for Air Pollutants) codes. However, both EDGAR and the two Swiss inventories are based on different nomenclatures, e.g., the IPCC nomenclature in case of EDGAR. Specific conversion tables were therefore developed mapping the different emission categories onto the most closely matching SNAP codes [Kuenen *et al.*, 2014]. In addition, a country mask was applied to the EDGAR inventory, a gridded inventory without national borders, in order to apply country-specific day-of-week and monthly profiles. Diurnal profiles were identical in all countries but were adjusted to the local time in each country. Monthly scaling factors were temporally interpolated between the centers (day 15) of each month. Finally, hourly fields of total (sum over all categories) emissions of CO₂ and CO were reprojected to the two simulation domains, and averaged to three-hourly resolution as used by FLEXPART-COSMO. The anthropogenic CO₂ and CO signals were then simulated with FLEXPART-COSMO.

4.4.4.4 Biospheric CO₂ signal

In order to evaluate the residual regional biospheric signals inferred from the observations, we also computed this signal directly by using the net ecosystem exchange (NEE) fluxes from the Vegetation Photosynthesis and Respiration Model (VPRM) model as a boundary condition Mahadevan *et al.* [2008]. NEE represents the net exchange of CO₂ between the atmosphere and the terrestrial biosphere and in the model is equal to photosynthesis minus ecosystem respiration, since this model does not include any perturbation fluxes arising from, e.g., fires or insect outbreak. The fluxes computed by VPRM are driven by satellite and meteorology data. Parameters in VPRM controlling these fluxes had been optimized using CarboEurope-IP eddy covariance flux observations at various sites as described in Pillai *et al.* [2012]. After converting to a surface mass flux and reprojecting to the simulation domain, the hourly NEE fields were averaged to three-hourly resolution, and the biospheric influence on each site was then simulated with FLEXPART-COSMO.

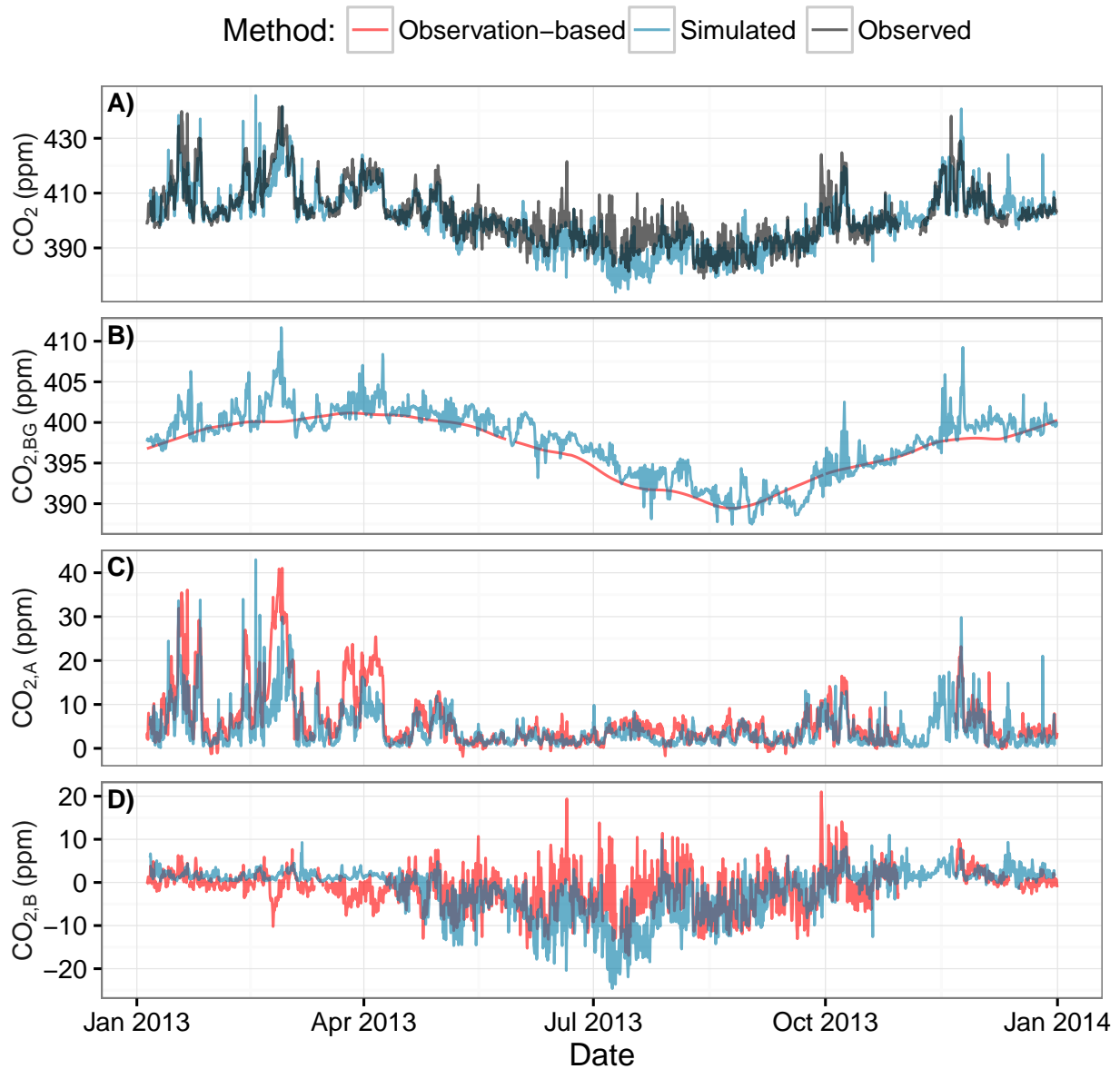


Figure 4.2: Observed CO_2 concentrations (A), observation-based (obs1) and FLEXPART-COSMO-modeled (mod1) CO_2 background (B), anthropogenic (C) and biospheric (D) components at Beromünster during 2013. Also shown in (A) is the sum of all simulated components. For an overview of the settings for obs1 and mod1 see Table 4.2.

4.5 Results & discussion

The atmospheric CO_2 concentrations observed at the two sites Beromünster and Lägern-Hochwacht exhibit the expected annual cycle for the northern hemisphere, with a summertime trough and a wintertime crest (Figs. 4.2 & 4.3, panel A). During the warmer months at Lägern-Hochwacht, the daily variation of CO_2 is due to a combination of biospheric activity and atmospheric boundary layer (ABL) dynamics [Oney *et al.*, 2015]. Beromünster's observations show these effects as well, but less strongly, due to a combination of

high inlet height and relatively high elevation above the Swiss Plateau owing to its location on top of a hill. Wintertime observations at Beromünster and Lägern-Hochwacht show relatively little diurnal variation, but contain samples of polluted air stretching for periods of days to weeks [Oney *et al.*, 2015; Satar *et al.*, 2016]. Being 40.5 km apart, the two sites usually sample related air masses, resulting in similar time series. This also suggests that local influences at the two sites are small.

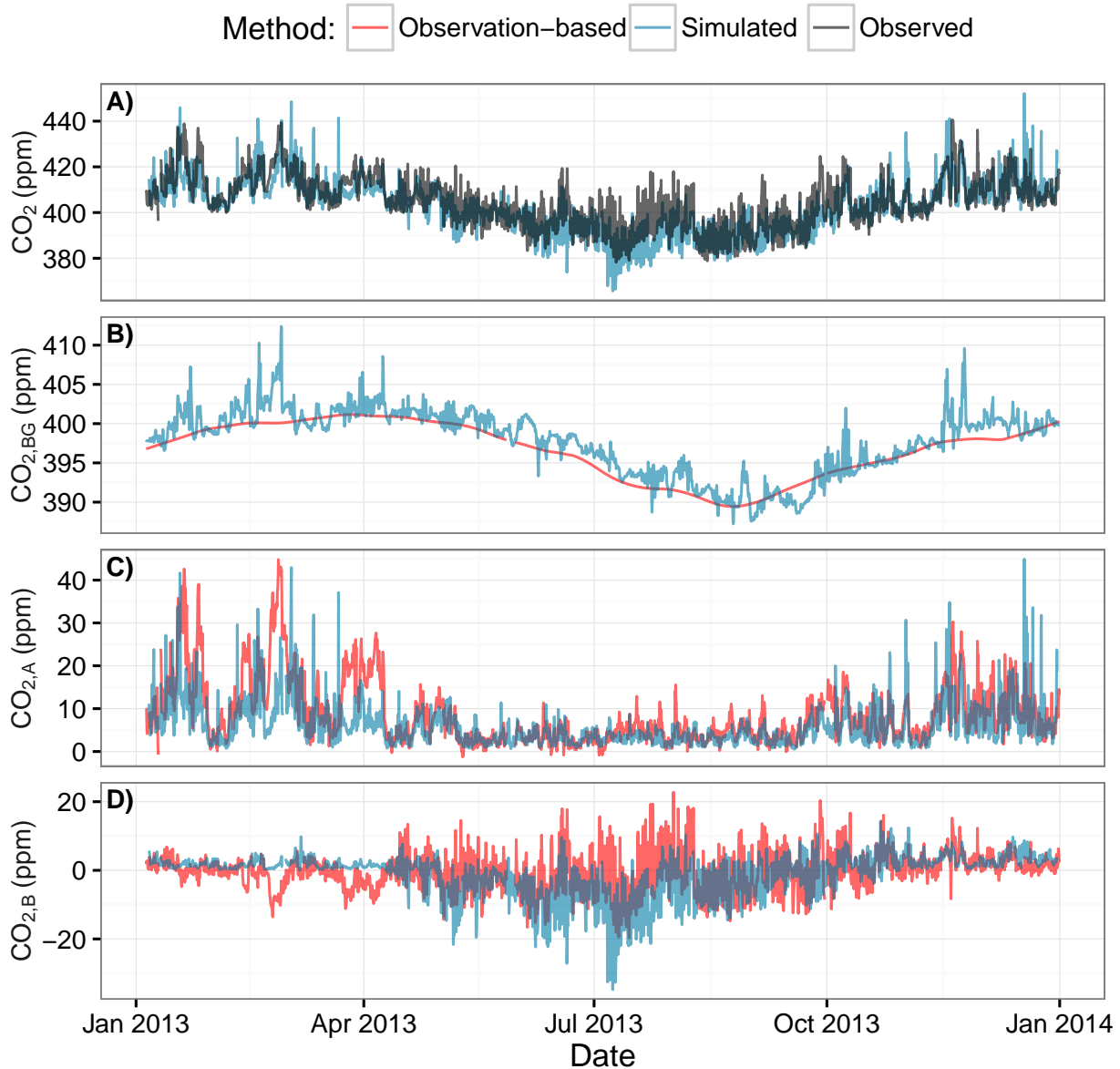


Figure 4.3: Same as Fig. 4.2 but at the Lägern-Hochwacht site.

The modeled atmospheric CO₂ concentrations represent the observations well (Figs. 4.2 & 4.3, panel **A**), but a closer inspection reveals considerable differences in summertime and during a few individual events in winter at both sites. These differences can come from any of the three modeled components, i.e., the background, the anthropogenic, and the biospheric signals, with the biospheric signal presumably being the most uncertain

one. Since we have derived estimates for each of these CO₂ components directly from co-located observations of CO₂ and CO (panel B–C), we can test whether this is indeed the case.

4.5.1 Background signals of CO₂ & CO

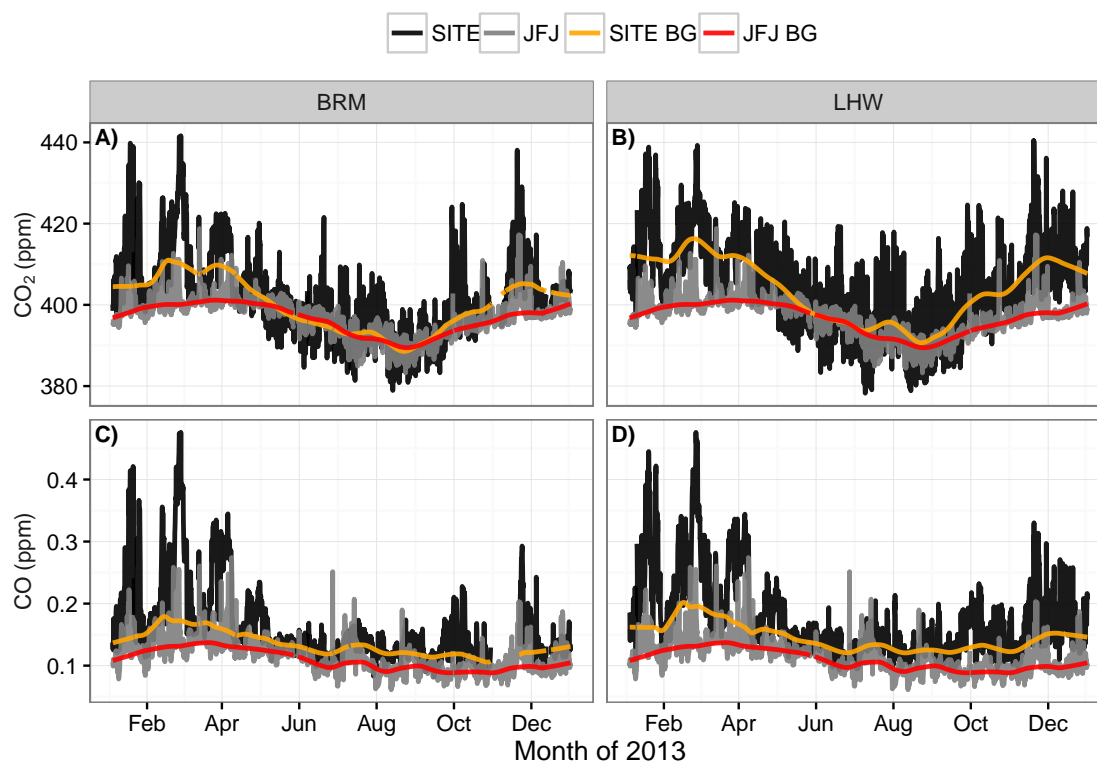


Figure 4.4: CO₂ (panels A–B) & CO (panels C–D) measured concentrations (black and gray) and “robust estimate of baseline signal” (REBS) estimates (red and orange) at Beromünster, Lägern-Hochwacht, and Jungfraujoch (JFJ) during 2013. The REBS background estimates are calculated with a 45-day local regression window.

Background sites such as Jungfraujoch are defined by their lack of local influence owing to them being far away from any anthropogenic emissions. Consequently, the concentration of CO is considerably lower at Jungfraujoch relative to Beromünster or Lägern-Hochwacht, where the proximity to CO sources is apparent (Fig. 4.4). Therefore, background CO signals estimated directly from Beromünster or Lägern-Hochwacht observations are typically greater than when Jungfraujoch is used as a background. Wintertime CO₂ background signals from Beromünster and Lägern-Hochwacht are also greater than those from Jungfraujoch owing to frequent sampling of polluted air with elevated concentrations of anthropogenic CO₂ at Beromünster and Lägern-Hochwacht, especially during periods of reduced vertical mixing. On the other hand, even though the air sampled at the high Alpine site Jungfraujoch exhibits little influence from Switzerland [Henne *et al.*, 2010], summertime Jungfraujoch CO₂ background signals differ little from those of Beromünster or Lägern-Hochwacht. This may partly be due to a balancing of anthropogenic emissions and biospheric uptake, but is mainly due to enhanced vertical mixing.

The Jungfraujoch CO₂ background signal overall behaves similarly to the modeled background concentration at Beromünster or Lägern-Hochwacht, although the Jungfraujoch-based background varies much less than

the modeled background (Figs. 4.2 and 4.3, panel **B**). However, the two background signals are not strictly compatible, because they are defined differently, i.e., with regard to different spatial and temporal domains. In the case of the model-based estimate, the size and structure of the signal depends highly on the model domain, which in this case is central Europe. In contrast, the observation-based background signal from Jungfraujoch attempts to remove all recent surface influence manifested in pollution and depletion peaks even if these originated outside the model domain. This difference is defined mainly by the observations and to a lesser degrees by the settings employed in the REBS method.

The large amount of variations in the model-based background suggests that our effective domain might have been too small, indicating that a backward integration time of four days is not always long enough for signatures from remote fluxes to fully dilute into the large-scale background. During these situations the air parcels likely begin and remain in the European ABL for four days time or more before reaching the observation station. This can also be seen in that the modeled CO_{2,A} and CO_{2,BG} are correlated, especially during winter when reduced vertical mixing causes CO_{2,A} emissions to accumulate in the lower troposphere. However, it should be noted that the short-term variation of model background is relatively small (< 10 ppm) compared to the anthropogenic CO₂ signal (< 40 ppm).

4.5.2 Anthropogenic CO₂ to CO ratio

The estimation of the apparent anthropogenic CO_{2,A} to CO_A concentration ratio, β , is one of the main challenges in the application of the CO-based method. Our standard approach was to use the slope of the wintertime relationship between the regional CO₂ and CO_A signals estimated by using Jungfraujoch as a background site. Fig. 4.5B,E reveals that these two signals are indeed highly correlated. To be consistent with previous studies, which reported the emission ratios of CO to CO₂, we report the ratios here as their inverse $R \equiv \beta^{-1}$. In wintertime an R (β^{-1}) of 8.39 ± 0.14 ppb CO/ppm CO₂ for Beromünster and an R of 7.70 ± 0.20 for Lägern-Hochwacht was observed (see Table 4.3).

For Beromünster, *Satar et al.* [2016] showed that in contrast to the high CO : CO₂ correlation in wintertime the cross-correlations are substantially weaker during the other seasons. Also, the slopes (ratios) are different reflecting the influence of other processes driving changes in the regional signals. Springtime ratios are marked by decreasing regional CO₂ likely related to initial plant growth, and high CO_A signals are likely related to domestic heating. In summer, the correlation weakens further due to the large and highly variable contribution of the net biospheric signal (± 20 ppm in regional CO₂) combined with weak CO_A signals. Observed autumn ratios reflect the weakening biopheric signals owing to smaller production and possibly increased litter decomposition combined with increasingly strong CO_A; i.e. they portray the gradual change from summer to winter. During winter, the correlation is strong suggesting that the biospheric influence is small and that regional CO₂ is driven mainly by human-induced combustion.

The extent of biospheric influence on the observed regional CO₂ signal becomes apparent when comparing the regional relationship β inferred from the observations with that inferred from simulated anthropogenic signals (Fig. 4.5A,D). Here, as expected, the correlations between the simulated CO_{2,A} and CO_A remain strong throughout the year, as these signals are purely driven by the anthropogenic emissions of CO₂ and CO. The variability in the modeled relationship reflects variations in air mass origin and the corresponding influence of the spatially non-uniform CO₂ to CO emission ratios in Europe, as well as differences in the temporal variations of CO₂ and CO emissions. Although variable, these processes do not lead to substantial seasonal variations in the slope between the modeled CO_{2,A} and CO_A. This supports the idea that observed wintertime β estimates appear to be representative for the entire year (Table 4.3).

Beromünster is located in a rural area where wood is frequently used for domestic heating and farm vehicle emission regulations are less strict than those for road traffic. Lägern-Hochwacht on the other hand is located

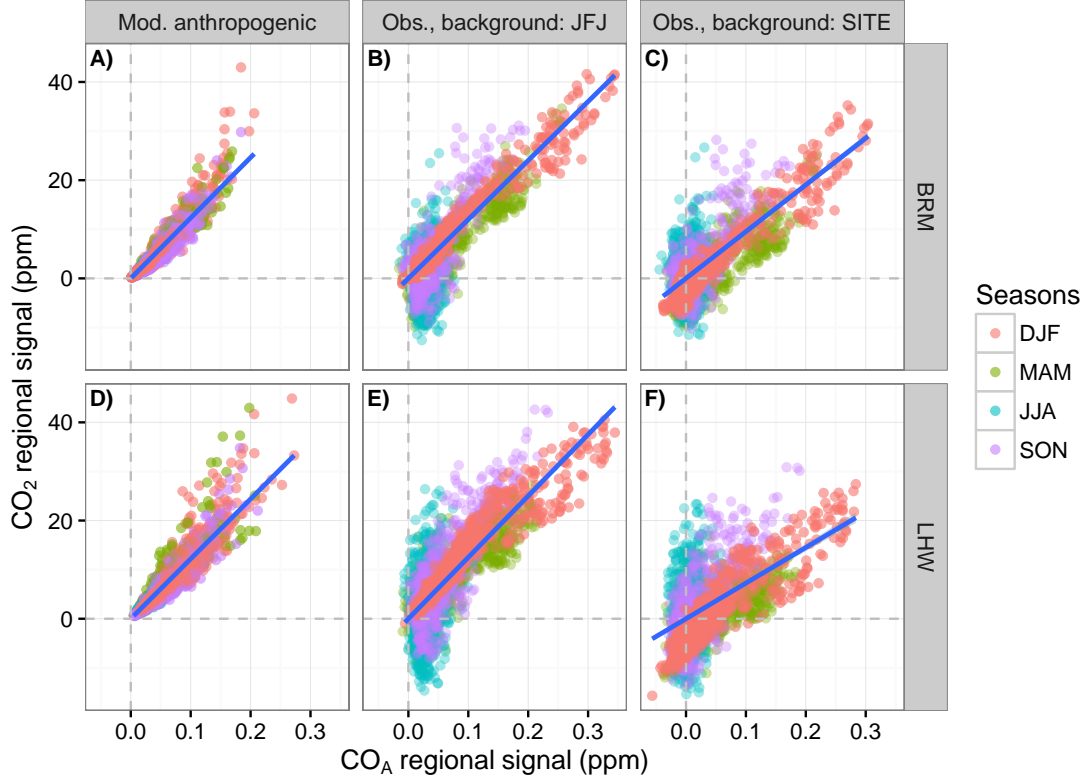


Figure 4.5: Modeled and measured CO_2 and CO regional signals at Beromünster and Lägern-Hochwacht, colored according to season. Panel **A**: modeled $\text{CO}_{2,A}$ and CO_A at Beromünster. The slope of the regression line corresponds to β_{mod} of method mod1. Panel **B**: $\text{CO}_{2,R}$ and CO_A regional signals above a background signal from Jungfrauoch. The slope of the regression line is calculated using only wintertime regional signals and corresponds to β_{obs} of method obs1. Panel **C**: the same is shown as in panel **B** except using background estimates from the target site Beromünster (method obs5). Panels **D-F**: the same as panels **A-C** shown with regional signals from Lägern-Hochwacht.

Table 4.3: Sensitivity of the inverse ratios $R_{obs} (\equiv \beta_{obs}^{-1})$ to the choice of observations used to determine the background signal, and to the choice of width of local regression window. Also shown are model-based ratios R_{mod} . The units of R_* are ppb CO /ppm CO_2 . The uncertainty (\pm) of R is determined as 2σ of the slope of the total weighted least squares regression.

Site	Background	R_{obs}	R_{mod}
Beromünster	JFJ, 30-day	8.38 ± 0.14	9.53 ± 0.14
	JFJ, 45-day	8.39 ± 0.14	"
	JFJ, 60-day	8.40 ± 0.14	"
	SITE, 30-day	10.70 ± 0.38	"
	SITE, 45-day	10.00 ± 0.30	"
	SITE, 60-day	9.77 ± 0.28	"
Lägern-Hochwacht	JFJ, 30-day	7.67 ± 0.19	8.98 ± 0.17
	JFJ, 45-day	7.70 ± 0.20	"
	JFJ, 60-day	7.71 ± 0.20	"
	SITE, 30-day	10.40 ± 0.52	"
	SITE, 45-day	10.20 ± 0.54	"
	SITE, 60-day	10.30 ± 0.56	"

in a relatively more densely populated and industrialized area, where combustion tends to be more efficient. The simulated apparent ratios reflect the expectation that air parcels observed at Beromünster (R_{mod} of 9.53 ± 0.14) are more CO-enriched than those at Lägern-Hochwacht (8.98 ± 0.17). Correspondingly, the observed air parcels at Beromünster tend to be more CO-enriched than those at Lägern-Hochwacht. Furthermore, seasonal variation in emission patterns and ABL dynamics has the potential to affect the apparent CO/CO₂ ratios. *Satar et al.* [2016] report significantly lower wintertime ratios for Beromünster, which is likely due to different time periods and regression approaches. They used data from two years (2013 and 2014) and applied the regression to deviations from 5-day running means. We only used data from the more polluted year 2013 and applied the regression to enhancements above the JFJ background and forced the offset to zero. Modeled ratios $R_{mod,week}$ derived from weekly instead of annual relationships range from 7.55 to 12.60 (median of 9.35) ppb CO/ppm CO₂ at Beromünster, and from 6.93 to 11.20 (median of 8.79) ppb CO/ppm CO₂ at Lägern-Hochwacht, respectively. This variability is partly due to spatial variations of CO/CO₂ emission ratios and due to different temporal profiles applied to different emission sectors in the emission inventories. However, it is also partly due to significant inconsistencies between the CO and CO₂ inventories which are based on different spatial surrogate data. We tested the option of using EDGAR v4.2 instead of TNO-MACC II also for CO but large inconsistencies in individual grid cells were still found, for example, showing strong emissions of CO but no emissions of CO₂ and vice versa. Furthermore, most of the surface influence on both Beromünster and Lägern-Hochwacht is usually within distances of ≤ 300 km [*Oney et al.*, 2015], and for Switzerland the emission inventories for CO and CO₂ correspond well, although also here different reference years (CO₂: 2010 and CO: 2005) of the inventories may lead to some spatial inconsistencies.

The observation-based ratios are relatively insensitive to the choice of the smoothing window required to determine the background signals in CO and CO₂ and thereby determining the remaining regional signal, but react sensitively to the choice of the background site (Table 4.3). If the site's observations are used to determine the background signals, then the ratios increase, largely owing to the regional signal in CO₂ during wintertime being smaller relative to that for CO (Figure 4.4). In other words, this is caused by the SITE baseline for CO₂ being considerably larger than JFJ baseline for CO₂, whereas the CO baseline estimates remain closer together. Classically, the background signal is a matter of definition and would typically correspond to the REBS estimate from Jungfraujoch or the modeled estimate instead of REBS estimate from one of the CarboCount sites. The ratios based on regional signals relative to site-based background signals (obs5-obs8) likely correspond to more localized areas surrounding each site and are thus likely not valid for larger areas such as the Swiss Plateau. Therefore, for this application, we cannot recommend the determination of the background signals from observations, in which the local influence is large relative to the background/global variation when applying this observation-based method. By extension, we considered the ratios based on regional signals relative to site-based background signals to be of limited value for our analyses and did not pursue them further.

When comparing our results of R_{obs} with those previously reported, fossil fuel based CO_A/CO_{2,FF} ratios (Table 4.4), our results are mostly smaller with the exception of two sites in coastal and remote environments. However, it needs to be emphasized that these results are not always directly comparable. First, our estimates are concentration ratios in the air, reflecting emissions and transport from a wide array of regions. Second, our anthropogenic components (CO_{2,A} and CO_A) include also the contribution of the combustion of non-fossil, carbonic materials. Due to wood-burning, the use of biofuels, and waste incineration [*Mohn et al.*, 2008], non-fossil combustion in Switzerland constitutes 14 % of CO₂ emissions according to the Swiss national emission inventory [*FOEN*, 2014]. Third, owing to many technological advances since the time of the outlined studies, the combustion efficiency has increased resulting in proportionally less CO being emitted, which further reduces the ratio.

Table 4.4: Summary of observed R 's found in previous studies. The upper portion of the table displays long-term observation results, and the lower half of the table displays observation campaign results. $\text{CO}_\text{A}/\text{CO}_{2,\text{R}}$ refers to ratios calculated from continuous CO_2 and CO observations above background, analogous to this study. $\text{CO}_\text{A}/\text{CO}_{2,\text{FF}}$ indicates fossil fuel CO_2 ($\text{CO}_{2,\text{FF}}$) calculated from ^{14}C [see *Levin et al.*, 2003]. The information used for the method is presented as the apparent ratio calculation, background, and the metric shown. The units of R are ppb CO /ppm CO_2 .

R_{obs}	Location	Period	Method	Study
12.4 ± 0.5	Harvard forest, USA	1996 Wintertime	$\text{CO}_\text{A}/\text{CO}_{2,\text{A}}$, monthly 20 th percentile, mean and standard deviation of three months	<i>Potosnak et al.</i> [1999]
12.2 ± 0.4	Heidelberg urban site, Germany	2001-09–2004-04	$\text{CO}_\text{A}/\text{CO}_{2,\text{FF}}$, Jungfraujoch ^{14}C & GLOBALVIEW- CO , mean and standard deviation	<i>Gamnitzer et al.</i> [2006]
15.5 ± 5.6 & 14.6 ± 5.5	Heidelberg urban site, Germany	2002–2009	$\text{CO}_\text{A}/\text{CO}_{2,\text{FF}}$, Jungfraujoch, weighted mean and standard deviation & median and interquartile range	<i>Vogel et al.</i> [2010]
9 ± 5	Lutjewad coastal site, Netherlands	2006–2009	$\text{CO}_\text{A}/\text{CO}_{2,\text{FF}}$, Jungfraujoch, mean \pm standard deviation	<i>Van Der Laan et al.</i> [2010]
11.2 ± 9 & 12.2 ± 11 & 11.9 ± 8	Coastal northeast USA	2004–2010; annual, summer, and winter	$\text{CO}_\text{A}/\text{CO}_{2,\text{FF}}$; Free troposphere observations, median and uncertainty (average of uncertainty range)	<i>Miller et al.</i> [2012]
~ 6.8	Beromünster tall tower, Switzerland	2012–2014	$\text{CO}_\text{A}/\text{CO}_{2,\text{R}}$ (above seasonal harmonics estimates), standard major axis regression	<i>Satar et al.</i> [2016]
6.8 ± 2.2 & 11.7 ± 5.5	Niwot Ridge mountain site, USA	2004-01-20 & 2004-03-02	$\text{CO}_\text{A}/\text{CO}_{2,\text{FF}}$, average from 2003-11–2004-04 with western winds, mean and standard deviation	<i>Turnbull et al.</i> [2006]
11.2 ± 2 & 14 ± 2	Sacramento metropolitan area, USA	2009-02-27 & 2009-03-06	$\text{CO}_\text{A}/\text{CO}_{2,\text{FF}}$, Free troposphere observations, linear regression slope $\pm \sigma$	<i>Turnbull et al.</i> [2011]
56 (33) & 22 (20)	Downwind of China and Japan, respectively (outliers removed)	2001-02-24 to 2001-04-10	$\text{CO}_\text{A}/\text{CO}_{2,\text{A}}$, none, reduced axis regression	<i>Suntharalingam</i> [2004]

4.5.3 Anthropogenic CO_2

The anthropogenic component $\text{CO}_{2,\text{A}}$ estimated in our base case (i.e., "obs1") is a considerable component of the total CO_2 at the two observing sites of the CarboCount CH network (Figure 4.2 and 4.3, panels **B**). In the "obs1" base case, Jungfraujoch is used as the background for both CO and CO_2 and β is inferred from the winter-time regional signals at the respective two sites (see Table 4.2). Particularly in wintertime, the variations in $\text{CO}_{2,\text{A}}$ ($\sigma = \pm 9.5$ ppm) dominate the variations in atmospheric CO_2 , explaining most of the observed variability. In summertime, the signals are substantially weaker ($\sigma = \pm 2$ ppm), largely owing to increased vertical mixing in the lower troposphere.

Our estimated $\text{CO}_{2,\text{A}}$ has only few negative excursions (1.6% & 0.5% of the time at Beromünster and Lägern-Hochwacht, respectively), even though there was no constraint on the method to ensure the expected positive definiteness of this component. This increases the confidence in this estimate. These few negative excursion

result from the few occasions when the background CO signal from Jungfraujoch was greater than the observed CO at Beromünster or Lägern-Hochwacht. Most of these negative excursions correspond to times when also CO₂ at the two sites was lower than the background at Jungfraujoch. Thus, these conditions occur when the air arriving at Jungfraujoch had a different origin than that arriving at our CarboCount CH sites.

The observation-based estimate of the anthropogenic CO₂ component also looks plausible when compared to the simulated anthropogenic signal (mod1) for the whole year 2013 (Figs. 4.2 and 4.3, panel C). In fact, the directly modeled anthropogenic signals (mod1) agree remarkably well with the estimates derived from the CO observations (obs1). The largest differences occur during wintertime and early spring, arising from any combination of errors in transport and mixing, and in the emission inventories of CO and CO₂ (Fig. 4.6).

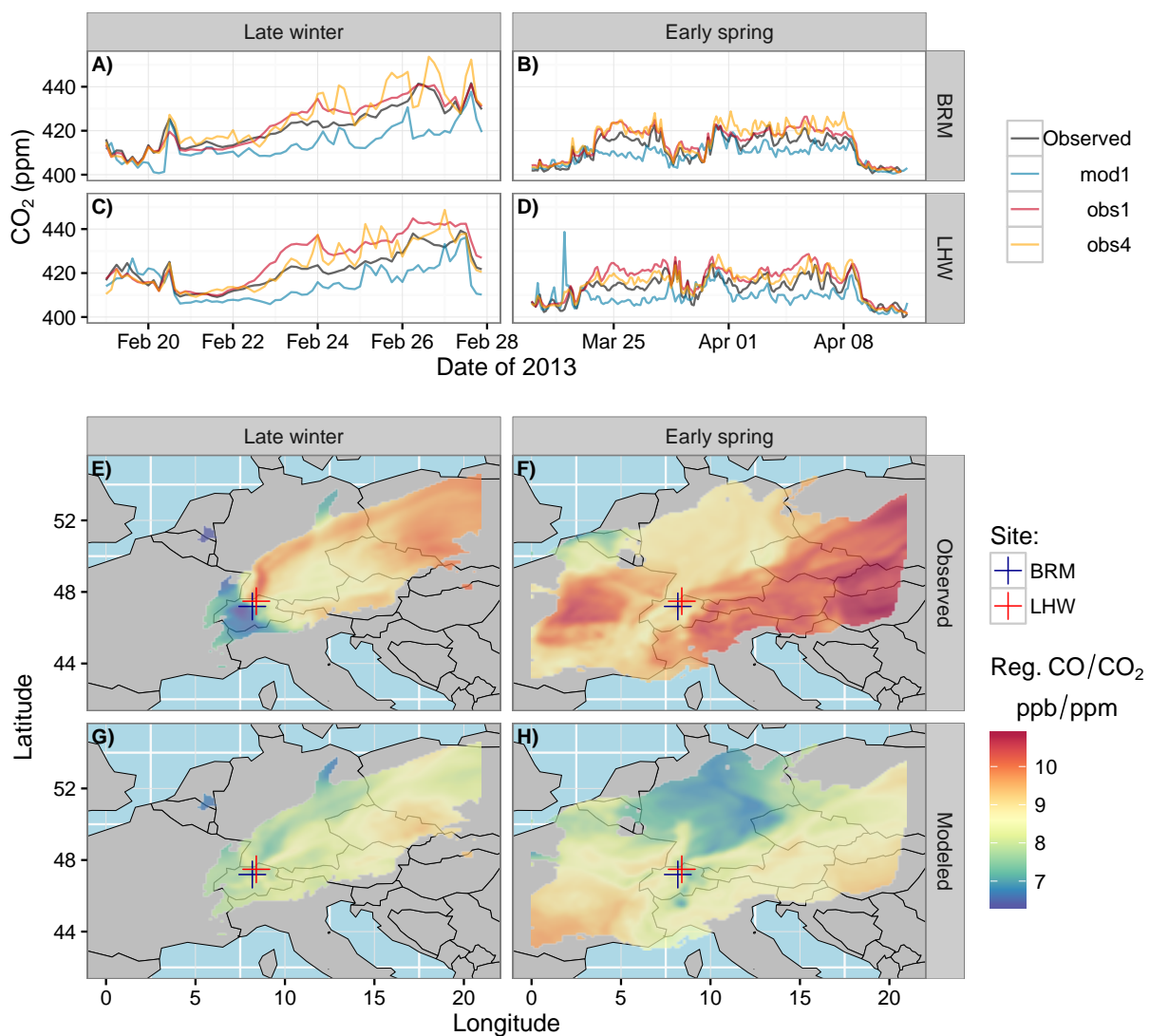


Figure 4.6: Late winter- and springtime pollution events during which neither observation based nor modeled estimates explain the observed CO₂ at Beromünster and Lägern-Hochwacht. Modeled and observed regional CO : CO₂ ratios above a threshold which denotes an isoline which includes 90 % of the cumulative sum of surface sensitivities [see *Oney et al.*, 2015]. Individual regional signals were spatially disaggregated according to *Stohl* [1996].

To investigate the potential contribution of errors in the emissions of CO and CO₂ to the largest mismatches, we analyzed the possible dependence of the CO : CO₂ ratios on the air mass origin during two pollution events “late winter” (February 19–28, 2013) and “early spring” (March 20 to April 12, 2013). To this end, a regional CO : CO₂ ratio map during these two anomalous periods was calculated by distributing the observed regional CO₂ and CO signals over the concurrent simulated surface sensitivities applying the trajectory statistics method of *Stohl* [1996], as in:

$$\chi_{i,j} = \frac{\sum \chi \cdot \tau_{i,j}}{\sum \tau_{i,j}}, \quad (4.5.1)$$

where χ is the measured mole fraction above background and $\tau_{i,j}$ are the scaled residence times (horizontal indices i, j) computed with FLEXPART-COSMO and the summation runs over all observations during a given period. For each time period, this was performed by combining the average concentration fields of CO and CO₂ produced by the trajectory statistics method for both sites separately and dividing the resulting CO_{i,j} and CO_{2i,j} fields by each other. The same was done with the modeled regional anthropogenic signals χ (Fig. 4.6, panels **E–H**).

During these pollution events, cold, northeasterly winds brought highly CO-enriched air from Eastern Europe resulting in anomalously high CO : CO₂ ratios, which differ substantially from the ratios observed during the rest of the winter and the ratios expected from the CO and CO₂ inventories (Fig. 4.6, panels **A–D**). Applying three-hourly ratios $R_{mod,3hr}$ (obs4) to convert observed regional CO_A to CO_{2,A} results in a similar overestimation of CO₂ since the modeled ratios are on average close to those observed during the rest of the winter, further supporting the conclusion that these events were anomalous. Because we use the same observed CO₂ to CO ratio for the entire winter and year (obs1), these special situations cause this ratio to increase, resulting in the underestimation of the anthropogenic component (by obs1) during the rest of the year, and thus a positive bias in the estimated biospheric signal.

During these events, the simulated CO₂ concentrations, and regional CO₂ and CO signals (mod1) are too low relative to the observed ones (Fig. 4.6, panels **E–H**). This suggests that the inventories do not account for these relatively large emissions. Specifically, it suggests that our employed inventories are strongly underrepresenting CO and CO₂ emissions in Eastern Europe. A general underrepresentation of CO emissions over Europe during winter was recently also reported by *Stein et al.* [2014] and *Giordano et al.* [2015]. A large share of coal and wood for domestic heating is likely responsible for larger emissions, especially CO and thus CO : CO₂ emission ratios in the eastern portions of Europe, specifically during the cold seasons. Current emission inventories do not seem to capture these differences adequately.

4.5.4 Biospheric signal

4.5.4.1 Evaluation

The afternoon (12–15 UTC) time series of our observation-based estimate of the biospheric signal (obs1) shows the expected release of CO₂ during winter and uptake of CO₂ during the spring to fall period (Fig. 4.7), reflecting the seasonal cycle of the balance between photosynthesis and ecosystem respiration, i.e., NEE. The biospheric signal typically varies between 0 to 5 ppm in winter, but varies from –5 to –10 ppm in summer with individual larger excursions in the range of –20 to +20 ppm. This variation indicates the high sensitivity of NEE to the environment. However, a framework for evaluation of the biospheric signal has yet to be established in this context. We evaluate our wintertime observation-based biospheric signals using FLEXPART-COSMO and VPRM simulations, when biospheric signals are typically small with low variability, and rely on the statistical distributions of the derived biospheric signals as a measure of plausibility. During summer afternoon, simulated atmospheric transport is usually most realistic, and therefore this time is

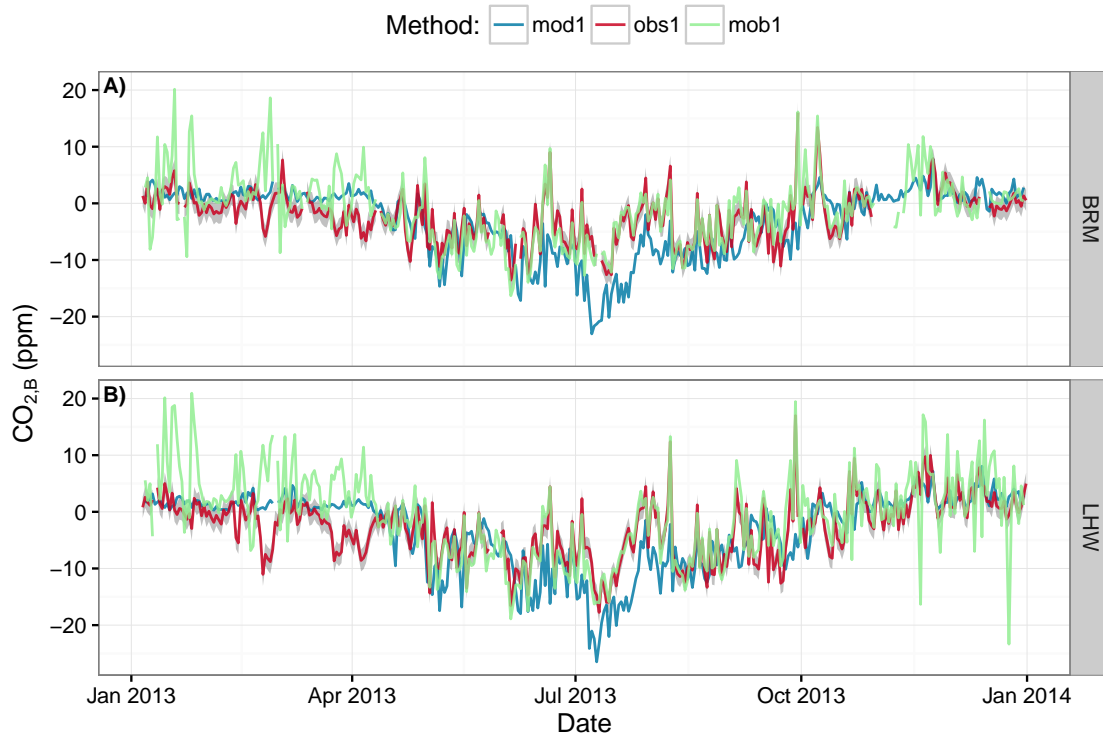


Figure 4.7: Afternoon (1200–1500 UTC) biospheric CO₂ signals at Beromünster and Lägern-Hochwacht during 2013. The modeled (mod1) and observation-based (obs1) biospheric signals ($\text{CO}_{2,B}$) are also shown in panel **D** of Figs. 4.2 & 4.3. The uncertainty (gray) enveloping the residual biospheric signal (obs1) accounts for the uncertainty introduced by the observation based background and anthropogenic CO₂ signals.

typically used in regional atmospheric inversions [e.g. *Goeckede et al.*, 2010a; *Tolk et al.*, 2011; *Meesters et al.*, 2012]. During this season and time of day, we evaluate observation-based biospheric signals using daytime residual biospheric signals resulting from subtracting FLEXPART-COSMO-simulated background and anthropogenic signals (mob1).

The VPRM-based modeled signals follows the same seasonal trend as the two residual time series with slightly positive values in winter and pronounced negative values in summer. During the growing season it follows the variations in the residual time series closely, except for a few weeks in summer with negative excursions, especially in July. During these periods, the total model simulated concentrations (Figs. 4.2 & 4.3, panel **A**) are lower than the observations suggesting that VPRM overestimates the biospheric sink in summer. Apart from this issue, the wintertime VPRM-based time series appears to be a plausible benchmark on which to evaluate the residual biospheric signals. This conclusion is also supported by *Ahmadov et al.* [2007] and *Ahmadov et al.* [2009] who demonstrated that VPRM combined with a regional scale transport model is able to capture the main observed features of the observed CO₂ distribution well.

During wintertime, when the biospheric signal is expected to be small and positive, owing to photosynthesis being negligible and both plant and soil respiration being weak, the time-series and distribution of VPRM-based biospheric signals fulfill these expectations (Fig. 4.8 & 4.9**A,E**). The wintertime model-based residual biospheric signal (mob1) shows unrealistically large fluctuations (bias-corrected RMSE [BRMSE] of mob1 versus mod1: BRM 28.2 ppm & LHW 50.4 ppm), which results from the inability to correctly represent $\text{CO}_{2,BG}$ and $\text{CO}_{2,A}$ concentrations. The observation-based biospheric signals (obs1-obs4) are considerably

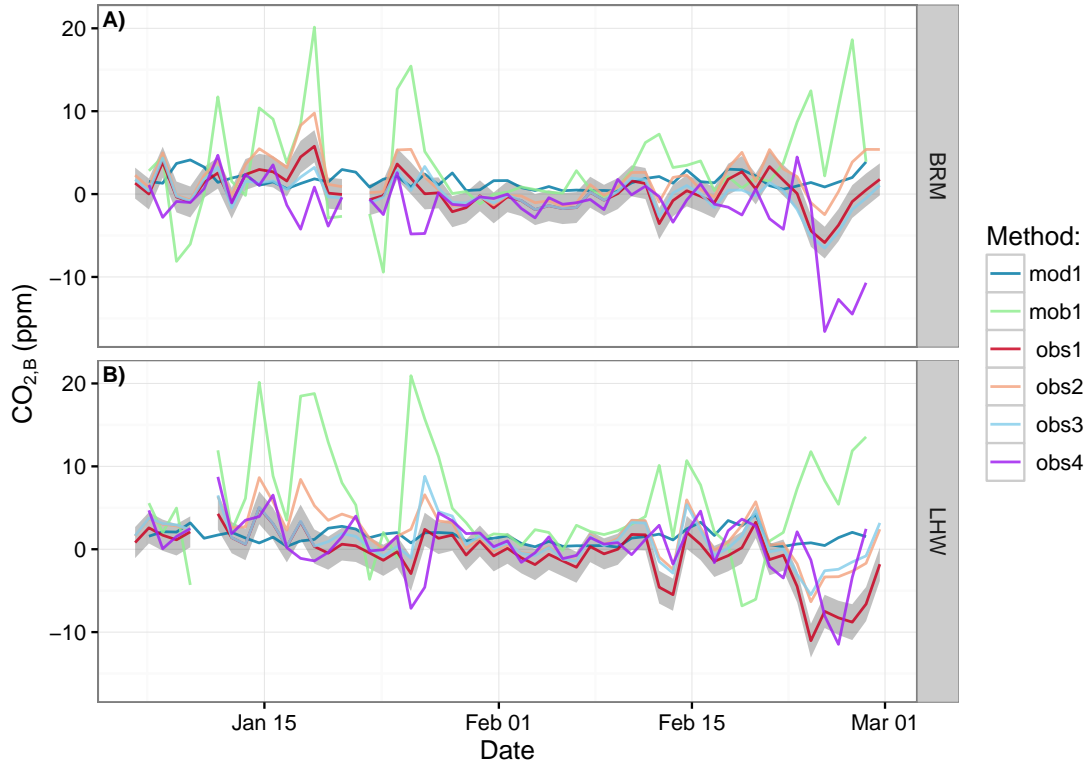


Figure 4.8: Comparison of biospheric CO_2 signals ($\text{CO}_{2,B}$) at Beromünster (panel **A**) and Lägern-Hochwacht (panel **B**) during the period of 2013-01 – 2013-03.

closer to the expected biospheric signal with much less scatter (BRMSE of obs1 versus mod1: BRM 4.2 ppm & LHW 8.3 ppm) and are therefore more realistic. However, during the late winter and spring pollution events, when CO -enriched air masses were advected from Eastern Europe, both observation- and model-based methods failed to yield realistic residual biospheric (Sect. 4.5.2). Here, the modeled $\text{CO}_{2,B}$ (mod1) is likely the most realistic. These examples illustrate well the consequences of inaccurately estimating the “other” CO_2 components.

During summertime afternoon (1200–1500 UTC), the model-based residual biospheric signal (mob1) is much more reliable than during wintertime, as is commonly assumed in regional biospheric flux inversion studies [e.g. *Goeckede et al.*, 2010a; *Tolk et al.*, 2011; *Meesters et al.*, 2012], for two reasons. First, uncertainties in model transport are comparatively low since the depth of the ABL, which is a major component of this uncertainty, is largest during summertime afternoons and well-represented in numerical weather forecast models [*Brunner et al.*, 2015]. Second, the anthropogenic signal is small as it is diluted within the well-mixed, deep ABL. There is good agreement (BRM: 4.2 ppm & LHW: 3.9 ppm BRMSE) between the model-based residual (mob1) and the observation-based biospheric signal (obs1) time-series (Fig. 4.7) and statistical distributions (Fig. 4.9C,G) during summertime afternoon. This supports the notion that the observation-based method is suitable to determine summertime biospheric signals. As a side note, during summertime at night (0000–0300 UTC), when predicting atmospheric mixing becomes difficult, differences increase somewhat (BRM: 6.6 ppm & LHW: 6.8 ppm BRMSE). This possibly indicates a further advantage of observation-based signals in that the method offers a possibility to evaluate transport and surface flux inventories during periods atmospheric mixing is most difficult to predict.

Accounting for weekly or three-hourly time-dependence of the anthropogenic $\text{CO}_2 : \text{CO}$ ratio β (obs3, obs4)

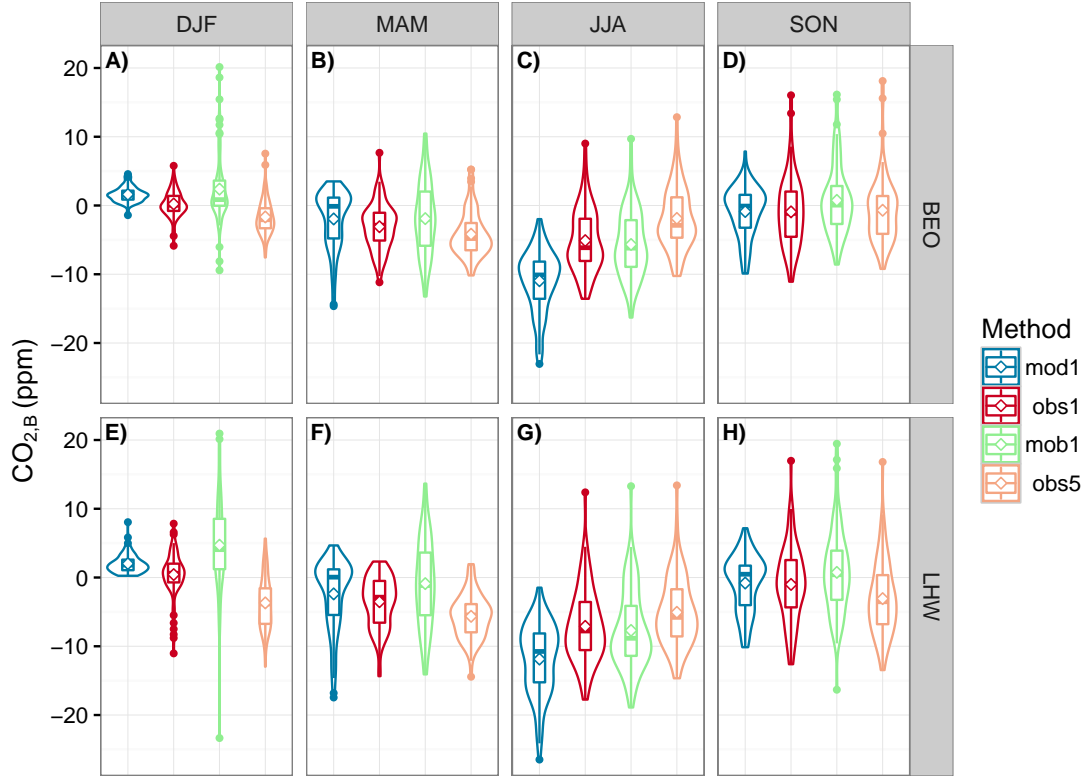


Figure 4.9: Comparison of the statistical distributions (box and violin [kernel density] plots) of afternoon (1200–1500 UTC) CO₂ biospheric signals at Beromünster (panels **A–D**) and Lägern-Hochwacht (panels **E–H**) during 2013, summarized by season for each method (Table 4.2). The mean of each distribution is marked by a diamond.

surprisingly did not significantly improve expected positive definiteness and generally small variability of biospheric signals (Fig. 4.8). Ideally, if the temporal and spatial variability of anthropogenic CO and CO₂ emissions were accurately represented in the model, the obs4 method should work best. Such variability, however, appears to be poorly represented in the emission inventories and/or temporal emission profiles. Currently, a fixed annual β (obs1 or obs2) appears to be the most robust approach.

The observation-based estimates depend on choices made when determining background and anthropogenic CO₂ signals, and the choice of observation site used for the background signal was found to have the largest effect on determining both the CO_A and the accompanying β and by extension the resulting residual biospheric signals (Fig. 4.9). The method employing the target site observations for determination of the background and anthropogenic signals (obs5) fails to capture the background CO signal (see Fig. 4.4), and thus fails to capture the regional CO₂ signal. It appears to represent a more local CO₂ signal. Here, we reiterate the preference for the use of Jungfraujoch observations for determination of the background signal and by extension CO_A and β in order to avoid possible biases in the residual biospheric signal, when applying our observation based method.

The estimated uncertainty of observation-based residual biospheric signal (obs1) is dominated by the uncertainty of the anthropogenic CO₂ signal, which scales with anthropogenic CO (see Eq. (4.4.2)). It is therefore lowest during summertime and highest during wintertime (Figs. 4.7 & 4.8), when the anthropogenic signal is greatest. However, simplifying assumptions of atmospheric CO chemistry likely result in artificially low uncertainty estimates, which could be corrected upwards based on the expected additional variation in CO,

in a regional inversion framework. Still, a transport model is necessary in order to invert the $\text{CO}_{2,B}$ signals, and therefore model transport error would still be introduced, albeit at a later stage, with likely weaker effect. In other words, our proposed method does not release regional-scale flux determination from the problem and task of improving atmospheric model transport.

4.5.4.2 Relation to environmental factors

Next, we address whether the variations in the observation-based biospheric residual (obs1) can be plausibly related to environmental drivers. In general, net photosynthesis has been found to be controlled by available photosynthetically active radiation (PAR), soil moisture, CO_2 , nutrients, and leaf level temperature [Bonan, 2008]. In contrast, heterotrophic respiration is mainly a function of soil temperature and soil moisture. Relationships between these environmental variables and net ecosystem exchange (NEE) were also established by eddy flux covariance measurements, which indicated that the local meteorological variables PAR, temperature, and soil moisture are the most important factors explaining the observed variability [Baldocchi *et al.*, 2001; Baldocchi, 2008; Beer *et al.*, 2010]. Here, we analyze our residual biospheric signal during the growing season (May to August) with meteorological variables as extracted from the COSMO-2 model analysis and interpolated to the location of the two measurement sites. The analyzed variables are temperature (averaged of preceding 24 hours), PAR (accumulated over the preceding 24 hours), as well as precipitation (accumulated over the preceding 21 days) as a proxy of soil moisture.

During the growing season the biospheric residual was mostly negative indicating biospheric uptake of CO_2 (Fig. 4.10) but also large variations on synoptic time scales were observed including periods when the biospheric residuals became positive, indicating a net biospheric source of CO_2 . Two periods in mid-June and late July/early August with positive biospheric residuals clearly corresponded to especially warm conditions with daily average temperatures between 20°C and 25°C and daytime maximum temperatures around 30°C (Fig. 4.10). At these high temperatures, photosynthetic activity may largely cease since stomata tend to close to avoid excessive transpiration. This may be further assisted by diminished leaf-level water availability. Furthermore, these periods occurred towards the end of the agricultural growing season when a large fraction of crops (esp. cereals) were already harvested and additional hay harvesting may have further reduced photosynthetic uptake by grasslands. This idea is supported by previous conclusions that the summertime surface sensitivity of both sites is dominated by crop- and grasslands and only to a lesser degrees by forests [Oney *et al.*, 2015]. We also observe a lag (~ 1 day) between increasing temperature and the biospheric response i.e. positive biospheric signals, which supports the notion that these environmental factors drive biospheric signal variation.

A closer, somewhat qualitative examination of the relationship between the biospheric residuals (obs1) and the environmental variables was carried out by fitting a non-parametric generalized additive regression model [GAM Wood and Augustin, 2002] to the biospheric residuals using the meteorological variables as predictors. This analysis was limited to specific meteorological situations (convective weather and afternoon values 1200–1500 UTC) in order to limit the influence of atmospheric transport and mixing on the observed biospheric residuals. The data from both sites were jointly analyzed in a single GAM, since similar response functions were expected at both sites due to their proximity. We observed the expected relationship between biospheric residuals and PAR with increasingly negative biospheric CO_2 signals with increasing PAR (Fig. 4.11). For 21-day-accumulated precipitation as a proxy for soil moisture the relationship was less clear but a tendency towards reduced biospheric activity under dry conditions appeared. With temperature, a form of threshold behavior was observed, where at 24-hour mean temperatures $> 20^\circ\text{C}$ the apparent terrestrial Swiss Plateau carbon sink turned into a net CO_2 source. This temperature is within the range of other studies that showed a drop-off of photosynthesis above a critical temperature of 30°C [e.g. Leuning, 2002], which may also be a bit low for a signal predominantly from grasslands. However, the combination of the acclimation

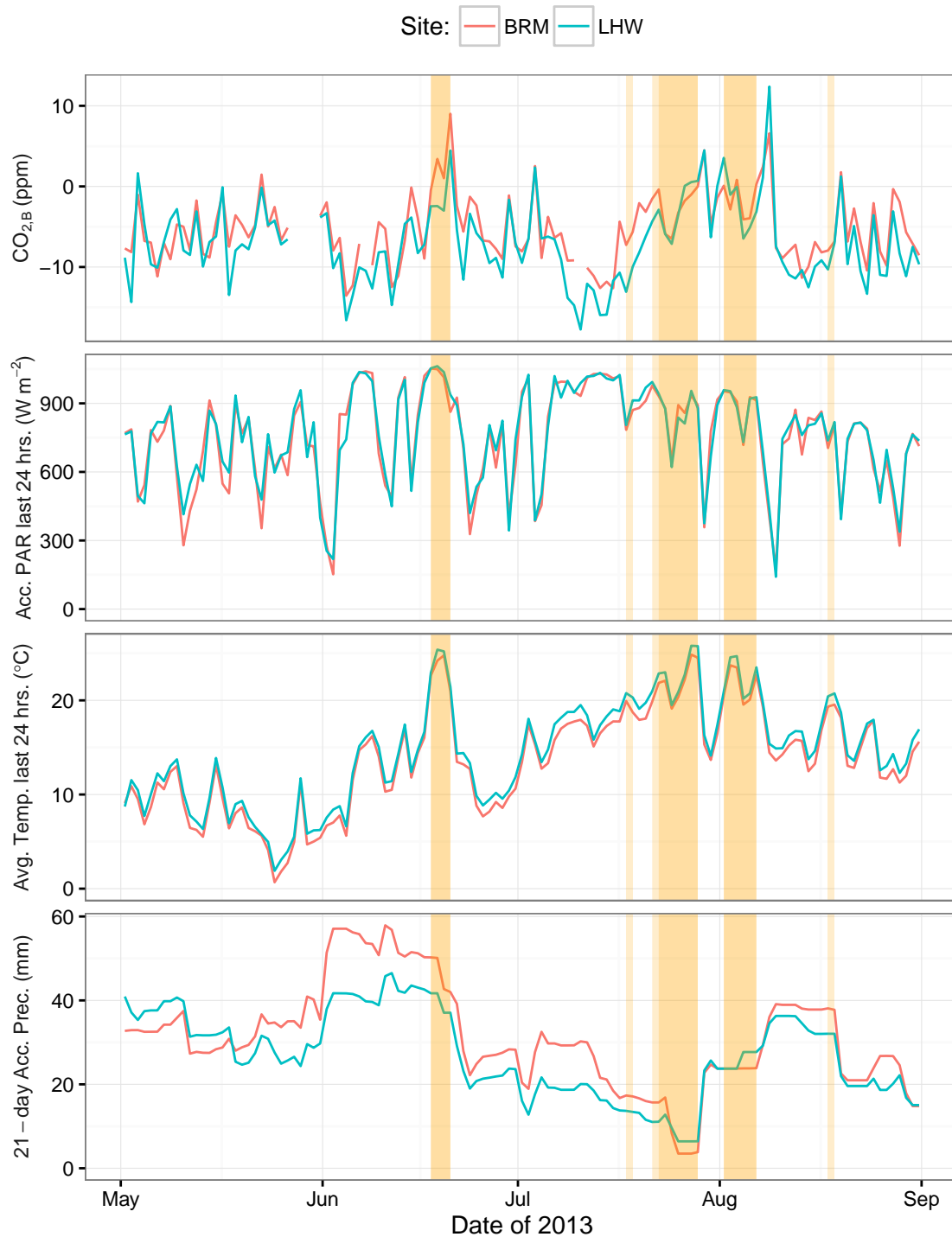


Figure 4.10: Observed afternoon (1200–1500 UTC) biospheric CO₂ signals (obs1) along with temperature (average of past 24 hours), photosynthetically active radiation (PAR) accumulated over the past 24 hours, as well as precipitation accumulated over the previous 21 days (as a proxy of soil moisture), during the main growing season (01 May–01 September) of 2013 interpolated from COSMO-2 analysis fields to the observation site positions, Beromünster and Lägern-Hochwacht at 250 m above model ground level. Shaded areas demarcate periods during which the average temperature of the preceding 24 hours was > 20°C.

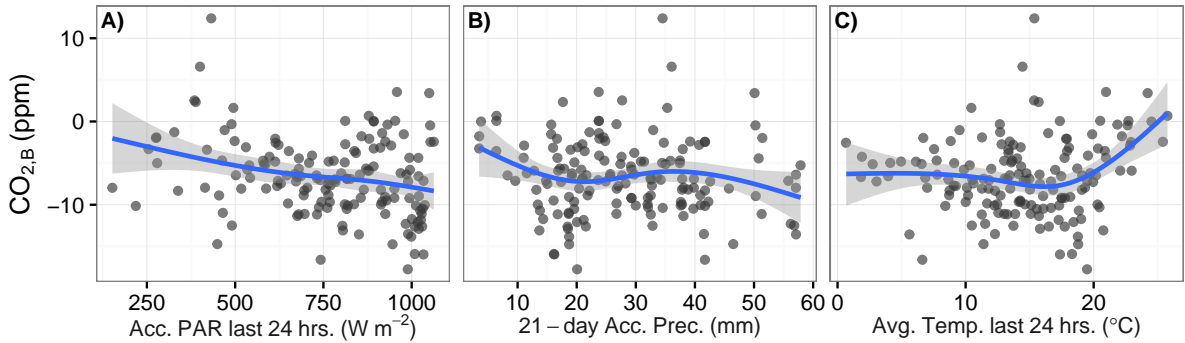


Figure 4.11: Response of observed afternoon (1200–1500 UTC) biospheric CO_2 signals (obs1) to modeled (described in Fig. 4.10) PAR, accumulated precipitation, and average temperature at both Beromünster and Lägern-Hochwacht during the growing season (01 May–01 September) of 2013. We narrowed our investigation to convective meteorological situations according to the categorization by *Weusthoff* [2011]. The blue line corresponds to a generalized additive model binned by the 95 % confidence interval.

of plants [*Kattge and Knorr*, 2007; *Groenendijk et al.*, 2011] to the cold spring, ensuing shock of a short but intense heatwave of June and ensuing sunny summer [*MeteoSwiss*, 2014] may help to explain these large and positive biospheric signals during a year with average temperatures [relative to 1981–2010 *MeteoSwiss*, 2014]. Furthermore, these observations may have also been influenced by co-occurrence of these high temperatures with agricultural harvests, particularly of hay.

4.6 Conclusions

We present a simple and effective method to derive the biospheric signal in atmospheric CO_2 mole fractions using co-located CO_2 and CO observations. Relative to many previous studies, where the biospheric signal was estimated by using model-based estimates of the background and the anthropogenic signals, this method circumvents the introduction of model transport error and inaccuracies of surface flux inventories into the residual biospheric CO_2 signals. The error in these two components might be as large as $\pm 20\%$ [*Peylin et al.*, 2011], which our method could substantially reduce. Nonetheless, a transport model would still be necessary in order to estimate the biospheric CO_2 surface fluxes from the observation-based biospheric signal. Therefore, considerable effort is still necessary to improve the skill of atmospheric transport models.

The observation-based methods (obs1 and obs2) using single annual $\text{CO} : \text{CO}_2$ apparent emission ratios performed well at our two CarboCount CH sites, but these ratios are site-specific and likely useful mainly for observation sites removed from large anthropogenic CO_2 and CO sources. Prominent examples of when these methods fail are when anomalous, large-scale pollution events with distinctly different emission ratios occurred. Emissions from large-scale biomass burning would cause an analogous situation. Furthermore, these large variations in the $\text{CO}_{2,A} : \text{CO}_A$ ratios would prevent the use of constant ratios. We expect that the methods using the time-dependent modeled $\text{CO}_{2,A} : \text{CO}_A$ ratios would perform better in environments where large variations in $\text{CO}_{2,A} : \text{CO}_A$ occur.

We emphasize the need to have consistency between CO and CO_2 inventories when developing the $\text{CO}_{2,A} : \text{CO}_A$ apparent ratio from model simulations [*Vogel et al.*, 2010; *Peylin et al.*, 2011]. Given a rigorously defined background CO and CO_2 signal, the proposed scaling of CO_A into $\text{CO}_{2,A}$ would provide a method compatible with regional carbon budget studies. This would offer the opportunity to evaluate both anthropogenic and biospheric flux inventories. Given both increasing and increasingly uncertain anthropogenic emissions

[Ballantyne *et al.*, 2015], this method might also provide an approach to monitor anthropogenic emissions, complementing the ¹⁴CO₂-based method [Gamnitzer *et al.*, 2006; Vardag *et al.*, 2015].

This study highlights the advantages of co-located CO₂ and CO observations. The observation of additional gas species useful in determining the background and anthropogenic signals will definitely improve the ability to estimate and understand the biospheric signal, and in the end hopefully reduce the uncertainty of the inversely estimated sources and sinks of atmospheric CO₂ over terrestrial systems. Because anthropogenic CO₂ emissions constitute the largest net CO₂ flux of Europe [Ciais *et al.*, 2010b], an emission verification system would bolster mitigation efforts. We therefore stress the need for co-located CO₂ and CO observations in such a verification system.

Acknowledgements

This study was funded by the Swiss National Funds (SNF) as part of the “CarboCount CH” Sinergia Project (Grant Number: CRSII2_136273). We acknowledge the use of the trace gas observations carried out by Martin Steinbacher, Empa, at the High Altitude Research Station Jungfraujoch run by the International Foundation (HFSJG), in the framework of the Integrated Carbon Observation System in Switzerland (ICOS-CH), SNF Grant 20FI21_1489921. We also acknowledge MeteoSwiss for the provision of their operational COSMO analysis products. We thank Christoph Gerbig for discussions, provision of the VPRM NEE flux data, and his very helpful comments on an earlier draft of this paper. We thank Frederic Chevallier for providing global CO₂ reanalysis fields (MACC-II, v13r1). The FLEXPART-COSMO simulations were conducted at the Swiss National Supercomputing Center CSCS. We also acknowledge MeteoSwiss for the provision of their operational COSMO analysis products.

Chapter 5

Synthesis and outlook

My work encompassed two major components of top-down surface carbon flux determination: atmospheric CO₂ mole fraction measurements and their simulation. My goal was to thereby contribute by using these observations with an atmospheric transport model to estimate the biospheric carbon flux of the Swiss Plateau. Toward this broader goal as a part of the CarboCount CH project, I have successfully:

- constructed and maintained the atmospheric carbon monitoring site Lägern-Hochwacht,
- described likely drivers of the variability observed at this and the other CarboCount network measurement sites,
- simulated observed CO₂ mole fractions using the high-resolution atmospheric model FLEXPART-COSMO of the site-wards transport of anthropogenic and biospheric carbon fluxes,
- investigated the relationship between CO and CO₂ observed at the Beromünster and Lägern-Hochwacht sites,
- employed this relationship to develop a technique to isolate the biospheric CO₂ signal based solely on observed mole fractions.

These larger tasks consisted of many smaller tasks and, in the process of completing these tasks, much was learned. Practical recommendations for future collaboration can be offered from this experience. Beyond that, future research tasks and directions informed by this work are also offered.

5.1 Summary

The measurement system at Lägern-Hochwacht was described in Chapter 2 and has performed reliably for more than three years now, except for a pump failure. The remaining CarboCount CH sites Beromünster, Gimmiz, and Frübüel have also performed very well, but had similar issues with the PICARRO suction pump. Overall, the CarboCount CH network provides precise and accurate atmospheric carbon observations that are within WMO-established quality guidelines [*Tans and Zellweger, 2014*] with excellent temporal coverage (> 95%). The reported uncertainties of these observations are taken from the target gas calibrations, because directly estimated uncertainties of the observations appear to be biased low. This is likely due to the insufficient accounting for the uncertainties introduced by the determination of cylinder mole fractions, the drifts in instrument baseline and sensitivity in between span calibrations, and/or the insufficient equilibration of gas concentrations after valve switching, or other unidentified sources of uncertainty. Further investigation

will be needed to better understand this discrepancy. But this also serves to emphasize the importance of target gas measurements.

In Chapter 3, the evaluation of the meteorology simulations highlighted various challenges for the atmospheric transport model at the different observation sites including the representation of topography-induced flows and the nocturnal boundary layer. Due to the site locations and the generally complex Swiss topography, the trend towards higher resolution is warranted here and would likely aid in reducing uncertainties related to atmospheric transport. This is especially true for the Lägern-Hochwacht observation site surrounded by steep topography, and for the site Frübüel located on a mountain plateau. Simulated nocturnal mixing appears to be overestimated in the analysis fields of the COSMO-2 model, which drive FLEXPART-COSMO. However, especially at Beromünster, the model simulations of wind and temperature are in excellent agreement with the observations on average as demonstrated by the comparison of wind roses and mean diurnal cycles. Furthermore, FLEXPART-COSMO surface sensitivity simulations at each site correspond to interpretations of the site's observations. Overall, it was found that COSMO and FLEXPART-COSMO are suitable tools to investigate carbon fluxes over the Swiss Plateau.

The observation site characteristics relevant to regional-scale modeling suggests that Beromünster and Lägern-Hochwacht provide observations useful for long-term carbon flux studies over the Swiss Plateau. These sites appear to be less sensitive to diurnal fluctuations due to their sampling above the nocturnal boundary layer. Furthermore, these sites have sufficient sensitivity to the entire Swiss Plateau. Sampling at high elevation appears to be an additional advantage in winter when the atmosphere is more stratified and, therefore, near-surface sites appear to be sensitive mostly to their immediate surroundings. Therefore, the near-surface sites Frübüel and Gimmiz provide observations that will need temporal filtering or may be used as evaluation sites, in that their observations are compared with simulations with inverted carbon fluxes, similar to *Henne et al.* [2016]. Despite its location in one of the most flat areas of Switzerland, Gimmiz turned out to be especially challenging due to a very stable nocturnal boundary layer that the model was unable to reproduce.

In Chapter 4, we developed and evaluated a CO-based method to determine the regional biospheric signal in atmospheric carbon dioxide using the observations of Beromünster and Lägern-Hochwacht. We found that the CO₂ mole fractions observed during the year of 2013 at the CarboCount network sites contained considerable anthropogenic signals, which, if not completely removed, would be mapped to the biospheric signals and thus biospheric fluxes. The regional biospheric signal is typically a small component of the observed CO₂ mole fraction relative to the combined large-scale background and regional anthropogenic emission signals. Isolating this signal is very challenging, and any errors in the quantification of the background and anthropogenic CO₂ components will translate into errors in the biospheric residual of CO₂ observations. Such errors could arise due to imperfectly known anthropogenic emissions, biases of background mole fractions, and/or inaccurately simulated atmospheric transport. However, we found that observations from Jungfraujoch provide information on background CO₂ and CO signals. Furthermore, the site's CO observations above these background signals provide information on regional anthropogenic CO₂ signals. These sources of information can thus provide an opportunity to circumvent the pitfalls associated with modeling the background and regional anthropogenic CO₂ signals, and allowing an observation-based derivation of the regional biospheric CO₂ signal.

Different approaches were taken to determine the biospheric CO₂ signals on the basis of CO₂ and CO observations. Determination of background signals was carried out with the “robust estimation of the baseline signal” (REBS) using data from the two sites as well as from Jungfraujoch. We found the choice of background site to be very important as it determines the spatial representativeness of the regional signals above the background and, thus, also the observed apparent anthropogenic CO/CO₂ ratio. The use of Jungfraujoch appears to be the best choice since the Jungfraujoch-derived background signals are similar to the modeled background. Furthermore, using the site's observations with the REBS method still yields good performance

but produces biospheric signals that appear to be of a scale smaller than the desired regional scale, and are thus less useful in this context. Except for a few events when cold, easterly winds brought anomalously CO-enriched air, the method outperforms the standard, model-based method deriving plausible, continuous biospheric signals.

Qualitative interpretation of the resulting biospheric signals indicate a biospheric carbon sink over the Swiss Plateau during the major growing season of 2013 (May to August). Furthermore, biospheric signals show a positive relationship with air temperature, where temperatures above a daily mean of $\sim 20^{\circ}\text{C}$ may correlate with a weakened Swiss Plateau carbon sink. Although the weather during 2013 was average relative to the climate of 1981–2010, the early winter and spring months were cold, and were followed by a hot summer. It is possible that Swiss Plateau vegetation had acclimated to cold spring temperatures, which were followed by hot summer weather to which the vegetation was not acclimated. This warm weather may have played an important role, but also likely coincided with agricultural harvests.

5.2 Lessons learned

The multifaceted work of environmental science in general and carbon cycle science in particular entails the management of many technical details and pitfalls. These seemingly (or scientifically) unimportant aspects may finally require the most attention or, in some cases, skew results. Exchange with more experienced researchers has inevitably saved both time and frustration. A selection of these lessons learned are offered here.

Data acquisition from the field needs to be continuous, automated, and occur within a short period (< 1 day) of collection in the field. Automated data quality checks helped to assure good temporal coverage. Yet, dedicated personnel contributed most to good temporal coverage of data by maintenance, and facilitating the exchange of experience and knowledge.

Reliability of field-deployable measurement devices is paramount to reducing costs of long-term carbon cycle observation. We second the experiences of *Richardson et al.* [2012] with PICARRO devices, but with one caveat. From our experience, PICARRO pumps are not very reliable and should be used solely as an ersatz, regardless of improvements claimed by PICARRO. The current KNF pump (see Table 2.3) has as of now operated for 3 years without issue. At the very least, a readily available replacement pump is necessary in case of failure, similar to the broader modular system described in *Andrews et al.* [2014].

As *Leuenberger et al.* [2015] have demonstrated, steel cylinders are not suitable for long-term storage of greenhouse gases, as mole fractions need to be known with high accuracy and exhibit high stability over time. Based on the recommendations from the in-house GAW World Calibration Center (Zellweger and Steinbacher, pers. comm.), we have employed aluminum cylinders, and can further give this recommendation. However, we have yet to remeasure all reference gas cylinders within the project. Specifically, slow mole fraction drifts, especially in CO, have also been observed in aluminum cylinders in the past (Zellweger and Steinbacher, pers. comm.).

The measurement system at Beromünster is by far the most sophisticated of those developed within the project. It can sample multiple heights within an hour's time, has an additional separate set of sampling lines, and can sample a large number of standard reference gases [*Berhanu et al.*, 2016]. The comparatively simple setup at Lägern-Hochwacht nevertheless resulted in reliable and accurate measurements with much lower maintenance requirements and lower initial costs. The setup included a simple box for switching between reference gases and ambient air, with no external computer but direct control of valves and operation modes through the PICARRO instrument, only three reference gas bottles with high and low standards and a target, and a simple USB stick for broadband data transmission. Such a setup could be a valuable model for the

operation of low-cost sites, complementing the more challenging and expensive setup required, e.g., for sites of the ICOS network.

Atmospheric transport models driven offline, i.e. with external meteorology, can offer improvements in accuracy and computational efficiency of transport simulations. Offline transport simulations require accurate driving meteorology which needs evaluation. Analysis meteorological fields, having been corrected to better agree with observations, may contain artifacts introduced by the assimilation procedure. Although unpublished, the COSMO-2 wind fields, which were evaluated in Chapter 3, are analysis fields which record an instantaneous snapshot of wind every hour. Visual inspection of these high-resolution wind fields near the ground reveals anomalously strong variations in the vertical wind component. When used to drive FLEXPART-COSMO simulations, this resulted in too strong mixing and, as a consequence, in the regional transport simulations, which greatly underestimated regional signal strength. Two solutions to minimize this problem were to use coarser resolution (0.06° versus 0.02°) meteorological fields, as was done in Chapter 4, and, for future studies, to use time-averaged instead of instantaneous meteorological fields. Here, caution is warranted and evaluation of offline meteorological fields is necessary.

Much of the work of this project was done devising and implementing computer-based programs to prepare data, run simulations, and analyze and visualize results. Shared computing facilities for project members helped to facilitate collaboration and to increase efficiency of computer resource use. Large data sets, such as driving meteorology, had only one centralized copy. Furthermore, resource use could be monitored which can lead to better support of scientific work. Debugging of large computer programs was also facilitated by the common computer architecture. Common computing facilities carries numerous advantages.

The carbon cycle is least understood on time-scales greater than one year, but this does not correspond to the typical time-scale of research. Throughout these experiences, two recurring themes appear and center around the necessity of long-term carbon cycle observation and research. The two pillars of measurement and modeling require both long-term infrastructure and dedicated personnel. These are critical for success in unraveling and understanding the carbon cycle on the regional scale. However, short-term research projects, such as CarboCount CH, GAUGE [Pitt *et al.*, 2016], CarboEurope [Dolman *et al.*, 2006], Mid-Continental Intensive campaign [Miles *et al.*, 2012], have helped to guide long-term infrastructure and research such as ICOS and the US tall tower network. Furthermore, tall tower “super sites”, where many chemical and meteorological variables are observed, are appearing as a critical element of long-term observation, but are too expensive and impractical for these guiding short-term projects. However, a site’s placement and equipment needs careful deliberation, for which such short-term projects are well-suited.

5.3 Outlook

The complexity of the land surface flux dictates many different approaches, all of which can be improved. Prioritizing which approach should be addressed next is difficult and is best informed by experience. The following outlook offers future research tasks and directions which, in my view, will lastingly advance the state of carbon cycle science of the Swiss Plateau.

The interplay between observational and modeling studies drives carbon cycle research. CarboCount CH represents one of the first interdisciplinary projects to tackle the Swiss carbon balance and has laid the foundation for future observational and modeling studies. Continued, long-term Swiss monitoring efforts such as the ICOS-CH (<http://www.gl.ethz.ch/research/bage/icos-ch.html>) are facilitated by the modeling expertise of the Center for Climate Systems Modeling (C2SM) at the ETH Zurich, for example. Furthermore, the experience and infrastructure observing the carbon cycle has been augmented by the CarboCount CH project through its network. Hopefully, future studies will continue to be highly interdisciplinary.

The regional-scale simulation of CO₂ mole fractions requires great effort to represent lateral boundary conditions and surface fluxes, as well as atmospheric transport modeling. This thesis details the tremendous work put into this task. The performance of the “standard method” in simulating observed CO₂ concentrations is encouraging, and demonstrates the ability of FLEXPART-COSMO to simulate atmospheric transport, the accuracy of the Swiss emissions inventories, and the potential of the relatively simple VPRM model. Although improving the accuracy of these surface fluxes is beneficial, improving the accuracy of atmospheric mixing of COSMO and FLEXPART-COSMO would likely yield the greatest benefit to future biospheric flux inversion studies.

Land-to-atmosphere flux datasets contain a great deal of spatial and temporal information. However, these data are necessarily aggregated to reduce for the high complexity of landscapes and the associated carbon fluxes. Prioritizing inclusion of further the biospheric and anthropogenic surface flux processes for Switzerland would likely include agricultural carbon fluxes. Crop models of varying complexity “grow” crop vegetation given environmental input such as sunlight, temperature, precipitation, and/or fertilizer. The Community Land Model (CLM) has such a crop scheme [Levis *et al.*, 2012], which is being actively developed and increasingly used [Drewniak *et al.*, 2013; Bilonis *et al.*, 2015; Lu *et al.*, 2015]. Within the CarboCount CH project much effort has gone into efficiently coupling CLM to COSMO and, in a next step, this system should be further developed to simulate agricultural carbon fluxes over the Swiss Plateau. As indicated in Chapter 3, local fluxes, possibly those of nearby vegetable crops, likely explain the highly enriched CO₂ observations at Gimmiz. Furthermore, approximately 4 Tg a⁻¹ of Swiss agricultural primary production are reported [Meyre, 2016], not including what is left on the field. Given a composition of approximately 5 % elemental carbon (from ~90 % water content and ~50 % C of dry mass), this amounts to approximately 200 Gg C harvested and transported away from fields. This is a significant number which warrants further investigation and refinement, and would likely improve accuracy of surface flux data sets, and by extension CO₂ mole fraction simulations.

The proposed method of scaling CO above a background CO signal into anthropogenic CO₂ depends on having an accurate apparent anthropogenic CO/CO₂ ratio, but this ratio is known to vary with time. Using time-dependent modeled ratios to account for this variability did not significantly improve the performance of this method, but it appears that this is due to uncertainties in the emissions inventories or atmospheric transport. Improving the accuracy of anthropogenic emissions inventories of CO and CO₂, both in spatial distribution and temporal signature, along with improved atmospheric transport simulations, would likely help to better understand the anthropogenic CO₂ signal.

Carbonyl sulfide observations, a tracer of stomatal exchange, would offer an independent alternative method to evaluate these observation-based biospheric signals. The Beromünster observation site with its multiple sampling heights would provide ideal observations to test whether the observation-based biospheric signals still contain anthropogenic CO₂ signals. Given this infrastructure, this could be carried out long-term and would likely help to improve the accuracy of this method.

Looking ahead, the application of this method to the observations from 2013 to 2015 helps to illustrate the variable response of vegetation to weather (Figure 5.1). The weather (cold spring and hot summer) of 2013 was anomalously variable although it averaged to be normal. The following growing season was opposite; it was preceded by a very warm winter and the high temperatures continued through the spring but were followed by a relatively cold and extremely cloudy and wet summer during 2014 [MeteoSwiss, 2015], during which less negative biospheric signals, i.e. weaker photosynthesis, were observed. Small-scale, eddy covariance observations have however observed the opposite; that is, diffuse radiation correlated with higher photosynthesis and thus NEE [for forest ecosystems Law *et al.*, 2002]. Further work is necessary to illuminate this contradiction.

During the very warm growing season of 2015 [MeteoSwiss, 2016], the vegetation across the Swiss Plateau

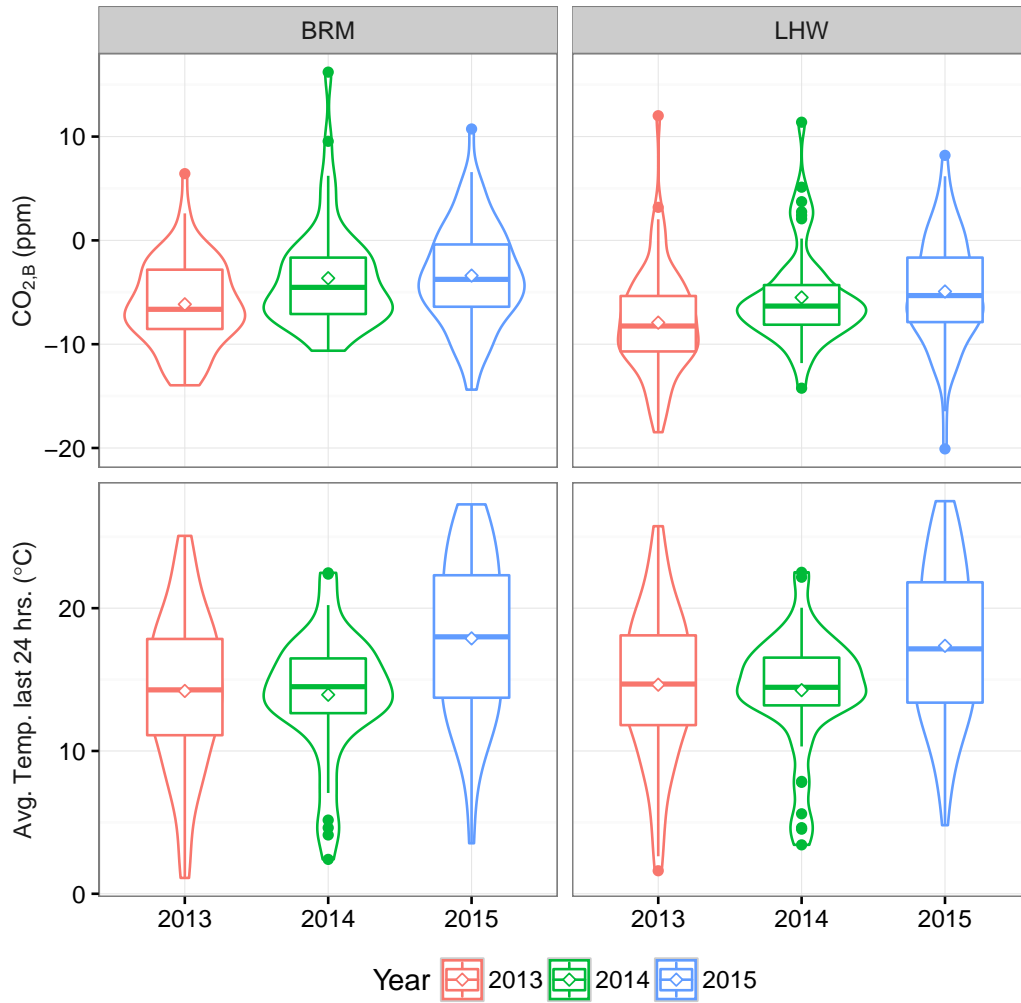


Figure 5.1: Distributions of observed afternoon (1200–1500 UTC) biospheric CO₂ signals (obs1) and observed average temperature (of the preceding 24 hours) at both Beromünster and Lägern-Hochwacht during the growing seasons (01 May–01 September) of 2013–2015. Observations shown are only during convective meteorological situations according to the categorization by *Weusthoff* [2011].

does not appear to have grown very well in the warm and sunny weather during spring and summer or ecosystem respiration appears to have increased enough to offset CO₂ uptake. Assuming that these interannual differences between the biospheric signals represent the effect of differing weather conditions on vegetation, the connection between higher temperatures and more positive biospheric signals, related to a weaker carbon sink, is apparent but is not very robust and varies between years and sites (Figure 5.2). Specifically, comparing the observed regional biospheric signals of 2014 and 2015 with 2013, we see highly positive CO₂ signals of both colder and wetter, and hotter and drier growing seasons of 2014 and 2015, respectively, relative to 2013 (Figure 5.1). Yet, when we correlate observed temperature with biospheric signals (Figure 5.2) in an approach similar to that detailed in Chapter 4, no robust pattern appears. Why do we observe these varying responses of biospheric CO₂ to changing temperatures? This likely means that simply correlating the biospheric CO₂ signal with local temperature is a poorly suited approach to understand observed biospheric signal variability, but also hints at the complexity of the relationship between weather and carbon fluxes.

Further analysis will likely shed light on these highly variable observations. Finally, it is questionable whether these biospheric signals contain biases. Accompanying model studies may reveal this possible caveat, and, although the observation-based approach to deriving biospheric CO_2 signals presented here was found to be valid in Chapter 4, further model work and/or carbonyl sulfide observations would help to evaluate these biospheric signal estimates.

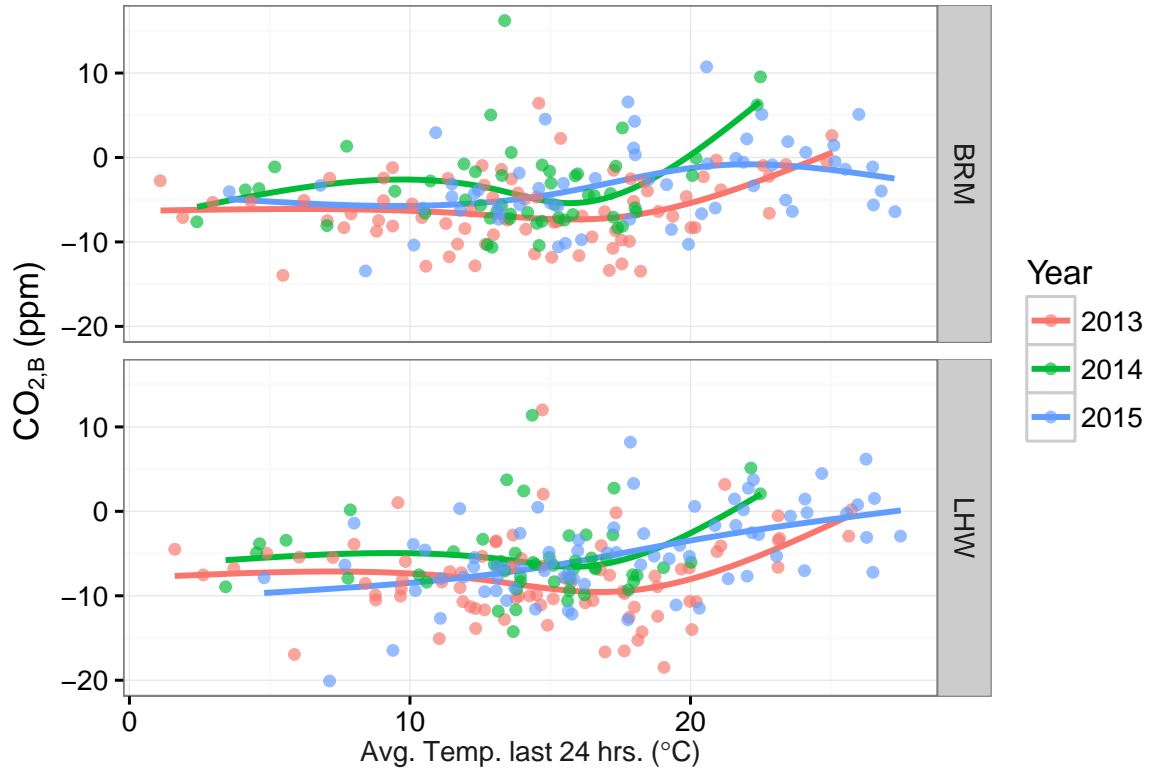


Figure 5.2: Response of observed afternoon (1200–1500 UTC) biospheric CO_2 signals (obs1) and observed temperature averaged of the preceding 24 hours at both Beromünster and Lägern-Hochwacht during the growing seasons (01 May–01 September) of 2013–2015. Observations shown are only during convective meteorological situations according to the categorization by *Weusthoff* [2011].

Gimmiz observes large variability mainly due to ABL dynamics and potentially large surface carbon fluxes. Although certainly difficult to reproduce, these observations could provide a benchmark for regional-scale carbon flux modeling of the Swiss Plateau. *Eugster and Siegrist* [2000] first documented nighttime accumulation and identified mesoscale airflow as the main driver of this variability. Given observed wind speeds, it is unlikely that mesoscale transport of atmospheric carbon can explain the strong accumulation at night which consistently results in an increase of several hundred ppm CO_2 . It is more likely that a shallow and stable nocturnal ABL combined with local, potentially large carbon fluxes causes this. Preliminary studies within this project have indicated that current surface flux inventories and atmospheric transport models largely underestimate nighttime observations. Surface sensitivity simulations indicate that surface fluxes in the Seeland are mostly responsible for this variability. This translates into a considerable amount of atmospheric carbon that accumulates in the nocturnal ABL in the Seeland, which we currently cannot explain. This discrepancy may be due to the atmospheric transport model overestimating nighttime vertical mixing. Significant progress appears to be forthcoming in the form of an improved turbulence scheme in COSMO, which greatly improves nighttime vertical mixing [*Raschendorfer*, 2016]. Furthermore, the nocturnal radiosondes at Payerne provide

considerable information that would aid in evaluating mesoscale airflow in the employed transport model and thereby the interpretation of the highly variable observations at Gimmiz. Therefore, it would be fruitful to carry out an intense observation campaign in order to best guide the placement of a long-term monitoring site in or near the Seeland. Furthermore, a tower sampling multiple heights would help to uncover and hopefully understand any problems in simulating observed vertical structure of CO₂ mole fractions.

Beyond carbon budgeting, the goal of understanding the relationship between the regional carbon cycle and climate presents a very difficult problem. A biospheric model must be calibrated to reproduce flux and/or mole fraction observations together with an atmospheric transport model. Here, the VPRM showed promising ability to simulate the biospheric signal and should be simple enough to calibrate in a transparent manner, which would aid understanding the carbon cycle-climate relationship. However, in its current implementation in CarboCount CH, it is driven by coarser ECMWF meteorological output, which has different topography and, most importantly, different land cover. This product is then reprojected to a higher resolution COSMO domain and its influence is simulated. Thereby, an uncertainty of scale mismatch is unnecessarily introduced, where the meteorology that drives the surface fluxes differs from the meteorology that drives transport. In a peer review of *Kountouris et al.* [2015], *Michalak* [2015] warns of the consequences of introducing such uncertainties into inverted fluxes. Such an error can also easily be made with Lagrangian transport models, where the surface sensitivity output and flux inversion grid can be flexibly defined, thereby creating a mismatch of scales. Given the simplicity of VPRM, implementation within COSMO and even FLEXPART-COSMO, such as in STILT-VPRM [*Matross et al.*, 2006; *Pillai et al.*, 2012], should not be too difficult. This attention to the spatial consistency between driving meteorological input and the flux inversion grid would help to avoid this problem.

To sample the Swiss Plateau, the Beromünster site would likely suffice and would thus greatly contribute to the Swiss ICOS network (<http://www.gl.ethz.ch/research/bage/icos-ch.html>). Jungfraujoch has been integrated in ICOS-CH, but its observations contain information from far beyond Switzerland and even beyond Europe [*Henne et al.*, 2010]. Beromünster, on the other hand, has been shown to cover the Swiss Plateau throughout the year, and, containing landscapes similar to most of central Europe, arguably provides a greater amount of information about European surface fluxes. Furthermore, global inversion efforts, such as CarbonTracker, would likely be able to integrate atmospheric carbon observations from Beromünster. Finally, from what we found, future atmospheric carbon monitoring efforts should benefit from measuring CO and CO₂. We have shown this method to be an advantageous approach to avoid introduction of uncertainties from model transport and anthropogenic emission inventories. The interpretation of the biospheric CO₂ signals since 2013 (Figure 5.1) provides insight into the complex relationship between biospheric activity and weather, and the challenges along the path of understanding terrestrial carbon fluxes on longer time-scales.

Appendix A

Measurement data processing code

A.1 Introduction

This document describes the technical aspects of the processing and calibration of the trace gas measurement data collected as part of the SNF Sinergia Project CarboCount CH (<http://carbocount.ch/>).

A.1.1 Site- and time-specific valve information

The following tables hold the information about the valve positions of the measurement system at each site. Specifically, what was measured **from** the date of the table, until the next table. For example, the first table with the date "2012-08-23-140000" in the section title is valid for the site Laegern from 2012-08-23 at 2 p.m. until the next table (when I replaced a bottle) dated 2012-09-28 replaces the valve information. See Table A.2 for another example. The R-function `check.site.info` efficiently checks whether the site information held with in the R-object `site.info` is valid for the particular date and time. The naming of the files must be (in POSIX notation) `SiteInfo-%Y-%m-%d-%H%M%S.csv`.

A.1.1.1 Example: SiteInfo-2014-08-21-090000

A.1.2 Site- and time-specific measurement device and calibration information

The following tables hold the information about the measurement devices at the respective measurement sites. Similar to the **SiteInfo-*** files/tables (see Table A.1), a table is valid after the date-time held in the file name, until the next table. For example, the first table with the dated name "SiteDeviceInfo-2012-08-23-140000" in the section title is valid for the site Laegern from 2012-08-23 at 2 p.m. until the next table (when the first successful span calibrations at Lägern-Hochwacht were carried out) dated 2012-11-19 replaces the calibration and measurement information. Another example, is the different measurement device placed at Beromünster after failure of the measurement system and before the reinstallation of the primary device. This information is handled and recognized with the R-function `check.device.info`, which efficiently checks whether the site information held with in the R-object `site.device.info` is current. Table A.1 is an example of the such information. Similarly, the naming of the files must be (in POSIX notation) `SiteDeviceInfo-%Y-%m-%d-%H%M%S.csv`, and these are in CSV-format, without quotes. These files can be found in: `/remote2/CarboCountCH/CarboCountDB/Documentation/` and are also under version control.

Table A.1: The latest table (`site.info`) from 2014-08-21 at 09:00:00 UTC, Ruediger Schanda changed the CO high bottle at Gimmiz. This table is written out by this org-mode (emacs) document with R as `SiteInfo-2014-08-21-090000.csv` in the directory where this file resides. NA stands for ‘not available’.

site	type	height	valvepos	nsecskip	duration	bottle
Laegern	work	NA	24	540	900	CB09862
Laegern	high	NA	17	540	900	CB09870
Laegern	low	NA	18	540	900	CB09881
Laegern	meas1	32	0	540	NA	NA
Fruebuel	work	NA	9	540	900	CB09886
Fruebuel	low	NA	10	540	900	CB09789
Fruebuel	high	NA	12	540	900	CB09884
Fruebuel	meas1	4	0	540	NA	NA
Beromuenster	work	NA	1	120	180	LK542087
Beromuenster	high	NA	2	240	360	CB09863
Beromuenster	low	NA	3	240	360	CB10095
Beromuenster	targ	NA	4	120	180	CB09890
Beromuenster	meas1	212	5	120	180	NA
Beromuenster	meas2	132	6	120	180	NA
Beromuenster	meas3	72	7	120	180	NA
Beromuenster	meas4	45	8	120	180	NA
Beromuenster	meas5	12	9	120	180	NA
Beromuenster	meas6	0	11	120	180	NA
Beromuenster	extra1	NA	12	120	NA	NA
Beromuenster	extra2	NA	13	120	NA	NA
Gimmiz	work	NA	1	420	540	CB09873
Gimmiz	high	NA	2	420	540	CB09861
Gimmiz	low	NA	3	420	540	CB09885
Gimmiz	targ	NA	4	420	540	CB09787
Gimmiz	meas1	32	5	720	NA	NA
Gimmiz	COhigh	NA	6	300	600	CB09872
Gimmiz	COlow	NA	7	300	600	556359
Gimmiz	COmeas	32	8	360	NA	NA

A.1.2.1 Example: SiteDeviceInfo-2014-04-29-093800

A.2 Data Processing and Management

Data come from PICARRO, HORIBA and meteorological sensors as raw data in both uncompressed (*dat and *TXT) and compressed (*ZIP or *TXT.gz) form. Furthermore, the R-code needs to be able to account for the repetition of the data within multiple-channel PICARRO (G2401, G2311-f and G2301) data files. The PICARRO devices vary within and across models but range between 20 (G2301) and 30 (G2311-f) measurements per minute (0.3–0.5Hz) per species. That is, to calculate the means and uncertainties correctly, one needs to use the data which are only from the measurement of a particular gas, which are repeated in PICARRO output, as indicated by the `species` column.

A.2.1 Data processing code

The data processing code is a set of `bash`-scripts and R-functions the latter of which are organized and documented in the custom R-package `ccchDataProc` (see below). General functions handle every site, for a common interface. The initial reading of data is the only exception to this where site-specific code is used.

Table A.2: The latest measurement device and calibration information from 2014-04-29 at 09:38:00, when the normal device at Beromünster was put back into service, replacing the ersatz G2311-f. This table is queried when calibration parameters are calculated (defining the calibration type) and raw data are checked to see whether they are feasible (*e.g.* is CO₂.dry > 6?). For example, this table is written out by this org-mode document with R as `SiteDeviceInfo-2014-04-29-093800.csv` in the directory where this file resides. NA stands for ‘not available’.

site	id	gas_name	limit	cal_type	Device	meas_per_min
Laegern	1	CO2.dry	6	p2.f	CFKADS2043	24
Laegern	2	CH4.dry	0.006	p2.f	CFKADS2043	24
Laegern	4	CO	0.006	p2.f	CFKADS2043	24
Laegern	3	H2O	0.05	NA	CFKADS2043	24
Fruebuel	1	CO2.dry	6	p2.f	CFADS2256	20
Fruebuel	2	CH4.dry	0.006	p2.f	CFADS2256	20
Fruebuel	3	H2O	0.05	NA	CFADS2256	20
Beromuenster	1	CO2.dry	6	p2.f	CFKADS2038	24
Beromuenster	2	CH4.dry	0.006	p2.f	CFKADS2038	24
Beromuenster	4	CO	0.006	p2.f	CFKADS2038	24
Beromuenster	3	H2O	0.05	NA	CFKADS2038	24
Gimmiz	1	CO2.dry	6	p2.f	CFADS2255	20
Gimmiz	2	CH4.dry	0.006	p2.f	CFADS2255	20
Gimmiz	3	H2O	0.05	NA	CFADS2255	20
Gimmiz	4	CO	0.006	p2.f.h	HORIBA_A360	60

An overview of the main scripts is presented in Table A.3.

The executables in Table A.3 are called automatically as cron jobs on the GNU/Linux workstation ddm04326. The current configuration of the cron jobs is as follows:

```
# --- CarboCount Processing chain
R_PROFILE=~ /Documents/Conf_files/R/Rprofile.site
LOGS=/remote2/CarboCountCH/logs
SRC=/remote2/CarboCountCH/CarboCountDB/scripts
# Update CarboCount Database
6 5 * * * $SRC/R/processRawData.R >> $LOGS/db_`date +%F`.log 2$>$&1
# Update Quicklooks
9 6-23 * * 1-6 $SRC/R/plotQuicklooks.R >> $LOGS/quicklooks_`date +%F`.log 2$>$&1
# operational calibration
12 6 * * 6 $SRC/R/runCalibration.R >> $LOGS/calibration_`date +%F`.log 2$>$&1
# Sync ftp
6 * * * * $SRC/bash/sftp_sync.sh >> $LOGS/sftp_`date +%F`.log 2$>$&1
# Check if we are receiving the necessary data and if they are healthy
9 */3 * * * $SRC/R/checkRawData.R >> $LOGS/checkData_`date +%F`.log 2$>$&1
# Organize and rezip Bern data
14 4 * * 6 $SRC/bash/organizeBeromuenster.sh >> $LOGS/bern.dataOrg_`date +%F`.log 2$>$&1
16 4 * * * $SRC/bash/organizeGimmiz.sh >> $LOGS/bern.dataOrg_`date +%F`.log 2$>$&1
# Organize and gzip Fruebuel Data
9 4 * * * $SRC/bash/organizeFruebuel.sh >> $LOGS/eth.dataOrg_`date +%F`.log 2$>$&1
# Gzip Laegern Data
10 4 * * * $SRC/bash/organizeLaegern.sh >> $LOGS/empa.dataOrg_`date +%F`.log 2$>$&1
```

Table A.3: The scripts use to control the execution of database organization, updates and evaluation.

Script	Description
processRawData.R	initialize processing; coordinates R-function: <code>DatabaseControl</code>
runCalibration.R	initialize calibration; coordinates R-function: <code>CalibrateControl</code>
plotQuicklooks.R	initialize plotting of the latest data; coordinates: <code>quicklooks</code>
checkRawData.R	coordinates <code>emailNotify</code> , which checks on data presence and size
sftp_sync.sh	get the data from the sftp
organizeBeromuenster.sh	organize and compress files retrieved from the sftp for Beromünster
organizeGimmiz.sh	organize and compress files retrieved from the sftp for Gimmiz
organizeFruebuel.sh	organize and compress files retrieved from the sftp for Fräebüel
organizeLaegern.sh	organize and compress files from the sftp for Lägern-Hochwacht
cleanup_Beromuenster.sh	remove old, archived files on sftp from Beromünster
cleanup_Gimmiz.sh	remove old, archived files on sftp from Gimmiz
cleanup_MeteoSchweiz.sh	remove old, archived files on sftp from MeteoSwiss

A.2.2 Traceability

Record of bad measurements as defined in Table 2.4 (>128) are kept within the site-wide CSV file, which has the site name, the time period and the reason for complete omission of measurement or calibration values. Complete absence of data for a day is also recorded. These records reside in this directory in the files:

- `Site-BadMeasurements.csv`
- `Site-BadCalibrations.csv`
- `Site-NoMeasurementDays.csv`

A.2.3 Processing Sequence to One-minute Averages

The processing procedure for greenhouse gas measurement data is done once for each site. In the below notation, the programming environment is noted first and a directional reference indicates a script (filename) being executed and the worker function being called, which calls other worker functions.

1. Data are (re-)compressed to a gzip-format.
 - sh: `organizeBeromuenster.sh`, `organizeGimmiz.sh`, `organizeFruebuel.sh`, `organizeLaegern.sh`
2. Initialized by the run-script `processRawData.R`, raw data are read from disk.
 - R: `processRawData.R` \rightarrow `ingestRawData`
3. Data in the valve transition period (`nsecskip`) are removed and measurement and calibration data are separately organized
 - R: `ingestRawData` \rightarrow `organize_daily_data`
4. Ambient measurements are checked for plausibility (see Table A.1).
 - R: `ingestRawData` \rightarrow `organize_daily_data` \rightarrow `check_measured_signal`
5. Ambient measurement data are summarized per minute and saved per day.
 - R: `ingestRawData` \rightarrow `organize_daily_data` \rightarrow `average_daily_data_to_one_minute`

6. Calibration data are saved in raw form per calibration.

- R: `ingestRawData` \rightarrow `save_standard_gas_measurements`

7. Calibration procedure is initialized.

- R: `runCalibration.R` \rightarrow `calibrateData`

8. Standard gas measurement data are summarized and surveyed and possibly flagged: updates or redoes the site's calibration database: `site-CalibrationDatabase.csv`

- R: `calibrateData` \rightarrow `update_calibration_database` \rightarrow `ingest_standard_gas_measurements`
`check_basic` \rightarrow `check_device` \rightarrow `check_measured_signal`
- R: `calibrateData` \rightarrow `plot.and.flag.cal.db`
- R: `calibrateData` \rightarrow `flag.cal.from.db`

9. Calibration parameters/coefficients are calculated: updates or redoes the site's calibration parameter database: `site-CalibrationParameterDatabase.csv`

- R: `calibrateData` \rightarrow `update_calibration_coefficient_database` \rightarrow `cal_3point`, `cal_2point`, `p3_o`, `p2_f`, `p1_z`, *etc.*

10. Target measurements are calibrated: updates or redoes the site's target calibration database: `site-TargetCalibrationDatabase.csv`

- R: `calibrateData` \rightarrow `checkTargets` \rightarrow `apply_calibration_data`

11. Measurement data are calibrated and flagged data (>16) are removed

- R: `calibrateData` \rightarrow `check_extreme_signal`
- R: `calibrateData` \rightarrow `apply_calibration_data`
- R: `calibrateData` \rightarrow `insert_target_uncertainty`

A.2.4 Automatic application of flagging system to ambient and calibration measurements

The ambient water concentration, and the carbonic gas concentrations also have lower limits. These constraints are summarized in Table A.4 and are removed and the abnormalities are saved in the `Site-Bad*.csv` files, depending on the operation mode.

A.2.5 Manual application of flagging system to ambient and calibration measurements

Where the R run scripts reside (`/remote2/CarboCountCH/CarboCountDB/scripts/R/`), there is also an interactive R-script with the names `manual.data.inspection.R`, where the averaged ambient measurement values are inspected and code therein records anomalies in: `Site-BadMeasurements.csv`.

Table A.4: The limits for standard gas and ambient greenhouse gas measurements. For exact numbers, please see Table A.1.

Variable	Limits	Unit	Application
H ₂ O	< 0.06	%	Raw trace gas concentration measurements.
CO ₂ -dry	< 6	ppm	
CO	< 0.006	ppm	
CH ₄ -dry	< 0.006	ppm	

A.2.6 The R-package `ccchDataProc`

A custom R-package was written for this project and is well-documented. Several programmatic ideas guided the development of this package. Except for the scripts mentioned above as run scripts, the focus has been on functional programming. The local paths for data input and output as well as time-dependent site descriptions (`site.info`) are held within the R-data file specific to this package `data(ccchData)`. There have been no package-specific classes defined. The section below describes the functions that can be found in the `R/` sub-directory of the package as R-source files. Often the main functions mentioned reside in a file with the same name.

A.2.6.1 R-functions for processing data

In order to run code and process data, one needs to source the R-file `config.ccchDataProc.R` for the below code to work OR install and load R-package `ccchDataProc` with `library(ccchDataProc)` as well as the data from the package `data(ccchData)`. See the R-script `processRawData.R` for an example. The R-help is thorough.

General code

- `config.ccchDataProc.R` script with various site-specific data and reads in all below functions
- `miscFunctions.R` **many** miscellaneous important functions from reading PICARRO files to lengthening vectors.
- `retrieve.site.information.R` functions to retrieve site-specific data such as:
 - `check.site.info` updates the `site.info` `data.frame` which contains information regarding changes in valve position *etc.*
 - `check.device.info` updates the `site.device.info` `data.frame` which contains info regarding the measurement devices, and gas-specific calibration strategy/routine.
- `tools.flagging.R` data quality assessment and recording functions
- `getFileInfo` retrieve the file's information along with the time stamp, which is deduced from the file name.
- `bern.data.processing` handle the Bernese data formats and problems

Plotting

- `quicklooks` for plotting the default quicklooks for the CarboCount CH project.
- `interactive.plots.R` contains functions for plotting the measurement data.
- `plot.cal.databases.R` contains functions for plotting the calibration data.

Diagnostics

- `emailNotify_dat.size.and.presence` checks on the presence and size of raw PICARRO files being received hourly from sites. This is only true for Früebüel and Lägern-Hochwacht, and of course only checks for those sites. The run script is in the R directory.
- `Gap.check` checks whether the averaged data correspond to the available **raw** data.

Higher Time Aggregates and Associated Uncertainty

- `tools.TS.R` contains functions such as: `Summary.gases.meteo` *et al.* which aggregate data over arbitrary periods.
- `ingestRawData` This function initially processes raw data for each site, taking care of averaging of measurement data and organizing calibration data.
- `organize_daily_data` takes the `nsecskip` into account and removes valve transition data accordingly
- `average_daily_data_to_one_minute` function for averaging over one minute intervals. The functions in the `picarro.summary.R` R-script *e.g.*
- `picarro.meas.summary` *et al.* are used to calculate the means and uncertainties while accounting for the repetition of the data within PICARRO *.dat files.
- `save_standard_gas_measurements` takes the calibration data and saves an accordingly named file for **each** calibration type.
- `calibrateData` This function coordinates summary of the calibration data, application to target (`targets_check`) and ambient measurements.
- `tools.calibration.R` contains functions to find span (high and low) and target gas measurements, as well as calibration functions for two-point calibrations *etc.* handling each site, situation and trace gas with zero-intercept and offset calibration capabilities.
- `cal_3point` span free-intercept, zero-intercept and offset calibration.
- `cal_2point` two-point free-intercept and zero-intercept calibration.
- `cal_1point` zero-intercept calibration.
- `update_calibration_database` reads in (new) calibration data for each site.
- `ingest_standard_gas_measurements` process raw calibration data, output is: mean, uncertainty, standard deviation, number of measurements.
- `plot.and.flag.cal.db` plots and allows for manual flagging (their record) of standard gas measurements.
- `flag.cal.from.db` flags calibrations based upon the sites calibration database.
- `update_calibration_coefficient_database` compiles and update the calibration parameter data for each site.
- `targets_check` apply the calibration scheme and data to target calibrations.
- `get.cal.parameters` which retrieves time-dependent calibration parameters for calibration of a certain day from the calibration databases.

- `apply_calibration_data` apply calibration data to target data.
- `get.targ.parameters` which retrieves time-dependent calibration parameters for target calibration of a certain day from the calibration databases.
- `apply_calibration_data` apply calibration data to measurement data.
- `insert_target_uncertainty` insert the target uncertainty for a certain period

A.2.6.2 Calibration Implementation Details

A few core R-functions (`cal_1point`, `cal_2point` `cal_3point`) implement the above methodology given different arguments and configured with time-dependent tabular information (*e.g.* Table A.1) using the R-function, which is designated by "Code", and described in Table A.5.

Table A.5: The calibration strategies used in CarboCount CH and respective R-function names as well as the standard gas types.

Type		Code	Bottles	Description
1-point intercept	zero	p1_z	work	The slope is calculated from the <i>ex situ</i> determined and measured concentration ratio for a standard gas and the uncertainty of the slope is calculated using the derivation of the Gaussian uncertainty propagation principle. The intercept is forced through zero, without uncertainty.
1-point intercept	zero	p1_z.l	low	Same as above, but for low standard gas.
2-point intercept	free	p2_f	high, low	The slope and intercept are solved for analytically and their uncertainties are directly calculated using the derivation of the Gaussian uncertainty propagation principle.
2-point intercept	free	p2_f.h	COhigh, COlow	Same as above, but for HORIBA to evaluate zero-level information.
2-point intercept	zero	p2_z	high, low	With a weighted total least square regression, the slope and intercept along with their uncertainties as well as the their covarariance are directly calculated. The intercept is forced through zero, without uncertainty.
3-point intercept	free	p3_f	high, work, low	With a weighted total least square regression, the slope and intercept along with their uncertainties as well as the their covarariance are directly calculated.
3-point intercept	zero	p3_z	high, work, low	With a weighted total least square regression, the slope and intercept along with their uncertainties as well as the their covarariance are directly calculated. The intercept is forced through zero, without uncertainty.
3-point offset		p3_o	high, work, low	The slope and intercept is initially calculated as a 2-point free-intercept (p2_z) from high and low calibrations. The intercept is then adjusted between span calibrations.

List of Tables

2.1	Location and instrumentation of the measurement sites of the SNF Sinergia CarboCount CH Project.	20
2.2	Approximate reference gas mole fractions of aluminum bottles. Mole fractions have units of $\mu\text{mol mol}^{-1}$ mole fraction or molar parts per million (ppm).	20
2.3	Parts of Lägern-Hochwacht measurement system which was mostly replicated at Früebüel. The legend indicates unapparent parts in Figure 2.1. The lower half contains specific Swagelok® parts.	23
2.4	Flag table for CarboCount CH measurement data.	31
2.5	Root mean square error (in ppm) between known and calibrated target reference gas mole fractions during their period of measurement (see Figure 2.5).	31
3.1	Details of the four measurement sites of the CarboCount CH network. From left to right: the site name, the site code, measurement commencement date, the measurement height(s), measured trace gases, the site’s altitude (m a.s.l.), and the geographic site locations.	43
3.2	Simulation characteristics for the four measurement sites of the CarboCount CH network. Listed from left to right are the FLEXPART-COSMO particle release heights (above model ground level), the “true” site altitudes (m a.s.l.), smoothed COSMO numerical weather prediction model’s ($\sim 4 \text{ km}^2$) site altitude, and the geographic site locations.	44
4.1	Simulation characteristics for two observation sites of the CarboCount CH network. Listed from left to right are observation heights (m above ground level), FLEXPART-COSMO particle release heights (m above model ground level), the “true” site altitudes (m above sea level), smoothed COSMO numerical weather prediction model’s ($\sim 4 \text{ km}^2$) site altitude, and the geographic site locations.	65
4.2	An overview of the model and observation based CO_2 component estimates. All observation-based estimates (obs*) calculate the CO_2 background with a 45-day REBS, and translate CO above a similar CO background estimate with the designated β . All modeled estimates were calculated with FLEXPART-COSMO and the data product listed.	67
4.3	Sensitivity of the inverse ratios R_{obs} ($\equiv \beta_{obs}^{-1}$) to the choice of observations used to determine the background signal, and to the choice of width of local regression window. Also shown are model-based ratios R_{mod} . The units of R_* are ppb CO /ppm CO_2 . The uncertainty (\pm) of R is determined as 2σ of the slope of the total weighted least squares regression.	75

4.4	Summary of observed R 's found in previous studies. The upper portion of the table displays long-term observation results, and the lower half of the table displays observation campaign results. $\text{CO}_A/\text{CO}_{2,R}$ refers to ratios calculated from continuous CO_2 and CO observations above background, analogous to this study. $\text{CO}_A/\text{CO}_{2,\text{FF}}$ indicates fossil fuel CO_2 ($\text{CO}_{2,\text{FF}}$) calculated from ^{14}C [see <i>Levin et al.</i> , 2003]. The information used for the method is presented as the apparent ratio calculation, background, and the metric shown. The units of R are ppb CO /ppm CO_2	77
A.1	The latest table (<code>site.info</code>) from 2014-08-21 at 09:00:00 UTC, Ruediger Schanda changed the CO high bottle at Gimmiz. This table is written out by this org-mode (emacs) document with R as <code>SiteInfo-2014-08-21-090000.csv</code> in the directory where this file resides. NA stands for 'not available'.	96
A.2	The latest measurement device and calibration information from 2014-04-29 at 09:38:00, when the normal device at Beromünster was put back into service, replacing the ersatz G2311-f. This table is queried when calibration parameters are calculated (defining the calibration type) and raw data are checked to see whether they are feasible (<i>e.g.</i> is <code>CO2_dry > 6?</code>). For example, this table is written out by this org-mode document with R as <code>SiteDeviceInfo-2014-04-29-093800.csv</code> in the directory where this file resides. NA stands for 'not available'.	97
A.3	The scripts use to control the execution of database organization, updates and evaluation. . .	98
A.4	The limits for standard gas and ambient greenhouse gas measurements. For exact numbers, please see Table A.1.	100
A.5	The calibration strategies used in CarboCount CH and respective R-function names as well as the standard gas types.	103

List of Figures

1.1	The global carbon cycle depicted as pools and fluxes. Arrows and their annotations denote annual carbon fluxes (PgC yr^{-1}). Boxes represent the carbon pools (PgC). Preindustrial flux and pool magnitudes are black and additional anthropogenic fluxes and pools are red. Figure is slightly modified from <i>Ciais et al.</i> [2013].	2
1.2	Partitioning of annual anthropogenic CO_2 emissions from 1750 to 2011 (positive) between the three major sinks: atmosphere, ocean, and land. Figure is slightly modified from <i>Ciais et al.</i> [2013].	3
1.3	Range of accumulated (PgC) and annual carbon flux (PgC yr^{-1}) from the atmosphere into the ocean or land surface as estimated by land surface models, which are driven by CO_2 emissions, and simulate the feedbacks between the carbon cycle and climate differently. The figure and simulations are from the fifth phase of the Coupled Model Intercomparison Project [CMIP5; Friedlingstein et al., 2014].	4
1.4	CO_2 time series measured at Mauna Loa, Hawai'i (MLO) and the South Pole Antarctica (SPO) by the Scripps Institute of Oceanography [Keeling et al., 2001].	8
1.5	Vertical, zonal profiles of CO_2 observations from a Maine to North Dakota and c from Idaho to Maine, USA, taken during the COBRA-2000 intense measurement campaign. From Gerbig et al. [2003a]	14
1.6	Retrievals of biospheric surface carbon fluxes constraining seasonal sets of biosphere model parameters (Post Params) and seasonal flux inventories (Post Pixels) compared with “known” biospheric fluxes (Prior). Taken from Meesters et al. [2012].	15
1.7	Schematic representation of the fundamental CarboCount CH project elements: tower observations, carbon fluxes (bidirectional arrows), and transport models (unidirectional arrows). Figure kindly provided by the Graphics Department, Empa.	18
2.1	Airflow schematic at Lägern-Hochwacht.	22
2.2	Left: Calibration with offset a and slope b . Standard errors of the calibration measurements are indicated by the horizontal arrows. Right: Similar to the left panel but the regression is forced through zero. Additional reference gas measurements may be included in both cases.	26
2.3	Example sequence with one LOW and HIGH reference gas measurements between ambient measurements MEAS.	27
2.4	Schematic of temporal interpolation (top) or temporal averaging (bottom) of calibration coefficients from “span” calibrations binning the targeted processing time t_{int}	28

2.5	Target gas calibration results at the CarboCount CH sites. Individual differences between known and calibrated target gas molar ratios are plotted, with independent analytical and target uncertainty bands (\pm).	32
2.6	Atmospheric carbon measurements (CO_2 , CH_4 , & CO) during afternoon (1200-1500 UTC, 1300-1600 LT) at the CarboCount CH sites. The Beromünster data are from the highest sampling height (212 m).	34
2.7	Seasonal average daily cycles of observed atmospheric carbon mole fractions from the CarboCount CH sites. Uncertainty bands correspond to $\pm 1\sigma$ at the respective time of day. Time zone is UTC.	35
3.1	An overview of CarboCount CH measurement site locations within Switzerland: Beromünster (BEO), Fröebüel (FRU), Gimmiz (GIM), and Lägern-Hochwacht (LAE). The sites are concentrated along the Swiss Plateau. The measurement heights and locations are listed in Table 3.1. Also shown are other sites with greenhouse gas concentration or flux measurements that complement the network. These include the sites of the Swiss FluxNet, the high Alpine research station Jungfraujoch, and sites of the Swiss air pollution monitoring network NABEL (National Air Pollution Monitoring Network).	41
3.2	Site surroundings including land use (first column), topography (second column), and Google aerial photo (third column), with Beromünster (a–c) in the first row, and Gimmiz (d–f) in the second row. The land use (a and d) is based on CORINE 2006 land cover classes color coded as follows – urban: red; food croplands: beige; evergreen forest: green; deciduous forest: light green; pasture: light brown; agroforestry areas: tan. Cyan contour lines in the topography panels (b and e) denote the COSMO-2 model topography.	47
3.3	Similar to Fig. 3.2 with Fröebüel (a–c) in the first row and Lägern-Hochwacht (d–f) in the second row.	48
3.4	Wind roses at the four measurement sites during the study period (1 March 2013–28 February 2014) for observed (first column) and simulated horizontal wind at two different model heights: at the height of the measurement a.m.g.l. (Model, second column), and at the true height of the measurement a.s.l. (True, third column). The wind roses display the wind speed probability distribution split into incident 30° wind direction bins. Wind from the north is upward and circular lines demarcate graduating 5th percentiles. Labels above each panel show the height above ground for the measurements (first column) and height above the COSMO-2 model ground for the simulated data (second and third columns).	50
3.5	Mean summer (June–August 2013) diurnal cycle of measured and simulated local meteorology at the sites Beromünster and Gimmiz: (a and b) temperature, (c and d) specific humidity (Sp. Hum.), and (e and f) wind speed (W. S.). Also shown are mean diurnal cycles of measured (g and h) regional CO_2 signals (ΔCO_2), and (i and j) regional CH_4 signals (ΔCH_4). The measurement and simulation heights above ground are listed in the figure legends. Simulated meteorology is shown for two different heights, the height of the measurement a.m.g.l. (Model, dark blue), and the simulation height a.m.g.l., which corresponds to the “true” measurement altitude a.s.l. (True, light blue). The time zone in Switzerland is central European time (CET or UTC + 1).	52
3.6	Similar to Fig. 3.5, the mean diurnal cycles during winter (December 2013–February 2014) at the sites Beromünster and Gimmiz.	53

3.7	Similar to Fig. 3.5, the mean diurnal cycles during summer (June–August 2013) at the sites Fröebüel and Lägern-Hochwacht. The Fröebüel meteorological measurements were made at 2 m a.g.l.	54
3.8	Similar to Fig. 3.5, mean diurnal cycles during winter (December 2013–February 2014) at the sites Fröebüel and Lägern-Hochwacht. The Fröebüel meteorological measurements were made at 2 m a.g.l.	55
3.9	Monthly (YYYYMM) mean nighttime (00:00–03:00 UTC; a , c , and e) and daytime (12:00–15:00 UTC; b , d , and f) measured regional carbon dioxide signals, ΔCO_2 , measured regional methane signals, ΔCH_4 , and simulated monthly total surface sensitivities, \bar{T}_t (Eq. 3.3.1), during the study’s time period (1 March 2013–28 February 2014). Regional signals are computed as the measured concentration minus a background concentration estimate from Jungfraujoch, and total surface sensitivities provide a linear estimate of how much arriving air parcels at a measurement site have been in contact with the model domain’s surface.	56
3.10	Monthly (YYYYMM) land cover type (LCT) contributions C_{LCT} (Eq. 3.3.2) for Beromünster (a), Fröebüel (b), Gimmiz (c), and Lägern-Hochwacht (d), calculated as the pixel-wise multiplication of the monthly mean surface sensitivities with the respective LCT fraction and divided by the monthly averaged total surface sensitivities.	57
3.11	Surface sensitivities as a function of distance from the measurement site position \bar{T}_k (Eq. 3.3.3). Lines are color coded according to measurement site (Beromünster: dark blue, Fröebüel: orange, Gimmiz: light blue, Lägern-Hochwacht: red). The vertical dotted line is the radius at which the cumulative surface sensitivity starting from the measurement site’s position reaches 50 % of the simulation domain total, τ_{s50} . (a) Summer (June–August 2013), (b) winter (December 2013–February 2014), and (c) and (d) summer afternoon (15:00 UTC) and at nighttime (03:00 UTC), respectively. Please note the logarithmic y axis and that, during winter, for Beromünster and Lägern-Hochwacht the 50 % vertical dotted lines overlap. The site-specific particle release heights are listed in Table 3.2. Local time is central European time (CET or UTC + 1).	58
3.12	Area of surface influence (Eq. 3.3.5) defined as the isoline at the site-dependent value τ_{s50} encompassing 50 % of the total mean surface sensitivities. Lines are color coded according to measurement site – Beromünster: dark blue, Fröebüel: orange, Gimmiz: light blue, Lägern-Hochwacht: red. (a) Summer (June–August, 2013), (b) winter (December 2013–February 2014), and (c) and (d) summer (June–August 2013) in the afternoon (15:00 UTC) and at nighttime (03:00 UTC), respectively. Local time is central European time (CET or UTC + 1).	59
4.1	Simulation domains of this study. The COSMO-7 represents the driving meteorology. The west European and Switzerland domains comprise the areas where surface sensitivity and flux influence is calculated for the past 4 days to simulate regional signals. Outside these temporal and spatial domains the initial concentration is taken as the background signal.	69
4.2	Observed CO_2 concentrations (A), observation-based (obs1) and FLEXPART-COSMO-modeled (mod1) CO_2 background (B), anthropogenic (C) and biospheric (D) components at Beromünster during 2013. Also shown in (A) is the sum of all simulated components. For an overview of the settings for obs1 and mod1 see Table 4.2.	71
4.3	Same as Fig. 4.2 but at the Lägern-Hochwacht site.	72

4.4	CO ₂ (panels A–B) & CO (panels C–D) measured concentrations (black and gray) and “robust estimate of baseline signal” (REBS) estimates (red and orange) at Beromünster, Lägern-Hochwacht, and Jungfrauoch (JFJ) during 2013. The REBS background estimates are calculated with a 45-day local regression window.	73
4.5	Modeled and measured CO ₂ and CO regional signals at Beromünster and Lägern-Hochwacht, colored according to season. Panel A : modeled CO _{2,A} and CO _A at Beromünster. The slope of the regression line corresponds to β_{mod} of method mod1. Panel B : CO _{2,R} and CO _A regional signals above a background signal from Jungfrauoch. The slope of the regression line is calculated using only wintertime regional signals and corresponds to β_{obs} of method obs1. Panel C : the same is shown as in panel B except using background estimates from the target site Beromünster (method obs5). Panels D–F : the same as panels A–C shown with regional signals from Lägern-Hochwacht.	75
4.6	Late winter- and springtime pollution events during which neither observation based nor modeled estimates explain the observed CO ₂ at Beromünster and Lägern-Hochwacht. Modeled and observed regional CO : CO ₂ ratios above a threshold which denotes an isoline which includes 90 % of the cumulative sum of surface sensitivities [see <i>Oney et al.</i> , 2015]. Individual regional signals were spatially disaggregated according to <i>Stohl</i> [1996].	78
4.7	Afternoon (1200–1500 UTC) biospheric CO ₂ signals at Beromünster and Lägern-Hochwacht during 2013. The modeled (mod1) and observation-based (obs1) biospheric signals (CO _{2,B}) are also shown in panel D of Figs. 4.2 & 4.3. The uncertainty (gray) enveloping the residual biospheric signal (obs1) accounts for the uncertainty introduced by the observation based background and anthropogenic CO ₂ signals.	80
4.8	Comparison of biospheric CO ₂ signals (CO _{2,B}) at Beromünster (panel A) and Lägern-Hochwacht (panel B) during the period of 2013-01 – 2013-03.	81
4.9	Comparison of the statistical distributions (box and violin [kernel density] plots) of afternoon (1200–1500 UTC) CO ₂ biospheric signals at Beromünster (panels A–D) and Lägern-Hochwacht (panels E–H) during 2013, summarized by season for each method (Table 4.2). The mean of each distribution is marked by a diamond.	82
4.10	Observed afternoon (1200–1500 UTC) biospheric CO ₂ signals (obs1) along with temperature (average of past 24 hours), photosynthetically active radiation (PAR) accumulated over the past 24 hours, as well as precipitation accumulated over the previous 21 days (as a proxy of soil moisture), during the main growing season (01 May–01 September) of 2013 interpolated from COSMO-2 analysis fields to the observation site positions, Beromünster and Lägern-Hochwacht at 250 m above model ground level. Shaded areas demarcate periods during which the average temperature of the preceding 24 hours was > 20° C.	84
4.11	Response of observed afternoon (1200–1500 UTC) biospheric CO ₂ signals (obs1) to modeled (described in Fig. 4.10) PAR, accumulated precipitation, and average temperature at both Beromünster and Lägern-Hochwacht during the growing season (01 May–01 September) of 2013. We narrowed our investigation to convective meteorological situations according to the categorization by <i>Weusthoff</i> [2011]. The blue line corresponds to a generalized additive model binned by the 95 % confidence interval.	85

5.1	Distributions of observed afternoon (1200–1500 UTC) biospheric CO ₂ signals (obs1) and observed average temperature (of the preceding 24 hours) at both Beromünster and Lägern-Hochwacht during the growing seasons (01 May–01 September) of 2013–2015. Observations shown are only during convective meteorological situations according to the categorization by <i>Weusthoff</i> [2011].	92
5.2	Response of observed afternoon (1200–1500 UTC) biospheric CO ₂ signals (obs1) and observed temperature averaged of the preceding 24 hours at both Beromünster and Lägern-Hochwacht during the growing seasons (01 May–01 September) of 2013–2015. Observations shown are only during convective meteorological situations according to the categorization by <i>Weusthoff</i> [2011].	93

Bibliography

- Ahmadov, R., C. Gerbig, R. Kretschmer, S. Koerner, B. Neininger, A. J. Dolman, and C. Sarrat, Mesoscale covariance of transport and CO₂ fluxes: Evidence from observations and simulations using the WRF-VPRM coupled atmosphere-biosphere model, *Journal of Geophysical Research: Atmospheres*, 112(22), 1–14, doi:10.1029/2007JD008552, 2007.
- Ahmadov, R., C. Gerbig, R. Kretschmer, S. Körner, C. Rödenbeck, P. Bousquet, and M. Ramonet, Comparing high resolution WRF-VPRM simulations and two global CO₂ transport models with coastal tower measurements of CO₂, *Biogeosciences*, 6(5), 807–817, doi:10.5194/bg-6-807-2009, 2009.
- Andreae, M. O., et al., Biogeochemical cycling of carbon, water, energy, trace gases, and aerosols in Amazonia: The LBA-EUSTACH experiments, *Journal of Geophysical Research*, 107(D20), 1–25, doi:10.1029/2001JD000524, 2002.
- Andres, R. J., et al., A synthesis of carbon dioxide emissions from fossil-fuel combustion, *Biogeosciences*, 9(5), 1845–1871, doi:10.5194/bg-9-1845-2012, 2012.
- Andrews, A. E., et al., CO₂, CO, and CH₄ measurements from tall towers in the NOAA Earth System Research Laboratory’s Global Greenhouse Gas Reference Network: instrumentation, uncertainty analysis, and recommendations for future high-accuracy greenhouse gas, *Atmospheric Measurement Techniques*, 7(2), 647–687, doi:10.5194/amt-7-647-2014, 2014.
- Anyamba, A., and C. Tucker, Analysis of Sahelian vegetation dynamics using NOAA-AVHRR NDVI data from 1981–2003, *Journal of Arid Environments*, 63(3), 596–614, doi:10.1016/j.jaridenv.2005.03.007, 2005.
- Arrhenius, S., XXXI. On the influence of carbonic acid in the air upon the temperature of the ground, *The London, Edinburgh, and Dublin Philosophical Magazine and Journal of Science*, 41(251), 237–276, 1896.
- Baccini, A., et al., Estimated carbon dioxide emissions from tropical deforestation improved by carbon-density maps, *Nature Climate Change*, 2(3), 182–185, doi:10.1038/nclimate1354, 2012.
- Baker, D. F., et al., TransCom 3 inversion intercomparison: Impact of transport model errors on the interannual variability of regional CO₂ fluxes, 1988–2003, *Global Biogeochemical Cycles*, 20(GB1002), 1–17, doi:10.1029/2004GB002439, 2006.
- Bakwin, P., K. Davis, C. Yi, and S. Wofsy, Regional carbon dioxide fluxes from mixing ratio data, *Tellus B*, 56B, 301–311, 2004.
- Bakwin, P. S., P. P. Tans, C. Zhao, W. Ussler, and E. Quesnell, Measurements of carbon dioxide on a very tall tower, *Tellus B*, 47, 535–549, 1995.
- Bakwin, P. S., P. P. Tans, J. W. C. White, and R. J. Andres, Determination of the isotopic (¹³C/¹²C) discrimination by terrestrial biology from a global network of observations, *Global Biogeochemical Cycles*, 12(3), 555–562, 1998.

- Baldauf, M., A. Seifert, J. Förstner, D. Majewski, M. Raschendorfer, and T. Reinhardt, Operational Convective-Scale Numerical Weather Prediction with the COSMO Model: Description and Sensitivities, *Monthly Weather Review*, 139(12), 3887–3905, doi:10.1175/MWR-D-10-05013.1, 2011.
- Baldocchi, D., TURNER REVIEW No. 15. 'Breathing' of the terrestrial biosphere: lessons learned from a global network of carbon dioxide flux measurement systems, *Australian Journal of Botany*, pp. 1–81, 2008.
- Baldocchi, D., et al., FLUXNET: a new tool to study the temporal and spatial variability of ecosystem-scale carbon dioxide, water vapor, and energy flux densities, *Bulletin of the American Meteorological Society*, pp. 2415–2434, 2001.
- Baldocchi, D. D., B. B. Hincks, and T. P. Meyers, Measuring biosphere-atmosphere exchanges of biologically related gases with micrometeorological methods, *Ecology*, 69(5), 1331–1340, 1988.
- Ballantyne, A. P., C. B. Alden, J. B. Miller, P. P. Tans, and J. W. C. White, Increase in observed net carbon dioxide uptake by land and oceans during the past 50 years, *Nature*, 488(7409), 70–72, doi:10.1038/nature11299, 2012.
- Ballantyne, A. P., et al., Audit of the global carbon budget: estimate errors and their impact on uptake uncertainty, *Biogeosciences*, 12(8), 2565–2584, doi:10.5194/bg-12-2565-2015, 2015.
- Bamberger, I., B. Oney, D. Brunner, S. Henne, M. Leuenberger, N. Buchmann, and W. Eugster, Observation of atmospheric methane and carbon dioxide mixing ratios: Tall tower or mountain top stations?, *submitted to Boundary Layer Meteorology*, pp. 1–29, 2016.
- Battle, M., M. L. Bender, P. P. Tans, J. W. White, J. T. Ellis, T. Conway, and R. J. Francey, Global carbon sinks and their variability inferred from atmospheric O₂ and $\delta^{13}\text{C}$, *Science*, 287(5462), 2467–2470, doi:10.1126/science.287.5462.2467, 2000.
- Beck, P. S., C. Atzberger, K. A. Høgda, B. Johansen, and A. K. Skidmore, Improved monitoring of vegetation dynamics at very high latitudes: A new method using MODIS NDVI, *Remote Sensing of Environment*, 100(3), 321–334, doi:10.1016/j.rse.2005.10.021, 2006.
- Beer, C., et al., Terrestrial gross carbon dioxide uptake: global distribution and covariation with climate., *Science*, 329(5993), 834–838, doi:10.1126/science.1184984, 2010.
- Berhanu, T. A., E. Satar, R. Schanda, P. Nyfeler, H. Moret, D. Brunner, B. Oney, and M. Leuenberger, Measurements of greenhouse gases at Beromünster tall-tower station in Switzerland, *Atmospheric Measurement Techniques*, 9(6), 2603–2614, doi:10.5194/amt-9-2603-2016, 2016.
- Bilionis, I., B. A. Drewniak, and E. M. Constantinescu, Crop physiology calibration in the CLM, *Geoscientific Model Development*, 8(4), 1071–1083, doi:10.5194/gmd-8-1071-2015, 2015.
- Bocquet, M., Inverse modelling of atmospheric tracers: non-Gaussian methods and second-order sensitivity analysis, *Nonlinear Processes in Geophysics*, 15(1), 127–143, doi:10.5194/npg-15-127-2008, 2008.
- Bonan, G. B., *Ecological climatology: concepts and applications*, 2nd ed ed., Cambridge University Press, Cambridge ; New York, 2008.
- Bonan, G. B., and S. Levis, Evaluating Aspects of the Community Land and Atmosphere Models (CLM3 and CAM3) Using a Dynamic Global Vegetation Model, *Journal of Climate*, 19(11), 2290–2301, doi:10.1175/JCLI3741.1, 2006.

- Bonan, G. B., S. Levis, L. Kergoat, and K. W. Oleson, Landscapes as patches of plant functional types: An integrating concept for climate and ecosystem models, *Global Biogeochemical Cycles*, 16(2), 5–1–5–23, doi:10.1029/2000GB001360, 2002a.
- Bonan, G. B., K. W. Oleson, M. Vertenstein, S. Levis, X. Zeng, Y. Dai, R. E. Dickinson, and Z.-L. Yang, The land surface climatology of the community land model coupled to the NCAR community climate model, *Journal of Climate*, 15(22), 3123–3149, 2002b.
- Bousquet, P., P. Ciais, P. Peylin, M. Ramonet, and P. Monfray, Inverse modeling of annual atmospheric CO₂ sources and sinks 1. Method and control inversion, *Journal of Geophysical Research*, 104(D21), 26,161, doi:10.1029/1999JD900342, 1999.
- Brooks, B.-G. J., A. R. Desai, B. B. Stephens, D. R. Bowling, S. P. Burns, A. S. Watt, S. L. Heck, and C. Sweeney, Assessing filtering of mountaintop CO₂ mole fractions for application to inverse models of biosphere-atmosphere carbon exchange, *Atmospheric Chemistry and Physics*, 12(4), 2099–2115, doi:10.5194/acp-12-2099-2012, 2012.
- Broquet, G., F. Chevallier, P. Rayner, C. Aulagnier, I. Pison, M. Ramonet, M. Schmidt, A. T. Vermeulen, and P. Ciais, A European summertime CO₂ biogenic flux inversion at mesoscale from continuous in situ mixing ratio measurements, *Journal of Geophysical Research: Atmospheres*, 116(D23303), 1–22, doi:10.1029/2011JD016202, 2011.
- Broquet, G., et al., Regional inversion of CO₂ ecosystem fluxes from atmospheric measurements: reliability of the uncertainty estimates, *Atmospheric Chemistry and Physics*, 13(17), 9039–9056, doi:10.5194/acp-13-9039-2013, 2013.
- Brunner, D., S. Henne, C. A. Keller, S. Reimann, M. K. Vollmer, S. O’Doherty, M. Maione, and S. O’Doherty, An extended Kalman-filter for regional scale inverse emission estimation, *Atmospheric Chemistry and Physics*, 12(12), 3455–3478, doi:10.5194/acp-12-3455-2012, 2012.
- Brunner, D., et al., Comparative analysis of meteorological performance of coupled chemistry-meteorology models in the context of AQMEII phase 2, *Atmospheric Environment*, 115, 470–498, doi:10.1016/j.atmosenv.2014.12.032, 2015.
- Callendar, G. S., Can carbon dioxide influence climate?, *Weather*, 4(10), 310–314, 1949.
- Chen, H., A. Karion, C. W. Rella, J. Winderlich, C. Gerbig, A. Filges, T. Newberger, C. Sweeney, and P. P. Tans, Accurate measurements of carbon monoxide in humid air using the cavity ring-down spectroscopy (CRDS) technique, *Atmospheric Measurement Techniques*, 6(4), 1031–1040, doi:10.5194/amt-6-1031-2013, 2013.
- Chevallier, F., On the parallelization of atmospheric inversions of CO₂ surface fluxes within a variational framework, *Geoscientific Model Development*, 6(3), 783–790, doi:10.5194/gmd-6-783-2013, 2013.
- Chevallier, F., On the statistical optimality of CO₂ atmospheric inversions assimilating CO₂ column retrievals, *Atmospheric Chemistry and Physics Discussions*, 15, 11,889–11,923, doi:10.5194/acpd-15-11889-2015, 2015.
- Chevallier, F., et al., CO₂ surface fluxes at grid point scale estimated from a global 21 year reanalysis of atmospheric measurements, *Journal of Geophysical Research*, 115(D21307), 1–17, doi:10.1029/2010JD013887, 2010.
- Ciais, P., P. P. Tans, M. Trolier, J. W. C. White, and R. J. Francey, A Large Northern Hemisphere Terrestrial CO₂ Sink Indicated by the 13c/12c Ratio of Atmospheric CO₂, *Science*, 269(5227), 1098–1102, 1995.

- Ciais, P., P. Rayner, F. Chevallier, P. Bousquet, M. Logan, P. Peylin, and M. Ramonet, Atmospheric inversions for estimating CO₂ fluxes: methods and perspectives, *Climatic Change*, 103, 69–92, doi:10.1007/s10584-010-9909-3, 2010a.
- Ciais, P., et al., Europe-wide reduction in primary productivity caused by the heat and drought in 2003., *Nature*, 437(7058), 529–533, doi:10.1038/nature03972, 2005.
- Ciais, P., et al., The European carbon balance. Part 1: fossil fuel emissions, *Global Change Biology*, 16(5), 1395–1408, doi:10.1111/j.1365-2486.2009.02098.x, 2010b.
- Ciais, P., et al., Carbon and Other Biogeochemical Cycles, in *Climate Change 2013: The Physical Science Basis. Contribution of Working Group I to the Fifth Assessment Report of the Intergovernmental Panel on Climate Change*, edited by T. Stocker, D. Qin, G.-K. Plattner, M. Tignor, S. Allen, J. Boschung, A. Nauels, Y. Xia, V. Bex, and P. Midgley, pp. 465–570, Cambridge University Press, Cambridge, United Kingdom and New York, NY, USA, 2013.
- Ciais, P., et al., Current systematic carbon-cycle observations and the need for implementing a policy-relevant carbon observing system, *Biogeosciences*, 11(13), 3547–3602, doi:10.5194/bg-11-3547-2014, 2014.
- Corbin, K. D., A. S. Denning, E. Y. Lokupitiya, A. E. Schuh, N. L. Miles, K. J. Davis, S. Richardson, and I. T. Baker, Assessing the impact of crops on regional CO₂ fluxes and atmospheric concentrations, *Tellus, Series B: Chemical and Physical Meteorology*, 62(5), 521–532, doi:10.1111/j.1600-0889.2010.00485.x, 2010.
- Crosson, E. R., A cavity ring-down analyzer for measuring atmospheric levels of methane, carbon dioxide, and water vapor, *Applied Physics B*, 92(3), 403–408, doi:10.1007/s00340-008-3135-y, 2008.
- Denning, A. S., D. A. Randall, G. J. Collatz, and P. J. Sellers, Simulations of terrestrial carbon metabolism and atmospheric CO₂ in a general circulation model. Part 2: Simulated CO₂ concentrations, *Tellus B*, 48(4), 543–567, doi:10.1034/j.1600-0889.1996.t01-1-00010.x, 1996.
- Dlugokencky, E. J., K. A. Masarie, P. M. Lang, and P. P. Tans, Continuing decline in the growth rate of the atmospheric methane burden, *Nature*, 393, 447–450, doi:10.1038/30934, 1998.
- Dlugokencky, E. J., R. C. Myers, P. M. Lang, K. A. Masarie, A. M. Crotwell, K. W. Thoning, B. D. Hall, J. W. Elkins, and L. P. Steele, Conversion of NOAA atmospheric dry air CH₄ mole fractions to a gravimetrically prepared standard scale, *Journal of Geophysical Research*, 110(D18), D18,306, doi:10.1029/2005JD006035, 2005.
- Dolman, A. J., C. Gerbig, J. Noilhan, C. Sarrat, and F. Miglietta, Detecting regional variability in sources and sinks of carbon dioxide: a synthesis, *Biogeosciences*, 6(6), 1015–1026, doi:10.5194/bg-6-1015-2009, 2009.
- Dolman, A. J., et al., The CarboEurope Regional Experiment Strategy, *Bulletin of the American Meteorological Society*, 87(10), 1367–1379, doi:10.1175/BAMS-87-10-1367, 2006.
- Drewniak, B., J. Song, J. Prell, V. R. Kotamarthi, and R. Jacob, Modeling agriculture in the Community Land Model, *Geoscientific Model Development*, 6(2), 495–515, doi:10.5194/gmd-6-495-2013, 2013.
- Duncan, B. N., J. A. Logan, I. Bey, I. A. Megretskaia, R. M. Yantosca, P. C. Novelli, N. B. Jones, and C. P. Rinsland, Global budget of CO, 1988 - 1997: Source estimates and validation with a global model, *Journal of Geophysical Research: Atmospheres*, 112(D22301), 1–29, doi:10.1029/2007JD008459, 2007.
- Enting, I. G., *Inverse problems in atmospheric constituent transport*, Cambridge University Press, 2002.

- Eugster, W., and F. Siegrist, The influence of nocturnal CO₂ advection on CO₂ flux measurements, *Basic and Applied Ecology*, 1, 177–188, 2000.
- FOEN, Switzerland’s greenhouse gas inventory 1990–2012, *Tech. rep.*, Federal Office of the Environment, Bern, Switzerland, 2014.
- Foken, T., The energy balance closure problem: an overview, *Ecological Applications*, 18(6), 1351–1367, 2008.
- Forster, C., A. Stohl, and P. Seibert, Parameterization of Convective Transport in a Lagrangian Particle Dispersion Model and Its Evaluation, *Journal of Applied Meteorology and Climatology*, 46(4), 403–422, doi:10.1175/JAM2470.1, 2007.
- Frankenberg, C., C. O’Dell, J. Berry, L. Guanter, J. Joiner, P. Köhler, R. Pollock, and T. E. Taylor, Prospects for chlorophyll fluorescence remote sensing from the Orbiting Carbon Observatory-2, *Remote Sensing of Environment*, 147, 1–12, doi:10.1016/j.rse.2014.02.007, 2014.
- Frankenberg, C., et al., New global observations of the terrestrial carbon cycle from GOSAT: Patterns of plant fluorescence with gross primary productivity, *Geophysical Research Letters*, 38(17), 1–6, doi:10.1029/2011GL048738, 2011.
- Friedlingstein, P., M. Meinshausen, V. K. Arora, C. D. Jones, A. Anav, S. K. Liddicoat, and R. Knutti, Uncertainties in CMIP5 Climate Projections due to Carbon Cycle Feedbacks, *Journal of Climate*, 27(2), 511–526, doi:10.1175/JCLI-D-12-00579.1, 2014.
- Gamnitzer, U., U. Karstens, B. Kromer, R. E. M. Neubert, H. A. J. Meijer, H. Schroeder, and I. Levin, Carbon monoxide: A quantitative tracer for fossil fuel CO₂?, *Journal of Geophysical Research*, 111(D22), 1–19, doi:10.1029/2005JD006966, 2006.
- Gatti, L. V., et al., Drought sensitivity of Amazonian carbon balance revealed by atmospheric measurements, *Nature*, 506(7486), 76–80, doi:10.1038/nature12957, 2014.
- Gerbig, C., D. Kley, A. Volz-Thomas, J. Kent, K. Dewey, and D. S. McKenna, Fast response resonance fluorescence CO measurements aboard the C-130: Instrument characterization and measurements made during North Atlantic Regional Experiment 1993, *Journal of Geophysical Research: Atmospheres*, 101(D22), 29,229–29,238, 1996.
- Gerbig, C., J. C. Lin, S. C. Wofsy, B. C. Daube, A. E. Andrews, B. B. Stephens, P. S. Bakwin, and C. A. Grainger, Toward constraining regional-scale fluxes of CO₂ with atmospheric observations over a continent: 1. Observed spatial variability from airborne platforms, *Journal of Geophysical Research-Atmospheres*, 108(D24), 1–27, 2003a.
- Gerbig, C., J. C. Lin, S. C. Wofsy, B. C. Daube, A. E. Andrews, B. B. Stephens, P. S. Bakwin, and C. A. Grainger, Toward constraining regional-scale fluxes of CO₂ with atmospheric observations over a continent: 2. Analysis of COBRA data using a receptor-oriented framework, *Journal of Geophysical Research-Atmospheres*, 108(D24), 1–14, 2003b.
- Gerbig, C., S. Körner, and J. C. Lin, Vertical mixing in atmospheric tracer transport models: error characterization and propagation, *Atmospheric Chemistry and Physics*, 8(3), 591–602, doi:10.5194/acp-8-591-2008, 2008.
- Gerbig, C., A. J. Dolman, and M. Heimann, On observational and modelling strategies targeted at regional carbon exchange over continents, *Biogeosciences*, 6(10), 1949–1959, doi:10.5194/bg-6-1949-2009, 2009.

- Giordano, L., et al., Assessment of the MACC reanalysis and its influence as chemical boundary conditions for regional air quality modeling in AQMEII-2, *Atmospheric Environment*, 115, 371–388, doi:10.1016/j.atmosenv.2015.02.034, 2015.
- Gloor, M., P. Bakwin, D. Hurst, L. Lock, R. Draxler, and P. Tans, What is the concentration footprint of a tall tower?, *Journal of Geophysical Research*, 106(D16), 17,831–17,840, doi:10.1029/2001JD900021, 2001.
- Goeckede, M., A. M. Michalak, D. Vickers, D. P. Turner, and B. E. Law, Atmospheric inverse modeling to constrain regional-scale CO₂ budgets at high spatial and temporal resolution, *Journal of Geophysical Research*, 115(D15), 1–23, doi:10.1029/2009JD012257, 2010a.
- Goeckede, M., D. P. Turner, A. M. Michalak, D. Vickers, and B. E. Law, Sensitivity of a subregional scale atmospheric inverse CO₂ modeling framework to boundary conditions, *Journal of Geophysical Research: Atmospheres*, 115(24), 1–15, doi:10.1029/2010JD014443, 2010b.
- Graven, H. D., and N. Gruber, Continental-scale enrichment of atmospheric 14CO₂ from the nuclear power industry: potential impact on the estimation of fossil fuel-derived CO₂, *Atmospheric Chemistry and Physics*, 11(23), 12,339–12,349, doi:10.5194/acp-11-12339-2011, 2011.
- Groenendijk, M., et al., Assessing parameter variability in a photosynthesis model within and between plant functional types using global Fluxnet eddy covariance data, *Agricultural and Forest Meteorology*, 151(1), 22–38, doi:10.1016/j.agrformet.2010.08.013, 2011.
- Gurney, K. R., D. Baker, P. Rayner, and S. Denning, Interannual variations in continental-scale net carbon exchange and sensitivity to observing networks estimated from atmospheric CO₂ inversions for the period 1980 to 2005, *Global Biogeochemical Cycles*, 22(GB3025), 1–17, doi:10.1029/2007GB003082, 2008.
- Gurney, K. R., D. L. Mendoza, Y. Zhou, M. L. Fischer, C. C. Miller, S. Geethakumar, and S. de la Rue du Can, High resolution fossil fuel combustion CO₂ emission fluxes for the United States., *Environmental Science & Technology*, 43(14), 5535–5541, 2009.
- Gurney, K. R., et al., Towards robust regional estimates of CO₂ sources and sinks using atmospheric transport models., *Nature*, 415(6872), 626–630, doi:10.1038/415626a, 2002.
- Gurney, K. R., et al., TransCom 3 CO₂ inversion intercomparison: 1. Annual mean control results and sensitivity to transport and prior flux information, *Tellus*, 55B(2), 555–579, doi:10.1034/j.1600-0889.2003.00049.x, 2003.
- Gurney, K. R., et al., Transcom 3 inversion intercomparison: Model mean results for the estimation of seasonal carbon sources and sinks, *Global Biogeochemical Cycles*, 18(GB1010), 1–18, doi:10.1029/2003GB002111, 2004.
- Hanna, S. R., Applications in Air Pollution Modeling, in *Atmospheric Turbulence and Air Pollution Modelling*, edited by F. T. M. Nieuwstadt and H. van Dop, 1 ed., pp. 275–310, Springer Netherlands, The Hague, 1982.
- Hansen, M. C., et al., High-resolution global maps of 21st-century forest cover change, *Science*, 342(6160), 850–853, doi:10.1126/science.1244693, 2013.
- Haszpra, L., Carbon dioxide concentration measurements at a rural site in Hungary, *Tellus B*, 47, 17–22, 1995.
- Heimann, M., The global atmospheric tracer model TM2, *Tech. Rep. Technical Report No. 10*, Deutsches Klimarechenzentrum, 1996.

- Heimann, M., and C. D. Keeling, A three-dimensional model of atmospheric CO₂ transport based on observed winds: 2. Model description and simulated tracer experiments, in *Aspects of Climate Variability in the Pacific and the Western Americas*, edited by D. H. Peterson, Geophysica, pp. 237–275, American Geophysical Union, Washington D.C., 1989.
- Heimann, M., and S. Körner, The global atmospheric tracer model TM3, in *Technical Report*, pp. 1–131, Max-Planck-Institut für Biogeochemie, Jena, Germany, 2003.
- Heimann, M., and M. Reichstein, Terrestrial ecosystem carbon dynamics and climate feedbacks., *Nature*, 451(17), 289–292, doi:10.1038/nature06591, 2008.
- Henne, S., D. Brunner, D. Folini, S. Solberg, J. Klausen, and B. Buchmann, Assessment of parameters describing representativeness of air quality in-situ measurement sites, *Atmospheric Chemistry and Physics*, 10(8), 3561–3581, 2010.
- Henne, S., D. Brunner, B. Oney, M. Leuenberger, W. Eugster, I. Bamberger, F. Meinhardt, M. Steinbacher, and L. Emmenegger, Validation of the Swiss methane emission inventory by atmospheric observations and inverse modelling, *Atmospheric Chemistry and Physics*, 16(6), 3683–3710, doi:10.5194/acp-16-3683-2016, 2016.
- Hiller, R. V., et al., Anthropogenic and natural methane fluxes in Switzerland synthesized within a spatially explicit inventory, *Biogeosciences*, 11(7), 1941–1959, doi:10.5194/bg-11-1941-2014, 2014.
- Hirsch, A. I., On using radon-222 and CO₂ to calculate regional-scale CO₂ uxes, *Atmospheric Chemistry And Physics*, 7, 3737–3747, 2007.
- Holloway, T., H. Levy, and P. Kasibhatla, Global distribution of carbon monoxide, *Journal of Geophysical Research*, 105(D10), 12,123–12,147, doi:10.1029/1999JD901173, 2000.
- Houghton, R. A., The annual net flux of carbon to the atmosphere from changes in land use 1850–1990, *Tellus B*, 51, 298–313, doi:10.1034/j.1600-0889.1999.00013.x, 1999.
- Houghton, R. A., Revised estimates of the annual net flux of carbon to the atmosphere from changes in land use and land management 1850–2000, *Tellus B*, 55(2), 378–390, doi:10.1034/j.1600-0889.2003.01450.x, 2003.
- Houghton, R. A., J. I. House, J. Pongratz, G. R. van der Werf, R. S. DeFries, M. C. Hansen, C. Le Quéré, and N. Ramankutty, Carbon emissions from land use and land-cover change, *Biogeosciences*, 9(12), 5125–5142, doi:10.5194/bg-9-5125-2012, 2012.
- Hu, L., et al., U.S. emissions of HFC-134a derived for 2008–2012 from an extensive flask-air sampling network, *Journal of Geophysical Research: Atmospheres*, 120, 801–825, doi:10.1002/2014JD022617.Received, 2015.
- Jung, M., et al., Global patterns of land-atmosphere fluxes of carbon dioxide, latent heat, and sensible heat derived from eddy covariance, satellite, and meteorological observations, *Journal of Geophysical Research: Biogeosciences*, 116(3), 2–4, doi:10.1029/2010JG001566, 2011.
- Kaminski, T., P. J. Rayner, M. Heimann, and I. G. Enting, On aggregation errors in atmospheric transport inversions, *Journal of Geophysical Research*, 106(D5), 4703, doi:10.1029/2000JD900581, 2001.
- Karstens, U., C. Schwingshackl, D. Schmidthusen, and I. Levin, A process-based 222-Rn flux map for Europe and its comparison to long-term observations, *Atmospheric Chemistry and Physics Discussions*, 15(12), 17,397–17,448, doi:10.5194/acpd-15-17397-2015, 2015.

- Kattge, J., and W. Knorr, Temperature acclimation in a biochemical model of photosynthesis: a reanalysis of data from 36 species, *Plant, Cell & Environment*, 30(9), 1176–1190, doi:10.1111/j.1365-3040.2007.01690.x, 2007.
- Keeling, C. D., The concentration and isotopic abundances of carbon dioxide in the atmosphere, *Tellus*, 12(2), 200–203, 1960.
- Keeling, C. D., R. B. Bacastow, A. F. Carter, S. C. Piper, T. P. Whorf, M. Heimann, W. G. Mook, and H. Roeloffzen, A three-dimensional model of atmospheric CO₂ transport based on observed winds: 1. Analysis of observational data, in *Aspects of Climate Variability in the Pacific and the Western Americas*, vol. 55, edited by D. H. Peterson, geophysics ed., pp. 165–236, American Geophysical Union, Washington D.C., 1989.
- Keeling, C. D., S. C. Piper, R. B. Bacastow, M. Wahlen, T. P. Whorf, M. Heimann, and H. A. Meijer, Exchanges of Atmospheric CO₂ and ¹³CO₂ with the Terrestrial Biosphere and Oceans from 1978 to 2000. I. Global Aspects, *SIO Reference Series*, No. 01-06, p. 88, 2001.
- Keeling, R. F., R. P. Najjar, M. L. Bender, and P. P. Tans, What atmospheric oxygen measurements can tell us about the global carbon cycle, *Global Biogeochemical Cycles*, 7(1), 37–67, 1993.
- Khatiwala, S., et al., Global ocean storage of anthropogenic carbon, *Biogeosciences*, 10(4), 2169–2191, doi:10.5194/bg-10-2169-2013, 2013.
- Komhyr, W. D., R. H. Gammon, T. B. Harris, L. S. Waterman, T. J. Conway, W. R. Taylor, and K. W. Thoning, Global atmospheric CO₂ distribution and variations from 1968–1982 NOAA/GMCC CO₂ flask sample data, *Journal of Geophysical Research: Atmospheres*, 90(D3), 5567–5596, 1985.
- Kountouris, P., et al., An objective prior error quantification for regional atmospheric inverse applications, *Biogeosciences Discussions*, 12, 9393–9441, doi:10.5194/bgd-12-9393-2015, 2015.
- Kozlova, E. A., and A. C. Manning, Methodology and calibration for continuous measurements of biogeochemical trace gas and O₂ concentrations from a 300-m tall tower in central Siberia, *Atmospheric Measurement Techniques*, 2(1), 205–220, doi:10.5194/amt-2-205-2009, 2009.
- Kretschmer, R., C. Gerbig, U. Karstens, G. Biavati, A. Vermeulen, F. Vogel, S. Hammer, and K. U. Totsche, Impact of optimized mixing heights on simulated regional atmospheric transport of CO₂, *Atmospheric Chemistry and Physics*, 14(14), 7149–7172, doi:10.5194/acp-14-7149-2014, 2014.
- Krol, M., S. Houweling, B. Bregman, M. van den Broek, A. Segers, P. van Velthoven, W. Peters, F. Dentener, and P. Bergamaschi, The two-way nested global chemistry-transport zoom model TM5: algorithm and applications, *Atmospheric Chemistry and Physics*, 5(2), 417–432, doi:10.5194/acp-5-417-2005, 2005.
- Krystek, M., and M. Anton, A weighted total least-squares algorithm for fitting a straight line, *Measurement Science and Technology*, 19(7), 79,801, 2008.
- Kuenen, J. J. P., A. J. H. Visschedijk, M. Jozwicka, and H. A. C. Denier van der Gon, TNO-MACC_{ii} emission inventory; a multi-year (2003–2009) consistent high-resolution European emission inventory for air quality modelling, *Atmospheric Chemistry and Physics*, 14(20), 10,963–10,976, doi:10.5194/acp-14-10963-2014, 2014.
- Lauvaux, T., O. Pannekoucke, C. Sarrat, F. Chevallier, P. Ciais, J. Noilhan, and P. J. Rayner, Structure of the transport uncertainty in mesoscale inversions of CO₂ sources and sinks using ensemble model simulations, *Biogeosciences*, 6, 1089–1102, 2009a.

- Lauvaux, T., A. Schuh, M. Bocquet, and L. Wu, Network design for mesoscale inversions of CO₂ sources and sinks, *Tellus B*, 1, 1–12, 2012a.
- Lauvaux, T., et al., Mesoscale inversion: first results from the CERES campaign with synthetic data, *Atmospheric Chemistry and Physics*, 8, 3459–3471, 2008.
- Lauvaux, T., et al., Bridging the gap between atmospheric concentrations and local ecosystem measurements, *Geophysical Research Letters*, 36(L19809), 1–5, doi:10.1029/2009GL039574, 2009b.
- Lauvaux, T., et al., Constraining the CO₂ budget of the corn belt: exploring uncertainties from the assumptions in a mesoscale inverse system, *Atmospheric Chemistry and Physics*, 12(1), 337–354, doi:10.5194/acp-12-337-2012, 2012b.
- Law, B., et al., Environmental controls over carbon dioxide and water vapor exchange of terrestrial vegetation, *Agricultural and Forest Meteorology*, 113(1-4), 97–120, doi:10.1016/S0168-1923(02)00104-1, 2002.
- Lawrence, D. M., et al., Parameterization improvements and functional and structural advances in version 4 of the Community Land Model, *Journal of Advances in Modeling Earth Systems*, 3, 1–29, 2011.
- Le Quéré, C., T. Takahashi, E. T. Buitenhuis, C. Rödenbeck, and S. C. Sutherland, Impact of climate change and variability on the global oceanic sink of CO₂, *Global Biogeochemical Cycles*, 24(GB4007), 1–10, doi:10.1029/2009GB003599, 2010.
- Le Quéré, C., et al., The global carbon budget 1959–2011, *Earth System Science Data*, 5(1), 165–185, doi:10.5194/essd-5-165-2013, 2013.
- Le Quéré, C., et al., Global carbon budget 2014, *Earth System Science Data*, 7(1), 47–85, doi:10.5194/essd-7-47-2015, 2015.
- Le Toan, T., et al., The BIOMASS mission: Mapping global forest biomass to better understand the terrestrial carbon cycle, *Remote Sensing of Environment*, 115(11), 2850–2860, doi:10.1016/j.rse.2011.03.020, 2011.
- Leuenberger, M. C., M. F. Schibig, and P. Nyfeler, Gas adsorption and desorption effects on cylinders and their importance for long-term gas records, *Atmospheric Measurement Techniques*, 8(12), 5289–5299, doi:10.5194/amt-8-5289-2015, 2015.
- Leuning, R., Temperature dependence of two parameters in a photosynthesis model, *Plant, Cell and Environment*, 25(9), 1205–1210, doi:10.1046/j.1365-3040.2002.00898.x, 2002.
- Levin, I., and U. Karstens, Inferring high-resolution fossil fuel CO₂ records at continental sites from combined 14co₂ and CO observations, *Tellus B*, 59B(2), 245–250, doi:10.1111/j.1600-0889.2006.00244.x, 2007.
- Levin, I., B. Kromer, M. Schmidt, and H. Sartorius, A novel approach for independent budgeting of fossil fuel CO₂ over Europe by 14co₂ observations, *Geophysical Research Letters*, 30(23), 1–5, doi:10.1029/2003GL018477, 2003.
- Levis, S., G. B. Bonan, E. Kluzek, P. E. Thornton, A. Jones, W. J. Sacks, and C. J. Kucharik, Interactive Crop Management in the Community Earth System Model (CESM1): Seasonal Influences on Land–Atmosphere Fluxes, *Journal of Climate*, 25(14), 4839–4859, doi:10.1175/JCLI-D-11-00446.1, 2012.
- Lin, J. C., and C. Gerbig, Accounting for the effect of transport errors on tracer inversions, *Geophysical Research Letters*, 32(1), 1–5, doi:10.1029/2004GL021127, 2005.
- Lin, J. C., C. Gerbig, S. C. Wofsy, A. E. Andrews, B. C. Daube, K. J. Davis, and C. A. Grainger, A near-field tool for simulating the upstream influence of atmospheric observations: The Stochastic Time-Inverted Lagrangian Transport (STILT) model, *Journal of Geophysical Research-Atmospheres*, 108(D16), 2003.

- Lin, J. C., et al., What have we learned from intensive atmospheric sampling field programmes of CO₂?, *Tellus B*, 58(5), 331–343, doi:10.1111/j.1600-0889.2006.00202.x, 2006.
- Louergue, L., et al., Orbital and millennial-scale features of atmospheric CH₄ over the past 800,000 years, *Nature*, 453(7193), 383–386, doi:10.1038/nature06950, 2008.
- Lu, Y., J. Jin, and L. M. Kueppers, Crop growth and irrigation interact to influence surface fluxes in a regional climate-cropland model (WRF3.3-CLM4crop), *Climate Dynamics*, 45(11-12), 3347–3363, doi:10.1007/s00382-015-2543-z, 2015.
- Lüthi, D., et al., High-resolution carbon dioxide concentration record 650,000–800,000 years before present., *Nature*, 453(7193), 379–382, doi:10.1038/nature06949, 2008.
- Mahadevan, P., et al., A satellite-based biosphere parameterization for net ecosystem CO₂ exchange: Vegetation Photosynthesis and Respiration Model (VPRM), *Global Biogeochemical Cycles*, 22(GB2005), 1–17, doi:10.1029/2006GB002735, 2008.
- Manning, A. J., D. B. Ryall, R. G. Derwent, P. G. Simmonds, and S. O’Doherty, Estimating European emissions of ozone-depleting and greenhouse gases using observations and a modeling back-attribution technique, *Journal of Geophysical Research*, 108(D14), 4405, doi:10.1029/2002JD002312, 2003.
- Masarie, K. A., and P. P. Tans, Extension and integration of atmospheric carbon dioxide data into a globally consistent measurement record, *Journal of Geophysical Research*, 100(D6), 11,593–11,610, doi:10.1029/95JD00859, 1995.
- Matross, D. M., et al., Estimating regional carbon exchange in New England and Quebec by combining atmospheric, ground-based and satellite data, *Tellus*, 58B(5), 344–358, doi:10.1111/j.1600-0889.2006.00206.x, 2006.
- Meesters, A. G. C. A., et al., Inverse carbon dioxide flux estimates for the Netherlands, *Journal of Geophysical Research: Atmospheres*, 117(D20306), 1–13, doi:10.1029/2012JD017797, 2012.
- MeteoSwiss, Klimabulletin Jahr 2013, *Tech. rep.*, Bundesamt für Meteorologie und Klimatologie MeteoSchweiz, Zurich, Switzerland, 2014.
- MeteoSwiss, Klimabulletin Jahr 2014, *Tech. rep.*, Bundesamt für Meteorologie und Klimatologie MeteoSchweiz, Zurich, Switzerland, 2015.
- MeteoSwiss, Klimabulletin Jahr 2015, *Tech. rep.*, Bundesamt für Meteorologie und Klimatologie MeteoSchweiz, Zurich, Switzerland, 2016.
- Meyre, S., Landwirtschaft und Ernährung - Taschenstatistik 2016, *Tech. Rep. 871-1600*, Bundesamt für Statistik (BFS), Neuchâtel, Switzerland, 2016.
- Michalak, A. M., Interactive comment on “An objective prior error quantification for regional atmospheric inverse applications” by P. Kountouris et al., *Biogeosciences Discussions*, 12, C5507–C5512, 2015.
- Michalak, A. M., A. Hirsch, L. Bruhwiler, K. R. Gurney, W. Peters, and P. P. Tans, Maximum likelihood estimation of covariance parameters for Bayesian atmospheric trace gas surface flux inversions, *Journal of Geophysical Research*, 110(D24107), 1–16, doi:10.1029/2005JD005970, 2005.
- Miles, N. L., S. J. Richardson, K. J. Davis, T. Lauvaux, A. E. Andrews, T. O. West, V. Bandaru, and E. R. Crosson, Large amplitude spatial and temporal gradients in atmospheric boundary layer CO₂ mole fractions detected with a tower-based network in the U.S. upper Midwest, *Journal of Geophysical Research*, 117(G01019), 1–13, doi:10.1029/2011JG001781, 2012.

- Miller, J. B., et al., Linking emissions of fossil fuel CO₂ and other anthropogenic trace gases using atmospheric 14CO₂, *Journal of Geophysical Research: Atmospheres*, 117(8), doi:10.1029/2011JD017048, 2012.
- Mohn, J., S. Szidat, J. Fellner, H. Rechberger, R. Quartier, B. Buchmann, and L. Emmenegger, Determination of biogenic and fossil CO₂ emitted by waste incineration based on 14CO₂ and mass balances, *Bioresource Technology*, 99(14), 6471–6479, doi:10.1016/j.biortech.2007.11.042, 2008.
- Mészáros, T., L. Haszpra, and A. Gelencsér, Tracking changes in carbon monoxide budget over Europe between 1995 and 2000, *Atmospheric Environment*, 39(38), 7297–7306, doi:10.1016/j.atmosenv.2005.09.021, 2005.
- Noilhan, J., and S. Planton, A simple parameterization of land surface processes for meteorological models, *Monthly Weather Review*, 117(3), 536–549, 1989.
- Novelli, P. C., J. W. Elkins, and L. P. Steele, The development and evaluation of a gravimetric reference scale for measurements of atmospheric carbon monoxide, *Journal of Geophysical Research: Atmospheres*, 96(D7), 13,109–13,121, 1991.
- Ogle, S. M., et al., An approach for verifying biogenic greenhouse gas emissions inventories with atmospheric CO₂ concentration data, *Environmental Research Letters*, 10, 1–11, doi:10.1088/1748-9326/10/3/034012, 2015.
- Olivier, J., G. Janssens-Maenhout, J. Peters, and J. Wilson, Long Term Trend in Global CO₂ Emissions, *Tech. rep.*, PBL Netherlands Environmental Assessment Agency and European Commission Publications Office, The Hague (Netherlands), 2011.
- Olivier, J. G. J., J. A. V. Aardenne, F. J. Dentener, V. Pagliari, L. N. Ganzeveld, and J. A. H. W. Peters, Recent trends in global greenhouse gas emissions: regional trends 1970–2000 and spatial distribution of key sources in 2000, *Environmental Sciences*, 2(2-3), 81–99, doi:10.1080/15693430500400345, 2005.
- Oney, B., S. Henne, N. Gruber, M. Leuenberger, I. Bamberger, W. Eugster, and D. Brunner, The CarboCount CH sites: characterization of a dense greenhouse gas observation network, *Atmospheric Chemistry and Physics*, 15(19), 11,147–11,164, doi:10.5194/acp-15-11147-2015, 2015.
- Pan, Y., et al., A large and persistent carbon sink in the world's forests., *Science*, 333(6045), 988–993, doi:10.1126/science.1201609, 2011.
- Peters, W., J. B. Miller, J. Whitaker, A. S. Denning, A. Hirsch, M. C. Krol, D. Zupanski, L. Bruhwiler, and P. P. Tans, An ensemble data assimilation system to estimate CO₂ surface fluxes from atmospheric trace gas observations, *Journal of Geophysical Research*, 110(D24), doi:10.1029/2005JD006157, 2005.
- Peters, W., et al., An atmospheric perspective on North American carbon dioxide exchange: CarbonTracker., *Proceedings of the National Academy of Sciences of the United States of America*, 104(48), 18,925–18,930, doi:10.1073/pnas.0708986104, 2007.
- Peters, W., et al., Seven years of recent European net terrestrial carbon dioxide exchange constrained by atmospheric observations, *Global Change Biology*, 16(4), 1317–1337, doi:10.1111/j.1365-2486.2009.02078.x, 2010.
- Petit, J. R., et al., Climate and atmospheric history of the past 420,000 years from the Vostok ice core, Antarctica, *Nature*, 399, 429–413, doi:10.1038/20859, 1999.
- Peylin, P., P. J. Rayner, P. Bousquet, C. Carouge, F. Hourdin, P. Heinrich, P. Ciais, and A. contributors, Daily CO₂ flux estimates over Europe from continuous atmospheric measurements: 1, inverse methodology, *Atmospheric Chemistry and Physics*, 5(12), 3173–3186, doi:10.5194/acp-5-3173-2005, 2005.

- Peylin, P., et al., Importance of fossil fuel emission uncertainties over Europe for CO₂ modeling: model intercomparison, *Atmospheric Chemistry and Physics*, 11(13), 6607–6622, doi:10.5194/acp-11-6607-2011, 2011.
- Peylin, P., et al., Global atmospheric carbon budget: results from an ensemble of atmospheric CO₂ inversions, *Biogeosciences*, 10(10), 6699–6720, doi:10.5194/bg-10-6699-2013, 2013.
- Phillips, O. L., et al., Drought sensitivity of the Amazon rainforest, *Science*, 323(5919), 1344–1347, doi:10.1126/science.1164033, 2009.
- Pillai, D., C. Gerbig, R. Ahmadov, C. Rödenbeck, R. Kretschmer, T. Koch, R. Thompson, B. Neininger, and J. V. Lavrié, High-resolution simulations of atmospheric CO₂ over complex terrain – representing the Ochsenkopf mountain tall tower, *Atmospheric Chemistry and Physics*, 11(15), 7445–7464, doi:10.5194/acp-11-7445-2011, 2011.
- Pillai, D., C. Gerbig, R. Kretschmer, V. Beck, U. Karstens, B. Neininger, and M. Heimann, Comparing Lagrangian and Eulerian models for CO₂ transport – a step towards Bayesian inverse modeling using WRF/STILT-VPRM, *Atmospheric Chemistry and Physics*, 12(19), 8979–8991, doi:10.5194/acp-12-8979-2012, 2012.
- Pitt, J. R., et al., The development and evaluation of airborne in situ N₂O and CH₄ sampling using a quantum cascade laser absorption spectrometer (QCLAS), *Atmospheric Measurement Techniques*, 9(1), 63–77, doi:10.5194/amt-9-63-2016, 2016.
- Potosnak, M. J., S. Wofsy, A. S. Denning, J. W. Munger, and D. H. Barnes, Influence of biotic exchange and combustion sources on atmospheric CO₂ concentrations in New England from observations at a forest flux tower, *Journal of Geophysical Research*, 104, 9561–9569, 1999.
- Powers, W., et al., Quantifying Greenhouse Gas Sources and Sinks in Animal Production Systems, in *Quantifying Greenhouse Gas Fluxes in Agriculture and Forestry: Methods for Entity-Scale Inventory*, edited by M. Eve, D. Pape, M. Flugge, R. Steele, D. Man, M. Riley-Gilbert, and S. Biggar, technical ed., p. 606, Office of the Chief Economist, U.S. Department of Agriculture, Washington, DC, 2014.
- Prentice, I. C., and S. P. Harrison, Ecosystem effects of CO₂ concentration: evidence from past climates, *Climate of the Past*, 5(3), 297–307, doi:10.5194/cp-5-297-2009, 2009.
- R Core Team, *R: A Language and Environment for Statistical Computing*, R Foundation for Statistical Computing, Vienna, Austria, 2014.
- Raschendorfer, M., New features of the common turbulence parameterization for COSMO and ICON, 2016.
- Rayner, P. J., M. Scholze, W. Knorr, T. Kaminski, R. Giering, and H. Widmann, Two decades of terrestrial carbon fluxes from a carbon cycle data assimilation system (CCDAS), *Global Biogeochem Cycles*, 19(GB2026), 1–23, doi:10.1029/2004GB002254, 2005.
- Regnier, P., et al., Anthropogenic perturbation of the carbon fluxes from land to ocean, *Nature Geoscience*, 6(8), 597–607, doi:10.1038/ngeo1830, 2013.
- Reichstein, M., et al., Reduction of ecosystem productivity and respiration during the European summer 2003 climate anomaly: a joint flux tower, remote sensing and modelling analysis, *Global Change Biology*, 13(3), 634–651, doi:10.1111/j.1365-2486.2006.01224.x, 2007.
- Rella, C. W., et al., High accuracy measurements of dry mole fractions of carbon dioxide and methane in humid air, *Atmospheric Measurement Techniques*, 6(3), 837–860, doi:10.5194/amt-6-837-2013, 2013.

- Richardson, S. J., N. L. Miles, K. J. Davis, E. R. Crosson, C. W. Rella, and A. E. Andrews, Field Testing of Cavity Ring-Down Spectroscopy Analyzers Measuring Carbon Dioxide and Water Vapor, *Journal of Atmospheric and Oceanic Technology*, 29(3), 397–406, doi:10.1175/JTECH-D-11-00063.1, 2012.
- Rigby, M., a. J. Manning, and R. G. Prinn, Inversion of long-lived trace gas emissions using combined Eulerian and Lagrangian chemical transport models, *Atmospheric Chemistry and Physics*, 11(18), 9887–9898, doi:10.5194/acp-11-9887-2011, 2011.
- Roedenbeck, C., C. Gerbig, K. Trusilova, and M. Heimann, A two-step scheme for high-resolution regional atmospheric trace gas inversions based on independent models, *Atmospheric Chemistry and Physics*, 9(1), 1727–1756, doi:10.5194/acpd-9-1727-2009, 2009.
- Rotach, M. W., G. Wohlfahrt, A. Hansel, M. Reif, J. Wagner, and A. Gohm, The World is Not Flat: Implications for the Global Carbon Balance, *Bulletin of the American Meteorological Society*, 95(7), 1021–1028, doi:10.1175/BAMS-D-13-00109.1, 2014.
- Ruckstuhl, A. F., S. Henne, S. Reimann, M. Steinbacher, M. K. Vollmer, S. O'Doherty, B. Buchmann, and C. Hueglin, Robust extraction of baseline signal of atmospheric trace species using local regression, *Atmospheric Measurement Techniques*, 5(11), 2613–2624, doi:10.5194/amt-5-2613-2012, 2012.
- Rödenbeck, C., S. Houweling, M. Gloor, and M. Heimann, CO₂ flux history 1982–2001 inferred from atmospheric data using a global inversion of atmospheric transport, *Atmospheric Chemistry and Physics*, 3(6), 1919–1964, doi:10.5194/acp-3-1919-2003, 2003.
- Saatchi, S. S., et al., Benchmark map of forest carbon stocks in tropical regions across three continents, *Proceedings of the National Academy of Sciences*, 108(24), 9899–9904, doi:10.1073/pnas.1019576108, 2011.
- Sabine, C. L., et al., The Oceanic Sink for Anthropogenic CO₂, *Science*, 305(5682), 367–371, doi:10.1126/science.1097403, 2004.
- Saeki, T., et al., Carbon flux estimation for Siberia by inverse modeling constrained by aircraft and tower CO₂ measurements, *Journal of Geophysical Research: Atmospheres*, 118(2), 1100–1122, doi:10.1002/jgrd.50127, 2013.
- Sander, S. P., et al., JPL Publication 06-2: Chemical Kinetics and Photochemical Data for Use in Atmospheric Studies, *Tech. Rep. Evaluation Number 15*, National Aeronautics and Space Administration, Pasadena, CA, 2006.
- Sarmiento, J. L., M. Gloor, N. Gruber, C. Beaulieu, a. R. Jacobson, S. E. Mikaloff Fletcher, S. Pacala, and K. Rodgers, Trends and regional distributions of land and ocean carbon sinks, *Biogeosciences*, 7(8), 2351–2367, doi:10.5194/bg-7-2351-2010, 2010.
- Sasakawa, M., et al., Continuous measurements of methane from a tower network over Siberia, *Tellus B*, 62B(5), 403–416, doi:10.1111/j.1600-0889.2010.00494.x, 2010.
- Satar, E., T. A. Berhanu, D. Brunner, S. Henne, and M. Leuenberger, Continuous CO₂/CH₄/CO measurements (2012–2014) at Beromünster tall tower station in Switzerland, *Biogeosciences*, 13(9), 2623–2635, doi:10.5194/bg-13-2623-2016, 2016.
- Schibig, M. F., M. Steinbacher, B. Buchmann, I. T. van der Laan-Luijkx, S. van der Laan, S. Ranjan, and M. C. Leuenberger, Comparison of continuous in situ CO₂ observations at Jungfraujoch using two different measurement techniques, *Atmospheric Measurement Techniques*, 8(1), 57–68, doi:10.5194/amt-8-57-2015, 2015.

- Schmidt, M., R. Graul, H. Sartorius, and I. Levin, Carbon dioxide and methane in continental Europe: A climatology, and 222radon-based emission estimates, *Tellus*, 48B, 457–473, 1996.
- Scholze, M., T. Kaminski, P. Rayner, W. Knorr, and R. Giering, Propagating uncertainty through prognostic carbon cycle data assimilation system simulations, *Journal of Geophysical Research: Atmospheres*, 112(17), 1–13, doi:10.1029/2007JD008642, 2007.
- Schraff, C. H., Mesoscale data assimilation and prediction of low stratus in the Alpine region, *Meteorology and Atmospheric Physics*, 64, 21–50, 1997.
- Schuh, A. E., et al., Evaluating atmospheric CO₂ inversions at multiple scales over a highly inventoried agricultural landscape, *Global Change Biology*, 19, 1424–1439, doi:10.1111/gcb.12141, 2013.
- Seibert, P., and A. Frank, Source-receptor matrix calculation with a Lagrangian particle dispersion model in backward mode, *Atmospheric Chemistry and Physics*, 4(1), 51–63, doi:10.5194/acp-4-51-2004, 2004.
- Sellers, P. J., D. A. Randall, G. J. Collatz, J. A. Berry, C. B. Field, D. A. Dazlich, C. Zhang, G. D. Collelo, and L. Bounoua, A revised land surface parameterization (SiB2) for atmospheric GCMs. Part I: Model formulation, *Journal of Climate*, 9(4), 676–705, 1996.
- Siegenthaler, U., et al., Stable Carbon Cycle-Climate Relationship During the Late Pleistocene, *Science*, 310, 1313–1317, doi:10.1126/science.1120130, 2005.
- Smil, V., *The Earth's biosphere: Evolution, dynamics, and change*, MIT Press, 2003.
- Stein, O., M. G. Schultz, I. Bouarar, H. Clark, V. Huijnen, A. Gaudel, M. George, and C. Clerbaux, On the wintertime low bias of Northern Hemisphere carbon monoxide found in global model simulations, *Atmospheric Chemistry and Physics*, 14(17), 9295–9316, doi:10.5194/acp-14-9295-2014, 2014.
- Stephan, K., S. Klink, and C. Schraff, Assimilation of radar-derived rain rates into the convective-scale model COSMO-DE at DWD, *Quarterly Journal of the Royal Meteorological Society*, 134, 1315–1326, doi:10.1002/qj.269, 2008.
- Stephens, B. B., N. L. Miles, S. J. Richardson, A. S. Watt, and K. J. Davis, Atmospheric CO₂ monitoring with single-cell NDIR-based analyzers, *Atmospheric Measurement Techniques*, 4(12), 2737–2748, doi:10.5194/amt-4-2737-2011, 2011.
- Stephens, B. B., et al., Weak northern and strong tropical land carbon uptake from vertical profiles of atmospheric CO₂, *Science*, 316(5832), 1732–1735, doi:10.1126/science.1137004, 2007.
- Stocker, B. D., R. Roth, F. Joos, R. Spahni, M. Steinacher, S. Zaehle, L. Bouwman, Xu-Ri, and I. C. Prentice, Multiple greenhouse-gas feedbacks from the land biosphere under future climate change scenarios, *Nature Climate Change*, 3(7), 666–672, doi:10.1038/nclimate1864, 2013.
- Stohl, A., Trajectory statistics - A new method to establish source-receptor relationships of air pollutants and its application to the transport of particulate sulfate in Europe, *Atmospheric Environment*, 30(4), 579–587, doi:10.1016/1352-2310(95)00314-2, 1996.
- Stohl, A., C. Forster, A. Frank, P. Seibert, and G. Wotawa, Technical note: The Lagrangian particle dispersion model FLEXPART version 6.2, *Atmospheric Chemistry and Physics*, 5, 2461–2474, 2005.
- Stöckli, R., and P. Vidale, European plant phenology and climate as seen in a 20-year AVHRR land-surface parameter dataset, *International Journal of Remote Sensing*, 25(17), 3303–3330, doi:10.1080/01431160310001618149, 2004.

- Stöckli, R., T. Rutishauser, D. Dragoni, J. O’Keefe, P. E. Thornton, M. Jolly, L. Lu, and a. S. Denning, Remote sensing data assimilation for a prognostic phenology model, *Journal of Geophysical Research: Biogeosciences*, *113*(G04021), 1–19, doi:10.1029/2008JG000781, 2008.
- Suess, H., Radiocarbon Concentration in Modern Wood, *Science*, *122*(3166), 415–417, doi:10.1126/science.122.3166.415-a, 1955.
- Suntharalingam, P., Improved quantification of Chinese carbon fluxes using CO₂/CO correlations in Asian outflow, *Journal of Geophysical Research*, *109*(D18), doi:10.1029/2003JD004362, 2004.
- Suyker, A. E., S. B. Verma, G. G. Burba, and T. J. Arkebauer, Gross primary production and ecosystem respiration of irrigated maize and irrigated soybean during a growing season, *Agricultural and Forest Meteorology*, *131*, 180–190, doi:10.1016/j.agrformet.2005.05.007, 2005.
- Szegvary, T., F. Conen, U. Stöhlker, G. Dubois, P. Bossew, and G. de Vries, Mapping terrestrial - dose rate in Europe based on routine monitoring data, *Radiation Measurements*, *42*(9), 1561–1572, doi:10.1016/j.radmeas.2007.09.002, 2007.
- Tans, P., and C. Zellweger, GAW Report No. 213, 17th WMO/IAEA Meeting on Carbon Dioxide, Other Greenhouse Gases and Related Tracers Measurement Techniques (GGMT-2013), *Tech. rep.*, World Meteorological Organization, Geneva, Switzerland, 2014.
- Tans, P. P., P. S. Bakwin, and D. W. Guenther, A feasible Global Carbon Cycle Observing System: a plan to decipher today’s carbon cycle based on observations, *Global Change Biology*, *2*(3), 309–318, doi:10.1111/j.1365-2486.1996.tb00082.x, 1996.
- Thiruchittampalam, B., Entwicklung und Anwendung von Methoden und Modellen zur Berechnung von räumlich und zeitlich hochaufgelösten Emissionen in Europa, Ph.D. thesis, University of Stuttgart, 2014.
- Thoning, K. W., P. P. Tans, and W. D. Komhyr, Atmospheric carbon dioxide at Mauna Loa Observatory: 2. Analysis of the NOAA GMCC data, 1974–1985, *Journal of Geophysical Research*, *94*(D6), 8549–8565, doi:10.1029/JD094iD06p08549, 1989.
- Thunis, P., et al., Evaluation of a Sectoral Approach to Integrated Assessment Modelling including the Mediterranean Sea, *Tech. rep.*, Joint Research Center, Ispra, Italy, 2008.
- Tiedtke, M., A comprehensive mass flux scheme for cumulus parameterization in large-scale models, *Monthly Weather Review*, *117*, 1779–1800, 1989.
- Tolk, L. F., A. G. C. A. Meesters, A. J. Dolman, and W. Peters, Modelling representation errors of atmospheric CO₂ concentrations at a regional scale, *Atmospheric Chemistry and Physics*, *8*, 6587–6596, doi:10.5194/acp-8-6587-20082008, 2008.
- Tolk, L. F., A. J. Dolman, A. G. C. A. Meesters, and W. Peters, A comparison of different inverse carbon flux estimation approaches for application on a regional domain, *Atmospheric Chemistry and Physics*, *11*(20), 10,349–10,365, doi:10.5194/acp-11-10349-2011, 2011.
- Turnbull, J. C., J. B. Miller, S. J. Lehman, P. P. Tans, R. J. Sparks, and J. Southon, Comparison of 14C, CO, and SF₆ as tracers for recently added fossil fuel CO₂ in the atmosphere and implications for biological CO₂ exchange, *Geophysical Research Letters*, *33*(1), 2–6, doi:10.1029/2005GL024213, 2006.
- Turnbull, J. C., et al., Assessment of fossil fuel carbon dioxide and other anthropogenic trace gas emissions from airborne measurements over Sacramento, California in spring 2009, *Atmospheric Chemistry and Physics*, *11*(2), 705–721, doi:10.5194/acp-11-705-2011, 2011.

- Van Der Laan, S., U. Karstens, R. Neubert, I. Van Der Laan-Luijkx, and H. Meijer, Observation-based estimates of fossil fuel-derived CO₂ emissions in the Netherlands using D14c, CO and 222radon, *Tellus B*, 62(5), 389–402, doi:10.1111/j.1600-0889.2010.00493.x, 2010.
- van der Laan, S., I. T. van der Laan-Luijkx, L. Zimmermann, F. Conen, and M. Leuenberger, Net CO₂ surface emissions at Bern, Switzerland inferred from ambient observations of CO₂, d(O₂/N₂), and 222rn using a customized radon tracer inversion, *Journal of Geophysical Research*, 119, 1580–1591, doi:10.1002/2013JD020307, 2014.
- van der Molen, M. K., and A. J. Dolman, Regional carbon fluxes and the effect of topography on the variability of atmospheric CO₂, *Journal of Geophysical Research: Atmospheres*, 112, 1–16, doi:10.1029/2006JD007649, 2007.
- Vardag, S. N., C. Gerbig, G. Janssens-Maenhout, and I. Levin, Estimation of continuous anthropogenic CO₂: model-based evaluation of CO₂, CO, d13c(CO₂) and D14c(CO₂) tracer methods, *Atmospheric Chemistry and Physics*, 15(22), 12,705–12,729, doi:10.5194/acp-15-12705-2015, 2015.
- Verma, S. B., et al., Annual carbon dioxide exchange in irrigated and rainfed maize-based agroecosystems, *Agricultural and Forest Meteorology*, 131(1-2), 77–96, doi:10.1016/j.agrformet.2005.05.003, 2005.
- Vermeulen, A., et al., CHIOTTO - Continuous High-Precision Tall Tower Observations of Greenhouse Gases, *Tech. rep.*, ECN - Energy research Centre of the Netherlands, 2004.
- Vermeulen, A. T., A. Hensen, M. E. Popa, W. C. M. van den Bulk, and P. A. C. Jongejan, Greenhouse gas observations from Cabauw Tall Tower (1992–2010), *Atmospheric Measurement Techniques*, 4(3), 617–644, doi:10.5194/amt-4-617-2011, 2011.
- Vesala, T., N. Kljun, U. Rannik, J. Rinne, A. Sogachev, T. Markkanen, K. Sabelfeld, T. Foken, and M. Y. Leclerc, Flux and concentration footprint modelling: state of the art., *Environmental pollution*, 152(3), 653–666, doi:10.1016/j.envpol.2007.06.070, 2008.
- Vogel, F., B. Tiruchittampalam, J. Theloke, R. Kretschmer, C. Gerbig, S. Hammer, and I. Levin, Can we evaluate a fine-grained emission model using high-resolution atmospheric transport modelling and regional fossil fuel CO₂ observations?, *Tellus B*, 1, 1–16, 2013.
- Vogel, F. R., S. Hammer, A. Steinhof, B. Kromer, and I. Levin, Implication of weekly and diurnal 14c calibration on hourly estimates of CO₂-based fossil fuel CO₂ at a moderately polluted site in southwestern Germany, *Tellus B*, 62(5), 512–520, doi:10.1111/j.1600-0889.2010.00477.x, 2010.
- Wade, L., A pristine Amazon’s last stand, *Science*, 347(6226), 1051–1052, doi:10.1126/science.347.6226.1051, 2015.
- Weusthoff, T., Weather Type Classification at MeteoSwiss - Introduction of new automatic classification schemes, *Tech. Rep. 235*, MeteoSchweiz, Zurich, Switzerland, 2011.
- Winderlich, J., H. Chen, C. Gerbig, T. Seifert, O. Kolle, J. V. Lavrič, C. Kaiser, A. Höfer, and M. Heimann, Continuous low-maintenance CO₂/CH₄/H₂O measurements at the Zotino Tall Tower Observatory (ZOTTO) in Central Siberia, *Atmospheric Measurement Techniques*, 3(4), 1113–1128, doi:10.5194/amt-3-1113-2010, 2010.
- Wood, S. N., and N. H. Augustin, GAMs with integrated model selection using penalized regression splines and applications to environmental modelling, *Ecological Modelling*, 157(2-3), 157–177, doi:10.1016/S0304-3800(02)00193-X, 2002.

- Worthy, D. E. J., A. Platt, R. Kessler, M. Ernst, R. Braga, and S. Racki, The Canadian Atmospheric Carbon Dioxide Measurement Program: Measurement Procedures, Data Quality and Accuracy, in *Report of the 11th WMO/IAEA Meeting of Experts on Carbon Dioxide Concentration and Related Tracer Measurement Techniques*, edited by S. Toru, S. and Kazuto, pp. 112–128, World Meteorological Organization Global Atmosphere Watch, Tokyo, Japan, 2003.
- Zahorowski, W., S. D. Chambers, and A. Henderson-Sellers, Ground based radon-222 observations and their application to atmospheric studies., *Journal of Environmental Radioactivity*, 76(1-2), 3–33, doi:10.1016/j.jenvrad.2004.03.033, 2004.
- Zeeman, M. J., R. Hiller, A. K. Gilgen, P. Michna, P. Plüss, N. Buchmann, and W. Eugster, Management and climate impacts on net CO₂ fluxes and carbon budgets of three grasslands along an elevational gradient in Switzerland, *Agricultural and Forest Meteorology*, 150(4), 519–530, doi:10.1016/j.agrformet.2010.01.011, 2010.
- Zellweger, C., J. Forrer, P. Hofer, S. Nyeki, B. Schwarzenbach, E. Weingartner, M. Ammann, and U. Baltensperger, Partitioning of reactive nitrogen (NO_y) and dependence on meteorological conditions in the lower free troposphere, *Atmospheric Chemistry and Physics*, 3, 779–796, 2003.
- Zellweger, C., M. Steinbacher, and B. Buchmann, Evaluation of new laser spectrometer techniques for in-situ carbon monoxide measurements, *Atmospheric Measurement Techniques*, 5(10), 2555–2567, doi:10.5194/amt-5-2555-2012, 2012.
- Zhao, C. L., and P. P. Tans, Estimating uncertainty of the WMO mole fraction scale for carbon dioxide in air, *Journal of Geophysical Research*, 111(D08S09), 1–10, doi:10.1029/2005JD006003, 2006.
- Zondervan, A., and H. A. J. Meijer, Isotopic characterisation of CO₂ sources during regional pollution events using isotopic and radiocarbon analysis, *Tellus B*, 48(4), 601–612, doi:10.1034/j.1600-0889.1996.00013.x, 1996.

Curriculum vitae

Brian Johannes Oney

Male, born Nov. 9th 1984, in Carlsbad, NM, USA

Email: brian.j.oney@gmail.com

Education

04/12–01/16	Ph.D. at Empa, Laboratory for Air Pollution / Env. Technology, Dübendorf, Switzerland, under supervision of Dr. Dominik Brunner and Prof. Dr. Nicolas Gruber – Center for Climate Systems Modeling, ETH Zurich
10/08–10/11	Master of Science in Global Change Ecology, Thesis supervised by Björn Reineking and Jürgen Kreyling – University of Bayreuth
9/03–5/07	Bachelor of Arts in German Studies <i>cum laude</i> – Weber State University (WSU)
9/03–5/07	Bachelor of Science in Zoology with Chemistry Minor <i>cum laude</i> – WSU

Literary Works

Oney, B.J., N. Gruber, S. Henne, M. Leuenberger, and D. Brunner, A CO₂-based method to determine the regional biospheric signal in atmospheric CO₂. *Tellus B*, submitted, 2016.

Oney, B. J., Toward using atmospheric carbon dioxide observations to estimate the biospheric carbon flux of the Swiss Plateau, Ph. D., ETH Zurich, Zurich, Switzerland, doi:10.3929/ethz-a-010677958, 2016.

Oney, B.J., S. Henne, N. Gruber, M. Leuenberger, I. Bamberger, W. Eugster, and D. Brunner, The CarboCount CH sites: characterization of a dense greenhouse gas observation network, *Atmospheric Chemistry and Physics*, 15(19), 11,147–11,164, doi:10.5194/acp-15-11147-2015, 2015.

Oney, B.J., Reineking, B., O'Neill, G., Kreyling, J. Intraspecific variation buffers projected climate change impacts on *Pinus contorta*. *Ecology & Evolution* 3(2): 437–449, doi:10.1002/ece3.426, 2013.

Oney, B.J., Shapiro, A., Wegmann, M., Evolution of water quality around the Island of Borneo during the last 8 years. *Procedia Environmental Sciences* 7: 200–205, doi:10.1016/j.proenv.2011.07.035, 2011.

Oney, B.J., Shapiro, A., Wegmann, M., Dech, S. (2011) Land use change affects coastal water quality around Borneo. Proceedings of the 34th International Symposium on Remote Sensing of Environment, April 10-15, 2011, Sydney, Australia.

Thanks

I would above all like to thank my advisor Dominik Brunner for his insight, patience, and tireless support. Without his support, most components for this dissertation would not have come to be. Stephan Henne provided code, patience, rigor, and humor, without which many of the modeling goals and CarboCount would have been wishful thinking. I greatly appreciate the time, and wisdom of my doctoral supervisor Niki Gruber. Without his exemplary guidance, I would not have learned a delicate balance between critical review and acceptance that provides fundament for progress and collaboration. Thanks to Lukas Emmenegger for helping to keep me on track. Thank you very much to Christoph Gerbig for kindly agreeing to review my dissertation. Thank you Nina Buchmann for sovereignly supervising my thesis defense and enriching its discussion.

I greatly appreciate the support of and fruitful discussions with Christoph Zellweger and Martin Steinbacher. Without their guidance and experience in measurement technique, it is possible that the measurement system at Lägern-Hochwacht or at Frübüel would not have worked. On the contrary, these systems functioned so well, that they were often forgotten, which left time for modeling and writing papers. Furthermore, their willingness to help encouraged me to ask and learn regardless how elementary the question. Martin Vollmer was instrumental in both the installation at Lägern-Hochwacht and the filling of the 21 aluminum bottles for the CarboCount CH project. His experience and detailed attention helped a great deal with initiation of the project.

Within CarboCount CH, my thanks is due to Markus Leuenberger, Ece Satar, Tesfaye Berhanu, René Bleisch, and especially to Rüdiger Schanda of the University of Bern for being patient with me. I hope the Beromünster and Gimmiz site run well for years to come.

Thank you to Erich Graf and Thomas Lehmann of Skyguide for the unrelenting and quick support the set-up and maintenance of the Lägern-Hochwacht measurement site. Have fun and be safe on the towers!

Thank you to my two fellows for the psychological support, well-meant insults, and bad jokes. Simon Eyer and Fabian Schoenenberger gave misery company à la suisse and hopefully will soon find release from the “joys” of being a PhD student at Empa. Thank you also to another fellow, Pascal Butti, for the philosophical walks and insight into music culture.

Thank you to Eliza Harris and Franz Holzknecht, Jana Jagerska, Markus Mangold, and Benjamin and Diana Wolf for the many wonderful evenings playing Schafkopf and Jassen. Gerne wieder! Thank you to the float crews for sharing time on the Limmat: Erkan Ibraim, Florian Arfeuille, Antoine Berchet, Gianluca Mussetti. To Julien Anet, Gianluca, Florian, and Fabian, hopefully we can get some ski tours in this winter, and more river floats next summer!

Thank you Carole Delemont for initiating ninepins (Chegle). Thank you Robert Gehrig, Joachim Mohn, and Christoph Hüglin for the suspense. Thanks to the rest for good sportsmanship and losing gracefully (except Lukas). I hope ninepins becomes tradition in this lab.

Thank you Béla Tuzson for the philosophical discussions about culture, politics, and science. Thank you

Stefan Bugmann for the beers and smiles. I know you will enjoy helping others after Empa. Thanks to new and gone office colleagues for the beers and laughs: Christoph Popp, Christoph Knote, Eirini Boleti, Yvo Strebel, Morten Hundt, Wilhelm Gutjahr, and Rebecca Hiller.

Thank you to Carl Beierkuhnlein for instrumenting the Global Change Ecology program at the University of Bayreuth for motivating me to study policy relevant environmental science. Thank you to my master's thesis advisors Björn Reineking and Jürgen Kreyling for the patience and support of my first dive into the analysis of environmental data.

Thanks to Tim Besser for looking over my German and for keeping my thoughts on sustainability grounded in reality.

Of course, great appreciation goes to my parents and little sister for their perspective, support, and love. I'll come home one of these days.

Without my wonderful girlfriend Sia Gosheva, life would be less exciting and less complete. Furthermore, her detailed comments and proofreading of this thesis most certainly improved its quality. I appreciate her patience, support, and love far beyond my ability to express this gratitude.